School of Earth and Planetary Sciences

Further Development and Testing of the Combined U-Th-disequilibrium/U-Pb and (U-Th)/He Zircon Dating Method and its Application to Quaternary Volcanic Rocks

Ruby Connemara Marsden
0000-0003-1681-6859

This thesis is presented for the Degree of
Doctor of Philosophy
of
Curtin University

August 2021

Declaration

To the best of my knowledge and belief this thesis contains no material previously published by any other person except where due acknowledgement has been made. This thesis contains no material which has been accepted for the award of any other degree or diploma in any university.

I have permission from the copyright owners to use my own published journal articles in which the copyright is held by the publishers. Every reasonable effort has been made to acknowledge the owners of copyright material. I would be pleased to hear from any copyright owner who has been omitted or incorrectly acknowledged.

<div align="right">

Ruby C. Marsden

18th of August, 2021

</div>

Acknowledgement of Country

I acknowledge the Traditional Custodians of this land on which I live, work and study, the Whadjuk people of the Noongar nation. I recognise the contributions of the Whadjuk people of the Noongar nation, as the first scientists of this land. I am respectful of their Elders past, present and emerging, and acknowledge they are the keepers of the local traditional Whadjuk culture, stories, sites, and natural environments in this region.

Abstract

Quaternary volcanic rocks can be found throughout the global geological record, occurring in many different formations, from lavas and ignimbrites, to ash layers in sediments. Dating young volcanic products is vitally important for understanding eruptive timescales of volcanoes and therefore hazard prediction. Additionally, the eruptive ages of tephra can be used as important isochronous markers in stratigraphy as ash can be widely dispersed and deposited thousands of kilometres from the source volcano.

Volcanic eruptions that are <1 Ma can be challenging to date, especially if specific minerals are not present in the eruptive product. Zircon double-dating (ZDD) is one of the few techniques that can be used to date young volcanic rocks, and combines the (U-Th)/He method with individual zircon crystallisation ages to yield eruption ages. For simplicity, crystallisation ages obtained by U-Pb or U-Th disequilibrium methods, are typically determined on the rim of the grain. While it is understood that zircon crystallisation is often more complex, interrogating the full crystallisation history (i.e., making these measurements on the core of the grains) introduces additional analytical complexities for eruption age determination.

This thesis presents several methodological improvements to ZDD including: evaluating the impact of interrogating the full crystallisation history on the calculated eruption age; verifying our theoretical understanding of the effects of investigating the full crystallisation history on the complexities introduced to the ZDD method via computer modelling; developing a new analytical and data reduction workflow for zircon U-Th disequilibrium analysis using Sensitive High Resolution Ion MicroProbe (SHRIMP), specifically the SHRIMP II instrument at Curtin University, alongside the development of Crayfish, a new computer program written in Python which aids in visualisation of raw count data reduction for SHRIMP .pd files. Crayfish allows for greater interaction with raw data, and the formal propagation of uncertainties from measurements to age; development of a new zircon age reference material for U-Th disequilibrium dating.

Additionally, two case studies are presented. The first, using samples from the Shikotsu-Toya volcanic field in Hokkaido, Japan, re-evaluates our understanding of the impact of protracted crystallisation history with a maximum of 15% difference in overall eruption age calculated between rim- and core-corrected (U–Th)/He ages. In addition, eruption ages for two tephras – Kimobetsu 1 (59–79 ka) and Kimobetsu 2 (96 ± 5 ka, 2σ) were presented.

The second case study applies ZDD to the trachytes on the Jeju Island intraplate volcano in South Korea, permitting assessment of the new ZDD ages in the context of a previously proposed model for trachyte eruption stages. The new ca. 2 ka eruption age determined for Jeju in this thesis is the first direct geochronological documentation of young trachyte eruptive activity on Jeju Island and the youngest ZDD age published. Additionally, the crystallisation age spectra from the Jeju trachytes were used to analyse the potential complexity of the Jeju magma plumbing system.

Publications during the course of this thesis

- Zircon double-dating of Quaternary eruptions on Jeju Island, South Korea (2021), Ruby C. Marsden, Martin Danišík, Ung-San Ahn, Bjarne Friedrichs, Axel K. Schmitt, Christopher L. Kirkland, Bradley J. McDonald, Noreen J. Evans
  In-press: Journal of Volcanology and Geothermal Research, 410

- Considerations for double-dating zircon in secular disequilibrium with protracted crystallisation histories (2021), Ruby C. Marsden, Martin Danišík, Hisatoshi Ito, Christopher L. Kirkland, Noreen J. Evans, Daisuke Miura, Bjarne Friedrichs, Axel K. Schmitt, Shimpei Uesawa, Matthew L. Daggitt
  In-press: Chemical Geology, 581

- A new approach to SHRIMP II zircon U-Th disequilibrium dating, Ruby C. Marsden, Christopher L. Kirkland, Martin Danišík, Matthew L. Daggitt, Ung-San Ahn, Bjarne Friedrichs, Noreen J. Evans
  In-press: Computers and Geosciences

- SS14-28: an age reference material for zircon U-Th disequilibrium dating, Ruby C. Marsden, Martin Danišík, Axel K. Schmitt, Kai Rankenburg, Marcel Guillong, Ung-San Ahn, Christopher L. Kirkland, Noreen J. Evans, Olivier Bachmann, Tommaso Tacchetto, Bradley McDonald, Hugo K. H. Olierook
  In-press: Geostandards and Geoanalytical Research

Other relevant co-authored publications

- Dating young zircon: A case study from Southeast Asian megacrysts (2020), Christopher L Kirkland, Martin Danišík, Ruby Marsden, Paula Piilonen, Milo Barham, Lin Sutherland
  In-press: Geochimica et Cosmochimica Acta

Authorship agreement form
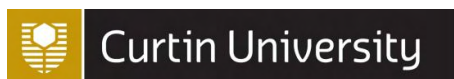
Curtin University

Authorship Agreement Form

The Curtin University Authorship, Peer Review and Publication of Research Findings Policy and Procedures[1] which references the Australian Code for the Responsible Conduct of Research[2], provides clear guidelines regarding attribution of authorship. This form is to assist researchers in capturing discussions around intended publications arising from joint work. It does not replace copyright or certification forms required by publishers.

1. Research

Project Title:	Further Development and Testing of the Combined U-Th-disequilibrium/U-Pb and (U-Th)/He Zircon Dating Method and its Application to Quaternary Volcanic Rocks		
Project identifier (if applicable)			
Principal Investigator			
Other named investigator/s[#]		Role	
Other researcher/s[#]		Role	

[#] Insert additional rows if required

2. Publications/Outputs – the intended outputs from the above research are identified below

Pub	Description (e.g. method paper)	Publication Type (Conference, journal article etc)
1	Zircon double-dating of Quaternary eruptions on Jeju Island	Journal article (in-press)
2	Considerations for double dating zircon in secular disequilibrium with protracted crystallisation histories	Journal article (in-press)
3	A new approach to SHRIMP II zircon U-Th disequilibrium dating	Journal article
4	SS14-28: an age reference material for zircon U-Th disequilibrium dating	Journal article

3. Proposed order of authors

(add rows as required for additional authors and/or if authorship will differ between multiple outputs)

Pub*	Author**	Corresponding? Y/N
1	Ruby C. Marsden	Y
1	Martin Danišík	N
1	Ung-San Ahn	N
1	Bjarne Friedrichs	N
1	Axel K. Schmitt	N
1	Christopher L. Kirkland	N
1	Bradley McDonald	N
1	Noreen J. Evans	N
2	Ruby C. Marsden	Y
2	Martin Danišík	N
2	Hisatoshi Ito	N
2	Christopher L. Kirkland	N
2	Noreen J. Evans	N
2	Daisuke Miura	N
2	Bjarne Friedrichs	N
2	Axel K. Schmitt	N

ix
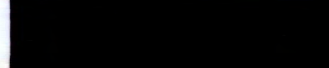
2	Shimpei Uesawa	N
2	Matthew L. Daggitt	N
3	Ruby C. Marsden	Y
3	Christopher L. Kirkland	N
3	Martin Danišík	N
3	Matthew L. Daggitt	N
3	Ung-San Ahn	N
3	Bjarne Friedrichs	N
3	Noreen J. Evans	N
4	Ruby C. Marsden	Y
4	Martin Danišík	N
4	Axel K. Schmitt	N
4	Kai Rankenburg	N
4	Marcel Guillong	N
4	Ung-San Ahn	N
4	Christopher L. Kirkland	N
4	Noreen J. Evans	N
4	Olivier Bachmann	N
4	Tommaso Tacchetto	N
4	Bradley McDonald	N
4	Hugo K. H. Olierook	N

* If multiple publications are intended under table 2, and author inclusion and order is the same, then insert "All"

** Attribution of authorship, and role of corresponding author, may have some discipline differences, however, in all cases, inclusion must be based upon substantive intellectual contribution as defined under the Policy. Acceptance should also be sought where intending to name an individual in the acknowledgements.

4. Confirmation of agreement

(add rows as required)

Author Name and Affiliation (if other than Curtin)	Author Signature	Date
Martin Danišík	▮	06/08/2021
Ung-San Ahn	▮	03/08/2021
Bjarne Friedrichs	▮	04/08/2021
Axel K. Schmitt	▮	03/08/2021
Christopher L. Kirkland	▮	03/08/2021
Bradley McDonald	▮	16/08/2021

Noreen J. Evans		03/08/2021
Hisatoshi Ito		2021/08/03
Daisuke Miura		3 Aug 2021
Shimpei Uesawa		2021/08/03
Matthew L. Daggitt		03/08/2021
Kai Rankenburg		05/08/2021
Marcel Guillong		13/08/2021
Olivier Bachmann		03/08/2021
Tommaso Tacchetto		03/08/2021
Hugo K. H. Olierook		03/08/2021

All authors should maintain a copy of this completed form for their reference.

Acknowledgements

This thesis could not have been completed without the support and guidance of a number of people who have taken considerable time and effort to help me. Firstly, I would like to acknowledge my supervisors Martin Danišík, Chris Kirkland and Noreen Evans who have pushed me to achieve more than I ever thought possible and supported me both scientifically and more generally. I would additionally like to thank Martin for the opportunities he created for me to travel to incredible places to carry out field work.

I would like to thank my co-authors for their many contributions, especially: Ung-San Ahn for showing us the wonderful volcanic rocks of Jeju Island, Bjarne Friedrichs who made every question I had about ZDD and U-Th disequilibrium dating interesting, Axel K. Schmitt who kindly let me visit and work in his laboratory, Bradley McDonald who helped me numerous times in the lab and Hugo K. H. Olierook for his encouragement and time.

I would like to acknowledge, in alphabetical order, the scientific contributions of: Simon Bodorkos for supplying example pd files for program testing, Jennifer Collister for statistics advice, Hao Gao for adding hardware to the SHRIMP II, Allen Kennedy for supplying reference zircon G4 and advice for SHRIMP II work, Anusha Shantha Kumara for assistance with zircon separation, J. Lim, S. Hong, and J. Lee for their additions to discussion and sampling in the field, Elaine Miller for assistance with SEM imaging, Taryn Scharf for rubber ducking, Sonja Storm for assistance in the Heidelberg Ion Probe Laboratory and Prok Vasilyev for his assistance with HF dissolution work.

Additionally, I would like to acknowledge Adam, Celia and Zdenka from the Argon lab who were both helpful and friendly and Jack who was always happy to be drawn into conversations about He dating and was an unexpected friend. My officemates, Andy, Dan, Louisa and Taryn, also are acknowledged for making our office a fun and supportive place.

I would never have even started this thesis had I not had role models to follow and I thank Sasha Turchyn, Tamsin Mather, Emily Flashman and Chris Marsden for being scientists (or past scientists!) that have both mentored and supported me at various times in my life.

My friends both in the UK and in Australia have made my life full of laughter and fun and given me the motivation to keep going. Merry and Mark who took me in when I

arrived and showed me Perth and made my transition to a new country almost seamless. My housemates Ophelie and Taryn both are thanked for their patience and laughter. I thank my family, for always being interested, for reading my papers and for putting up with the fact that we haven't seen in each other in almost 2 years.

Finally, I acknowledge the heartache and hardwork of a co-author, fellow scientist, best friend and partner. Matthew – this past three and a half years was made a thousand times more fun because of you.

Contents

List of Figures

List of Tables

Chapter 1

Introduction

The study of geology is the study of Earth's history through analysis of the rock record. It comes as no surprise then, that geologists are all secretly (and not so secretly) obsessed with time. Time is an important concept for both large scale questions such as: "when did continental crust start to form on Earth?" to smaller scale questions such as: "how much time does it take for zircons to grow in a magma chamber?". Furthermore, temporal context is critical in understanding the rates of geological process, be that an explosive, tephra producing volcanic event (e.g., Óladóttir et al., 2008), or the diffusion of elements through a crystal structure (e.g., Cherniak and Watson, 2001; Guenthner et al., 2013). Ever since the first attempts to quantitatively date the rock record (e.g., Strutt, 1908, 1909; Nier, 1939), geochronologists have been using a combination of physics, chemistry and, in some cases, biology to develop a growing toolkit of techniques to accurately and precisely measure ages of geological materials, thereby shedding light on the timings of both large and small-scale processes.

Methodological developments within geochronology involve both the exploration of new techniques and the refinement of those that already exist. These developments increase the accuracy and precision of the geological ages obtained, which are then utilised to more exactly pinpoint a geological event in time. Quantification of age uncertainty is important when knowledge of timing provides critical insight into geological processes. For example, it is possible to monitor the evolution of igneous systems using the relatively small age difference between generations of monazite crystallisation only because the different generations of crystal growth are both accurately and precisely known (Harrison et al., 1999). Geochronologists also aim to expand the temporal range over which geological material can be dated.

1.1   The importance of dating volcanic eruptions

There are 1,406 active or dormant subaerial volcanoes documented on Earth (Smithsonian Institution and Venzke, 2013). These are volcanoes which erupted in the past 10,000 years (i.e., in the Holocene). More than 85% of recorded fatalities caused by volcanic hazards in the last 400 years occurred between 5 km and 30 km from the eruption centre (Auker et al., 2013) and the total global population living within 30 km of such a volcano is ¿ 230 million (Brown et al., 2015). Understanding the likelihood of an eruption from any individual volcano is therefore vital to minimise the risk to human life and livelihood for those living in close proximity to volcanoes. This is particularly pertinent for those volcanoes that appear dormant and for which geochronology provides the only way of assessing their periodicity (e.g., Schmitt et al., 2014a; Friedrichs et al., 2020a) . Periodicity cannot be understood without accurate dating of past eruptions.

In addition to hazard awareness, the dating of volcanic eruptions can also be used to place minimum or maximum ages on geological or archaeological deposits stratigraphically above or below the eruptive deposit, a technique known as tephrochronology (Sarna-Wojcicki, 2000; Lowe, 2011). Tephrochronology is a particularly powerful technique as volcanic ash layers can extend more than 2000 km from the eruptive source (e.g., Pyle et al., 2006; Matthews et al., 2012), and therefore provide isochronous marker horizons. Such markers can be used to date both archaeological sites (e.g., Newnham et al., 1998; Ulusoy et al., 2019) and to provide temporal constraints on paleoclimatic records (e.g., Hammer et al., 1978; Shane and Sandiford, 2003; Brendryen et al., 2010; Jensen et al., 2011; Danišík et al., 2012; Gençalioğlu-Kuşcu et al., 2020). Alternatively, archaeological materials can also be dated by association, as for example in Schmitt et al. (2014), where dating of a pumice veneer identified and dated the volcanic eruption depicted in a Neolithic painting.

1.2   Zircon double-dating and volcanic eruptions in the Quaternary Period

It is a somewhat cruel irony that older geological materials are in many ways easier to date using isotope-based techniques, as a greater quantity of the radiogenic daughter product has been generated. One of the periods of time which can be particularly challenging is the Quaternary period (i.e., between 0 ka and 2.6 Ma), and this thesis focusses on measuring the eruption age of volcanic deposits in the younger half of this period (i.e. between 0 ka and 1 Ma). Given that it is challenging to date material in this period, it is important to apply as many independent geo- and thermochronological techniques as possible to a given sample, as repeated independent measurements increase confidence in the reliability of the ages and often reveal more detail of the thermal history. Figure 1.1 shows a number

of geochronological techniques that are applicable to dating volcanic material in this age range.
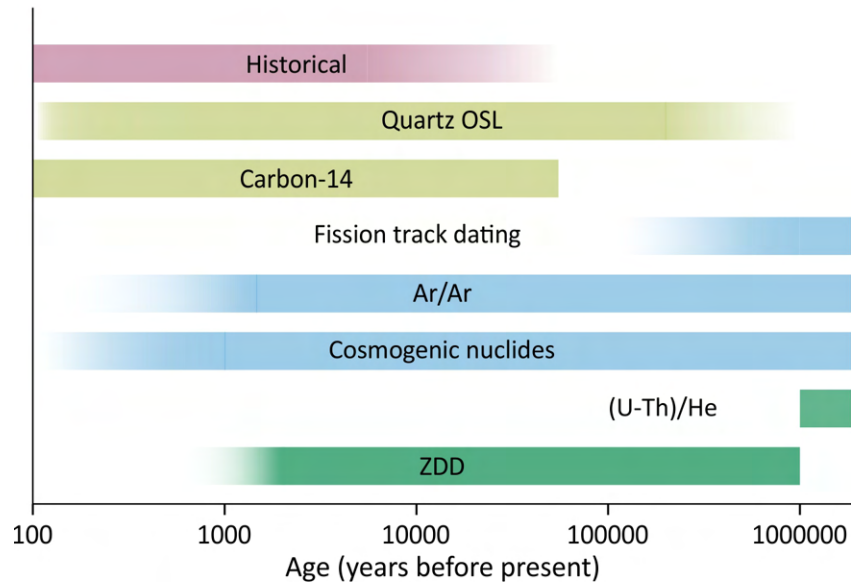
Figure 1.1: Age ranges of techniques used to date the event of a volcanic eruption from 100 years before present (BP) to 1.1 million years BP plotted on a base 10 logarithmic scale. Blue indicates a radiometric method used to directly date a sample. Lime green indicates a radiometric method used for dating sediments or carbon bearing clasts either entrained or stratigraphically constraining the sample. Pink indicates human records of volcanism. Green indicates ZDD and (U-Th)/He dating. References are as follows: fission track dating (Walter, 1989; Kohn et al., 1992; Pillans et al., 2005; Ito and Hasebe, 2011); Ar/Ar (Lanphere et al., 2007; Wright et al., 2015); cosmogenic nuclides (Espanon et al., 2014; Alcalá-Reygosa et al., 2018); Carbon-14 (Gertisser and Keller, 2003; Reimer et al., 2020); Quartz OSL (Li et al., 2007; Wintle and Adamiec, 2017); Historical (Auker et al., 2013; Matchan et al., 2020).

The accuracy of (U-Th)/He dating of zircon (assuming secular equilibrium) deteriorates <1 Ma due to the disequilibrium in the (U-Th)/He system, as first postulated by Farley et al. (2002). This thesis focuses primarily on the zircon double-dating (ZDD) technique developed by Schmitt et al. (2006), and coined as a term by Danišík et al., (2017b) for brevity, as a solution to this challenge. ZDD combines two geochronological systems; the zircon crystallisation age (closure temperature ~900 °C; Cherniak and Watson, 2001) which is determined on single zircon crystals using either U-Th disequilibrium or U-Pb dating (Schmitt, 2011; Schaltegger et al., 2015), and the zircon cooling age for He diffusion (closure temperature ~180 - 220 °C; Reiners et al., 2004; Guenthner et al., 2013) which is determined on the same crystal from its (U-Th)/He systematic (Farley, 2002; Reiners, 2005). These individual (U-Th)/He dates for a single sample are combined to calculate the sample eruption age. The double-date on an individual crystal offers a direct internal consistency check can be carried out to verify that the (U-Th)/He dates are analytically reasonable (i.e., the cooling age of the crystal must be younger than or overlap within uncertainty with the crystallisation age) (Danišík et al., 2017b).

3

As shown in Figure 1.1, ZDD is one of a number of a methods which can be used to absolutely date Quaternary aged volcanic rocks. It must be acknowledged that tephrochronology is used to relatively date tephra compared to marker beds with great success (e.g.,). However, in some situations, ZDD has significant advantages over the other methods.

Firstly, ZDD is one of the techniques which directly determines the eruption age of the volcanic product, alongside fission track dating, $^{40}Ar/^{39}Ar$ dating and cosmogenic nuclide dating. This is advantageous because, unlike Quartz OSL dating or carbon-14, ZDD depends on the radiogenic ingrowth of the daughter isotope in the volcanic product rather than in entrained particles or material in the layers located stratigraphically above or below it. Secondly, ZDD covers a considerable age range between 2 ka and 1 Ma (Schmitt et al., 2010, 2013), comparable to that of Quartz OSL, $^{40}Ar/^{39}Ar$ dating and cosmogenic nuclide dating. In contrast, carbon-14 dating is not calibrated and therefore is considered inaccurate above 55 ka (Reimer et al., 2020). Furthermore, depending on the concentration of U, fission track dating of zircon generally becomes imprecise at ages less than ca. 1 Ma (Walter, 1989). It should be noted that fission track measurements to at least ca. 0.35 ± 0.08 Ma (2σ) have been made (this is a mean value, with individual zircon values ranging from 0.2 - 0.8 Ma; Kohn et al., 1992). Fission track dating of glass has been developed to date volcanic eruptions of 0.5 - 1 Ma, with the challenge of fission tracks in volcanic glass being reduced in size at ambient temperature (Pillans et al., 2005; Ito and Hasebe, 2011).

Figure 1.2: Lush vegetation on Jeju Island suggests high rainfall and therefore shows an increased potential for high levels of weathering of trachyte lavas. Photo by Martin Danišík.

Thirdly, zircon crystals are refractory, and therefore ZDD is suited to samples where there is evidence of weathering and heavy vegetation (Figure 1.2). In contrast, these

environments may not suit ^{40}Ar/^{39}Ar or cosmogenic nuclide dating given that ^{40}Ar/^{39}Ar ages can be affected by weathering (McDougall et al., 1999; Kelley, 2002) and cosmogenic nuclides suffer from reduced exposure to cosmic rays. Cosmogenic nuclides are commonly used to date the exposure of lavas (Espanon et al., 2014; Alcalá-Reygosa et al., 2018), however if a lava is never exposed to cosmogenic rays or is only exposed to cosmogenic rays for minimal time between eruption and measurement (e.g. because it is overlaid by another lava), this technique may struggle to yield the age of eruption as not a sufficient volume of radioactive cosmogenic nuclides is produced to carry out burial dating (Dunai, 2010). Additionally, as silicic tephra have deposit surfaces that can easily be modified, this again causes challenges for cosmogenic nuclide dating (Valentine et al., 2019).

However, it is suggested that alteration has the potential to cause significant implantation of alpha particles into crystals, this is observed predominantly in apatite and magnetite crystals (e.g., Blackburn et al, 2007; Spiegel et al, 2009; Cooperdock and Stockli, 2016). This is because they have considerably lower ^{238}U and ^{232}Th concentrations by an order of magnitude compared to surrounding mineral phases (Schwartz et al., 2020). This is less of a concern in zircon because of its relatively high concentrations of ^{238}U and ^{232}Th, however it should be kept in mind, especially if whole rock levels of ^{238}U and ^{232}Th are high.

Finally, in many situations single crystal ^{40}Ar/^{39}Ar dating of sanidine is more precise than ZDD, and similarly covers the whole of the Quaternary period with ages as low as 1.91 ± 0.07 ka reported (Lanphere et al., 2007). However, sanidine can be affected by excess argon and pre-eruptive partitioning of Ar (Kelley, 2002; Hora et al., 2010), and sanidine does not always grow within eruptive systems (e.g. in some island arc tholeiites due to low potassium concentrations; Jakes and Gill, 1970). In this way ZDD is complementary to ^{40}Ar/^{39}Ar dating as its main disadvantage is that zircon crystals must be present in the eruptive product.

ZDD is therefore especially well-suited for analysis of silicic melts, which lead to the most explosive eruptions, and typically contain abundant zircon (Poldervaart, 1956; Watson and Harrison, 1983; Boehnke et al., 2013) yet may be barren for many other minerals used in other geochronology approaches.

1.3   Notable uses of ZDD

ZDD has been used to date the eruption age of a wide range of volcanic products from lava to pyroclastic flow and ash fall deposits (e.g., Gebauer et al., 2014; Burgess et al., 2019; Ito and Danišík, 2020; Friedrichs et al., 2020a). Not only can these products be used to date volcanic eruptions, and therefore contribute to volcanic hazard assessments (Schmitt et al., 2014a; Friedrichs et al., 2020a; Marsden et al., 2021), ZDD has also been used to answer a range of questions within the fields of archaeology (e.g., Schmitt et al.,

2013, 2014; Friedrichs et al., 2020b). Similarly, ZDD has been used to constrain the timing of geological events outside of volcanology, such as fault quiescence and the depositional ages of overlying stratigraphy (Österle et al., 2020).

Furthermore, the ZDD is a uniquely useful tool for understanding timescales of magma chamber processes. This because a) its resolution is on the same time scale as magma chamber and eruptive processes, b) the method measures both the crystallisation age and the eruption age of the zircon and c) it is often abundant in silicic melts. Moreover, zircon preserves a geochemical signature of its growth environment which may provide additional key information to understand magma petrogenesis (e.g., Lukács et al., 2015).

For example, ZDD has been used to answer a number of geological questions about timescales of magma chamber and eruptive processes (Schmitt et al., 2014b; Harangi et al., 2015; Mucek et al., 2017; Kósik et al., 2021) (Friedrichs et al., 2020), and has contributed to the ongoing debate over cold or warm storage of magma (Barboni et al., 2016; Rubin et al., 2017; Friedrichs et al., 2021b). It has also been used in analysing the post-eruptive recovery of supervolcanoes (Mucek et al., 2017).

1.4 Current ZDD methodology

As outlined above, ZDD applies two dating techniques on each zircon crystal. First, the crystallisation age is measured on the rim of a zircon crystal using U-Th disequilibrium or U-Pb dating. This measurement is most often made using SIMS techniques on the CAMECA 1280 IMS or SHRIMP RG (Reid et al., 1997; Coble et al., 2017), but recent advances have allowed these measurements to be made on the LA-ICPMS (e.g., Guillong et al., 2016). SIMS methods have decreased pit volume compared to LA-ICPMS and this is important for two reasons. Firstly, the decreased analysis volume on the rim of the crystal ensures that the latest crystallisation age is measured, and secondly during the (U-Th)/He analysis it is preferrable to measure the greatest volume of crystal possible in order to maximise the concentration of ^{4}He.

Next, in a destructive process, the (U-Th)/He age is determined on the whole crystal. Initially, the ^{4}He concentration is measured using laser induced heating of the zircon crystal, liberating the ^{4}He from the crystal and measuring the ^{4}He/^{3}He ratio using a ^{3}He spike on a noble gas mass spectrometer (Danišík et al., 2017b). Subsequently, the zircon crystals are fully dissolved (Evans et al., 2005) and solution ICP MS is used to measure the ^{238}U and ^{232}Th concentrations (Danišík et al., 2017b). While (U-Th)/He ages can be measured non-destructively using laser ablation (Danišík et al., 2017a), for Quaternary eruptive products the concentration of ^{4}He is below the limit of detection unless the whole crystal ^{4}He is measured. To complete the (U-Th)/He calculation, the ejection of alpha particles must be taken into account (Farley et al., 1996). An alpha ejection correction

factor must be calculated from crystal geometry, which is measured either by photographs or micro-CT (e.g., Evans et al., 2008; Glotzbach et al., 2019; Cooperdock et al., 2019). This correction factor is then applied to the raw (U-Th)/He age (Farley et al., 1996). Finally, the crystallisation age and crystal and assumed melt concentrations of relevant isotopes are used correct the (U-Th)/He date for U-series disequilibrium giving a final sample eruption age (Farley et al., 2002; Lovera et al., 2009; Schmitt et al., 2010).

1.5   Current limitations of the technique

Although ZDD protocols have been established and the approach, in many cases, provides accurate, sufficiently precise and geologically meaningful eruption ages (e.g. Danišík et al., 2012), there are still some limitations of the technique and several potential areas where improvements could be made.

1. ZDD takes disequilibrium corrected (U-Th)/He dates for multiple zircon crystals from a single sample and statistically unifies these ages to a single sample eruption age (Schmitt et al., 2006; Lovera et al., 2009; Schmitt et al., 2010; Danišík et al., 2017b). While ZDD has been used to successfully date Quaternary volcanic eruptions (e.g., Danišík et al., 2012; Ito and Danišík, 2020), there are some cases where there is evidence of over-dispersion in the individual disequilibrium corrected (U-Th)/He ages (e.g., for 11 analyses of U-Th/He ages for sample Dpm the MSWD = 2.7; Ito and Danišík, 2020). No overall eruption age for the sample can be confidently determined in this case (Schmitt et al., 2010; Danišík et al., 2017b). Individual crystal disequilibrium corrected (U-Th)/He date outliers could result from the undetected presence of He-rich fluid inclusions or voids acting as He traps (Danišík et al., 2017a), partial resetting of the (U-Th)/He dates by post-depositional reheating of the tephra (e.g., Mitchell and Reiners, 2003), or contamination of the deposit by zircon crystals from another source. It is important to note that radiation damage (Shuster et al., 2006; Flowers et al., 2007; Guenthner et al., 2013) is not considered as a reason for over dispersion in <1 Ma zircons (Cherniak and Watson, 2001) as it would require unreasonably high U and Th concentrations or >100 Ma retention in the zircon partial He retention zone (Reiners et al., 2004; Reiners, 2005; Guenthner et al., 2013). Nevertheless, in some cases, no valid reason for over-dispersion is apparent, leaving the issue unresolved, and often, these cases correlate with significant crystallisation age zonation observed in the dated zircon grains (Friedrichs et al., 2021a).

2. U-Th disequilibrium dating on the SIMS has been developed for the CAMECA IMS 1280 and the SHRIMP RG instruments (Reid et al., 1997; Coble et al., 2017), but has not been developed for the SHRIMP II. While U-Th disequilibrium dating has

been developed on the LA-ICPMS (Guillong et al., 2016), the low analysis volume would make an additional SIMS technique advantageous.

3. The U-Th disequilibrium dating method has no zircon age reference material, instead it relies on the use of a reference material which is in secular equilibrium to ensure the technique is accurate. This is due to a lack of sufficient quantities of homogeneous, < 350 ka zircon crystals. Therefore, inter-laboratory accuracy testing is problematic.

1.6   Objectives of this work

The objectives of this thesis are as follows:

1. To investigate the over-dispersion of disequilibrium corrected (U-Th)/He ages and test whether this is due to the current ZDD protocol of taking the crystallisation age solely on the rim of the crystal.

2. To develop and test new ZDD protocols for <1 Ma zircon crystals with substantial crystallisation age zonation.

3. To develop U-Th disequilibrium dating methodology for the SHRIMP II.

4. To find a suitable zircon age reference material for U-Th disequilibrium dating.

5. To showcase the importance of the ZDD method by applying it to regional case studies.

1.7   Thesis structure

This thesis is made up of four main chapters, each of which comprises a manuscript that has either been published in, accepted by, or submitted to, an international peer-reviewed journal. These manuscripts address the objectives outlined above.

Chapter 2: Considerations for double dating zircon in secular disequilibrium with protracted crystallisation histories, presents a case study from SW Hokkaido (Japan) of ZDD carried out on zircon with crystallisation age zoning. This study shows a potential 15% difference in sample eruption age between using the core or rim crystallisation age for disequilibrium correction. The method presented is supported by computer modelling results verifying that grinding a crystal to interrogate the interior does not alter the alpha ejection correction factor used within the (U-Th)/He dating method.

Chapter 3: A new approach to SHRIMP II zircon U-Th disequilibrium dating, develops the U-Th disequilibrium method for dating crystallisation ages of zircon on the SHRIMP II instrument at the John de Laeter Centre, Curtin University. This

development required an investigation of the background interferences on the SHRIMP II and a programming solution (the open-source Crayfish software) for the removal of multiple background measurements.

Chapter 4: SS14-28: an age reference material for zircon U-Th disequilibrium dating, presents an age reference material for zircon U-Th disequilibrium dating. This material is age-appropriate, reliable and plentiful and is the first material to fulfil these requirements for an age reference material. As part of this study an inter-laboratory verification of age accuracy was carried out, showing the same age for the reference material within uncertainty in three separate laboratories.

Chapter 5: Zircon double-dating of Quaternary eruptions on Jeju Island, is a case study for ZDD where there is no zonation of age of crystallisation in zircon. This study presents eruption ages and crystallisation ages for trachyte outcrops around the island, as well as a new (and somewhat alarming) 2 ka eruption age for a single deposit, which determines Jeju as an active trachyte volcano according to the current definition (Smithsonian Institution and Venzke, 2013). Additionally, it compares the trachyte eruptions on Jeju to trachyte eruptions worldwide to test a previous model for trachyte evolution.

1.8   References

Alcalá-Reygosa J., Arce J. L., Schimmelpfennig I., Salinas E. M., Rodríguez M. C., Léanni L., Aumaître G., Bourlès D. and Keddadouche K. (2018) Revisiting the age of the Jumento volcano, Chichinautzin Volcanic Field (Central Mexico), using in situ-produced cosmogenic 10Be. Journal of Volcanology and Geothermal Research 366, 112-119.

Auker M. R., Sparks R. S. J., Siebert L., Crosweller H. S. and Ewert J. (2013) A statistical analysis of the global historical volcanic fatalities record. J Appl. Volcanol. 2, 2.

Barboni M., Boehnke P., Schmitt A. K., Harrison T. M., Shane P., Bouvier A.-S. and Baumgartner L. (2016) Warm storage for arc magmas. Proceedings of the National Academy of Sciences 113, 13959-13964.

Blackburn, T.J., Stockli, D.F., Walker, J.D., 2007. Magnetite (U-Th)/He dating and its application to the geochronology of intermediate to mafic volcanic rocks. Earth and Planetary Science Letters 259, 360-371.

Boehnke P., Watson E. B., Trail D., Harrison T. M. and Schmitt A. K. (2013) Zircon saturation re-revisited. Chemical Geology 351, 324-334.

Brendryen J., Haflidason H. and Sejrup H. P. (2010) Norwegian Sea tephrostratigraphy of marine isotope stages 4 and 5: Prospects and problems for tephrochronology in the North Atlantic region. Quaternary Science Reviews 29, 847-864.

Brown S. K., Auker M. R. and Sparks R. S. J. (2015) Populations around Holocene volcanoes and development of a Population Exposure Index. In Global Volcanic Hazards and Risk (eds. C. Vye-Brown, S. K. Brown, S. Sparks, S. C. Loughlin, and S. F. Jenkins). Cambridge University Press, Cambridge. pp. 223-232.

Burgess S. D., Coble M. A., Vazquez J. A., Coombs M. L. and Wallace K. L. (2019) On the eruption age and provenance of the Old Crow tephra. Quaternary Science Reviews 207, 64-79.

Cherniak D. J. and Watson E. B. (2001) Pb diffusion in zircon. Chemical Geology 172, 5-24.

Coble M. A., Burgess S. D. and Klemetti E. W. (2017) New zircon (U-Th)/He and U/Pb eruption age for the Rockland tephra, western USA. Quaternary Science Reviews 172, 109-117.

Cooperdock, E.H.G., Stockli, D.F., 2016. Unraveling alteration histories in serpentinites and associated ultramafic rocks with magnetite (U-Th)/He geochronology. Geology 44, 967-970.

Cooperdock E. H. G., Ketcham R. A. and Stockli D. F. (2019) Resolving the effects of 2-D versus 3-D grain measurements on apatite (U-Th)/He age data and reproducibility. Geochronology 1, 17-41.

Danišík M., McInnes B. I. A., Kirkland C. L., McDonald B. J., Evans N. J. and Becker T. (2017a) Seeing is believing: Visualization of He distribution in zircon and implications for thermal history reconstruction on single crystals. Science Advances 3, e1601121.

Danišík M., Schmitt A. K., Stockli D. F., Lovera O. M., Dunkl I. and Evans N. J. (2017b) Application of combined U-Th-disequilibrium/U-Pb and (U-Th)/He zircon dating to tephrochronology. Quaternary Geochronology 40, 23-32.

Danišík M., Shane P., Schmitt A. K., Hogg A., Santos G. M., Storm S., Evans N. J., Keith Fifield L. and Lindsay J. M. (2012) Re-anchoring the late Pleistocene tephrochronology of New Zealand based on concordant radiocarbon ages and combined ^{238}U/^{230}Th disequilibrium and (U-Th)/He zircon ages. Earth and Planetary Science Letters 349-350, 240-250.

Dunai T. J. (2010) Cosmogenic Nuclides: Principles, Concepts and Applications in the Earth Surface Sciences., Cambridge University Press.

Espanon V. R., Honda M. and Chivas A. R. (2014) Cosmogenic ^{3}He and 21Ne surface exposure dating of young basalts from Southern Mendoza, Argentina. Quaternary Geochronology 19, 76-86.

Evans N. J., Byrne J. P., Keegan J. T. and Dotter L. E. (2005) Determination of Uranium and Thorium in Zircon, Apatite, and Fluorite: Application to Laser (U-Th)/He Thermochronology. J Anal Chem 60, 1159-1165.

Evans N. J., McInnes B. I. A., Squelch A. P., Austin P. J., McDonald B. J. and Wu Q. (2008) Application of X-ray micro-computed tomography in (U-Th)/He thermochronology. Chemical Geology 257, 101-113.

Farley K. A. (2002) (U-Th)/He Dating: Techniques, Calibrations, and Applications. Reviews in

Mineralogy and Geochemistry 47, 819-844.

Farley K. A., Kohn B. P. and Pillans B. (2002) The effects of secular disequilibrium on (U-Th)/He systematics and dating of Quaternary volcanic zircon and apatite. Earth and Planetary Science Letters 201, 117-125.

Farley K. A., Wolf R. A. and Silver L. T. (1996) The effects of long alpha-stopping distances on (U-Th)/He ages. Geochimica et Cosmochimica Acta 60, 4223-4229.

Flowers R. M., Shuster D. L., Wernicke B. P. and Farley K. A. (2007) Radiation damage control on apatite (U-Th)/He dates from the Grand Canyon region, Colorado Plateau. Geology 35, 447-450.

Friedrichs B., Atıcı G., Danišík M., Atakay E., Çobankaya M., Harvey J. C., Yurteri E. and Schmitt A. K. (2020a) Late Pleistocene eruptive recurrence in the post-collisional Mt. Hasan stratovolcanic complex (Central Anatolia) revealed by zircon double-dating. Journal of Volcanology and Geothermal Research 404, 107007.

Friedrichs B., Atıcı G., Danišík M., Yurteri E. and Schmitt A. K. (2021a) Sequence modeling in zircon double-dating of early Holocene Mt. Erciyes domes (Central Anatolia). Quaternary Geochronology 61, 101129.

Friedrichs B., Schindlbeck-Belo J. C., Danišík M., Jenkins S. F., Yurteri E., Çobankaya M., Frische M., Wang K.-L., Lee H.-Y., Atıcı G., Schmitt A. K. and Sparks R. S. J. (2020b) New insights into source and dispersal of Mediterranean S1 tephra, an early Holocene marker horizon erupted at Mt. Erciyes (Turkey). Quaternary Science Reviews 249, 106606.

Friedrichs B., Schmitt A. K., Lovera O. M. and Atıcı G. (2021b) Zircon as a recorder of contrasting magma recharge and eruptive recurrence patterns. Earth and Planetary Science Letters 571, 117104.

Friedrichs B., Schmitt A. K., McGee L. and Turner S. (2020c) U-Th whole rock data and high spatial resolution U-Th disequilibrium and U-Pb zircon ages of Mt. Erciyes and Mt. Hasan Quaternary stratovolcanic complexes (Central Anatolia). Data in Brief 29, 105113.

Gebauer S. K., Schmitt A. K., Pappalardo L., Stockli D. F. and Lovera O. M. (2014) Crystallization and eruption ages of Breccia Museo (Campi Flegrei caldera, Italy) plutonic clasts and their relation to the Campanian ignimbrite. Contrib Mineral Petrol 167, 953.

Gençalioğlu-Kuşcu G., Uslular G., Danišík M., Koppers A., Miggins D. P., Friedrichs B. and Schmitt A. K. (2020) U-Th disequilibrium, (U-Th)/He and 40Ar/39Ar geochronology of distal Nisyros Kyra tephra deposits on Datça peninsula (SW Anatolia). Quaternary Geochronology 55, 101033.

Gertisser R. and Keller J. (2003) Temporal variations in magma composition at Merapi Volcano (Central Java, Indonesia): magmatic cycles during the past 2000 years of explosive activity. Journal of Volcanology and Geothermal Research 123, 1-23.

Glotzbach C., Lang K. A., Avdievitch N. N. and Ehlers T. A. (2019) Increasing the accuracy of

(U-Th(-Sm))/He dating with 3D grain modelling. Chemical Geology 506, 113-125.

Guenthner W. R., Reiners P. W., Ketcham R. A., Nasdala L. and Giester G. (2013) Helium diffusion in natural zircon: Radiation damage, anisotropy, and the interpretation of zircon (U-Th)/He thermochronology. Am J Sci 313, 145-198.

Guillong M., Sliwinski J. T., Schmitt A., Forni F. and Bachmann O. (2016) U-Th Zircon Dating by Laser Ablation Single Collector Inductively Coupled Plasma-Mass Spectrometry (LA-ICP-MS). Geostandards and Geoanalytical Research 40, 377-387.

Hammer C. U., Clausen H. B., Dansgaard W., Gundestrup N., Johnsen S. J. and Reeh N. (1978) Dating of Greenland Ice Cores by Flow Models, Isotopes, Volcanic Debris, and Continental Dust. Journal of Glaciology 20, 3-26.

Harangi S., Lukács R., Schmitt A. K., Dunkl I., Molnár K., Kiss B., Seghedi I., Novothny Á. and Molnár M. (2015) Constraints on the timing of Quaternary volcanism and duration of magma residence at Ciomadul volcano, east-central Europe, from combined U-Th/He and U-Th zircon geochronology. Journal of Volcanology and Geothermal Research 301, 66-80.

Harrison M. T., Grove M., Mckeegan K. D., Coath C. D., Lovera O. M. and Fort P. L. (1999) Origin and Episodic Emplacement of the Manaslu Intrusive Complex, Central Himalaya. Journal of Petrology 40, 3-19.

Hora J. M., Singer B. S., Jicha B. R., Beard B. L., Johnson C. M., de Silva S. and Salisbury M. (2010) Volcanic biotite-sanidine 40Ar/39Ar age discordances reflect Ar partitioning and pre-eruption closure in biotite. Geology 38, 923-926.

Ito H. and Danišík M. (2020) Dating late Quaternary events by the combined U-Pb LA-ICP-MS and (U-Th)/He dating of zircon: A case study on Omachi Tephra suite (central Japan). Terra Nova 32, 134-140.

Ito K. and Hasebe N. (2011) Fission-track dating of Quaternary volcanic glass by stepwise etching. Radiation Measurements 46, 176-182.

Jakes P. and Gill J. (1970) Rare earth elements and the island arc tholeiitic series. Earth and Planetary Science Letters 9, 17-28.

Jensen B. J. L., Preece S. J., Lamothe M., Pearce N. J. G., Froese D. G., Westgate J. A., Schaefer J. and Begét J. (2011) The variegated (VT) tephra: A new regional marker for middle to late marine isotope stage 5 across Yukon and Alaska. Quaternary International 246, 312-323.

Kelley S. (2002) Excess argon in K-Ar and Ar-Ar geochronology. Chemical Geology 188, 1-22.

Kohn B. P., Pillans B. and McGlone M. S. (1992) Zircon fission track age for middle Pleistocene Rangitawa Tephra, New Zealand: stratigraphic and paleoclimatic significance. Palaeogeography, Palaeoclimatology, Palaeoecology 95, 73-94.

Kósik S., Németh K., Danišík M., Procter J. N., Schmitt A. K., Friedrichs B. and Stewart R. B. (2021) Shallow subaqueous to emergent intra-caldera silicic volcanism of the Motuoapa Peninsula,

Taupo Volcanic Zone, New Zealand - New constraints from geologic mapping, sedimentology and zircon geochronology. Journal of Volcanology and Geothermal Research 411, 107180.

Lanphere M., Champion D., Melluso L., Morra V., Perrotta A., Scarpati C., Tedesco D. and Calvert A. (2007) 40Ar/39Ar ages of the AD 79 eruption of Vesuvius, Italy. Bull Volcanol 69, 259-263.

Li S.-H., Chen Y.-Y., Li B., Sun J. and Yang L.-R. (2007) OSL dating of sediments from deserts in northern China. Quaternary Geochronology 2, 23-28.

Lovera O., Schmitt A. K. and Stockli D. (2009) Improving combined U-Th and (U-Th)/He geochronology by Monte Carlo statistical corrections for uranium series disequilibrium.

Lowe D. J. (2011) Tephrochronology and its application: A review. Quaternary Geochronology 6, 107-153.

Lukács R., Harangi S., Bachmann O., Guillong M., Danišík M., Buret Y., von Quadt A., Dunkl I., Fodor L., Sliwinski J., Soós I. and Szepesi J. (2015) Zircon geochronology and geochemistry to constrain the youngest eruption events and magma evolution of the Mid-Miocene ignimbrite flare-up in the Pannonian Basin, eastern central Europe. Contrib Mineral Petrol 170, 52.

Marsden R. C., Danišík M., Ahn U.-S., Friedrichs B., Schmitt A. K., Kirkland C. L., McDonald B. and Evans N. J. (2021) Zircon double-dating of Quaternary eruptions on Jeju Island. Journal of Volcanology and Geothermal Research, 107171.

Matchan E. L., Phillips D., Jourdan F. and Oostingh K. (2020) Early human occupation of southeastern Australia: New insights from 40Ar/39Ar dating of young volcanoes. Geology 48, 390-394.

Matthews N. E., Smith V. C., Costa A., Durant A. J., Pyle D. M. and Pearce N. J. G. (2012) Ultra-distal tephra deposits from super-eruptions: Examples from Toba, Indonesia and Taupo Volcanic Zone, New Zealand. Quaternary International 258, 54-79.

McDougall I., Harrison T. M. and Harrison T. M. (1999) Geochronology and Thermochronology by the 40Ar/39Ar Method., Oxford University Press on Demand.

Mitchell S. G. and Reiners P. W. (2003) Influence of wildfires on apatite and zircon (U-Th)/He ages. Geology 31, 1025-1028.

Mucek A. E., Danišík M., Silva S. L. de, Schmitt A. K., Pratomo I. and Coble M. A. (2017) Post-supereruption recovery at Toba Caldera. Nature Communications 8, 15248.

Newnham R. M., Lowe D. J., McGlone M. S., Wilmshurst J. M. and Higham T. F. G. (1998) The Kaharoa Tephra as a Critical Datum for Earliest Human Impact in Northern New Zealand. Journal of Archaeological Science 25, 533-544.

Nier A. O. (1939) The Isotopic Constitution of Radiogenic Leads and the Measurement of Geological Time. II. Phys. Rev. 55, 153-163.

Óladóttir B. A., Sigmarsson O., Larsen G. and Thordarson T. (2008) Katla volcano, Iceland:

magma composition, dynamics and eruption frequency as recorded by Holocene tephra layers. Bull Volcanol 70, 475-493.

Österle J. E., Stockli D. F., Seward D. and Little T. A. (2020) Dating of young (<1 Ma) tephras: Using U-Pb (zircon) and (U-Th[-Sm])/He (zircon, apatite, magnetite) chronometers to unravel the eruption age of a tephra in the Woodlark Rift of Papua New Guinea. Terra Nova 32, 345-354.

Pillans B., Alloway B., Naish T., Westgate J., Abbott S. and Palmer A. (2005) Silicic tephras in Pleistocene shallow-marine sediments of Wanganui Basin, New Zealand. Journal of the Royal Society of New Zealand 35, 43-90.

Poldervaart A. (1956) Zircon in rocks; 2, Igneous rocks. Am J Sci 254, 521-554.

Pyle D. M., Ricketts G. D., Margari V., van Andel T. H., Sinitsyn A. A., Praslov N. D. and Lisitsyn S. (2006) Wide dispersal and deposition of distal tephra during the Pleistocene 'Campanian Ignimbrite/Y5' eruption, Italy. Quaternary Science Reviews 25, 2713-2728.

Reid M. R., Coath C. D., Mark Harrison T. and McKeegan K. D. (1997) Prolonged residence times for the youngest rhyolites associated with Long Valley Caldera: ^{230}Th—^{238}U ion microprobe dating of young zircons. Earth and Planetary Science Letters 150, 27-39.

Reimer P. J., Austin W. E. N., Bard E., Bayliss A., Blackwell P. G., Ramsey C. B., Butzin M., Cheng H., Edwards R. L., Friedrich M., Grootes P. M., Guilderson T. P., Hajdas I., Heaton T. J., Hogg A. G., Hughen K. A., Kromer B., Manning S. W., Muscheler R., Palmer J. G., Pearson C., Plicht J. van der, Reimer R. W., Richards D. A., Scott E. M., Southon J. R., Turney C. S. M., Wacker L., Adolphi F., Büntgen U., Capano M., Fahrni S. M., Fogtmann-Schulz A., Friedrich R., Köhler P., Kudsk S., Miyake F., Olsen J., Reinig F., Sakamoto M., Sookdeo A. and Talamo S. (2020) The IntCal20 Northern Hemisphere Radiocarbon Age Calibration Curve (0-55 cal kBP). Radiocarbon 62, 725-757.

Reiners P. W. (2005) Zircon (U-Th)/He Thermochronometry. Reviews in Mineralogy and Geochemistry 58, 151-179.

Reiners P. W., Spell T. L., Nicolescu S. and Zanetti K. A. (2004) Zircon (U-Th)/He thermochronometry: He diffusion and comparisons with 40Ar/39Ar dating. Geochimica et Cosmochimica Acta 68, 1857-1887.

Rubin A. E., Cooper K. M., Till C. B., Kent A. J. R., Costa F., Bose M., Gravley D., Deering C. and Cole J. (2017) Rapid cooling and cold storage in a silicic magma reservoir recorded in individual crystals. Science 356, 1154-1156.

Sarna-Wojcicki A. (2000) Tephrochronology. In Quaternary Geochronology American Geophysical Union (AGU). pp. 357-377.

Schaltegger U., Schmitt A. K. and Horstwood M. S. A. (2015) U-Th-Pb zircon geochronology by ID-TIMS, SIMS, and laser ablation ICP-MS: Recipes, interpretations, and opportunities. Chemical Geology 402, 89-110.

Schmitt A. K. (2011) Uranium Series Accessory Crystal Dating of Magmatic Processes. Annu.

Rev. Earth Planet. Sci. 39, 321-349.

Schmitt A. K., Danišík M., Aydar E., Şen E., Ulusoy İ. and Lovera O. M. (2014a) Identifying the Volcanic Eruption Depicted in a Neolithic Painting at Çatalhöyük, Central Anatolia, Turkey. PLOS ONE 9, e84711.

Schmitt A. K., Danišík M., Siebel W., Elitok Ö., Chang Y.-W. and Shen C.-C. (2014b) Late Pleistocene zircon ages for intracaldera domes at Gölcük (Isparta, Turkey). Journal of Volcanology and Geothermal Research 286, 24-29.

Schmitt A. K., Martín A., Stockli D. F., Farley K. A. and Lovera O. M. (2013) (U-Th)/He zircon and archaeological ages for a late prehistoric eruption in the Salton Trough (California, USA). Geology 41, 7-10.

Schmitt A. K., Stockli D. F. and Hausback B. P. (2006) Eruption and magma crystallization ages of Las Tres Vírgenes (Baja California) constrained by combined $^{230}Th/^{238}U$ and (U-Th)/He dating of zircon. Journal of Volcanology and Geothermal Research 158, 281-295.

Schmitt A. K., Stockli D. F., Niedermann S., Lovera O. M. and Hausback B. P. (2010) Eruption ages of Las Tres Vírgenes volcano (Baja California): A tale of two helium isotopes. Quaternary Geochronology 5, 503-511.

Schwartz, S., Gautheron, C., Ketcham, R.A., Brunet, F., Corre, M., Agranier, A., Pinna-Jamme, R., Haurine, F., Monvoin, G., Riel, N., 2020. Unraveling the exhumation history of high-pressure ophiolites using magnetite (U-Th-Sm)/He thermochronometry. Earth and Planetary Science Letters 543, 116359.

Shane P. and Sandiford A. (2003) Paleovegetation of marine isotope stages 4 and 3 in northern new zealand and the age of the widespread rotoehu tephra. Quaternary Research 59, 420-429.

Shuster D. L., Flowers R. M. and Farley K. A. (2006) The influence of natural radiation damage on helium diffusion kinetics in apatite. Earth and Planetary Science Letters 249, 148-161.

Smithsonian Institution and Venzke E. (2013) Volcanoes of the World, v. 4.3.4.

Spiegel, C., Kohn, B., Belton, D., Berner, Z., Gleadow, A., 2009. Apatite (U-Th-Sm)/He thermochronology of rapidly cooled samples: The effect of He implantation. Earth and Planetary Science Letters 285, 105-114.

Strutt R. J. (1908) On the accumulation of helium in geological time. Proceedings of the Royal Society of London. Series A, Containing Papers of a Mathematical and Physical Character 81, 272-277.

Strutt R. J. (1909) The accumulation of helium in geological time.-II. Proc. R. Soc. Lond. A 83, 96-99.

Ulusoy İ., Sarıkaya M. A., Schmitt A. K., Şen E., Danišík M. and Gümüş E. (2019) Volcanic eruption eye-witnessed and recorded by prehistoric humans. Quaternary Science Reviews 212, 187-198.

Valentine G. A., Briner J. P., van Wyk de Vries B., Macorps É. and Gump D. (2019) 10Be exposure ages for the Late Pleistocene Gour de Tazenat maar (Chaîne des Puys volcanic field, Auvergne, France). Quaternary Geochronology 50, 8-13.

Walter R. C. (1989) Application and limitation of fission-track geochronology to quarternary tephras. Quaternary International 1, 35-46.

Watson E. B. and Harrison T. M. (1983) Zircon saturation revisited: temperature and composition effects in a variety of crustal magma types. Earth and Planetary Science Letters 64, 295-304.

Wintle A. G. and Adamiec G. (2017) Optically stimulated luminescence signals from quartz: A review. Radiation Measurements 98, 10-33.

Wright H. M., Vazquez J. A., Champion D. E., Calvert A. T., Mangan M. T., Stelten M., Cooper K. M., Herzig C. and Schriener A. (2015) Episodic Holocene eruption of the Salton Buttes rhyolites, California, from paleomagnetic, U-Th, and Ar/Ar dating. Geochemistry, Geophysics, Geosystems 16, 1198-1210.

Chapter 2

Considerations for double-dating zircon in secular disequilibrium with protracted crystallisation histories

While this chapter consists of a published paper changes in line with examiner comments have been made post-publication.

Abstract

Zircon double-dating utilises (U-Th)/He dating coupled with U-Th disequilibrium or U-Pb dating to determine eruption ages for volcanic rocks between ca. 2 ka to 1 Ma. This approach depends on understanding the crystallisation history of each zircon crystal analysed. For lack of better constraints, zircon crystallisation is generally assumed to be represented by a single crystallisation age, which is routinely determined on the natural rim of an un-sectioned and unpolished zircon pressed into indium metal. While zircon crystallisation is often protracted, interrogating the crystallisation history of a zircon crystal usually requires grinding the grain, which can introduce uncertainty to the alpha ejection (Ft) correction, critical for accurate (U-Th)/He ages. Theoretically, grinding a zircon crystal to exactly 50% of its original width, to a plane of symmetry, leaves the Ft correction factor unchanged relative to that of the whole crystal. This is verified by a new computer program - GriFt, which also allows the calculation of accurate Ft correction factors for a range of different grinding depths, opening the opportunity to measure both the core and rim crystallisation ages and integrate these into a more robust disequilibrium correction of (U-Th)/He data.

   The feasibility of this approach is tested here in a case study of zircon crystals with protracted crystallisation histories from the Shikotsu-Toya volcanic field in Hokkaido, Japan. A maximum of 15% difference in overall eruption age is calculated between rim-

and core-corrected (U-Th)/He ages. Eruption ages were determined for two tephras - Kimobetsu 1 (59-79 ka) and Kimobetsu 2 (96 ± 5 ka, 2σ). The geological implication from these dates is that a regionally important tephra, Toya, may be younger (<96 ± 5 ka) than previously reported (109 ± 3 ka). In addition, the maximum eruption ages determined from crystallisation age distributions calculated for samples from eruptions at Shikotsu and Kuttara (48 ± 17 and 49 ± 21 ka, respectively) are within uncertainty of previous measurements (44-41 ka and >43 ka, respectively).

2.1   Introduction

Dating Quaternary volcanic eruptions improves our understanding of eruptive recurrence which can be used to inform a greater understanding of magma system dynamics and is important for future volcanic hazard prediction (Scandone et al., 1993; Connor et al., 2000; Marzocchi and Bebbington, 2012). Furthermore, dating volcanic products may provide temporal constraints on geological, paleoclimatic, and archaeological records (Ruxton and McDougall, 1967; Hammer et al., 1978; Shane and Sandiford, 2003; Brendryen et al., 2010; Jensen et al., 2011) and inform on the recharge tempo of magmatic systems (Schmitt et al., 2011). However, dating volcanic eruptions that occurred <1 Ma presents significant analytical challenges for modern geochronology as only a few dating methods can be applied to this time interval with sufficient accuracy and precision. For example, radiocarbon dating is calibrated only to 50 ka (Reimer et al., 2020); moreover, volcanic samples containing carbon may not always be available. Another technique, $^{40}Ar/^{39}Ar$ geochronology can be challenging if high K minerals are absent or excess argon is present and cannot be adequately identified and corrected for (McDougall and Harrison, 1999).

Zircon double-dating (ZDD) is a powerful tool for constraining the timing of <1 Ma volcanic eruptions (Schmitt et al., 2006; Schmitt et al., 2010; Schmitt et al., 2011; Danišík et al., 2012) and provides the opportunity to date zircon-bearing volcanic products in the critical ~50 ka - 1 Ma window of the Quaternary Period (Schmitt et al., 2014; Coble et al., 2017; Danišík et al., 2017b; Mucek et al., 2017; Burgess et al., 2019; Friedrichs et al., 2020a; Friedrichs et al., 2020b; Österle et al., 2020). ZDD combines the crystallisation age (measured by U–Th disequilibrium or U–Pb dating methods) and cooling age (measured by (U–Th)/He method) of individual zircon crystals to derive eruption ages for <1 Ma old volcanic products (Farley et al., 2002; Schmitt et al., 2010; Danišík et al., 2017b).

The determination of a (U–Th)/He age requires two corrections: first, an alpha ejection (Ft) correction is applied to raw (U–Th)/He ages, to account for ^4He atoms ejected out of a crystal during alpha decay of parent isotopes (Farley et al., 1996; Farley, 2002). The proportion of lost ^4He atoms is routinely estimated using the size and geometry of the crystal, and results in a (U–Th)/He age correction, which is usually in the range of ~25–50%

for typical zircon grains. Second, a correction is required for U-series disequilibrium if the time between crystallisation and eruption of the crystal is less than ca. 350 ka (five half-lives of ^{230}Th, which is the time taken for the system to be in secular equilibrium; Farley et al., 2002; Schmitt et al., 2006). In this case, the ^{238}U decay system is not in secular equilibrium (i.e., a non-standard number of alpha particles is produced per parent nuclide decay and unit time) and disequilibrium can result in an apparent (U–Th)/He age that is either younger or older than the true eruption age depending upon initial disequilibrium in the activity of ^{230}Th/^{238}U. A disequilibrium correction can be calculated from the crystallisation age and the uncorrected (U-Th)/He age and, in the most extreme cases, this can result in a final eruption age that is 50% older than the uncorrected (U-Th)/He age (Farley et al., 2002).

Principles and analytical procedures of ZDD are reviewed by Danišík et al. (2017b). Currently, a typical ZDD procedure utilises single crystallisation ages determined on the rims of unground crystals using spot analysis approaches (e.g., secondary ionisation mass spectrometry, SIMS, or high-resolution laser ablation inductively coupled plasma mass spectrometry, LA-ICP-MS; Schmitt et al., 2011; Ito and Danišík, 2020). Assuming that the crystallisation of the core and rim was coeval, these ages are then used to correct (U-Th)/He data for U-series disequilibrium (Lovera et al., 2009; Schmitt et al., 2010; Danišík et al., 2017b). However, if the zircon crystallised over an extended period of time, this assumption is invalid and using the rim crystallisation age to correct for disequilibrium may result in an overestimated (U-Th)/He age (Friedrichs et al., 2020a). Significant rim/core age differences of >190 ka have been reported on <1 Ma zircon crystals (e.g., Storm et al., 2011; Storm et al., 2012; Harangi et al., 2015; Friedrichs et al., 2020b), and addressing this issue is an important step in improving the accuracy of the ZDD method.

One approach used to measure the crystallization history is to deeply section the grain and measure U- Pb or U-Th disequilibrium ages in a traverse from the rim to the grain interior (e.g., Friedrichs et al., 2021). Given that zircon crystals are prismatic and typically < ca. 100 microns in width, the typical diameter of an ion microprobe sputter pit (ca. 20-30 microns for young grains) generally yields only a few age measurements when proper spacing is maintained to minimize surface charging. Because the resolution of the ion microprobe is greatest in the depth dimension, a more highly resolved crystallization age sequence can be measured by serial sectioning and repeated analysis of the grain. However, this method can introduce complications for the Ft correction, analogous to utilising broken crystals in (U-Th)/He dating (Brown et al., 2013). If a crystal is haphazardly ground to expose the interior in order to facilitate core crystallisation age determination prior to whole crystal (U-Th)/He dating, the magnitude of the Ft correction factor is essentially unknown. The ability to accurately calculate an Ft correction factor for a ground crystal could be a significant methodological improvement to ZDD.

This study presents a general solution to this problem. First, the effect of reducing the volume of a zircon crystal during sectioning of the grain for ion probe analysis on the Ft correction factor is investigated to establish whether core crystallisation ages can be measured without compromising the Ft correction. Second, the magnitude of core-rim crystallisation age disequilibrium corrections on (U-Th)/He ages is evaluated using stratigraphically well-defined late Quaternary tephras from the Shikotsu-Toya volcanic field in the Hokkaido region of Japan.

2.2 Theory and calculations

2.2.1 Impact of grain sectioning during ion microprobe sample preparation upon the Ft correction.

The Ft correction factor is defined as the ratio of the He measured (He_m) to the total He produced (He_p) (Farley et al., 1996; Farley, 2002).

$$Ft = \frac{He_m}{He_p}$$

The He_m is mostly dependent on both the volume and the geometry of the crystal, as only He particles from parent isotopes located within stopping distance of the crystal surface, referred to here as the 'boundary layer', can be ejected and lost from the crystal. Considerable work on Ft correction factors has been completed, including analysis of zoning affects (Hourigan et al., 2005; Danišík et al., 2017a), grinding and abrasion of crystals (Blackburn et al., 2007; Reiners et al., 2007; Danišík et al., 2008, Danišík et al., 2010), the effects of broken crystals (Brown et al., 2013) and analyses of crystal shape measurement techniques (Evans et al., 2008; Cooperdock et al., 2019; Glotzbach et al., 2019).

Because the effects of alpha particle ejection are integrated over the volume of the entire crystal in standard Ft corrections (e.g., Reiners, 2005), grinding away some of the crystal will change the number of He atoms within the original boundary layer relative to the number of He atoms within the crystal interior. Consequently, the decrease in He_m may not be proportional to the decrease in He_p, thereby altering the Ft correction factor in a complex manner.

As suggested by Reiners et al. (2007), grinding down a crystal to a plane of symmetry preserves the ratio of the number of sources in the boundary layer to the number of the sources in the crystal interior, as exactly half the original boundary layer and half the interior are lost (Eq. (2)). This therefore preserves the ratio of He_m to He_p, thereby leaving the Ft correction factor unchanged.

$$\frac{He_m}{2} = Ft \times \frac{He_p}{2}$$

For completeness, it is noted that grinding down to a plane of symmetry is not the only way to preserve the He_m:He_p ratio. In general, any crystal with two-fold rotational symmetry can be ground down to a plane containing the two-fold axis, and the ratio of boundary layer to interior will remain constant. Some examples are shown in Figure 2.i.

2.2.2 Simulation via GriFt

Grinding to exactly 50% of a crystal is often difficult, especially if a mount contains multiple crystals with different diameters. As such, it is important to understand how deviation from grinding to exactly half-width affects the relative error in the Ft correction factor and how this deviation might vary with crystal shape and zoning of parent isotope concentration in the grain. In order to investigate these consequences and to validate the original 50% hypothesis, a Python code (GriFt - available here; https://github.com/RubyMarsden/GriFt) was developed to simulate the impact of partial removal of a zircon crystal during sectioning process for SIMS analysis upon the standard Ft correction.

The GriFt program, takes as inputs, a series of nested polyhedra, specified by their vertices, representing the crystal and its internal zones. Each zone can be assigned a concentration of alpha particle sources by the user. The program then generates a random uniform distribution of 'alpha particle sources' throughout the polyhedron (Figure 2.1), using rejection sampling of points randomly generated within the polyhedron's bounding cuboid (Wells et al., 2004). In order to calculate the local Ft value for each source, the source is assigned a constant shell of alpha particles at a user-defined stopping distance, and the proportion of the alpha particles that remain within the crystal is calculated. For a whole crystal that has not been ground the final Ft correction factor is calculated by averaging the local Ft value of all the sources.

To simulate grinding parallel to the crystallographic c-axis, a user-defined parameter 'grinding depth' is available. The local Ft value is then calculated for all sources, regardless of whether they have been removed from the crystal or not, with alpha particles being counted as outside if they are either exterior to the crystal or have been ground away. The final Ft value is calculated by summing the local Ft value of all the sources and dividing by the number of sources that remain in the crystal after grinding. This means that alpha particle sources which were above the grinding plane during the decay stage (i.e., those that would implant daughter product into the crystal), are still taken into account.
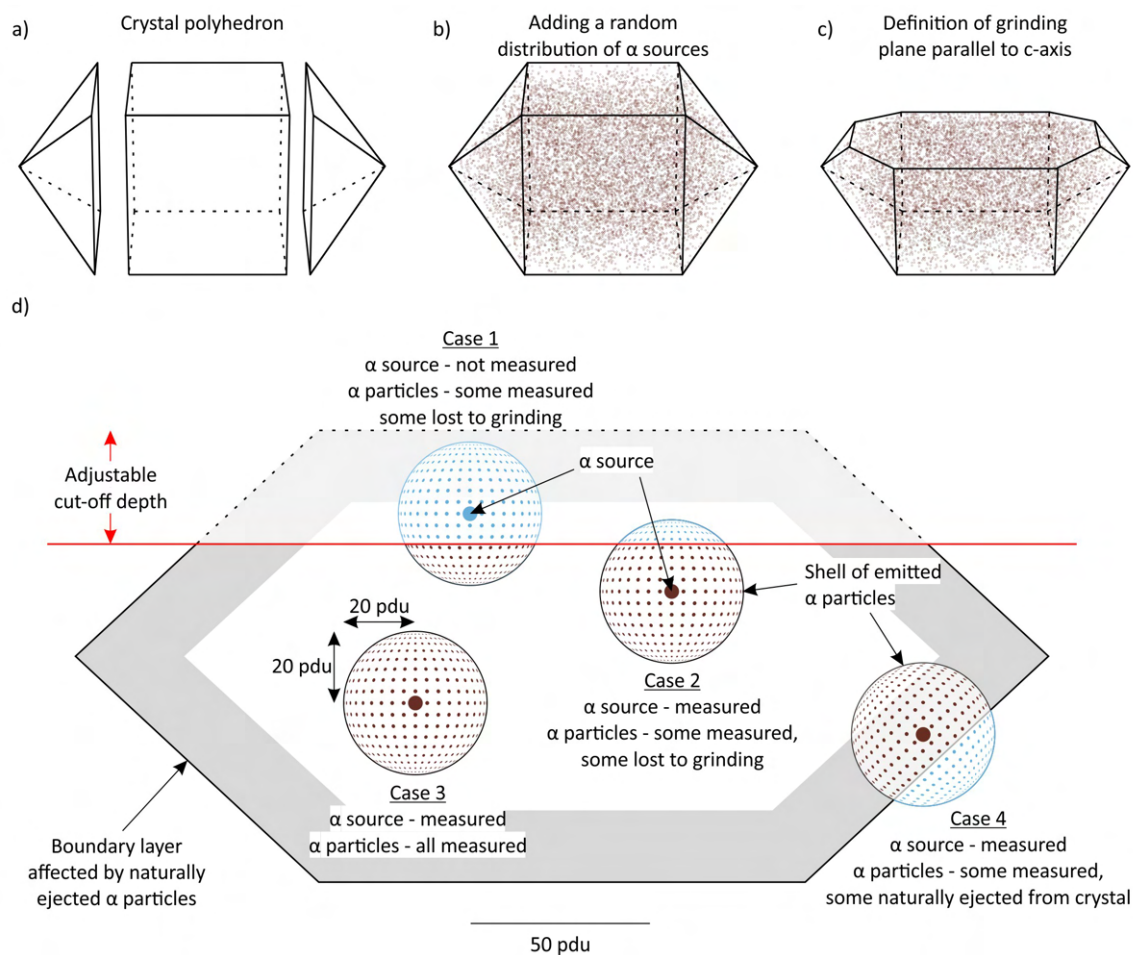
Figure 2.1: A conceptual diagram of GriFt simulation showing a) construction of the crystal polyhedral, b) the random distribution of alpha sources, c) the plane of grinding the polyhedron and d) a 2D diagram showing the different possible relationships between the alpha particle sources, the alpha particles, the original geometry of the crystal and the adjustable 'cut-off depth' simulating grinding. The boundary layer is designed after Farley (2002). Zoning of alpha particle source concentration is not represented here.

2.3　The Shikotsu-Toya volcanic field

2.3.1　Volcanologic and compositional context

The Shikotsu-Toya volcanic field (STVF) is a Neogene-Quaternary volcanic field located in SW Hokkaido, comprising three caldera volcanoes (Toya, Kuttara, and Shikotsu and their post-caldera volcanoes) and the Yotei and Shiribetsu stratovolcanoes (Figure 2.2). Four silicic tephras from the STVF are investigated in this study (in stratigraphic order from bottom to top): Km-2, Km-1, Kt-1, and Sp-1 (Figure 2.3). Km-2 and Km-1 tephras (Kimobetsu ignimbrite 2 and 1) were derived from the Shiribetsu-dake volcanic complex (Uesawa and Nakagawa, 2016; Goto et al., 2020). Km-2 and Km-1 deposits around the Shiribetsu-dake complex are 10-20 m thick and have estimated bulk volumes of 7.0 and 3.4 km3, respectively. Both Km-2 and Km-1 comprise a crystal rich rhyodacite (bulk SiO_2 = 67-68 wt%) containing approximately 1-3 mm long phenocrysts of amphibole and quartz (Goto et al., 2020). On the basis of stratigraphic relationships, the inferred ages of Km-1 and Km-2 are 70-80 and 110-130 ka, respectively (Amma-Miyasaka et al., 2020). Zircon fission track ages of 70 ± 20 ka and 130 ± 30 ka for units Km-1 and Km-2, respectively, coincide with the ages determined from stratigraphy (Goto et al., 2020). The Km-2 and Km-1 tephras are separated by the Toya tephra, which is an important stratigraphic marker horizon in Japan (e.g., Machida, 1999). Toya has a range of stratigraphic and geochronological ages that converge to a commonly cited eruption age of 109 ± 3 ka (Tomiya and Miyagi, 2020).

Kt-1 is a tephra deposit representing the latest volcanic episode in the Kuttara caldera complex. Kt-1 comprises a series of silicic subunits of pumice fall and pyroclastic density current (PDC) deposits (Yamagata, 1994). The white pumice of Kt-1 comprises a crystal rich rhyodacite (bulk SiO_2 = 65-73 wt%; Moriizumi, 1998) including approximately 1-3 mm sized phenocrysts of quartz and, more rarely, amphibole. The presence of quartz phenocrysts and the high content of K_2O (2-3 wt%) in the glass of the Kt-1 rhyodacite are characteristic in comparison with other Kuttara tephras. A charcoal sample from Kt-1 yielded a calibrated 14C age of 44.7-43.5 cal ka (Amma-Miyasaka et al., 2020).

Sp-1 is the tephra deposit from the latest caldera-forming episode at the Shikotsu caldera. The Sp-1 tephra comprises deposits of a lower pumice fall and an upper pyroclastic density current, which are named Sp-1 pfa and Sp-1 pfl, respectively. The Sp-1 pfa pumice deposit and the Sp-1 pfl co-ignimbrite ash fall deposit form a marker tephra in a broad region of southeast Hokkaido and in the surrounding offshore area. Dominant white pumice of Sp-1 comprises a crystal poor rhyodacite-rhyolite (bulk SiO_2 = 68-77 wt%; Nakagawa et al., 2018) and includes phenocrysts of plagioclase and pyroxene (<5 wt%), and rare hornblende. The presence of crystal-poor textures and a high K_2O content in the glass (2.5-3 wt%) of the Sp-1 rhyodacite-rhyolite is distinctive in comparison with
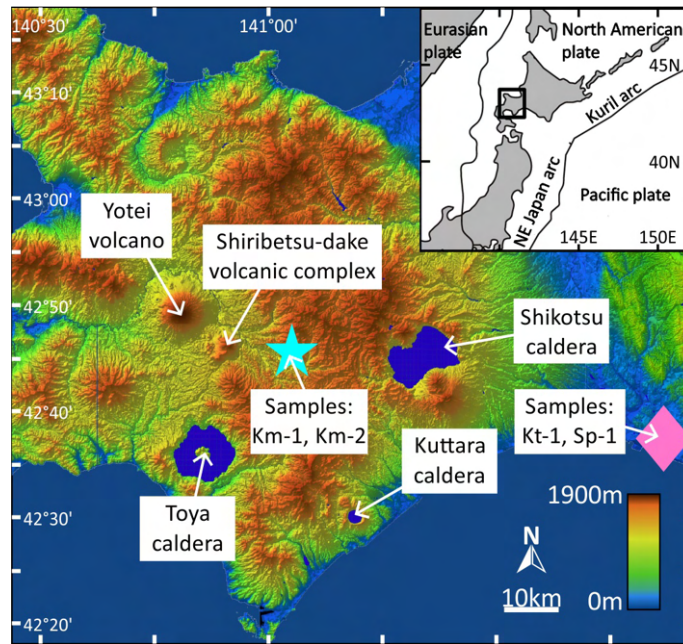
Figure 2.2: Digital elevation model of the Shikotsu Toya volcanic field (STVF) (digital topographic data issued by the Geospatial Information Authority of Japan). The cyan star is the locality of Km-2 and Km-1; and the pink diamond is the locality for Kt-1 and Sp-1. Inset: Simplified tectonic setting of NW Japan modified from Amma-Miyasaka et al. (2020) with plate boundaries indicated by black lines. The main figure area is indicated by the rectangle.

other tephras in the volcanic suite, excluding Toya. The 14C ages for charcoal in Sp-1 were obtained from the lowermost part of the proximal fall, and from the interior of distal PDC deposits. The 14C ages for the Sp-1 have been reported as 46.5-45.1 cal ka (Uesawa et al., 2016), and 44.4-43.2 and 41.8-40.9 cal ka (Amma-Miyasaka et al., 2020). A thin volcaniclastic paleosol is observed separating Kt-1 from Sp-1, implying a dormant period between eruptions (Amma-Miyasaka et al., 2020).

2.3.2 Sample sites

Pumice clasts of Km-2 and Km-1 ignimbrites were collected from the type sections (42°45' 52.45" N 141°00' 10.82" E) as designated by Uesawa and Nakagawa (2016) and Goto et al. (2020). Here, the exposed sequence consists of (from bottom to top; Figure 2.3a): > 10 m thick Km-2, 0.5-1.0 m thick reworked Toya, 15 m thick Km-1, 20 cm thick Sp-1 fall unit and a ∼5 m thick pyroclastic flow deposit. This bracketing of the reworked Toya tephra shows that Toya is younger than Km-2 and older than Km-1. The Km-1 and Km-2 site is ca. 25 km from the Toya caldera and ca. 10 km from the Shiribetsu Volcano.

Pumice clasts of Kt-1 and Sp-1 fall deposits were collected from site DS5 (42°37'22.02"N, 141°53'21.56"E; Figure 2.3b, c), where the exposed tephras are well documented (see Figure 2.8 of Amma-Miyasaka et al., 2020). The representative site DS5 exposes a nearly complete section of STVF tephras. In addition to Kt-1 and Sp-1, other tephras from
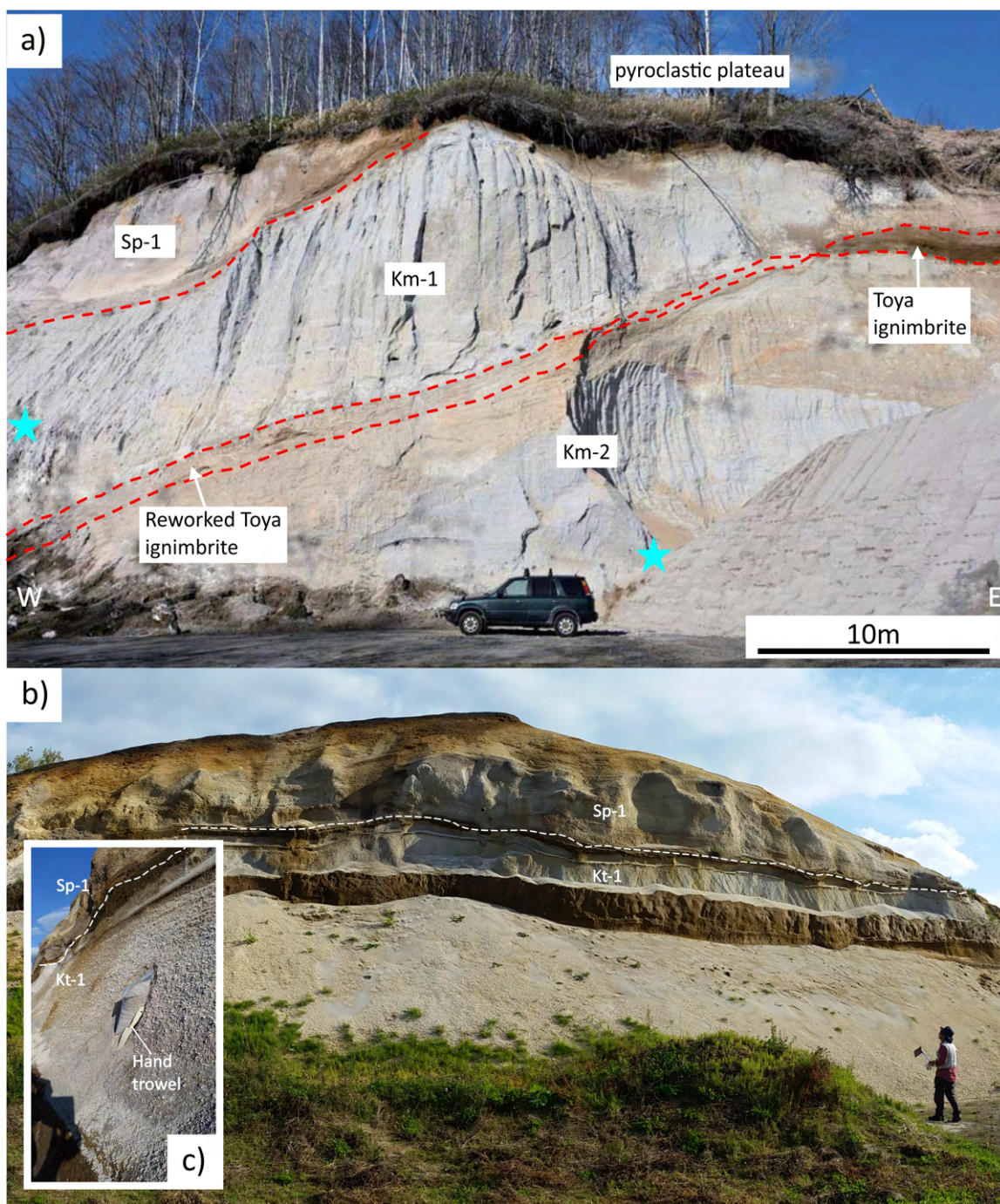
Figure 2.3: a) Field photographs of sampling site for the Km-2 and Km-1 tephras (marked by cyan stars) modified from Goto et al. (2020). b) Field photographs of sampling site DS5 showing tephra Kt-1 and Sp-1. The white dashed line shows approximate stratigraphic boundary. c) Inset shows sampling site of Kt-1 with Sp-1 above, hand trowel (for scale) is ca. 20 cm.

a range of calderas (Kuttara, Shikotsu, Shiribetsu-dake, Toya and Kutcharo - the only caldera listed here not part of the STVF) are exposed. Thicknesses for the sampled fall deposits of Kt-1 and Sp-1 are 1.2 m and 4 m, respectively. The Kt-1 and Sp-1 site is ca. 50 km from the Shikotsu caldera and ca. 60 km from the Kuttara caldera.

2.4   Methods

2.4.1   Modelling the impact of grinding on Ft correction factor

For this work, a 'zircon crystal approximation' comprising a cube (dimensions $100 \times 100 \times 100$ procedurally defined units (pdu)) with bi-pyramidal terminations (height - 50 pdu) was simulated using GriFt. To simulate zonation, an inner polyhedron was defined with a different concentration of alpha source particles to the outer polyhedron. Four zoned experiments were carried out: the first with a symmetric enriched inner zone, the second with a symmetric depleted inner zone, the third with an asymmetric enriched inner zone and the fourth with an asymmetric depleted inner zone. A concentration difference of a factor of 10 between zones was assigned, estimated as a representative difference from the magnitude of U (ppm) variation in the samples measured in this study.

One hundred thousand alpha particle sources were simulated per experiment. This value was chosen to be conservatively above the point at which adding further sources did not significantly change the resulting Ft correction factor. Each source was assigned a shell of 450 alpha particles (constrained by computational complexity) at a stopping distance of 20 pdu, chosen as an order of magnitude approximation to the average alpha stopping distance in zircon (Ketcham et al., 2011) as used in previous Ft correction modelling (Gautheron et al., 2012). The parameter 'grinding depth' was increased in steps of 2 pdu from 0 to 100 pdu.

2.4.2   Analytical methods used in the case study

Zircon was separated from four rhyolite pumice samples (Km-2, Km-1, Kt-1 and Sp-1) using jaw crushing, disc-milling, Wilfley table, magnetic separation, and heavy liquids. After initial separation of zircon, the ZDD standard procedure was followed for all samples. Additionally, for zircons in samples Km-2 and Km-1, a modified procedure that includes grinding was carried out. Samples Kt-1 and Sp-1 did not yield sufficient zircon on which to perform ZDD analysis. The procedural differences are described below and illustrated in Figure 2.ii.

2.4.2.1 Procedure 1 - the standard ZDD procedure (rim crystallisation ages)

Procedure 1 follows the standard method described in Danišík et al., 2017b, Danišík et al., 2020. Whole rock U-Th values were measured at LabWest Minerals Analysis Pty Ltd, Perth (Australia), using whole rock microwave assisted dissolution of samples and analysis of U and Th by external calibration on a Perking Elmer NexION 300Q ICP-MS.

Whole zircon crystals were pressed into indium mounts and U-Th disequilibrium dating was carried out using the CAMECA ims 1280-HR instrument in the Heidelberg Ion Probe laboratory (Heidelberg University, Germany) using procedures developed and set out in Reid et al. (1997), Schmitt et al., 2006, Schmitt et al., 2011, Schmitt (2011) and Friedrichs et al. (2020c). The ^{230}Th/^{232}Th and ^{238}U/^{232}Th isotope ratios of the mineral surfaces were measured using a nominal 40 nA intensity beam with a 20 μm diameter spot. Reference materials for this procedure were 91500 zircon (for U isotopic concentrations; Wiedenbeck et al., 1995) and AS3 (for secular equilibrium standardisation; Paces and Miller, 1993).

After U-Th disequilibrium ages were determined, the maximum eruption age (as the youngest crystallisation must pre-date eruption) was calculated using the method of Keller et al. (2018), more detail on this method can be found in Supplementary material 1.

After SIMS analysis, zircon crystals were plucked out of the indium mounts and photographed under an optical microscope along two crystallographic axes. Crystal dimensions were measured for Ft correction calculation (Farley et al., 1996; Farley, 2002). Crystals were placed into niobium microtubes and analysed for ^{4}He on the Alphachron^{TM} II at the John de Laeter Centre (JdLC), Curtin University (Perth, Australia). Zircon crystals were degassed in an ultra-high vacuum using a 970 nm diode laser that heated individual niobium capsules for 15 min at 1250 °C. The gas extracted from the crystals was spiked with ^{3}He and measured for ^{4}He on a quadrupole PrismaPlus QMG 220 by isotope dilution. After each analysis, the individual capsules were re-heated to ensure complete He extraction. Blank corrections were made using ^{4}He measurements of empty niobium microtubes. Zircon crystals, within their capsules, were then individually spiked with ^{230}Th and ^{235}U and dissolved in 350 μl of HF and HNO3 in Parr pressure digestion vessels for 60 h at 230 °C (Evans et al., 2005; Danišík et al., 2017b, Danišík et al., 2020). After removal from the oven, the individual solutions were dried at ca. 50 °C for 2 days to remove HF. The fluoride salts remaining from this process were then dissolved in 300 μl of HCl in the Parr bombs at 200 °C for 24 h. These solutions, diluted with Milli-Q water, were analysed by isotope dilution for ^{238}U and ^{232}Th, and by external calibration for 147Sm on an Element XR^{TM} High Resolution ICP-MS. The total analytical uncertainty was calculated as the square root of the sum of the following: the uncertainty of the He measurement squared and the weighted uncertainties of the U, Th, and Sm measurements squared. The Ft correction was calculated using the Flojt program (Gautheron and

Tassan-Got, 2010) assuming a homogenous distribution of U, Th and Sm.

MCHeCalc software (Schmitt et al., 2010) was used to correct the Ft-corrected (U-Th)/He ages for disequilibrium in the U-series and for crystal residence time before eruption (Farley et al., 2002). This software requires the following parameters: Ft-corrected (U-Th)/He ages, U-Th crystallisation ages, associated uncertainties, D230 and D231. The D230 and D231 values are parameters describing the fractionation of ^{230}Th and ^{231}Pa relative to U from the melt into zircon crystals. Calculation of D230 (Farley et al., 2002) was achieved by dividing the Th/U measured from individual crystals by the Th/U of the whole rock. This calculation assumes that the magma was in secular equilibrium at the time of zircon crystallisation and that the whole rock value of Th/U is the same as that of the magma from which the zircon crystallised. It is also assumed that D231 is a constant value of 3.3 based on an average of published values of Pa/U zircon-rhyolite melt partition coefficients (Schmitt, 2007; Schmitt, 2011; Sakata et al., 2017). The output of MCHeCalc is a best-fit eruption age for a sample's zircon population which is here termed a ZDD eruption age.

2.4.2.2 Procedure 2 - the altered ZDD procedure allowing inspection of crystal interiors

Procedure 2 varies from Procedure 1 in that it includes measurement of the crystallisation age on the zircons' cores, and makes use of the hypothesis put forward in Section 2.2. It was applied only to zircon grains from Km-2 and Km-1, these two samples had a sufficient abundance of zircon that the two methods on two separate populations could be compared. The He gas extraction and dissolution of grains analysed using Procedure 2 were carried out during the same analytical sessions as those in Procedure 1. The differences between the two approaches occur pre- and post-SIMS analysis.

Selection of the largest, most euhedral zircon crystals was followed by imaging under a binocular microscope. These images were then used to measure the crystals shape and size in order to calculate the Ft correction factor. Crystals were then mounted in epoxy rounds with their c-axes parallel to the surface, ground and polished to an estimated half-width (Figure 2.4) as suggested by the theoretical analysis in Section 2.2. All selected zircon grains were approximately the same diameter prior to grinding and polishing. The exposed crystal interiors were imaged using cathodoluminescence (CL) on the TESCAN MIRA3 at the JdLC to investigate U and Th zonation. U-Th disequilibrium dating on the CAMECA ims 1280-HR was carried out following the methods set out in Procedure 1. Spot locations were chosen based on CL images of the zircon crystals. After the interior of the crystals were analysed using SIMS, the zircons were plucked out of the epoxy mounts under ethanol and mounted into indium mounts with the unground side facing the surface. SIMS analysis of the outer rim was then carried out in the same manner as undertaken in

Procedure 1.

Crystals were then plucked out of the indium mounts and re-photographed under an optical microscope. These micrographs were then compared to the original micrographs of the unground crystals to ensure that crystals were ground parallel to the crystallographic c-axis and to half the crystal width. If crystals did not meet these criteria, they were not used for (U-Th)/He measurements. The resultant crystal fragments were placed into niobium microtubes and analysed first for He and subsequently for U, Th and Sm, as in Procedure 1.

Raw (U-Th)/He ages were corrected using the Ft correction factor calculated from the images of whole crystals as in Procedure 1. The Ft-corrected ages and associated uncertainties were used alongside two sets of U-Th disequilibrium ages (rim and core), D230 and D231 in the MCHeCalc program to correct for two different pre-eruptive crystal residence times. This resulted in two ZDD eruption ages for each sample population.
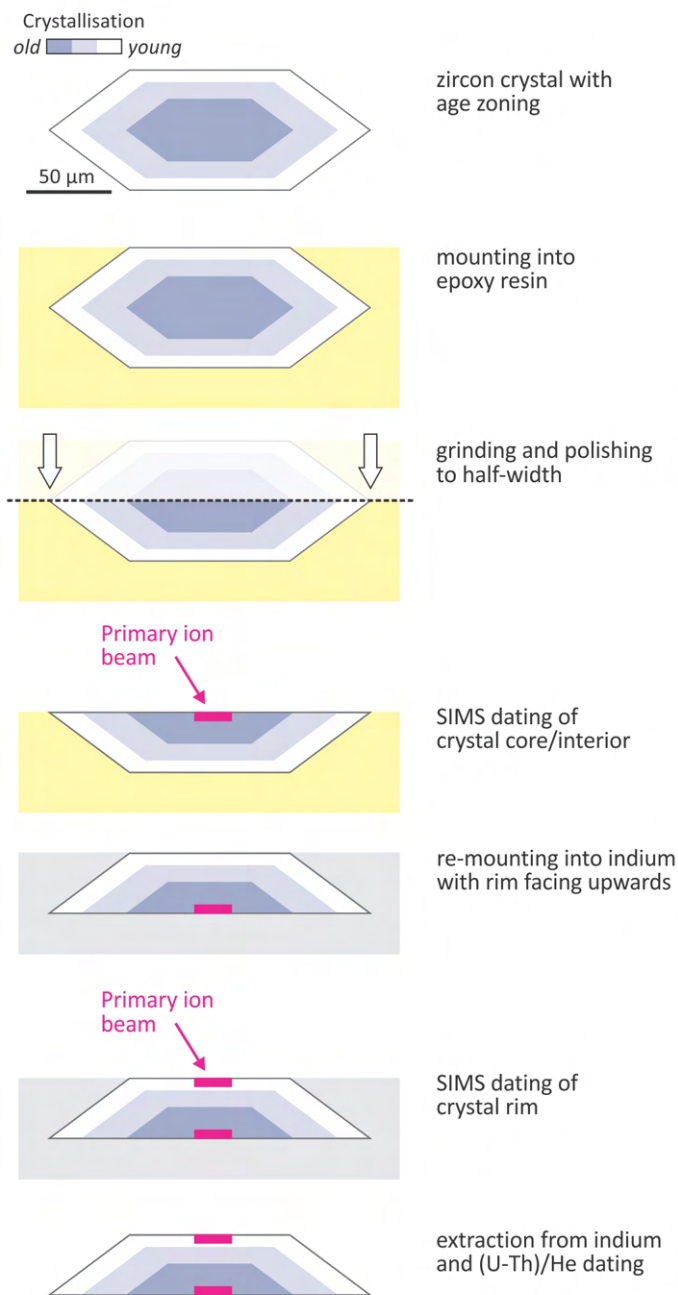
Figure 2.4: Schematic of procedure 2 showing: mounting of zircon crystal into epoxy, grinding and polishing of zircon crystal to half-width (important for Ft correction factor conservation), SIMS dating of the interior, removal of crystal from epoxy resin, re-mounting into indium, SIMS dating of the rim and extraction of the crystal to be followed by (U-Th)/He dating.

2.5 Results

2.5.1 Ft correction modelling results

As postulated by Reiners et al. (2007) and predicted by the hypothesis in Section 2.2, the results from the GriFt simulations confirms no change to the Ft correction factor between a whole crystal and one ground to half-width (50%) along a line of symmetry, regardless of morphology or symmetrical zonation (Figure 2.5). This observation facilitates use of ground crystal cores for crystallisation age calculation, suggesting that polishing to half-width to an axis of symmetry has no detrimental effect on Ft correction calculation. As expected, in the experiments with asymmetric zonation the Ft correction factor is not conserved at 50% grinding and the percentage difference for this offset zonation is 3.8% for an enriched rim and 1.4% for a depleted rim (Figure 2.5).
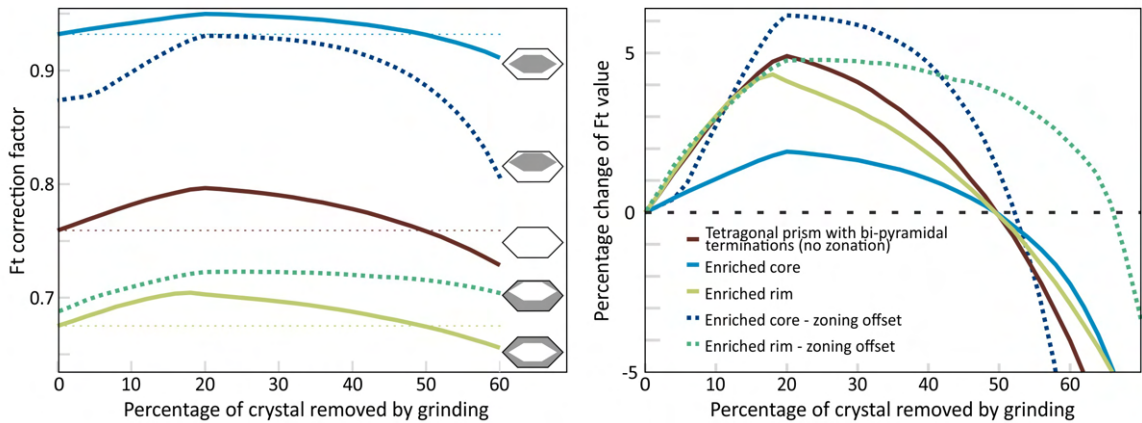
Figure 2.5: Results from the GriFt program showing absolute Ft correction factor variation and relative variation from full crystal Ft correction factor for a: zircon crystal approximation (cube with two pyramidal ends) without zonation - maroon; zircon crystal approximation with enriched rim - lime green; zircon crystal approximation with depleted rim - light blue; zircon crystal approximation with enriched rim and offset zonation - dark green, and zircon crystal approximation with depleted rim and offset zonation - navy. The schematic figures show a central cross-section through the crystal perpendicular to the direction of polishing. The concentration difference between enriched and depleted parent nuclide values was a factor of 10, estimated from the U (ppm) variation of the samples measured in this study. The alpha stopping distance used was 20 pdu and the crystal models were propagated with 100,000 sources of alpha emission. The modelling shows that, assuming symmetry, the Ft correction factor for an unground crystal and for a crystal ground to half-width (50%) are identical, regardless of whether parent nuclides are enriched or depleted in the rim and core.

2.5.2 Geochronology analytical results

Table 2.1 and Figure 2.6 give summaries of all dating results for all procedures. All uncertainties in the text are 2σ uncertainties. Some crystal ages were removed from the

calculation of sample ages as discussed further below and this is represented in Figure 2.6. Full results are reported in Supplementary materials 2, 3 and 4, including raw (U-Th)/He ages and whole rock data.

Table 2.1: Summary of all dating results.

Sample ID	Procedure	Core/ Rim	n_{U-Th}[a]	U-Th minimum age ±2σ[b] (ka)	U-Th maximum age ±2σ[b] (ka)	Max. eruption age from crystallisation age ±2σ (ka)[c]	n_{ZDD}[d]	ZDD eruption age ±2σ (ka)[e]	ZDD eruption age after discussion ±2σ (ka)
Kt-1	1	Rim	7	48.7 ± 20.9	109.7 ± 38.3	48.7 ± 20.9			
Sp-1	1	Rim	11	48.1 ± 17.2	200.0 ± 330.3	48.1 ± 17.2			
Km-1	1	Rim	21	79.0 ± 24.4	>350	67.0 ± 7.8	13	No overlapping distributions	No overlapping distributions
Km-2	1	Rim	16	97.7 ± 28.7	262.3 ± 84.1	94.7 ± 8.2	10	104.1 ± 5.7	110.9 ± 6.3
Km-1	2	Rim	9	73.7 ± 19.9	173.0 ± 91.5	67.0 ± 7.8	5	73.0 ± 5.6	73.0 ± 5.6
Km-1	2	Core	36	120.1 ± 25.2	>350	67.0 ± 7.8	10	61.7 ± 3.0	61.7 ± 3.0
Km-2	2	Rim	15	97.5 ± 34.5	273.2 ± 91.0	94.7 ± 8.2	9	124.6 ± 6.5	114.2 ± 7.3
Km-2	2	Core	34	148.3 ± 26.8	>350	94.7 ± 8.2	9	96.4 ± 5.3	96.4 ± 5.3

[a] *Number of U-Th dated SIMS spots*

[b] *2σ values for U-Th disequilibrium data are the mean of the positive and negative uncertainties*

[c] *Calculated as in Keller et al. (2018)*

[d] *Number of crystals analysed by ZDD*

[e] *ZDD Eruption age calculated using MCHeCalc (Schmitt et al., 2010)*

AS3 had a measured (^{230}Th)/(^{238}U) ratio of 1.014 ± 0.006 (2σ, MSWD = 0.86, n = 119), and all U-Th disequilibrium data were re-calculated to an AS3 unity value.

2.5.2.1   U-Th disequilibrium dating results

U-Th disequilibrium ages calculated from Km-2 and Km-1 zircon rims and cores cover a range greater than the mean analytical uncertainty by a factor of 10. The rim ages for sample Km-2 range from 98 ± 35 ka to 273 ± 91 ka and the core ages range from 148 ± 27 ka to secular equilibrium (implying an age of at least 350 ka). The greatest difference between rim and core age, in an individual crystal, was >250 ka and the smallest was ca. 55 ka. The rim ages for sample Km-1 range from 74 ± 20 ka to >350 ka and the core ages range from 120 ± 25 ka to >350 ka. The greatest difference between rim and core age in an individual crystal was >300 ka and the smallest was 62 ka. These ages are consistent with the clear textural distinction between cores and rims (Figure 2.7). Zircon from Kt-1 and Sp-1 span ages from 49 ± 21 ka to 110 ± 38 ka (n = 7) and from 48 ± 17 ka to 81 ± 20 ka with a low U concentration 'outlier' at 200 + 520/-142 ka which was removed due to low U concentration, respectively.

The maximum eruption ages (cf. Keller et al., 2018) of Km-2 and Km-1 are 95 ± 8
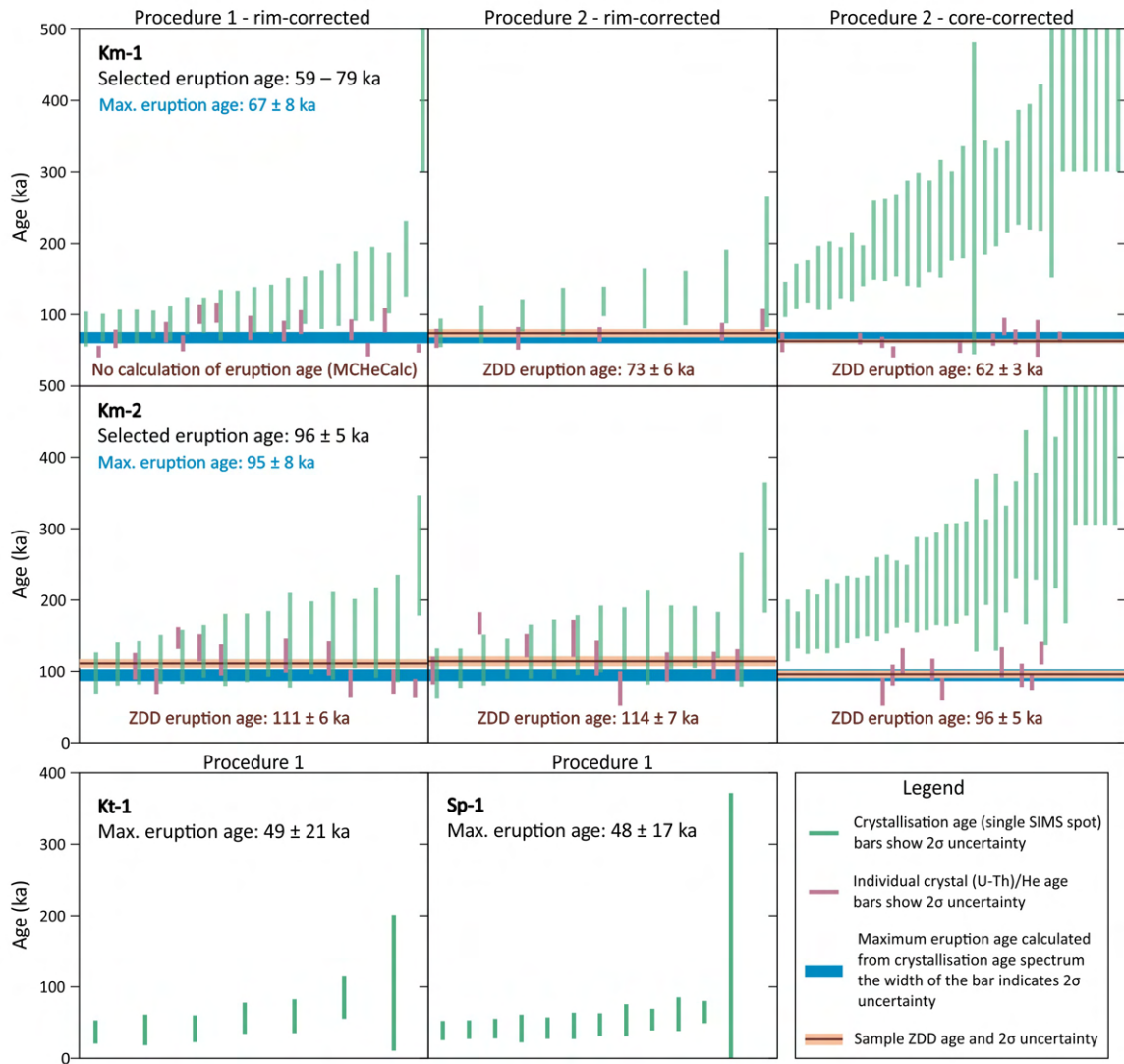
Figure 2.6: Rank-order plots for crystallisation ages from SIMS U-Th dating for samples Km-2, Km-1, Kt-1 and Sp-1 and individual zircon (U-Th)/He ages for samples Km-2 and Km-1. ZDD eruption ages for each procedure for samples Km-1 and Km-2 are shown, as are maximum eruption ages calculated from the crystallisation age spectra.
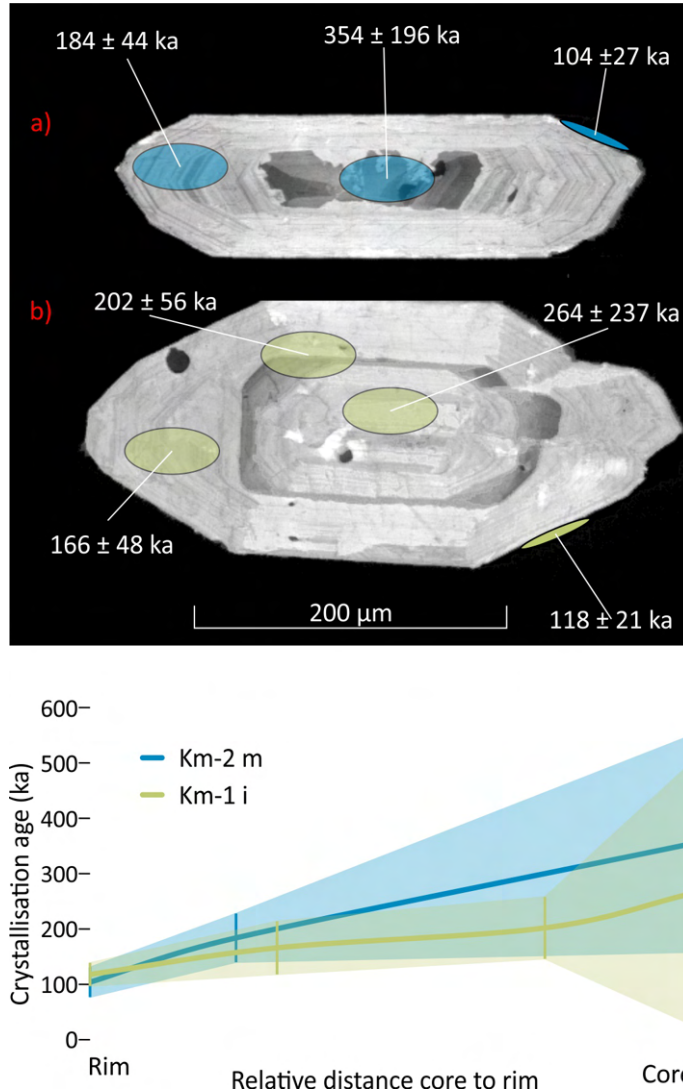
Figure 2.7: Top panel: CL images of example zircons from samples a) Km-2 and b) Km-1 with SIMS U-Th spots and ages marked with blue (Km-2 m) and light green (Km-1 i) ellipses, respectively. The ages on the bi-pyramidal terminations of the crystals represent the rim crystallisation age taken as in Procedure 1. Bottom panel: a plot of U-Th SIMS spot ages and their relative distance from the core of the crystal, with 2σ uncertainty bars for each crystallisation age shown. The ages and their uncertainties are joined using linear interpolation to show how crystallisation ages may vary throughout an individual crystal.

ka and 67 ± 8 ka, respectively.

For zircons from samples Kt-1 and Sp-1 the youngest crystallisation age and its associated uncertainty was used as a maximum eruption age. These ages are 49 ± 21 ka and 48 ± 17 ka, respectively.

2.5.2.2   ZDD results

Zircon from Km-2 using Procedure 1 has a rim-corrected ZDD eruption age of 104 ± 6 ka, within error of the maximum eruption age from U-Th disequilibrium ages. The distribution of disequilibrium corrected (U-Th)/He zircon ages for sample Km-1 is too broad to calculate a sample eruption age and has no clear outliers. For samples Kt-1 and Sp-1 the majority of disequilibrium corrected (U-Th)/He ages were older than corresponding crystallisation ages, therefore they are excluded from the interpretation.

Zircon from Km-2 using Procedure 2 yielded a rim-corrected eruption age of 125 ± 7 ka and a core-corrected eruption age of 96 ± 5 ka. The latter is within error of the ZDD eruption age calculated from Procedure 1 (104 ± 6 ka) and the maximum eruption age calculated from U-Th disequilibrium ages (95 ± 8 ka). The rim-corrected ZDD eruption age is older than both of these ages.

Zircon from Km-1 using Procedure 1 yielded a rim-corrected eruption age of 73 ± 6 ka and a core-corrected eruption age of 62 ± 3 ka. The maximum eruption age calculated from U-Th disequilibrium ages (67 ± 8 ka) is within error of both these ages.

2.6   Discussion

2.6.1   The impact of grinding on Ft correction factor

The theoretical argument that removing exactly 50% of the crystal along a line of symmetry leaves the Ft correction factor unchanged (Reiners et al., 2007), has been validated by the results of the computational modelling in Section 4.1 (Figure 2.5). This provides a sound theoretical basis for the use of grinding to understand the crystallisation history of complex zircons which are going to be analysed using ZDD.

However, grinding to exactly 50% of a crystal width can be challenging due to unknown depth parameters and varying crystal sizes. The effects of inaccurate grinding, investigated via simulations using GriFt, reveals that a 10% uncertainty in fraction of a crystal ground yields <5% uncertainty on the Ft correction factor (Figure 2.5) and that this relationship holds across a variety of shapes and concentration patterns.

Additionally, while the modelling suggests that uncertainties in grinding distances are within the 3-5% uncertainty usually assigned to the Ft correction factor calculation (Evans et al., 2008; Cooperdock et al., 2019; Glotzbach et al., 2019; Danišík et al., 2020)

as postulated by Reiners et al. (2007), additional measures can be taken to minimise uncertainty in grinding distance. For example, grains of similar dimension should be mounted together, and several ceramic or glass spheres (e.g., ball bearings or sand-blasting glass beads) with known diameters could be mounted with the zircon grains to ensure depth control while grinding as the depth ground to will directly control the diameter of exposed sphere. Furthermore, when the crystals are removed from the mounts and prepared for (U-Th)/He analysis, a second set of photographs (as described above in Procedure 2) permits verification of grinding parallel to the c axis and as close to half-width as possible. It is suggested that crystals ground to percentages $\neq 50\%$ should not be considered for further (U-Th)/He analysis. Additionally, asymmetric zonation in zircon is an additional limiting factor (Figure 2.ii). The extent of variation introduced from asymmetry in zonation is shown in Figure 2.5.

However, for practical reasons it is envisaged that grinding to a plane of symmetry to half-width will remain the dominant approach as the majority of crystals will be embedded in epoxy with their c-axes parallel to the epoxy mount surface due to the elongation of euhedral zircon crystals (Poldervaart, 1956). In summary, the measured (U-Th)/He age for a 50% ground down crystal can be accurately corrected for alpha ejection, assuming a symmetrical compositional zonation (Hourigan et al., 2005; Danišík et al., 2017a).

2.6.2 Comparison of rim-corrected eruption ages from Procedures 1 & 2

Theory predicts that the rim-corrected eruption ages from Procedures 1 and 2 should be within uncertainty of each other, because both the crystal population sampled and the calculation method are identical for both procedures. However, this is not the case in the results for either sample Km-2 or Km-1. It is hypothesised that this reflects variation in disequilibrium corrections at the individual zircon level.

Sample Km-2 has two rim-corrected ZDD ages: 104 ± 6 ka from Procedure 1 and 125 ± 7 ka from Procedure 2. While these ZDD ages appear disparate there are two clear 'outliers' in each dataset which, when removed from calculations, lead to two indistinguishable rim-corrected ZDD age, as predicted by the theory. For Procedure 1 the rim crystallisation ages contained one 'outlier' age (262 +100/-68 ka (2σ)), which is ca. 100 ka greater than the other rim ages (98 +31/-27 ka to 160 +88/-63 ka). The inclusion of this outlier reduces the ZDD eruption age of Procedure 1 and if it is removed from analysis, the ZDD eruption age is 111 ± 6 ka (an increase of 6.4%; Figure 2.6). This demonstrates that the choice of crystallisation age can have a large effect on the calculated ZDD age, and confirms that careful consideration should be given to grain selection and outlier evaluation (Danišík et al., 2017b; Friedrichs et al., 2020a). For Procedure 2, Zircon Km-2

d yielded a rim crystallisation age of 118.2 ± 28.2 ka and a Ft-corrected (U-Th)/He age of 118.7 ± 13.2 ka. It also yielded a core crystallisation age of 318 ± 109 ka. The rim disequilibrium corrected (U-Th)/He age for this crystal is 167.6 ± 15.4 ka, significantly older than the rim crystallisation age, which is the maximum eruption age for the crystal. There are several explanations which account for this discrepancy. Firstly, the analysis of a crystal containing undetected He-rich fluid inclusions could result in an older than expected (U-Th)/He age (e.g., Lippolt et al., 1994; Danišík et al., 2017a). Alternatively, if a thin rim crystallised shortly prior to eruption onto a much older, more voluminous core, the disequilibrium age will overcorrect the (U-Th)/He age (example in Figure 2.8). This is because the majority of the crystal (represented by the core) is closer to secular equilibrium (older) but the rim is younger, leading to an overcorrection for this crystal. In this case, the grain analysis should be excluded from the calculation of an overall ZDD age. If the ZDD age is recalculated without this outlier, then the resultant rim-corrected ZDD age for Km-2 is 114 ± 7 ka (Figure 2.6). Following such considerations sample Km-2 now has two rim-corrected ZDD ages which are statistically indistinguishable.
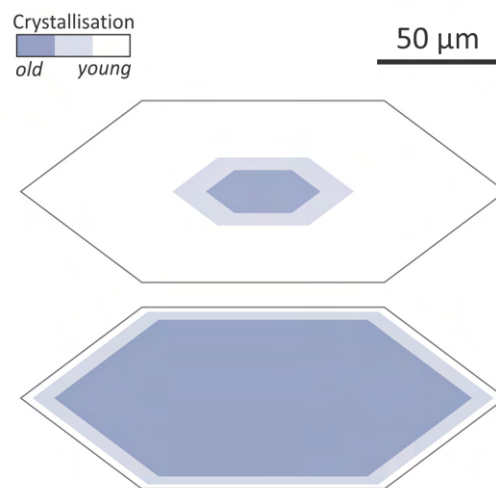
Figure 2.8: Example of potential variation in age zonation in a zircon crystal.

Sample Km-1 has a rim-corrected age measured using Procedure 2 of 73 ± 6 ka, but using Procedure 1 there was no successful ZDD age calculated due to the broad distribution of individual disequilibrium corrected (U-Th)/He ages, yet no outliers were observed. This apparent age distribution can be explained by a range of rim crystallisation ages causing variable disequilibrium corrections, undetected inclusions and/or potential contamination of reworked crystals from other tephras, consistent with the pumice clasts for samples Km-2 and Km-1 embedded into an unconsolidated deposit.

2.6.3 Comparisons of rim and core disequilibrium corrected eruption ages

Having verified that the Ft correction factor for a crystal remains unchanged after grinding to 50%, the crystal's rim and core disequilibrium corrected (U-Th)/He ages can be calculated. Measuring only the rim crystallisation age and assuming that it is the same as the interior crystallisation age, results in over-correction of (U-Th)/He ages if crystallisation was protracted (e.g., Schmitt, 2011; Friedrichs et al., 2020a; Friedrichs et al., 2020b; Friedrichs et al., 2021). Conversely, measuring only the interior and assuming that the rim crystallisation age is the same results in under corrected, and erroneously young, eruption ages if crystallisation was protracted.

The results in Figure 2.9 validate this prediction. Samples Km-2 and Km-1 were investigated in order to examine the extent of under- or over-correction that can occur. These samples had extended crystallisation durations and considerable variation in the rim and core zircon crystallisation age. This is important to note as it has a variable effect on the extent of over- or under-disequilibrium correction on the ZDD age. Figure 2.7 shows CL images of representative zircon crystals with annotated crystallisation ages. Zircon Km-2 m appears to have a thin outer growth and comparatively older interior crystallisation age. Zircon Km-1 i appears to have a volumetrically larger rim and overall less variation in rim and core crystallisation age.
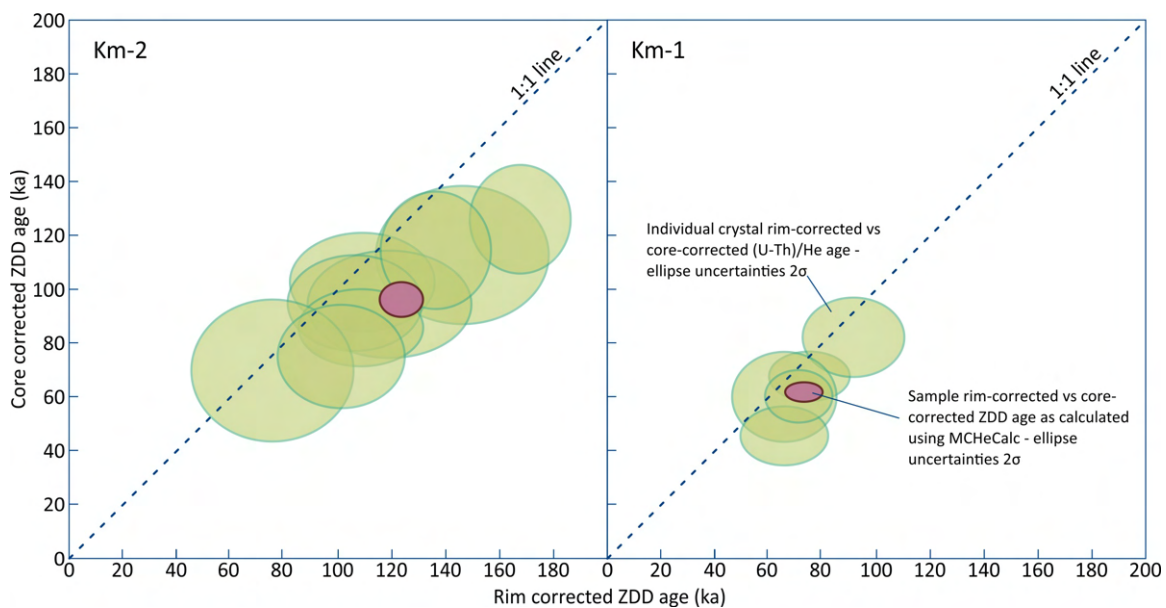
Figure 2.9: Bi-variant plots of samples Km-2 and Km-1. Light green circles are individual crystal (U-Th)/He ages corrected for disequilibrium. Dark red circles are sample ZDD ages calculated out of the same population (both rim and core dated crystals).

For both samples Km-2 and Km-1, the ZDD eruption age calculated using core and rim crystallisation age correction for Procedures 1 and 2 show no statistical overlap with

the core-corrected ZDD eruption age < rim-corrected ZDD eruption age (Figure 2.6, Figure 2.9). Comparing core-corrected and rim-corrected ZDD ages in this way shows that if crystallisation is protracted, then utilising Procedure 1 for disequilibrium correction could potentially result in inaccurate eruption ages.

2.6.4   Proposed eruption ages

The range of age values provided by the ZDD approach offers several options for determining eruption age, a representative eruption age is proposed from the data. For sample Km-2 the core-corrected ZDD eruption age (96 ± 5 ka; n = 9) and the maximum eruption age calculated from the zircon crystallisation age spectrum (95 ± 8 ka; n = 65) overlap within uncertainty. Given these convergent ages, we propose that the eruption age of Km-2 is more accurately measured in this instance by the core-corrected ZDD age (96 ± 5 ka).

In the case of sample Km-1, the eruption ages range between 62 ± 3 ka to 73 ± 6 ka, and the maximum eruption age (67 ± 8 ka) would support the use of the range between a rim-corrected or core-corrected ZDD eruption age. The results suggest that Km-1 erupted between 73 ± 6 ka (rim-corrected) and 62 ± 3 ka (core-corrected; Figure 2.10). As the extent of crystallisation age variation in Km-1 zircon crystals is not fully determined, an eruption age range is best interpreted as 59-79 ka (Figure 2.6).

2.6.5   Tephrostratigraphic implications

The advantage of applying Procedure 2 to an area with established tephro-stratigraphic framework in the study localities (Figure 2.3) provides a means to test the accuracy of the ZDD method. Samples Km-1 (59-79 ka) and Km-2 (96 ± 5 ka) give ages which fit their stratigraphic position as Km-2 is underlying Km-1 and thus has to be older. However, stratigraphic constraints do allow for further refinement of the eruption age for Km-1 because the overlying tephra (Sp-1, 47 ± 17 ka) is significantly younger than the permissible eruption ages which can be defined from the geochronological data. Kt-1 and Sp-1 have maximum eruption ages of 49 ± 21 ka and 48 ± 17 ka, respectively, and also fit the relative stratigraphic constraints.

Since Km-2 and Km-1 bracket the Toya tephra (Figure 2.3a) the accuracy of existing Toya geochronology can be addressed. A wide range of eruption ages have been reported for the Toya eruption ranging from 104 ± 15 to 130 ± 30 ka (e.g., Okumura and Sangawa, 1984; Ganzawa and Ike, 2011). Tomiya and Miyagi (2020) summarised the geochronological data for the Toya tephra and argued for an age of 109 ± 3 ka which is currently accepted. Figure 2.10 shows a probability density plot of the existing geochronological data for the Toya eruption. In addition, it shows the Marine Isotope Stage (MIS) 5.33 which the Toya eruption potentially lies within (Tomiya and Miyagi, 2020) and the eruption age
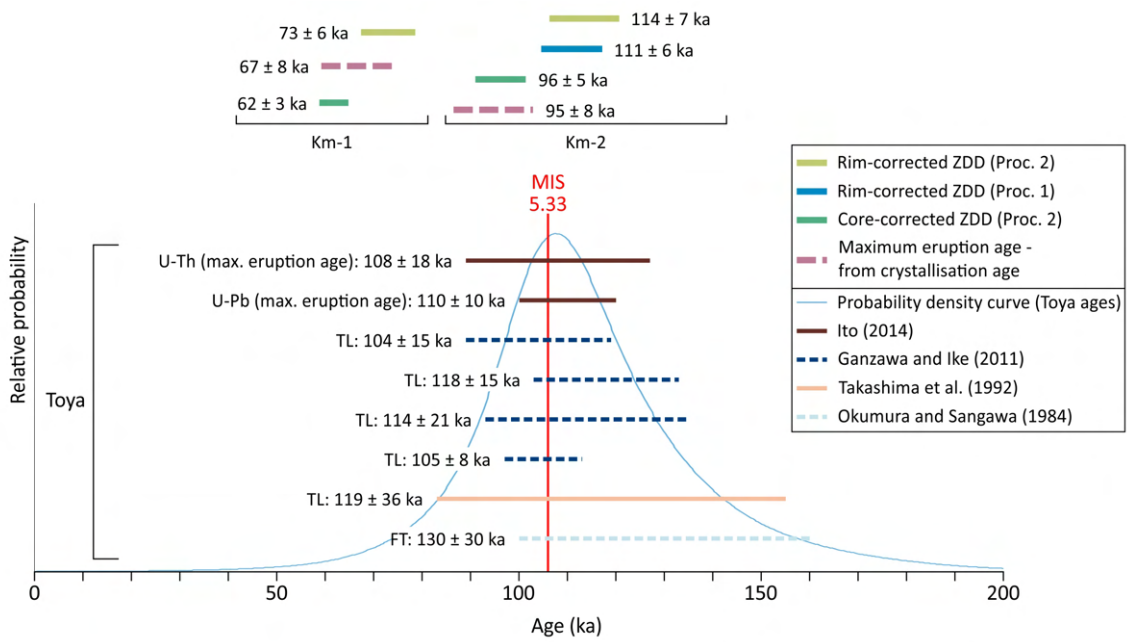
Figure 2.10: Toya geochronology based on the following techniques: U-Th: U-Th disequilibrium age, TL: thermoluminescence, FT: fission track, summarised in Tomiya and Miyagi (2020) from Okumura and Sangawa (1984), Takashima et al. (1992), Ganzawa and Ike (2011) and Ito (2014). The ages from the literature are used to create a probability density curve for the Toya eruption age. The various eruption ages measured for samples Km-1 and Km-2 are indicated above the Toya geochronology. Marine isotope stage (MIS) 5.33 is shown. All age bars have 2σ uncertainties except for MIS 5.33.

constraints from samples Km-2 and Km-1 of this study.

The ages determined in this work have geological implications for the age of the Toya tephra as while Km-2 underlies Toya and is thus older, the proposed eruption age (96 ± 5 ka) is younger than the currently accepted age for Toya (109 ± 3 ka). However, Tomiya and Miyagi (2020) indicate that there are some complications in their collated data. It is suggested that sedimentary considerations that place Toya within MIS 5.33 are potentially incorrect due to high rates of sedimentation. Additionally, the U-Th disequilibrium and U-Pb ages (Ito, 2014) are crystallisation ages, which give a maximum bound on the eruption age. Furthermore, some methodological corrections of the U-Th disequilibrium work carried out on Toya (Ito, 2014) have been questioned (Guillong et al., 2015). While taking these considerations into account, the results from this work suggest that Toya may have erupted more recently than previously thought. However, it must be acknowledged that there are assumptions made in the calculation of our preferred eruption age and that the disequilibrium correction is complicated. This is reflected in the rim-corrected eruption ages of Km-2 of 114 ± 7 ka and 111 ± 6 ka which are older than the currently accepted eruption age for Toya. These discrepancies in potential age for the Toya tephra suggest further investigation of these tephras should take place.

The calculation of both rim- and core-corrected ZDD ages using Procedure 2 enabled us to fully investigate and better understand the potential range of eruption age of Km-2. Moreover, the above-presented evidence for an eruption age of Km-2 at 96 ± 5 ka supports the argument that the eruption age of another fall deposit (Srb-3), previously inferred to be coeval or older than Km-2 (Amma-Miyasaka et al. (2020), is indeed older than Km-2.

Amma-Miyasaka et al. (2020) proposed an eruption age of >43 ka for the Kt-1 tephra, compatible with the maximum eruption age of 49 ± 21 ka determined in this work. Unit Sp-1 has a proposed age of 44-41 ka (Amma-Miyasaka et al., 2020) or 46-40 ka (Uesawa and Nakagawa, 2016). We report a maximum eruption age of 48 ± 17 ka for Sp-1, within uncertainty of the previously reported age ranges.

2.6.6 The new ZDD protocol

The results of this study suggest that interrogation of the interior of crystals can yield a more comprehensive eruption age. However, if zircon crystals have no age zoning, rim-corrected ZDD ages are appropriate. It is also prudent to remove individual zircon crystals from ZDD age calculations if the un-corrected (U-Th)/He age of that crystal is greater than the crystallisation age (Schmitt, 2011; Danišík et al., 2017b).

The interior of zircon crystals can be measured for crystallisation age via either grinding the crystal to 50% width (conserving the Ft correction factor), or using depth-profile LA-ICPMS crystallisation age measurements (Österle et al., 2020). Both these approaches are useful tools with different applicability in different situations such as

instrument availability and grain size of zircon crystals. This study shows that if a zircon experienced protracted crystallisation, the difference in calculated ZDD eruption ages between core- and rim-corrected zircon crystal populations can be up to ca. 15% (e.g., Km-1: 62 and 73 ka), highlighting the importance of investigating crystal rims and interiors. A downside of this approach is that grinding young crystals increases the uncertainty in the He measurement as total He abundance is lower than that of the whole crystal. The maximum eruption age can help identify which ZDD eruption age is more accurate (e.g., Schmitt et al., 2006). If the U-Th-Pb data do not help resolve discrepancies between rim- and core-corrected ZDD eruption ages and there are no other age constraints available, it is suggested that an eruption age range is calculated from the maximum (rim-corrected + uncertainty) and minimum (core-corrected - uncertainty) ZDD eruption age.

2.7   Conclusion

This study proposes new ZDD protocols for zircons with protracted crystallisation histories that utilise (U-Th)/He ages combined with rim and core crystallisation ages. Modelling the changes to Ft correction imposed by grinding zircon crystals has revealed the robustness of the Ft correction and the efficacy of the new protocols has been demonstrated on samples well-constrained by stratigraphy. Additionally, the conservation of the Ft correction factor in ground crystals has implications for improving the accuracy of the (U-Th)/He method in general, particularly when applied to crystals severely zoned in U and Th.

New eruption ages for units Km-2 and Km-1 are proposed as 96 ± 5 ka (core-corrected ZDD age) and 59-79 ka (range between core- and rim- corrected ZDD age), respectively. In addition, units Kt-1 and Sp-1 from the Kuttara and Shikotsu caldera forming eruptions have maximum eruption ages (from single crystallisation ages), which are within uncertainty of previous eruption ages of >43 ka and 44-41 ka, respectively.

These proposed protocols are nominally more labour intensive than previous ZDD methods, but may lead to an increase in accuracy in eruption ages. The methodological improvements are particularly important for crystals with protracted crystallisation histories and identifiable inherited cores and significantly less important for crystals with a simple, short duration, crystallisation history. Enhancing geochronological accuracy in the eruption age of young volcanic rocks yields a clearer picture of magma system dynamics and recent volcanic events.

2.8   References

Amma-Miyasaka M., Miura D., Nakagawa M., Uesawa S. and Furukawa R. (2020) Stratigraphy and chronology of silicic tephras in the Shikotsu-Toya volcanic field, Japan: Evidence of a Late

Pleistocene ignimbrite flare-up in southwestern Hokkaido. Quaternary International.

Blackburn T. J., Stockli D. F. and Walker J. D. (2007) Magnetite (U-Th)/He dating and its application to the geochronology of intermediate to mafic volcanic rocks. Earth and Planetary Science Letters 259, 360-371.

Brendryen J., Haflidason H. and Sejrup H. P. (2010) Norwegian Sea tephrostratigraphy of marine isotope stages 4 and 5: Prospects and problems for tephrochronology in the North Atlantic region. Quaternary Science Reviews 29, 847-864.

Brown R. W., Beucher R., Roper S., Persano C., Stuart F. and Fitzgerald P. (2013) Natural age dispersion arising from the analysis of broken crystals. Part I: Theoretical basis and implications for the apatite (U-Th)/He thermochronometer. Geochimica et Cosmochimica Acta 122, 478-497.

Burgess S. D., Coble M. A., Vazquez J. A., Coombs M. L. and Wallace K. L. (2019) On the eruption age and provenance of the Old Crow tephra. Quaternary Science Reviews 207, 64-79.

Coble M. A., Burgess S. D. and Klemetti E. W. (2017) New zircon (U-Th)/He and U/Pb eruption age for the Rockland tephra, western USA. Quaternary Science Reviews 172, 109-117.

Connor C. B., Stamatakos J. A., Ferrill D. A., Hill B. E., Ofoegbu G. I., Conway F. M., Sagar B. and Trapp J. (2000) Geologic factors controlling patterns of small-volume basaltic volcanism: Application to a volcanic hazards assessment at Yucca Mountain, Nevada. Journal of Geophysical Research: Solid Earth 105, 417-432.

Cooperdock E. H. G., Ketcham R. A. and Stockli D. F. (2019) Resolving the effects of 2-D versus 3-D grain measurements on apatite (U-Th)/He age data and reproducibility. Geochronology 1, 17-41.

Danišík M., Lowe D. J., Schmitt A. K., Friedrichs B., Hogg A. G. and Evans N. J. (2020) Sub-millennial eruptive recurrence in the silicic Mangaone Subgroup tephra sequence, New Zealand, from Bayesian modelling of zircon double-dating and radiocarbon ages. Quaternary Science Reviews 246, 106517.

Danišík M., McInnes B. I. A., Kirkland C. L., McDonald B. J., Evans N. J. and Becker T. (2017a) Seeing is believing: Visualization of He distribution in zircon and implications for thermal history reconstruction on single crystals. Science Advances 3, e1601121.

Danišík M., Pfaff K., Evans N. J., Manoloukos C., Staude S., McDonald B. J. and Markl G. (2010) Tectonothermal history of the Schwarzwald Ore District (Germany): An apatite triple dating approach. Chemical Geology 278, 58-69.

Danišík M., Sachsenhofer R. F., Privalov V. A., Panova E. A., Frisch W. and Spiegel C. (2008) Low-temperature thermal evolution of the Azov Massif (Ukrainian Shield-Ukraine) - Implications for interpreting (U-Th)/He and fission track ages from cratons. Tectonophysics 456, 171-179.

Danišík M., Schmitt A. K., Stockli D. F., Lovera O. M., Dunkl I. and Evans N. J. (2017b) Application of combined U-Th-disequilibrium/U-Pb and (U-Th)/He zircon dating to tephrochronology. Quaternary Geochronology 40, 23-32.

Danišík M., Shane P., Schmitt A. K., Hogg A., Santos G. M., Storm S., Evans N. J., Keith Fifield L. and Lindsay J. M. (2012) Re-anchoring the late Pleistocene tephrochronology of New Zealand based on concordant radiocarbon ages and combined ^{238}U/^{230}Th disequilibrium and (U-Th)/He zircon ages. Earth and Planetary Science Letters 349-350, 240-250.

Evans N. J., Byrne J. P., Keegan J. T. and Dotter L. E. (2005) Determination of Uranium and Thorium in Zircon, Apatite, and Fluorite: Application to Laser (U-Th)/He Thermochronology. J Anal Chem 60, 1159-1165.

Evans N. J., McInnes B. I. A., Squelch A. P., Austin P. J., McDonald B. J. and Wu Q. (2008) Application of X-ray micro-computed tomography in (U-Th)/He thermochronology. Chemical Geology 257, 101-113.

Farley K. A. (2002) (U-Th)/He Dating: Techniques, Calibrations, and Applications. Reviews in Mineralogy and Geochemistry 47, 819-844.

Farley K. A., Kohn B. P. and Pillans B. (2002) The effects of secular disequilibrium on (U-Th)/He systematics and dating of Quaternary volcanic zircon and apatite. Earth and Planetary Science Letters 201, 117-125.

Farley K. A., Wolf R. A. and Silver L. T. (1996) The effects of long alpha-stopping distances on (U-Th)/He ages. Geochimica et Cosmochimica Acta 60, 4223-4229.

Friedrichs B., Atıcı G., Danišík M., Atakay E., Çobankaya M., Harvey J. C., Yurteri E. and Schmitt A. K. (2020a) Late Pleistocene eruptive recurrence in the post-collisional Mt. Hasan stratovolcanic complex (Central Anatolia) revealed by zircon double-dating. Journal of Volcanology and Geothermal Research 404, 107007.

Friedrichs B., Atıcı G., Danišík M., Yurteri E. and Schmitt A. K. (2021) Sequence modeling in zircon double-dating of early Holocene Mt. Erciyes domes (Central Anatolia). Quaternary Geochronology 61, 101129.

Friedrichs B., Schindlbeck-Belo J. C., Danišík M., Jenkins S. F., Yurteri E., Çobankaya M., Frische M., Wang K.-L., Lee H.-Y., Atıcı G., Schmitt A. K. and Sparks R. S. J. (2020b) New insights into source and dispersal of Mediterranean S1 tephra, an early Holocene marker horizon erupted at Mt. Erciyes (Turkey). Quaternary Science Reviews 249, 106606.

Friedrichs B., Schmitt A. K., McGee L. and Turner S. (2020c) U-Th whole rock data and high spatial resolution U-Th disequilibrium and U-Pb zircon ages of Mt. Erciyes and Mt. Hasan Quaternary stratovolcanic complexes (Central Anatolia). Data in Brief 29, 105113.

Ganzawa Y. and Ike M. (2011) SAR-RTL dating of single grains of volcanic quartz from the late Pleistocene Toya Caldera. Quaternary Geochronology 6, 42-49.

Gautheron C., Tassan-Got L., Ketcham R. A. and Dobson K. J. (2012) Accounting for long alpha-particle stopping distances in (U-Th-Sm)/He geochronology: 3D modeling of diffusion, zoning, implantation, and abrasion. Geochimica et Cosmochimica Acta 96, 44-56.

Glotzbach C., Lang K. A., Avdievitch N. N. and Ehlers T. A. (2019) Increasing the accuracy of

(U-Th(-Sm))/He dating with 3D grain modelling. Chemical Geology 506, 113-125.

Goto Y., Miyoshi M., Danhara T. and Tomiya A. (2020) Evolution of the Quaternary silicic volcanic complex of Shiribetsu, Hokkaido, Japan: an example of ignimbrite shield volcanoes in an island arc setting. Int J Earth Sci (Geol Rundsch).

Guillong M., Schmitt A. K. and Bachmann O. (2015) Comment on "Zircon U-Th-Pb dating using LA-ICP-MS: Simultaneous U-Pb and U-Th dating on 0.1Ma Toya Tephra, Japan" by Hisatoshi Ito. Journal of Volcanology and Geothermal Research 296, 101-103.

Hammer C. U., Clausen H. B., Dansgaard W., Gundestrup N., Johnsen S. J. and Reeh N. (1978) Dating of Greenland Ice Cores by Flow Models, Isotopes, Volcanic Debris, and Continental Dust. Journal of Glaciology 20, 3-26.

Harangi S., Lukács R., Schmitt A. K., Dunkl I., Molnár K., Kiss B., Seghedi I., Novothny Á. and Molnár M. (2015) Constraints on the timing of Quaternary volcanism and duration of magma residence at Ciomadul volcano, east-central Europe, from combined U-Th/He and U-Th zircon geochronology. Journal of Volcanology and Geothermal Research 301, 66-80.

Hourigan J. K., Reiners P. W. and Brandon M. T. (2005) U-Th zonation-dependent alpha-ejection in (U-Th)/He chronometry. Geochimica et Cosmochimica Acta 69, 3349-3365.

Ito H. (2014) Zircon U-Th-Pb dating using LA-ICP-MS: Simultaneous U-Pb and U-Th dating on the 0.1Ma Toya Tephra, Japan. Journal of Volcanology and Geothermal Research 289, 210-223.

Ito H. and Danišík M. (2020) Dating late Quaternary events by the combined U-Pb LA-ICP-MS and (U-Th)/He dating of zircon: A case study on Omachi Tephra suite (central Japan). Terra Nova 32, 134-140.

Jensen B. J. L., Preece S. J., Lamothe M., Pearce N. J. G., Froese D. G., Westgate J. A., Schaefer J. and Begét J. (2011) The variegated (VT) tephra: A new regional marker for middle to late marine isotope stage 5 across Yukon and Alaska. Quaternary International 246, 312-323.

Keller C. B., Schoene B. and Samperton K. M. (2018) A stochastic sampling approach to zircon eruption age interpretation. Geochem. Persp. Let., 31-35.

Ketcham R. A., Gautheron C. and Tassan-Got L. (2011) Accounting for long alpha-particle stopping distances in (U-Th-Sm)/He geochronology: Refinement of the baseline case. Geochimica et Cosmochimica Acta 75, 7779-7791.

Lippolt H. J., Leitz M., Wernicke R. S. and Hagedorn B. (1994) (Uranium + thorium)/helium dating of apatite: experience with samples from different geochemical environments. Chemical Geology 112, 179-191.

Lovera O., Schmitt A. K. and Stockli D. (2009) Improving combined U-Th and (U-Th)/He geochronology by Monte Carlo statistical corrections for uranium series disequilibrium.

Machida H. (1999) The stratigraphy, chronology and distribution of distal marker-tephras in and around Japan. Global and Planetary Change 21, 71-94.

Marzocchi W. and Bebbington M. S. (2012) Probabilistic eruption forecasting at short and long time scales. Bull Volcanol 74, 1777-1805.

McDougall I., Harrison T. M. and Harrison T. M. (1999) Geochronology and Thermochronology by the 40Ar/39Ar Method., Oxford University Press on Demand.

Moriizumi M. (1998) The growth history of the Kuttara volcanic group, Hokkaido, Japan. Kazan 43, 95-111.

Mucek A. E., Danišík M., Silva S. L. de, Schmitt A. K., Pratomo I. and Coble M. A. (2017) Post-supereruption recovery at Toba Caldera. Nature Communications 8, 15248.

Nakagawa M., Amma-Miyasaka M., Tomijima C., Matsumoto A. and Hase R. (2018) Eruption sequence of the 46 ka caldera-forming eruption of Shikotsu volcano, inferred from stratigraphy of proximal deposits at south of Lake Shikotsu, Japan. JOURNAL OF GEOGRAPHY-CHIGAKU ZASSHI 127, 247-271.

Okumura K. and Sangawa A. (1984) Age and distribution of Toya pyroclastic flow (Abstracts of Papers Presented at the Fall Meeting of the Society). Second Series Bulletin of the Volcanological Society of Japan 29, 338.

Österle J. E., Stockli D. F., Seward D. and Little T. A. (2020) Dating of young (<1 Ma) tephras: Using U-Pb (zircon) and (U-Th[-Sm])/He (zircon, apatite, magnetite) chronometers to unravel the eruption age of a tephra in the Woodlark Rift of Papua New Guinea. Terra Nova 32, 345-354.

Paces J. B. and Miller J. D. (1993) Precise U-Pb ages of Duluth Complex and related mafic intrusions, northeastern Minnesota: Geochronological insights to physical, petrogenetic, paleomagnetic, and tectonomagmatic processes associated with the 1.1 Ga Midcontinent Rift System. Journal of Geophysical Research: Solid Earth 98, 13997-14013.

Poldervaart A. (1956) Zircon in rocks; 2, Igneous rocks. Am J Sci 254, 521-554.

Reid M. R., Coath C. D., Mark Harrison T. and McKeegan K. D. (1997) Prolonged residence times for the youngest rhyolites associated with Long Valley Caldera: ^{230}Th—^{238}U ion microprobe dating of young zircons. Earth and Planetary Science Letters 150, 27-39.

Reimer P. J., Austin W. E. N., Bard E., Bayliss A., Blackwell P. G., Ramsey C. B., Butzin M., Cheng H., Edwards R. L., Friedrich M., Grootes P. M., Guilderson T. P., Hajdas I., Heaton T. J., Hogg A. G., Hughen K. A., Kromer B., Manning S. W., Muscheler R., Palmer J. G., Pearson C., Plicht J. van der, Reimer R. W., Richards D. A., Scott E. M., Southon J. R., Turney C. S. M., Wacker L., Adolphi F., Büntgen U., Capano M., Fahrni S. M., Fogtmann-Schulz A., Friedrich R., Köhler P., Kudsk S., Miyake F., Olsen J., Reinig F., Sakamoto M., Sookdeo A. and Talamo S. (2020) The IntCal20 Northern Hemisphere Radiocarbon Age Calibration Curve (0-55 cal kBP). Radiocarbon 62, 725-757.

Reiners, P.W., 2005, Zircon (U-Th)/He Thermochronometry, in Reiners, P.W. and Ehlers, T.A. (Eds.), Thermochronology, Reviews in Mineralogy and Geochemistry 58, 151-176.

Reiners P. W., Thomson S. N., McPhillips D., Donelick R. A. and Roering J. J. (2007) Wildfire

thermochronology and the fate and transport of apatite in hillslope and fluvial environments. Journal of Geophysical Research: Earth Surface 112.

Ruxton B. P. and McDougall I. (1967) Denudation rates in northeast Papua from potassium-argon dating of lavas. Am J Sci 265, 545-561.

Sakata S., Hirakawa S., Iwano H., Danhara T., Guillong M. and Hirata T. (2017) A new approach for constraining the magnitude of initial disequilibrium in Quaternary zircons by coupled uranium and thorium decay series dating. Quaternary Geochronology 38, 1-12.

Scandone R., Arganese G. and Galdi F. (1993) The evaluation of volcanic risk in the Vesuvian area. Journal of Volcanology and Geothermal Research 58, 263-271.

Schmitt A., Danisik M., Evans N., Siebel W., Kiemele E., Aydin F. and C. Harvey J. (2011) Acigöl rhyolite field, Central Anatolia (part 1): High-resolution dating of eruption episodes and zircon growth rates. Contributions to Mineralogy and Petrology 162, 1215-1231.

Schmitt A. K. (2007) Ion microprobe analysis of $(^{231}Pa)/(^{235}U)$ and an appraisal of protactinium partitioning in igneous zircon. American Mineralogist 92, 691-694.

Schmitt A. K. (2011) Uranium Series Accessory Crystal Dating of Magmatic Processes. Annu. Rev. Earth Planet. Sci. 39, 321-349.

Schmitt A. K., Danišík M., Aydar E., Şen E., Ulusoy İ. and Lovera O. M. (2014) Identifying the Volcanic Eruption Depicted in a Neolithic Painting at Çatalhöyük, Central Anatolia, Turkey. PLOS ONE 9, e84711.

Schmitt A. K., Stockli D. F. and Hausback B. P. (2006) Eruption and magma crystallization ages of Las Tres Vírgenes (Baja California) constrained by combined $^{230}Th/^{238}U$ and (U-Th)/He dating of zircon. Journal of Volcanology and Geothermal Research 158, 281-295.

Schmitt A. K., Stockli D. F., Niedermann S., Lovera O. M. and Hausback B. P. (2010) Eruption ages of Las Tres Vírgenes volcano (Baja California): A tale of two helium isotopes. Quaternary Geochronology 5, 503-511.

Shane P. and Sandiford A. (2003) Paleovegetation of marine isotope stages 4 and 3 in northern new zealand and the age of the widespread rotoehu tephra. Quaternary Research 59, 420-429.

Storm S., Shane P., Schmitt A. K. and Lindsay J. M. (2011) Contrasting punctuated zircon growth in two syn-erupted rhyolite magmas from Tarawera volcano: Insights to crystal diversity in magmatic systems. Earth and Planetary Science Letters 301, 511-520.

Storm S., Shane P., Schmitt A. K. and Lindsay J. M. (2012) Decoupled crystallization and eruption histories of the rhyolite magmatic system at Tarawera volcano revealed by zircon ages and growth rates. Contrib Mineral Petrol 163, 505-519.

Takashima I., Yamazaki T., Nakata E. and Yukawa K. (1992) TL age of the Quaternary volcanic rocks and pyroclastic flow deposits around the Lake Toya, Hokkaido, Japan. Journal of Mineralogy, Petrology and Economic Geology 87, 197-206.

Tomiya A. and Miyagi I. (2020) Age of the Toya Eruption. Bulletin of the Volcanological Society of Japan 65, 13-18.

Uesawa S. and Nakagawa M. (2016) Tephrostratigraphy and geochemisty of tephras from Yotei and Shiribetsu-dake volcanoes. IWCC 6 Excursion Guide Book, 26-33.

Uesawa S., Nakagawa M. and Umetsu A. (2016) Explosive eruptive activity and temporal magmatic changes at Yotei Volcano during the last 50,000years, southwest Hokkaido, Japan. Journal of Volcanology and Geothermal Research 325, 27-44.

Wells M. T., Casella G. and Robert C. P. (2004) Generalized Accept-Reject sampling schemes. A Festschrift for Herman Rubin, 342-347.

Wiedenbeck M., Allé P., Corfu F., Griffin W. L., Meier M., Oberli F., Quadt A. V., Roddick J. C. and Spiegel W. (1995) Three Natural Zircon Standards for U-Th-Pb, Lu-Hf, Trace Element and Ree Analyses. Geostandards Newsletter 19, 1-23.

Yamagata K. (1994) Tephrochronological study on the Shikotsu and Kuttara volcanoes in southwestern Hokkaido, Japan. Journal of Geography (Chigaku Zasshi) 103, 268-285.

2.9 Author contributions

Ruby C. Marsden: Methodology, Software, Validation, Formal analysis, Investigation, Data Curation, Writing - Original Draft, Visualisation
Martin Danišík: Conceptualisation, Methodology, Writing - Review & Editing, Supervision, Funding acquisition, Visualisation
Hisatoshi Ito: Resources, Conceptualisation, Writing - Original Draft, Writing - Review & Editing
Christopher L. Kirkland: Methodology, Writing - Review & Editing
Noreen J. Evans: Methodology, Writing - Review & Editing
Daisuke Miura: Resources, Conceptualisation, Writing - Review & Editing
Bjarne Friedrichs: Methodology, Writing - Review & Editing
Axel K. Schmitt: Methodology, Writing - Review & Editing
Shimpei Uesawa: Resources, Conceptualisation, Writing - Review & Editing
Matthew L. Daggitt: Methodology, Software, Formal analysis, Writing - Review & Editing, Visualisation

2.10   Appendices

Supplementary material I
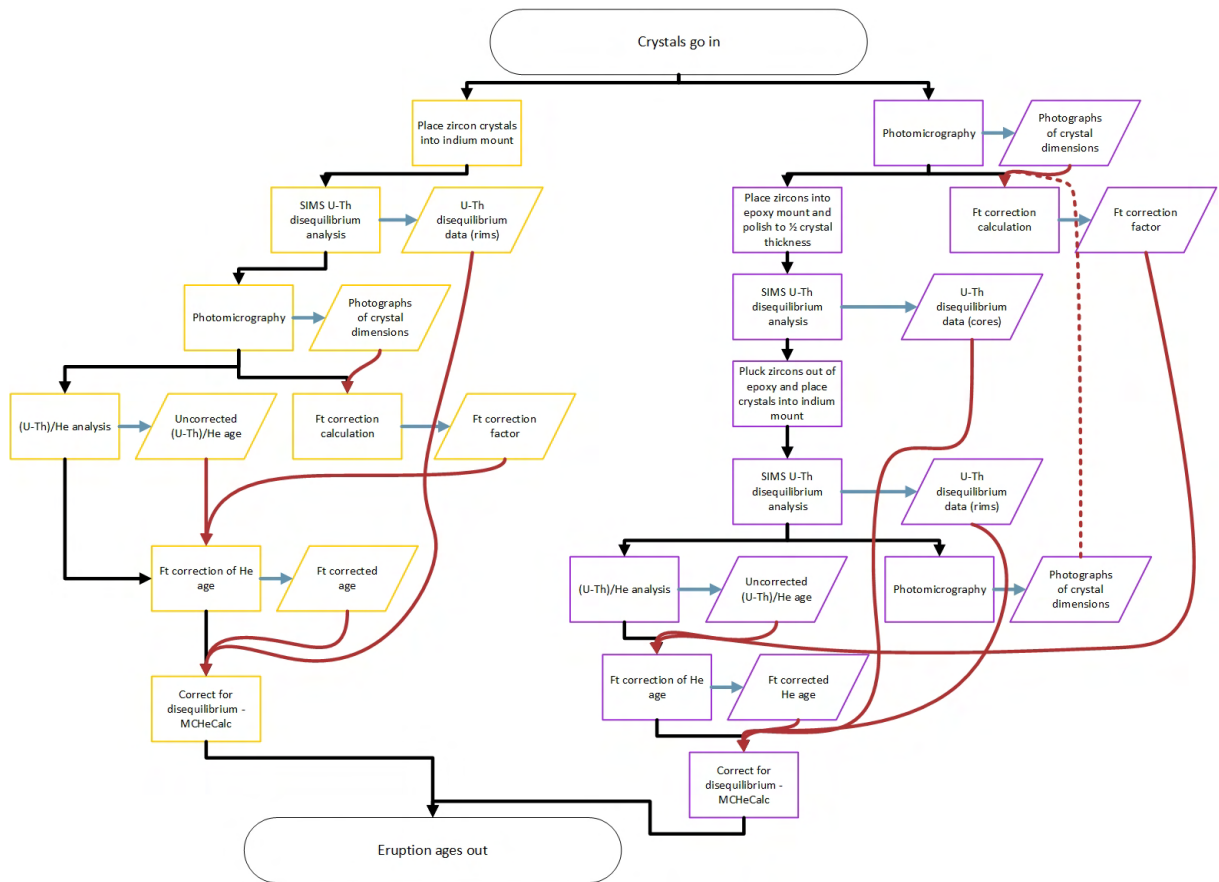
Figure 2.i: Flowchart showing the comparison of the procedure 1 method (yellow boxes) and the procedure 2 method (purple boxes). Square boxes indicate a procedural point whereas the parallelograms indicate data. Red arrows indicate a further use of the data, blue arrows indicate production of data and black arrows indicate the routine procedure.
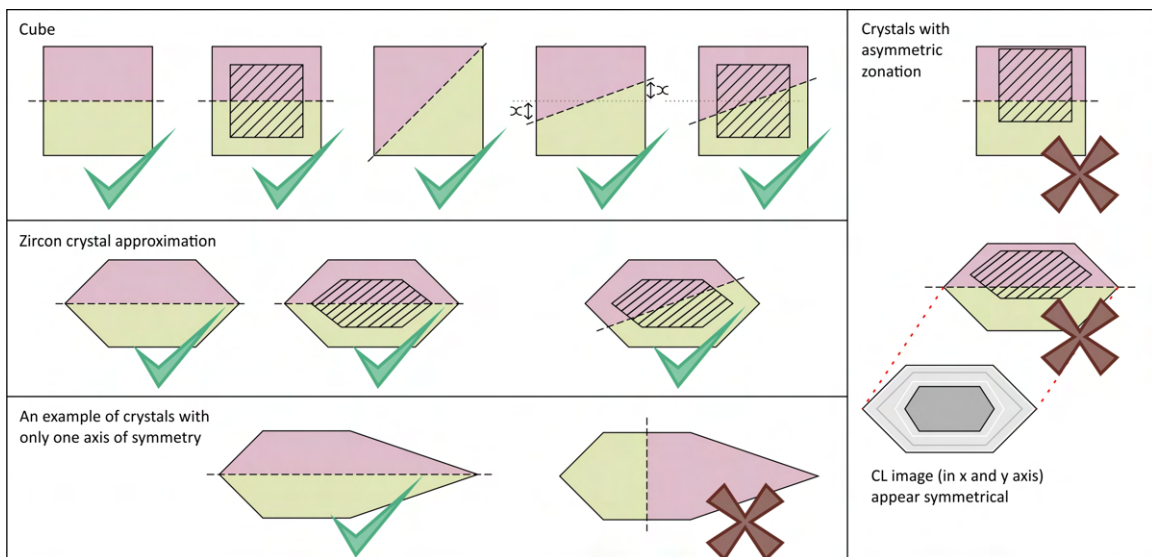
Figure 2.ii: Examples of symmetry classes which fulfil the symmetry requirements for Ft factor conservation. Green arrows indicate fulfilment of the requirements and red crosses indicate crystals where the line of polishing will not conserve Ft correction factor.

Supplementary Material II

Sample	Crystal identifier	Spot number	Core/ Rim	(238U/232Th)	1s	(230Th/232Th)	1s	m	1s	Th age ka	1s + ka	1s - ka	U ppm
Km-2	1		Rim	9.23	0.24	6.89	0.45	0.719	0.058	138.5	25.4	-20.6	196
Km-2	2		Rim	12.38	0.25	8.21	0.56	0.637	0.051	110.8	16.5	-14.3	176
Km-2	3		Rim	9.83	0.23	6.64	0.42	0.643	0.050	112.5	16.4	-14.3	162
Km-2	4		Rim	13.83	0.29	9.55	0.71	0.669	0.057	120.6	20.7	-17.4	129
Km-2	5		Rim	9.30	0.24	7.17	0.56	0.746	0.070	149.8	35.0	-26.5	160
Km-2	6		Rim	6.82	0.16	4.80	0.30	0.658	0.054	117.2	18.6	-15.9	211
Km-2	8		Rim	13.77	0.26	12.60	0.35	0.909	0.033	262.3	50.0	-34.2	517
Km-2	10		Rim	5.84	0.13	4.31	0.24	0.691	0.052	128.3	20.1	-17.0	210
Km-2	12		Rim	12.65	0.26	9.79	0.78	0.757	0.069	154.4	36.2	-27.1	160
Km-2	13		Rim	10.64	0.22	8.24	0.50	0.754	0.054	153.0	27.0	-21.6	219
Km-2	15		Rim	9.87	0.40	7.46	0.65	0.731	0.079	143.6	38.1	-28.2	244
Km-2	17		Rim	11.46	0.34	8.25	0.69	0.696	0.069	130.0	28.2	-22.4	211
Km-2	18		Rim	10.48	0.50	8.28	0.62	0.770	0.076	160.3	44.0	-31.3	171
Km-2	19		Rim	11.21	0.25	7.00	0.53	0.591	0.053	97.7	15.3	-13.4	244
Km-2	22		Rim	13.06	0.36	9.47	0.74	0.704	0.064	133.0	26.6	-21.4	172
Km-2	23		Rim	13.04	0.26	9.89	0.70	0.740	0.060	147.2	28.4	-22.5	182
Km-2	a	1 Interior		7.76	0.15	6.18	0.31	0.769	0.048	160.1	25.6	-20.7	193
Km-2	a	2 Interior		3.41	0.07	3.01	0.06	0.841	0.035	200.6	26.8	-21.5	1196
Km-2	b	1 Interior		9.90	0.18	8.15	0.35	0.805	0.042	178.8	26.7	-21.5	241
Km-2	b	2 Interior		14.69	0.27	13.75	0.15	0.932	0.021	292.7	40.2	-29.3	3226
Km-2	c	1 Interior		12.09	0.23	9.70	0.55	0.786	0.052	168.4	30.1	-23.6	163
Km-2	c	2 Interior		10.34	0.19	9.17	0.34	0.876	0.040	228.1	43.0	-30.7	364
Km-2	c	3 Interior		4.90	0.13	4.46	0.19	0.890	0.056	241.3	78.9	-45.3	271
Km-2	d	1 Interior		5.78	0.11	4.65	0.18	0.770	0.041	160.3	21.4	-17.9	310
Km-2	d	2 Interior		8.33	0.15	7.92	0.12	0.945	0.025	317.5	67.7	-41.5	1747
Km-2	e	1 Interior		6.10	0.11	5.37	0.19	0.861	0.041	215.2	38.2	-28.3	327
Km-2	e	2 Interior		3.93	0.13	3.84	0.12	0.971	0.058	386.7	∞	-120.5	806
Km-2	f	1 Interior		9.73	0.18	7.85	0.37	0.787	0.045	169.1	26.1	-21.0	225
Km-2	f	2 Interior		11.63	0.27	10.92	0.31	0.934	0.037	296.6	90.8	-48.9	531

Km-2	g	1 Interior	6.57	0.12	5.11	0.15	0.743	0.031	148.3	14.2	-12.6	519
Km-2	g	2 Interior	8.26	0.15	7.09	0.27	0.841	0.040	200.5	31.8	-24.6	301
Km-2	g	3 Interior	9.05	0.17	8.20	0.42	0.895	0.055	246.3	81.7	-46.2	199
Km-2	h	1 Interior	8.75	0.18	7.41	0.33	0.830	0.046	193.4	34.2	-26.0	228
Km-2	h	2 Interior	10.23	0.19	9.71	0.32	0.945	0.039	316.0	131.8	-58.0	356
Km-2	i	1 Interior	5.91	0.11	5.20	0.19	0.859	0.043	213.9	39.5	-28.9	337
Km-2	i	2 Interior	8.00	0.16	8.14	0.67	1.020	0.098	∞[a]	∞[a]	∞[a]	63
Km-2	j	1 Interior	7.48	0.14	6.68	0.22	0.878	0.039	230.1	42.0	-30.3	353
Km-2	j	2 Interior	6.14	0.32	6.20	0.42	1.013	0.101	∞[a]	∞[a]	∞[a]	494
Km-2	k	1 Interior	11.46	0.23	11.26	0.67	0.981	0.067	∞[a]	∞[a]	∞[a]	143
Km-2	k	2 Interior	7.25	0.14	7.09	0.14	0.976	0.030	∞[a]	∞[a]	∞[a]	927
Km-2	l	1 Interior	4.33	0.08	3.94	0.09	0.886	0.034	237.1	39.2	-28.8	728
Km-2	l	2 Interior	12.04	0.22	10.87	0.25	0.895	0.029	246.2	35.1	-26.5	872
Km-2	l	3 Interior	3.97	0.09	3.93	0.08	0.987	0.041	∞[a]	∞[a]	∞[a]	1251
Km-2	m	1 Interior	4.82	0.09	4.09	0.12	0.814	0.037	183.5	24.0	-19.6	476
Km-2	m	2 Interior	10.94	0.20	10.55	0.20	0.961	0.028	354.1	136.9	-58.9	1063
Km-2	n	1 Interior	12.22	0.23	10.05	0.39	0.809	0.038	180.6	24.0	-19.7	316
Km-2	n	2 Interior	14.40	0.27	13.52	0.16	0.935	0.022	298.2	45.2	-31.9	2471
Km-2	n	3 Interior	7.86	0.15	7.16	0.20	0.899	0.034	250.5	45.2	-31.8	489
Km-2	o	1 Interior	3.91	0.07	3.43	0.07	0.841	0.030	201.0	22.8	-18.8	1103
Km-2	o	2 Interior	7.18	0.15	6.36	0.20	0.870	0.039	222.4	38.2	-28.3	568
Km-2	a	1 Rim	12.34	0.25	9.34	0.56	0.737	0.052	146.0	24.0	-19.7	213
Km-2	b	1 Rim	10.15	0.31	7.37	0.48	0.699	0.057	131.2	22.8	-18.8	218
Km-2	b	2 Rim	10.84	0.34	8.00	0.48	0.715	0.054	136.9	22.9	-18.9	204
Km-2	c	1 Rim	10.04	0.51	8.16	0.65	0.794	0.083	172.6	56.7	-37.1	182
Km-2	d	1 Rim	11.09	0.23	7.64	0.42	0.661	0.044	118.1	15.2	-13.3	222
Km-2	e	1 Rim	6.18	0.12	5.75	0.13	0.918	0.032	273.2	54.7	-36.3	883
Km-2	f	1 Rim	10.42	0.25	7.91	0.50	0.736	0.056	145.5	25.9	-20.9	158
Km-2	g	1 Rim	12.16	0.32	9.25	0.54	0.741	0.052	147.7	24.6	-20.1	216
Km-2	h	1 Rim	7.93	0.15	6.16	0.24	0.749	0.037	150.8	17.5	-15.1	349
Km-2	i	1 Rim	10.75	0.28	7.70	0.49	0.690	0.053	127.9	20.6	-17.4	185
Km-2	j	1 Rim	10.88	0.42	6.79	0.59	0.590	0.064	97.5	18.6	-15.9	195
Km-2	k	1 Rim	5.65	0.15	4.01	0.25	0.655	0.056	116.1	19.4	-16.5	267

Sample	ID	Spot	1	2	3	4	5	6	7	8	9	10
Km-2	m	1 Rim	10.23	0.21	6.64	0.43	0.615	0.048	104.3	14.6	-12.9	192
Km-2	n	1 Rim	5.58	0.14	4.37	0.21	0.742	0.051	148.0	23.9	-19.6	320
Km-2	o	1 Rim	7.71	0.37	5.94	0.44	0.740	0.076	147.3	37.8	-28.0	247
Km-1	1	Rim	9.37	0.32	5.91	0.36	0.592	0.048	97.8	13.7	-12.2	277
Km-1	2	Rim	8.04	0.27	4.65	0.26	0.524	0.042	81.1	10.1	-9.2	333
Km-1	3	Rim	13.77	0.31	13.17	1.10	0.953	0.089	∞[a]	∞[a]	∞[a]	85
Km-1	4	Rim	13.41	0.28	8.34	0.80	0.595	0.065	98.6	19.1	-16.3	131
Km-1	5	Rim	10.26	0.21	8.42	0.40	0.803	0.047	177.5	29.6	-23.3	238
Km-1	6	Rim	7.20	0.16	5.11	0.37	0.667	0.062	120.0	22.4	-18.6	193
Km-1	7	Rim	8.30	0.16	6.29	0.46	0.728	0.064	142.3	29.3	-23.1	206
Km-1	8	Rim	7.86	0.17	5.92	0.41	0.721	0.062	139.5	27.3	-21.8	219
Km-1	9	Rim	14.27	0.35	9.20	0.71	0.620	0.056	105.7	17.3	-14.9	168
Km-1	10	Rim	11.13	0.27	7.93	0.60	0.687	0.062	126.9	23.9	-19.6	163
Km-1	11	Rim	10.81	0.35	6.01	0.50	0.515	0.054	79.0	12.9	-11.5	265
Km-1	12	Rim	4.24	0.08	2.72	0.13	0.543	0.040	85.5	10.1	-9.2	472
Km-1	13	Rim	12.28	0.27	7.66	0.50	0.593	0.046	98.3	13.1	-11.7	220
Km-1	14	Rim	12.38	0.32	7.24	0.54	0.552	0.050	87.6	12.9	-11.5	164
Km-1	15	Rim	12.70	0.26	7.16	0.58	0.530	0.051	82.5	12.5	-11.2	161
Km-1	16	Rim	6.74	0.14	4.55	0.33	0.624	0.058	106.9	18.4	-15.8	203
Km-1	17	Rim	10.25	0.22	7.73	0.45	0.730	0.052	143.2	23.2	-19.1	239
Km-1	18	Rim	11.42	0.27	7.74	0.58	0.650	0.057	114.5	19.6	-16.6	166
Km-1	19	Rim	12.23	0.29	8.44	0.54	0.665	0.051	119.4	18.0	-15.4	239
Km-1	20	Rim	13.14	0.27	7.41	0.59	0.531	0.050	82.8	12.3	-11.0	211
Km-1	22	Rim	10.10	0.24	6.54	0.45	0.613	0.051	103.6	15.5	-13.6	216
Km-1	a	1 Interior	9.94	0.18	9.83	0.33	0.988	0.042	∞[a]	∞[a]	∞[a]	320
Km-1	a	2 Interior	6.96	0.13	6.79	0.12	0.973	0.029	∞[a]	∞[a]	∞[a]	1363
Km-1	a	3 Interior	9.87	0.22	9.67	0.32	0.977	0.043	∞[a]	∞[a]	∞[a]	515
Km-1	b	1 Interior	7.80	0.14	5.85	0.26	0.717	0.041	138.0	17.2	-14.9	243
Km-1	b	2 Interior	13.94	0.27	12.91	0.15	0.921	0.022	276.7	36.1	-27.1	2805
Km-1	c	1 Interior	9.03	0.17	8.65	0.38	0.953	0.051	∞[a]	∞[a]	∞[a]	233
Km-1	c	2 Interior	16.56	0.31	15.15	0.32	0.910	0.027	262.9	39.4	-28.9	878
Km-1	d	1 Interior	10.72	0.20	9.46	0.33	0.872	0.038	224.1	38.0	-28.1	357
Km-1	d	2 Interior	11.71	0.22	11.08	0.11	0.941	0.022	308.9	49.8	-34.1	4287

Km-1	e	1 Interior	6.56	0.12	4.68	0.20	0.667	0.038	120.1	13.3	-11.9	294
Km-1	e	2 Interior	7.16	0.16	6.89	0.27	0.957	0.050	∞[a]	∞[a]	∞[a]	250
Km-1	f	1 Interior	6.90	0.13	5.97	0.21	0.845	0.040	203.3	32.6	-25.1	329
Km-1	f	2 Interior	7.12	0.13	6.20	0.21	0.851	0.038	207.9	32.0	-24.7	377
Km-1	g	1 Interior	9.63	0.18	8.44	0.39	0.863	0.049	217.2	47.9	-33.2	191
Km-1	g	2 Interior	9.31	0.17	8.51	0.23	0.905	0.033	257.4	47.4	-32.9	518
Km-1	g	3 Interior	4.69	0.09	4.17	0.16	0.863	0.047	217.2	45.9	-32.2	285
Km-1	h	1 Interior	17.96	0.33	16.00	0.46	0.885	0.032	236.2	35.6	-26.8	573
Km-1	h	2 Interior	10.27	0.20	9.76	0.11	0.945	0.024	316.9	61.4	-39.1	4820
Km-1	i	1 Interior	6.71	0.12	5.44	0.26	0.781	0.048	165.9	26.8	-21.5	224
Km-1	i	2 Interior	7.61	0.14	6.55	0.24	0.842	0.039	201.7	31.4	-24.3	399
Km-1	i	3 Interior	11.78	0.23	10.81	0.74	0.911	0.071	263.8	173.4	-63.9	152
Km-1	j	1 Interior	7.64	0.14	6.05	0.24	0.764	0.039	157.8	19.9	-16.8	295
Km-1	j	2 Interior	3.82	0.08	3.19	0.05	0.785	0.028	168.0	15.5	-13.6	6875
Km-1	k	1 Interior	5.59	0.10	4.36	0.15	0.737	0.036	145.9	15.9	-13.9	433
Km-1	k	2 Interior	15.09	0.28	14.22	0.19	0.939	0.023	305.1	52.1	-35.1	2084
Km-1	l	1 Interior	8.59	0.19	6.70	0.39	0.755	0.054	153.5	27.2	-21.8	219
Km-1	l	2 Interior	12.67	0.25	11.61	0.29	0.910	0.032	262.7	47.7	-33.1	632
Km-1	m	1 Interior	7.50	0.14	6.74	0.26	0.885	0.043	235.9	51.2	-34.7	290
Km-1	m	2 Interior	4.94	0.09	4.82	0.22	0.968	0.060	∞[a]	∞[a]	∞[a]	249
Km-1	n	1 Interior	7.54	0.14	5.88	0.32	0.750	0.051	151.5	25.2	-20.5	240
Km-1	n	2 Interior	12.63	0.24	12.13	0.26	0.957	0.030	343.6	128.5	-57.4	799
Km-1	a	1 Rim	15.04	0.58	12.15	1.05	0.795	0.081	173.0	55.1	-36.4	156
Km-1	b	1 Interior	6.81	0.12	5.73	0.20	0.817	0.038	185.4	25.2	-20.5	379
Km-1	b	2 Interior	9.23	0.17	8.58	0.22	0.921	0.033	277.8	58.7	-38.0	598
Km-1	c	1 Rim	7.48	0.14	5.64	0.42	0.720	0.066	138.8	29.1	-22.9	208
Km-1	d	1 Interior	10.89	0.20	10.11	0.32	0.922	0.037	278.9	71.4	-42.8	444
Km-1	e	1 Rim	11.22	0.31	7.02	0.39	0.593	0.042	98.1	11.9	-10.7	217
Km-1	f	1 Rim	11.27	0.44	5.99	0.43	0.491	0.046	73.7	10.4	-9.5	158
Km-1	f	2 Rim	10.74	0.43	6.27	0.49	0.545	0.055	86.1	14.1	-12.5	180
Km-1	g	1 Interior	5.10	0.09	4.88	0.19	0.947	0.049	321.4	305.6	-72.3	315
Km-1	h	1 Interior	17.87	0.45	16.42	0.33	0.914	0.031	268.5	49.1	-33.8	1714
Km-1	i	1 Rim	6.31	0.12	4.47	0.15	0.660	0.032	117.6	10.8	-9.9	434

Km-1	k	1 Rim	9.79	0.25	6.89	0.47	0.674	0.056	122.3	20.7	-17.4	173
Km-1	l	1 Rim	5.94	0.23	4.29	0.27	0.672	0.062	121.8	23.0	-19.0	246
Km-1	n	1r Rim	11.13	0.34	7.17	0.56	0.612	0.059	103.4	18.0	-15.4	258
Kt-1	2	Rim	6.70	0.13	3.88	0.39	0.505	0.069	76.8	16.3	-14.2	135
Kt-1	3	Rim	6.47	0.15	3.67	0.35	0.489	0.065	73.3	14.9	-13.1	158
Kt-1	4	Rim	69.91	2.62	28.84	1.50	0.404	0.027	56.5	5.0	-4.8	1311
Kt-1	5	Rim	7.60	0.17	3.52	0.52	0.382	0.079	52.6	15.0	-13.2	91
Kt-1	6	Rim	9.57	0.44	6.43	0.47	0.634	0.063	109.7	20.8	-17.5	237
Kt-1	7	Rim	6.52	0.13	2.98	0.33	0.360	0.061	48.7	11.0	-10.0	140
Kt-1	8	Rim	6.20	0.12	3.04	0.34	0.394	0.066	54.6	12.7	-11.3	120
Spfa-1	1	Rim	6.26	0.12	2.96	0.35	0.401	0.064	56.0	12.4	-11.1	97
Spfa-1	2	Rim	6.45	0.12	3.10	0.31	0.413	0.056	58.2	10.9	-9.9	113
Spfa-1	4	Rim	5.47	0.15	2.92	0.21	0.460	0.048	67.4	10.1	-9.3	209
Spfa-1	5	Rim	5.55	0.12	4.78	0.69	0.840	0.145	200.0	259.8	-70.5	47
Spfa-1	6	Rim	6.38	0.12	2.87	0.28	0.377	0.051	51.6	9.3	-8.6	126
Spfa-1	7	Rim	6.34	0.12	2.74	0.28	0.356	0.051	48.1	9.0	-8.3	129
Spfa-1	8	Rim	6.59	0.13	2.88	0.27	0.365	0.048	49.6	8.6	-7.9	138
Spfa-1	9	Rim	7.92	0.35	4.36	0.46	0.504	0.068	76.6	16.2	-14.1	102
Spfa-1	10	Rim	8.05	0.16	3.48	0.54	0.375	0.074	51.2	13.8	-12.3	76
Spfa-1	11	Rim	3.86	0.08	2.37	0.12	0.523	0.043	80.7	10.3	-9.5	359
Spfa-1	12	Rim	6.79	0.16	3.04	0.33	0.379	0.055	52.0	10.1	-9.3	115
Spfa-1	13	Rim	6.72	0.13	3.47	0.43	0.456	0.072	66.6	15.5	-13.6	122

a) The infinity mark denotes samples which are in secular equilibrium or are within error of secular equilibrium

Whole rock activity ratios are shown in supplementary material iV.

Supplementary Material III

(U-Th)/He data

Procedure 1

Sample code	232Th (ng)	±1σ (%)	238U (ng)	±1σ (%)	4He (ncc)	±1σ (%)	TAU (%)	Th/U	Unc. age (ka)	±1σ (ka)	Ft	Ft-Cor. age (ka)	±1σ (ka)	Rim crystallisation age 238U/230Th age (ka)	±1σ (ka)	Core crystallisation age 238U/230Th age (ka)	±1σ (ka)	D230	Rim-corrected age Dsq.-Cor. (ka)	±1σ (ka)	Core-corrected age Dsq.-Co (ka)	±1σ (ka)
Km-1-1	0.712	1.3	1.514	2.0	0.0066	4.8	5.1	0.467	32.4	1.7	0.778	41.7	3.0	97.8	12.9	-	-	0.1405	58.5	5.6	-	-
Km-1-2	0.558	1.3	1.131	1.9	0.0040	6.6	6.8	0.489	25.8	1.8	0.816	31.6	2.7	81.1	9.6	-	-	0.1473	46.0	4.7	-	-
Km-1-3	4.535	1.3	7.380	2.0	0.0451	1.9	2.6	0.610	44.0	1.2	0.870	50.5	2.9	400[a]	100[a]	-	-	0.1836	51.5	3.1	-	-
Km-1-4	2.255	2.2	3.625	2.5	0.0286	3.0	3.7	0.618	56.6	2.1	0.800	70.8	4.4	98.6	17.7	-	-	0.1859	99.3	7.0	-	-
Km-1-7	0.510	1.3	1.040	1.8	0.0045	5.1	5.4	0.487	32.2	1.7	0.788	40.8	3.0	142.3	26.2	-	-	0.1467	49.9	4.7	-	-
Km-1-8	1.791	1.3	4.565	2.2	0.0315	2.1	2.9	0.389	52.0	1.5	0.852	61.0	3.5	139.5	24.6	-	-	0.1172	78.0	7.3	-	-
Km-1-9	1.051	1.9	2.955	2.3	0.0181	4.5	5.0	0.353	46.4	2.3	0.838	55.4	3.9	105.7	16.1	-	-	0.1062	80.4	8.4	-	-
Km-1-13	1.177	1.3	3.557	1.9	0.0242	3.9	4.3	0.328	51.9	2.2	0.786	66.1	4.4	98.3	12.4	-	-	0.0988	101.7	7.2	-	-
Km-1-14	1.657	1.3	3.291	1.9	0.0181	6.2	6.4	0.500	40.5	2.6	0.807	50.1	4.1	87.6	12.2	-	-	0.1503	74.7	7.2	-	-
Km-1-15	1.058	1.3	1.765	1.8	0.0084	6.3	6.5	0.595	34.4	2.2	0.774	44.5	3.7	82.5	11.8	-	-	0.1791	65.4	6.4	-	-
Km-1-17	1.455	1.3	3.168	1.9	0.0236	3.0	3.5	0.456	55.3	1.9	0.775	71.3	4.3	143.2	21.2	-	-	0.1372	91.4	8.6	-	-
Km-1-18	2.191	1.9	4.807	2.2	0.0307	2.4	3.2	0.453	47.4	1.5	0.848	55.9	3.3	114.5	18.1	-	-	0.1362	76.4	7.2	-	-
Km-1-19	1.910	1.3	5.991	1.8	0.0416	1.5	2.2	0.317	53.1	1.2	0.849	62.5	3.4	119.4	16.7	-	-	0.0952	88.0	8.4	-	-
Best fit eruption age (ka) +-2sig (ka)																		**No overlapping distributions**				
Km-2-3	0.659	1.3	1.523	1.9	0.0120	5.8	6.1	0.430	59.0	3.6	0.800	73.7	5.8	112.5	15.4	-	-	0.1275	106.0	9.3	-	-
Km-2-4	2.961	1.3	7.728	2.0	0.0895	0.8	2.0	0.380	87.3	1.8	0.828	105.5	5.7	120.6	19.0	-	-	0.1128	145.5	7.9	-	-
Km-2-5	1.126	2.0	3.346	2.3	0.0330	2.8	3.6	0.334	75.3	2.7	0.831	90.6	5.6	149.8	30.7	-	-	0.0991	118.6	12.3	-	-
Km-2-6	0.433	1.3	1.014	2.0	0.0068	4.7	5.1	0.424	49.8	2.5	0.802	62.0	4.4	117.2	17.2	-	-	0.1257	87.3	9.1	-	-
Km-2-8	0.587	1.3	1.631	2.0	0.0122	5.0	5.3	0.357	56.8	3.0	0.799	71.1	5.2	262.3	42.1	-	-	0.1059	76.8	6.4	-	-
Km-2-10	0.694	2.0	1.692	2.3	0.0176	4.2	4.7	0.407	78.1	3.7	0.829	94.2	6.5	128.3	18.5	-	-	0.1207	132.4	9.7	-	-
Km-2-13	0.458	1.3	1.225	1.8	0.0085	6.5	6.7	0.372	52.3	3.5	0.795	65.8	5.5	153.0	24.3	-	-	0.1102	83.2	9.5	-	-

Sample																						
Km-2-15	0.901	1.3	2.342	1.9	0.0232	3.5	3.9	0.382	74.9	2.9	0.811	92.3	5.8	143.6	33.2	-	-	0.1134	122.5	12.2	-	-
Km-2-17	0.932	1.8	2.160	2.2	0.0199	4.5	4.9	0.428	68.8	3.4	0.811	84.8	5.9	130.0	25.3	-	-	0.1271	115.7	11.0	-	-
Km-2-18	0.810	1.3	1.911	1.8	0.0142	2.5	3.0	0.421	55.6	1.6	0.787	70.6	4.1	160.3	37.7	-	-	0.1249	85.9	8.6	-	-
Best fit eruption age (ka) +-2sig (ka)																			**104.1**	**5.7**		
Best fit eruption age - outliers removed (ka) +-2sig (ka)																			**110.9**	**6.3**		
Sp-1-1*	0.331	1.4	0.568	1.9	0.0140	6.6	6.8	0.578	178.7	12.2	0.750	238.2	20.1	56.0	11.7	-	-	0.1419	-	-	-	-
Sp-1-2	0.381	1.4	0.482	2.0	0.0019	11.1	11.2	0.785	27.6	3.1	0.703	39.3	4.8	58.2	10.4	-	-	0.1928	59.2	7.1	-	-
Sp-1-4	0.217	1.4	0.373	1.8	0.0015	11.4	11.5	0.579	28.8	3.3	0.723	39.8	5.0	67.4	9.7	-	-	0.1422	63.4	8.1	-	-
Sp-1-6*	0.158	1.9	0.116	2.3	0.0466	1.1	2.1	1.351	2499.7	52.2	0.783	3192.4	173.0	51.6	9.0	-	-	0.3316	-	-	-	-
Sp-1-8*	0.170	2.0	0.175	2.3	0.0023	8.5	8.7	0.965	88.2	7.7	0.696	126.8	12.8	49.6	8.2	-	-	0.2369	-	-	-	-
Sp-1-9*	0.384	1.3	0.351	1.8	0.0033	7.8	7.9	1.087	60.8	4.8	0.635	95.7	9.0	76.6	15.1	-	-	0.2669	-	-	-	-
Sp-1-11*	0.224	1.4	0.385	2.0	0.0235	3.3	3.7	0.576	441.0	16.4	0.773	570.5	35.5	80.7	9.9	-	-	0.1415	-	-	-	-
Sp-1-12*	1.246	1.9	1.530	2.2	0.0524	0.7	2.0	0.808	236.1	4.7	0.730	323.5	17.4	52.0	9.7	-	-	0.1985	-	-	-	-
Insufficient number of crystals analysed successfully for statistically significant results																						
Kt-1-2	0.262	1.3	0.514	1.8	0.0028	7.9	8.1	0.507	39.7	3.2	0.792	50.1	4.8	76.8	15.3	-	-	0.1651	74.7	7.5	-	-
Kt-1-3*	0.257	1.3	0.634	1.8	0.0056	5.3	5.6	0.403	66.4	3.7	0.817	81.3	6.1	73.3	14.0	-	-	0.1313	121.0	6.9	-	-
Kt-1-4	3.688	1.3	8.248	2.1	0.0230	5.4	5.7	0.444	20.8	1.2	0.822	25.3	1.9	56.5	4.9	-	-	0.1447	41.1	3.7	-	-
Kt-1-6	0.420	1.3	0.800	2.0	0.0025	10.4	10.6	0.521	22.5	2.4	0.787	28.6	3.3	109.7	19.1	-	-	0.1700	36.6	4.9	-	-
Kt-1-7*	0.735	1.9	1.470	2.3	0.0242	3.7	4.2	0.497	121.4	5.1	0.761	159.5	10.4	48.7	10.5	-	-	0.1619	-	-	-	-
Insufficient number of crystals analysed successfully for statistically significant results																						

Procedure 2

Sample																						
Km-1-a	14.827	1.3	20.627	1.8	0.1742	0.8	1.8	0.714	59.4	1.1	0.906	65.6	3.5	173.0	45.7	400[a]	100[a]	0.2147	75.0	6.2	66.9	3.8
Km-1-b	0.984	1.3	2.499	2.0	0.0220	4.2	4.6	0.391	66.3	3.0	0.869	76.3	5.2	185.4	22.9	276.7	31.6	0.1177	91.4	7.7	82.4	6.0
Km-1-c	1.549	2.0	4.904	2.3	0.0329	3.0	3.7	0.314	51.4	1.9	0.866	59.4	3.7			262.9	34.1	0.0943			64.2	4.4
Km-1-d	1.037	1.3	3.113	2.1	0.0217	5.0	5.4	0.331	53.1	2.8	0.828	64.1	4.7			308.9	41.9	0.0995			67.7	5.2
Km-1-e	1.046	1.3	2.626	1.9	0.0134	7.9	8.1	0.395	38.3	3.1	0.847	45.2	4.3	98.1	11.3	120.1	12.6	0.1189	65.7	8.0	60.1	6.8
Km-1-f	0.514	1.3	1.229	1.8	0.0055	7.4	7.6	0.415	33.7	2.6	0.828	40.7	3.7	73.7	10.0	207.9	28.4	0.1250	65.0	6.6	45.6	4.5
Km-1-g	1.921	1.9	3.940	2.2	0.0234	3.7	4.2	0.484	43.8	1.8	0.887	49.3	3.2			257.4	40.2	0.1456			53.0	3.9
Km-1-h	0.077	1.9	0.192	2.2	0.0013	18.3	18.4	0.397	49.3	9.1	0.783	62.9	12.0			316.9	50.3	0.1194			65.6	12.9
Km-1-i	3.036	1.3	5.896	2.0	0.0379	1.4	2.3	0.511	47.2	1.1	0.884	53.4	2.9	117.6	10.3	201.7	27.9	0.1538	71.3	5.1	60.3	4.0
Km-1-j	8.132	1.8	10.282	2.2	0.0721	1.4	2.3	0.785	48.6	1.1	0.863	56.4	3.1			168.0	14.5	0.2362			65.4	4.1
Best fit eruption age (ka) +-2sig (ka)																			**73.0**	**5.7**	**61.7**	**3.0**

Km-2-a	0.177	1.4	0.256	2.0	0.0019	13.7	13.8	0.689	52.6	7.3	0.853	61.6	9.1	146.0 21.9	200.6 24.2 0.2043	75.5 12.5	69.6 10.7
Km-2-b	0.561	1.2	1.823	1.7	0.0215	6.6	6.8	0.305	90.6	6.1	0.863	105.0	8.8	136.9 20.9	292.7 34.8 0.0906	147.4 13.1	113.5 10.5
Km-2-c	2.902	1.2	6.304	1.7	0.0656	1.6	2.2	0.457	77.2	1.7	0.845	91.4	5.0	172.6 46.9	228.1 36.8 0.1356	108.9 11.0	103.0 7.5
Km-2-d	1.248	1.7	3.491	2.0	0.0451	1.5	2.4	0.355	98.1	2.3	0.826	118.7	6.6	118.1 14.3	317.5 54.6 0.1052	167.8 7.5	126.1 8.2
Km-2-f	0.697	1.2	1.903	1.7	0.0190	5.4	5.6	0.364	75.5	4.2	0.857	88.1	6.6	145.5 23.4	296.6 69.8 0.1078	118.0 12.6	94.7 8.2
Km-2-g	1.598	1.2	3.819	1.7	0.0375	2.5	2.9	0.415	73.5	2.2	0.900	81.7	4.7	147.7 22.3	200.5 28.2 0.1232	105.9 10.3	95.1 7.3
Km-2-h	1.514	1.6	4.148	2.0	0.0403	1.6	2.5	0.362	73.6	1.8	0.897	82.0	4.6	150.8 16.3	316.0 94.9 0.1075	109.2 9.4	86.0 5.9
Km-2-i	1.828	1.2	3.830	1.7	0.0466	1.4	2.1	0.474	89.9	1.9	0.903	99.6	5.4	127.9 19.0	213.9 34.2 0.1405	137.7 8.4	114.3 8.9
Km-2-j	0.843	1.3	1.960	1.8	0.0152	7.6	7.8	0.427	57.8	4.5	0.850	68.0	6.3	97.5 17.2	230.1 36.2 0.1267	99.8 9.6	75.1 7.8
Best fit eruption age (ka) +-2sig (ka)																**124.6 6.5**	**96.4 5.3**
Best fit eruption age - outliers removed (ka) +-2sig (ka)																**114.2 7.3**	

a) For samples where the crystallisation age was not measured due to secular equilibrium an age of 400 ± 100 (1σ) ka was used in calculations in MCHeCalc so ages could be calculated

b) Outliers (which are detailed in the chapted) are denoted using red, data removed as the (U-Th)/He date is >> than crystallisation age is marked grey

Supplementary Material IV

Whole rock analyses

Sample	232Th ppm	1σ ppm	238U ppm	1σ ppm	Th 2σ %	U 2σ %	Th/U	Th/U 2σ %	Th/U 2σ absolute	(238U/ 232Th)	2σ
Km-2	4.18	0.02	1.24	0.01	0.96	1.61	3.371	1.88	0.063	0.900	0.010
Sp-1	7.17	0.1	1.76	0.02	2.79	2.27	4.074	3.60	0.147	0.745	0.024
Km-1	4.52	0.02	1.36	0.01	0.88	1.47	3.324	1.72	0.057	0.913	0.015
Kt-1	3.16	0.02	1.03	0.01	1.27	1.94	3.068	2.32	0.071	0.989	0.026

(230Th/ 232Th)	2σ
0.900	0.010
0.745	0.024
0.913	0.015
0.989	0.026

Chapter 3

A new approach to SHRIMP II zircon U-Th disequilibrium dating

Abstract

U-Th disequilibrium dating of zircon is used to determine the crystallisation age of zircon crystals which formed $\lesssim$350 ka. In this work we present a new analytical and data reduction workflow for zircon U-Th disequilibrium analysis using a Sensitive High Resolution Ion MicroProbe (SHRIMP), specifically the SHRIMP II instrument at Curtin University. This is the first zircon U-Th disequilibrium work carried out on the SHRIMP II, and the workflow was investigated with both 3 nA and 6 nA primary beam intensities, using an inverted mass run sequence (from high to low mass). The data reduction was affected by the complex background corrections on the ^{230}Th mass peak, which yields extremely low counts on ^{230}Th, and a logarithmic high mass tail from shouldering mass peaks. A new approach to data reduction and a new computer program (Crayfish) written in Python is presented to address these complexities. Crayfish aids in visualisation of reduction of the raw count data from SHRIMP .pd files, allowing for more interaction with raw data during reduction, and formally propagates uncertainties from measurements to age. A case study testing the new approach was undertaken using trachytic samples from Jeju Island, South Korea, an active volcanic field and a UNESCO world heritage site. The newly derived SHRIMP crystallisation ages of 13 $\pm$ 27 to 212 $\pm$ 324 ka replicate measurements performed using a CAMECA IMS 1280 (2σ uncertainties). In addition, these ages are older than previously calculated eruption ages, which supports their accuracy.

3.1 Introduction

The crystallisation age of zircon grains which are $\lesssim$350 ka can be measured using U-Th disequilibrium dating (Schmitt, 2011). The method has been used to understand magma

evolution in the crust (Schmitt, 2006; Schmitt et al., 2010b), and can also be combined with (U-Th)/He dating to correct $\lesssim$350 ka eruption ages for disequilibrium (zircon double-dating) (Danišík et al., 2017). Methods for SIMS zircon U-Th disequilibrium dating have been developed on the CAMECA IMS 1280 (Schmitt, 2011) following development on the CAMECA IMS 1270 (Reid et al., 1997; Schmitt, 2006) and on the SHRIMP RG (Bacon and Lowenstern, 2005).

One challenge when using the method is that the background signal can potentially interfere with the relatively small ^{230}Th peak (on the order of 10 counts per second). Prior work has proposed several different methods of correcting for this interference. For example, Bacon and Lowenstern (2005) use a single constant background correction for measurements made on the SHRIMP RG, whereas Schmitt (2006, 2011) measured two background masses on the CAMECA IMS 1280 (multi-collector): one at AMU 244.3 (considerably before the ^{230}Th^{16}O peak at 246) and the other at AMU 246.3 (immediately after the ^{230}Th^{16}Opeak). An average of these two values can be used (e.g., Schmitt et al., 2010a, 2017), however, in several cases only the background measured at AMU 246.3 is used as a constant correction (e.g., Zou et al., 2010).

This paper presents a zircon U-Th disequilibrium dating methodology, developed specifically for the SHRIMP II. Firstly, it tests two different primary beam intensities in order to investigate the feasibility of measuring the ^{230}Th^{16}O peak with a low intensity primary beam. Secondly, it proposes using an exponential background correction for the interference of the high-energy mass peak tail from the previous ^{90}Zr^{92}Zr^{16}O$_4$ peak with the ^{230}Th^{16}O peak, and assesses the accuracy of this new background correction method on mass peaks with extremely low counts. This comparison utilises zircon crystals previously dated on the CAMECA IMS 1280 in Heidelberg University, Germany (Marsden et al., 2021), a subsection of which have been shown to have consistent intra-crystal ages.

To facilitate this analysis, a new data reduction computer program (Crayfish), has been written in Python to allow for more complex, user-specified background corrections and enhanced data visualisation compared to the existing approaches (e.g., SQUID 2.5; Ludwig, 2009). Both executables for Windows and Linux and the source code for the program are available online.

3.2 Samples and Methods

3.2.1 Samples for the case study

Five Quaternary trachyte samples from Jeju Island were selected for analysis. These samples, SS14-28, SS15-45, SS15-66, SS18-12 and SS36-6 have been previously dated by ion microprobe and (U-Th)/He, for crystallisation and eruption age, respectively

(Marsden et al., 2021). The igneous zircon crystals from these trachytic rocks have oscillatory zoning (from cathodoluminescence images) and their shape is well-defined with bipyramidal terminations. While these crystals were found to have mostly homogeneous U-Th disequilibrium age distributions (sample SS18-12 was only analysed on the crystal rim), the U concentration within single crystals and between crystals from a given sample was more variable.

3.2.2 Sensitive High Resolution Ion MicroProbe methodology

The following methods were developed on the SHRIMP II instrument at the John de Laeter Centre, Curtin University, Perth. Two separate experimental setups for determining U-Th disequilibrium ages were investigated in this study. The first used a lower intensity beam with longer count times and the second used a higher intensity beam with shorter count times, thereby exploring the trade-off between accuracy, analysis time and sample volume consumption. A limit was observed for the higher intensity beam related to increasing beam instability. For both setups the mass resolution was ca. 5000, the dead time was 25 nA, and the post-ESA monitors were set on the 30 nA scale.

3.2.2.1 Low intensity beam

The primary O_2^- beam intensity for this run was 3 nA, with a spot diameter of 30 μm using a 100 μm Kohler aperture. Setup for the low intensity beam run was performed on reference zircon GJ1 (Jackson et al., 2004) and the $^{230}Th^{16}O$ offset value from the reference $^{232}Th^{16}O$ peak AMU was measured on this material using a slow scan (10 s per mass station, 1 AMU) across the $^{230}Th^{16}O$ peak. Samples SS14-28, SS15-45, SS15-66, SS18-12 and SS36-6 and reference zircons R33 (Black et al., 2004), GJ-1 and Plešovice (Sláma et al., 2008) were analysed in the low intensity beam session. The following masses with associated count times and delay times (the wait times between measurements) were measured in this order:

Mass	Count time (s)	Delay time (s)	Centring time if applicable (s)
254 ($^{238}U^{16}O$)	2	8	4
248 ($^{232}Th^{16}O$)	5	3	3
246.08791 (B2)	20	5	
246 ($^{230}Th^{16}O$)	200	5	
245.91209 (B1)	20	5	
238 (^{238}U)	5	3	3
196 ($^{92}Zr_2^{16}O$)	2	3	3

Table 3.1: Masses measured in the low intensity primary beam session and their associated count times, delay times and reference peak centring times

3.2.2.2   High intensity beam

The primary O_2^- beam intensity for the second run was 6 nA, achieved using a Kohler aperture of 200 μm. The spot diameter was approximately 50 μm. The retardation lens was set to its active voltage (9960 V) and was used in order to filter out low energy secondary ions and hence remove the low energy tail from mass peaks and increases abundance sensitivity (Freeman et al., 1967; Kaiser and Stevens, 1969). The G4 reference zircon was used to find the $^{230}Th^{16}O$ peak and the necessary measurement offset (Nasdala et al., 2004) using a 10s 1 AMU mass scan. This variation was used because it became clear that access to a higher U concentration reference material would prove useful to ensure that the $^{230}Th^{16}O$ mass peak was identified. The following masses, count times and delay times were measured, in this order:

Mass	Count time (s)	Delay time (s)	Centring time if applicable (s)
251 ($^{235}U^{16}O$)	2	8	4
248 ($^{232}Th^{16}O$)	5	3	3
246.0454 (B2)	10	5	
246 ($^{230}Th^{16}O$)	30	5	
245.9556 (B1)	10	5	
196 ($^{92}Zr_2{}^{16}O$)	2	3	3

Table 3.2: Masses measured in the high intensity primary beam session and their associated count times, delay times and reference peak centring times

$^{235}U^{16}O$ was measured instead of $^{238}U^{16}O+$ due to the concern that the high intensity secondary beam of $^{238}U^{16}O+$ ions would cause premature aging of the electron multiplier. ^{238}U was not measured. An estimate of $^{238}U^{16}O$ was then calculated using the natural $^{238}U/^{235}U$ ratio. Only zircon crystals from the SS14-28 trachyte were measured using the high intensity beam method. These crystals have not previously been individually dated.

3.3   Theory

3.3.1   Assumptions

In order to develop a suitable data reduction scheme, it is first necessary to first identify the assumptions about the operation of the SHRIMP II and the underlying physical processes. The assumptions made are as follows:

(i) There are two sources of background that affect the measurements, noise on the instrument and interference from other mass peaks.

(ii) The background for the $^{238}U^{16}O$, $^{232}Th^{16}O$, ^{238}U peaks is composed only of instrument noise with no interference.

(iii) The background for the ^{230}Th^{16}O peak is composed of both noise on the instrument and interference from the high energy scattered ions from a previous mass peak, assumed to be ^{90}Zr^{92}Zr^{16}O$_4$.

(iv) The measurement at B1 is composed of both background noise and interference coming from the high energy tail of the ^{90}Zr^{92}Zr^{16}O$_4$ peak.

(v) The measurement at B2 comprises only instrument noise.

(vi) The true background noise and interference are assumed to be constant over a spot. The latter is assumed to be constant as it is thought that the high-energy mass tail comes from the ^{90}Zr^{92}Zr^{16}O$_4$ peak which assumed constant throughout the crystal matrix. Therefore, so too are the true values at B1 and B2.

(vii) It is assumed that ^{238}U^{16}O, ^{232}Th^{16}O, ^{238}U, and ^{230}Th^{16}O are constant over a scan, but not down hole through the spot. This is due to the natural variation in U and Th within zircon crystals at the μm scale (e.g., Storm et al., 2014).

3.3.2   Background corrections

As discussed in assumption iii, the ^{230}Th^{16}O peak is influenced by both instrument noise and interference. This background is highly influential as this peak has very low counts (Schmitt, 2011). In order to correct for this background, it is necessary to construct a model of the interference.

There have been several models proposed: the constant and average corrections used by Bacon and Lowenstern (2005) and Schmitt (2006, 2011) both assume that there is no interference on the ^{230}Th^{16}O peak; this assumption comes from work carried out by Reid et al. (1997) on the CAMECA IMS 1270. Alternatively, the average correction (Schmitt, 2006, 2011) uses background measurements at $\approx$244.3 and 246.3 AMU. Note that this is not a linear interpolation and assumes constant background, which is the mean of these two measurements.

However, having performed a slow scan over the ^{230}Th^{16}O peak on the SHRIMP II, a more complex background signal is observed (Figure 3.1) that cannot be fully modelled by either the constant or average models. In particular, the tail of the ^{90}Zr^{92}Zr^{16}O$_4$ peak appears to have a significant affect at the measured AMUs. Consequently, two further possible corrections are explored in this paper – a linear model and an exponential model. This work is therefore the first to take interference from high mass energy tails into account for background correction of the ^{230}Th^{16}O peak on the SHRIMP II.

In Figure 3.1c and Figure 3.1d the position of the background measurements used in our experiments are shown in red, and hypothetical constant, linear and exponential background models are overlaid. For the low intensity run, both the exponential and the linear models
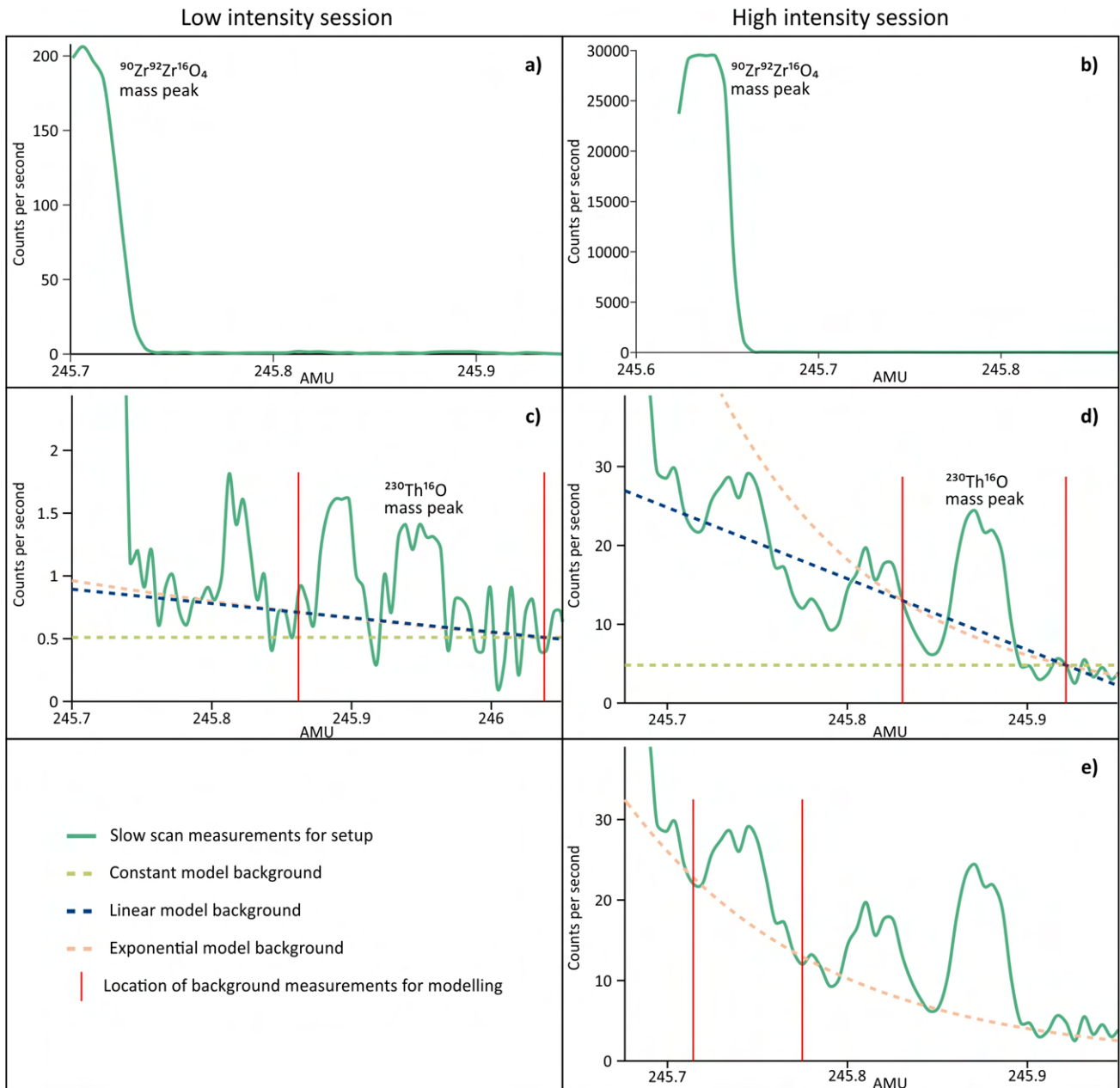
Figure 3.1: a) Low intensity slow scan on reference zircon GJ1; b) High intensity slow scan on reference zircon G4 around the ^{230}Th^{16}O peak; c) Zoomed in scan measurements for the low intensity setup work showing actual placement of background measurements d) Zoomed in scan measurements for the high intensity setup work showing actual placement of background measurements and e) Zoomed in scan measurements for the high intensity setup work showing hypothetical improved placement for background measurements.

appear to be a good fit for the background signal. However, in the final experiments the exponential model was used to correct the low intensity data as it more accurately reflects the actual measurements. In the high intensity run, Figure 3.1d illustrates the importance of siting background measurements correctly; the background measurements were made at AMUs which did not reflect the interference from the $^{90}Zr^{92}Zr^{16}O_4$ peak, but rather from the second smaller interference peak, making the linear and exponential models of the background significantly less accurate. In this case, because of the misplacement of the background measurements, the constant background model was used to correct the high intensity data. However, it should be emphasised that the exponential background model is still the most appropriate if the background measurements can be sited appropriately. To illustrate this, Figure 3.1e shows the fit of the exponential model for two hypothetical background measurements made at better points.

Additionally, the two smaller peaks situated on the shoulder of the $^{90}Zr^{92}Zr^{16}O_4$ are not thought to influence the background correction. While they are not significant in terms of background correction for this work, their identification as potentially $^{174}Yb^{28}Si_2^{16}O$ and $^{197}Au^{16}O^3H$ (Schmitt, 2009) may prove useful in future experiments.

3.3.3 Inverted mass order

An inverted mass order cycle (that is running from high mass to low mass throughout a cycle) was developed because the 246 AMU peak (for measuring $^{230}Th^{16}O+$ ions) was too low to be automatically located. Similarly to the 204Pb peak in U-Pb age dating, the AMU at which the $^{230}Th^{16}O$ peak is measured is calculated as a fixed offset from a distinct, automatically located reference peak (Schmitt, 2011). The mass peak $^{90}Zr^{92}Zr^{16}O_4+$ was tested for this purpose at a mass of $\sim$246, however it was not found to be sufficiently well resolved to allow reliable identification by the SHRIMP II. Instead, the 248 peak ($^{232}Th^{16}O+$ ions) was used as the reference peak to calculate the offset required for the $^{230}Th^{16}O$ peak. However, the $^{232}Th^{16}O$ peak is at a higher mass than the $^{230}Th^{16}O$ peak and therefore, in order to use it as a reference peak, the masses were measured from highest to lowest in the magnet cycle (Table 1 & Table 2).

3.3.4 When to collate scan measurements into spot measurements

During data reduction, current known methodologies (Ludwig, 2009; Schmitt, 2011; Bodorkos et al., 2020) average all scan measurements into one counts per second (cps) value per mass peak per spot and then calculate a single age for the spot from these values. By averaging before calculating the age, this implicitly assumes that each scan is measuring the same true concentration, or equivalently that U and Th concentration does

not vary between scans. This assumption may be justified for the CAMECA IMS 1280, for example, which uses relatively short burn times (12mins; Marsden et al., 2021) and therefore is assumed to sample the same zone of the crystal in each scan.

However, the low intensity primary beam method proposed in this paper uses a maximum burn times of 200 s and therefore over multiple scans has the potential to liberate secondary ions from an increased depth within the crystal. As zircon crystals have been shown to have variable U and Th concentrations over the μm scale (Storm et al., 2014), repeated scans of the same spot may therefore not be measuring the same concentrations of U and Th, even if the crystallisation age remains constant between scans.

As described by Schmitt (2011) and discussed in Section 3.4.1.2, Equation 9, age is a function of the gradient of the two point isochron created by subtracting the whole rock $(^{238}U/^{232}Th)$ and $(^{230}Th/^{232}Th)$ activity ratios from the measured $(^{238}U/^{232}Th)$ and $(^{230}Th/^{232}Th)$ activity ratios, where activity is the number of decays of an isotope in a system per unit time. Therefore age is a non-linear function of the measured ^{238}U and ^{230}Th concentrations in cps. Consequently, using cps to represent the cps measurement for a scan, because $E(age(cps)) \neq age(E(cps)))$ and the cps measurements vary between scans, it is vital that averaging only occurs after calculating the age for each scan. Additionally, if the age of crystallisation does vary per scan, averaging after the age calculation per scan affords the user a better understanding of potential age variation throughout the crystal. This scan-by-scan method was also used in depth-profiling experiments by Reid and Vazquez (2017) and Tierney et al., (2019). The age variation in these studies can be up to the order of 100s of kyrs.

3.4 Computation

3.4.1 Crayfish development

Existing approaches (Ludwig, 2009; Bodorkos et al., 2020) for the reduction of data from the SHRIMP II have two limitations when used for U-Th disequilibrium dating. Firstly, existing software SQUID 1 & 2, is unable to handle masses measured in reverse mass order, that is, cyclically from high to low. Secondly, all versions of SQUID can only perform a constant background correction. Consequently, in order to address these limitations and support enhanced visualisation of intermediate results, a new data reduction program for U-Th disequilibrium dating on the SHRIMP II has been developed: Crayfish. This software is open source and available at https://github.com/RubyMarsden/Crayfish.

3.4.1.1   SHRIMP data format

SHRIMP II supplies raw output data in a .pd file, an example of which is shown in Figure 3.2. Each named analysis (referred to as a 'spot') consists of a fixed number of scans through the mass stations. In each scan, the measurement of each mass peak is split into 10 time periods by the SHRIMP instrumentation, hereafter referred to as 'blocks'. For each block, the secondary beam monitor (SBM) also measures the secondary beam strength to create a corresponding 'block' of SBM counts, which can be used as a proxy for the primary beam strength at that point in time. The SBM zero measurement is the SBM measurement when the primary beam is switched off.
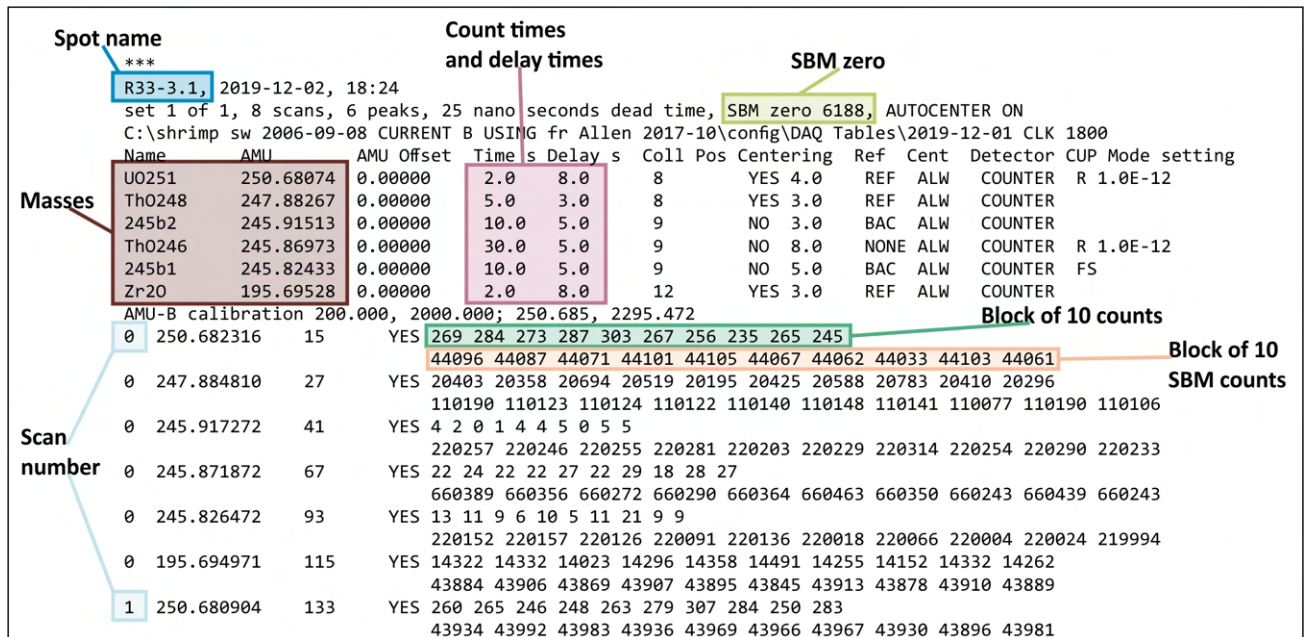
Figure 3.2: An example the beginning of the .pd file from the high intensity primary beam session.

Mathematically this is defined as follows. Let $count^m$ be a single set of measurements on mass peak m. For $counts_{i,j}^m$ the subscript i denotes the scan number and the subscript j denotes the block number within a scan. In the low intensity primary beam experiment there are 10 scans and 10 blocks so both i and j range from 1 to 10. In the high intensity primary beam experiment, only 8 scans were used and so i ranged between 1 and 8, while j continued to range from 1 to 10. For example, $counts_{1,2}^{232Th16O}$ is the 2nd measurement in the 1st scan for mass ^{232}Th^{16}O. Likewise $SBM\_counts_{i,j}^m$ represents the jth measurement in the ith scan of SBM counts for mass peak m.

3.4.1.2   Data reduction

1. Crayfish first subtracts the SBM zero measurement from each SBM measurement in order to correct for background noise. SBM measurements are then normalised to

counts per second (cps) by dividing the measurement by the count time per block (i.e., count time for the mass divided by 10). The blocks are kept separate due to potentially long count times and possible variations in U concentration within the target material.

$$SBM\_CPS_{i,j}^m = \frac{10 \times SBM\_counts_{i,j}^m - SBM\_zero}{count\_time^m}$$

2. The counts for each mass peak are then normalised to cps.

$$CPS_{i,j}^m = \frac{10 \times counts_{i,j}^m}{count\_time^m}$$

3. Optionally, but strongly recommended, the CPS values are then divided by the normalised SBM values in order to compensate for fluctuations in primary beam strength.

$$CPS\_norm_{i,j}^m = \frac{CPS_{i,j}^m}{SBM\_CPS_{i,j}^m}$$

From this point onwards the mathematics continue as if SBM normalisation has taken place, however if the operator chooses not to SBM normalise, the process remains identical.

The values of $SBM\_CPS_{i,j}^m$ and $CPS\_norm_{i,j}^m$ are then displayed so each spot can be assessed by the operator. At this point, the operator can "flag" individual suspect spots, preventing them from being used in future calculations. For example, a spot might be flagged if the primary beam intensity dropped, or it is clear that the sample being analysed is not a zircon crystal. It is widely accepted that individual block measurements should be averaged using an outlier resistant mean (Ludwig, 2009; Bodorkos et al., 2020). Outliers are identified using the medcouple approach for skewed data due to the inherent skew in low count data (Hubert and Van der Veeken, 2008) as outlined in Supplementary Material I.

4. The scan outlier resistant mean and standard deviation are calculated for all non-background counts. After outliers are removed mean and standard deviation are calculated. Going forward uncertainties are not discussed, but details can be found in Supplementary Material III. Let $\mathcal{O}(\cdot)$ be the function which calculates the outlier resistant mean of the set of measurements.

$$\widetilde{CPS\_norm}_i^m = \mathcal{O}_j(CPS\_norm_{i,j}^m)$$

5. In contrast, the background counts are treated differently. Due to assumption vi, it is assumed that while U and Th concentration may vary between scans, the background

is constant over the entire spot. Therefore, the weighted mean of all background measurements across a single spot are calculated from the individual scan data. Let $\mathcal{W}(x, y)$ be the weighted mean and standard deviation of the set of measurements x, weighted by the associated values y.

$$\widetilde{CPS\_norm}_i^{B1} = \mathcal{W}(\widetilde{CPS\_norm}_i^{B1}, \sigma)$$

$$\widetilde{CPS\_norm}_i^{B2} = \mathcal{W}(\widetilde{CPS\_norm}_i^{B2}, \sigma)$$

It is important to note that at this point the equivalent data reduction procedure on the CAMECA IMS 1280 (Schmitt, 2011) averages over the scan measurements from each spot, in order to obtain a single normalised cps measurement per spot. In contrast, as described in the steps below, Crayfish proceeds to calculate an age for each individual scan and only then averages them at the end to calculate a single age per spot as is discussed in Section 3.3.4.

6. The program then separates the mass peaks into the ^{230}Th^{16}O peak, which can have a variable background, and the other mass peaks, which are assumed only to be affected by a constant background noise. In the latter case, a simple subtraction of the background measurement from the mass peak measurement is performed.

$$CPS\_bci^{232Th16O} = \widetilde{CPS\_norm}_i^{232Th16O} - \widetilde{CPS\_norm}_i^{B2} \tag{3.1}$$

$$CPS\_bci^{238U16O} = \widetilde{CPS\_norm}_i^{238U16O} - \widetilde{CPS\_norm}_i^{B2} \tag{3.2}$$

For the ^{230}Th^{16}O background correction, the program provides three background models for correction: exponential, linear and constant where the constant background correction method is the same as the correction method for all other peaks.

$$\text{Constant: CPS\_bc}_i^{230Th16O} = \widetilde{CPS\_norm}_i^{230Th16O} - \widetilde{CPS\_norm}_i^{B2} \tag{3.3}$$

$$\text{Linear: CPS\_bc}_i^{230Th16O} = \widetilde{CPS\_norm}_i^{230Th16O} - \widetilde{CPS\_norm}_i^{B-linear} \tag{3.4}$$

$$\text{Exponential: CPS\_bc}_i^{230Th16O} = \widetilde{CPS\_norm}_i^{230Th16O} - \widetilde{CPS\_norm}_i^{B-exponential} \tag{3.5}$$

As discussed in Section 3.3.2, these complex background corrections are required

due to the high-mass tail from the shoulder of the nearby $^{90}\text{Zr}^{92}\text{Zr}^{16}\text{O}_4$ peak. The exponential background calculations and linear background calculation equations are detailed in Supplementary Material II.

7. Next, the activity ratios, $(^{238}\text{U}/^{232}\text{Th})$ and $(^{230}\text{Th}/^{232}\text{Th})$, are calculated for each individual scan. The decay constant for each isotope is represented using λ_m, decay constants in this study are the same as those used in Marsden et al. (2021) for comparison purposes.

$$\left(\frac{238U_i}{232Th_i}\right) = \frac{\text{CPS\_bc}_i^{238U16O}}{\text{CPS\_bc}_i^{232Th16O}} \times \frac{\lambda_{232}}{\lambda_{238}} \tag{3.6}$$

$$\left(\frac{230Th_i}{232Th_i}\right) = \frac{\text{CPS\_bc}_i^{230Th16O}}{\text{CPS\_bc}_i^{232Th16O}} \times \frac{\lambda_{232}}{\lambda_{230}} \tag{3.7}$$

8. The scan activity ratios for reference zircons are then plotted on a single graph. The $(^{230}\text{Th}/^{232}\text{Th})$ versus $(^{238}\text{U}/^{232}\text{Th})$ values should all fall on the equiline if the material is in secular equilibrium (Schmitt, 2011). However, this line may not have a gradient of exactly 1, and the offset represents instrumental mass fractionation. Accordingly, the activity ratio for unknown samples is corrected by the standard gradient factor determined on reference materials, which are in secular equilibrium.

9. The gradient,m_i , for each two-point isochron is calculated from the activity ratios of the whole rock and each non-reference spot. The age for each scan is calculated using the equation from Schmitt (2011).

$$t_i = \frac{-ln(1 - m_i)}{\lambda_{230}} \tag{3.8}$$

10. The age for the entire spot is calculated using the error weighted mean over the individual scan ages.

$$t = \mathcal{W}(t_i, \sigma) \tag{3.9}$$

These ages are then plotted and displayed to the user who can then export the results to a csv file for further analysis. Additionally, the user can easily alter the various data reduction options, such as the background correction model, allowing for near instantaneous comparison of their effects. Screenshots of the UI can be seen in Supplementary Material V.

3.5 Case study results

3.5.1 Low intensity beam results

The SBM readings for the low intensity beam session are shown in Figure 3.3. As the SBM is a proxy for the strength of the primary beam, these readings suggest that the primary beam was broadly stable throughout the run. However, each spot shows a decrease in secondary beam cps with time, and this decrease is approximately 25% from the initial value. This provides additional evidence for the need to normalise by SBM, as described in step 3 in Section 3.3.1.
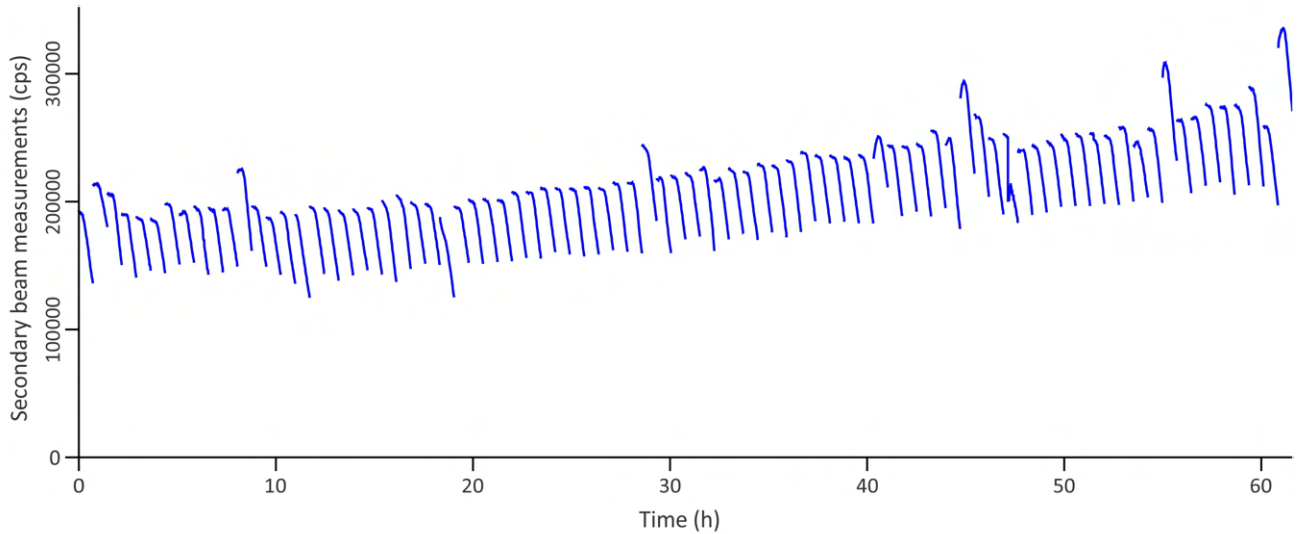
Figure 3.3: SBM measurements for the low intensity beam U-Th disequilibrium work session – screenshot taken from the Crayfish program.

The exponential background-corrected results are plotted in Figure 3.4. The Jeju samples have ages and 2σ uncertainties as follows:

Sample	Youngest age (ka)	Oldest age (ka)
SS14-28	52 ± 23	205 ± 298
SS15-45	10 ± 27	315 ± 754 (or secular equilibrium)
SS15-66	45 ± 79	329 ± 117 (or secular equilibrium)
SS18-12	8 ± 26	145 ± 105
SS36-6	27 ± 23	131 ± 52

Table 3.3: Youngest and oldest crystallisation ages for the Jeju samples measured in the low intensity primary beam session.

3.5.2 High intensity beam results

The SBM readings for the high intensity beam session are shown in Figure 3.5. The decrease in SBM over a single spot was approximately a 7% reduction from the initial value.
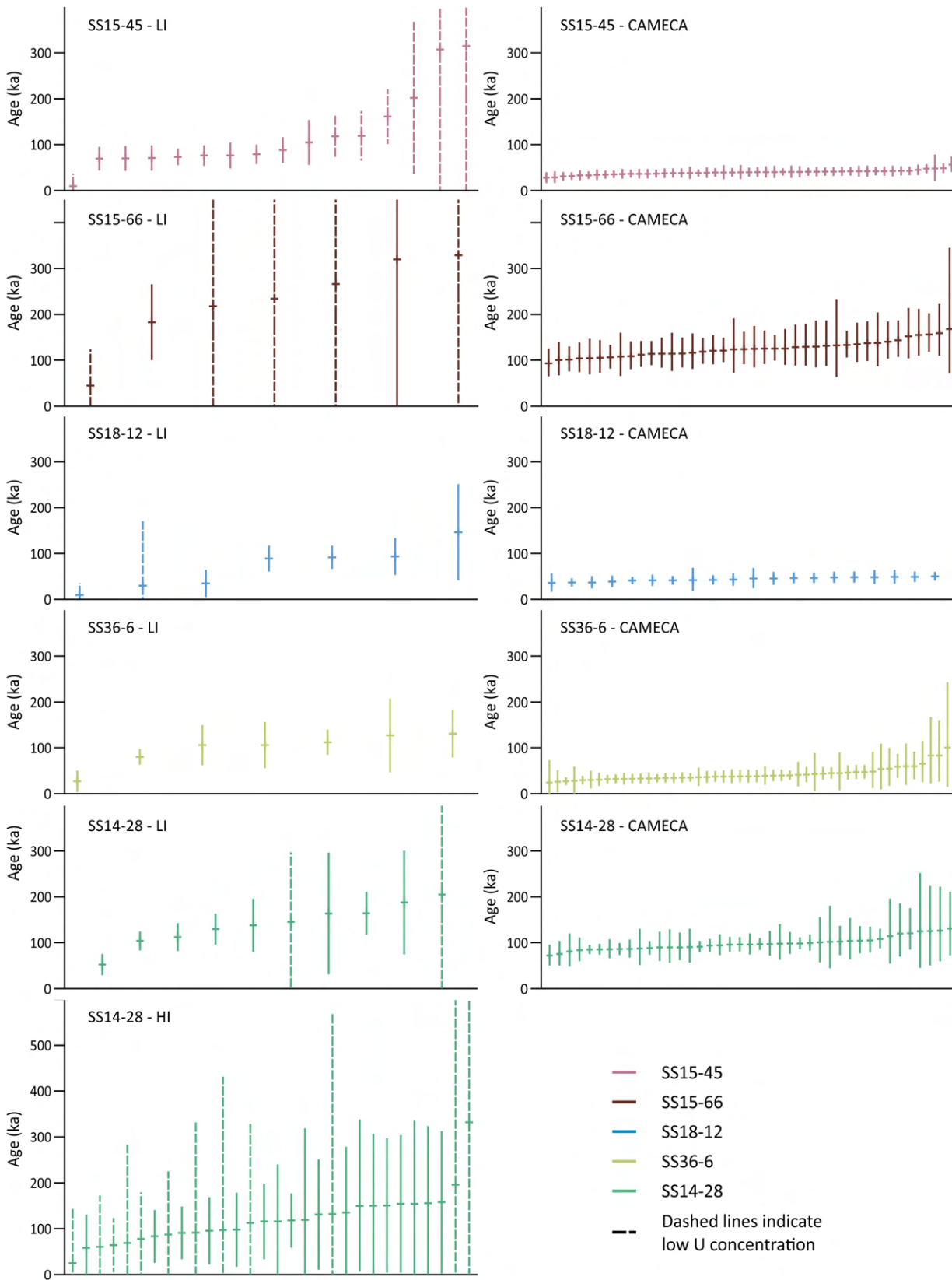
Figure 3.4: U-Th disequilibrium age results for the low and high intensity primary beam sessions, uncertainties are 2σ. LI indicates results from the low intensity primary beam session, HI from the high intensity primary beam session and CAMECA indicates U-Th disequilibrium results from the CAMECA IMS 1280 in Heidelberg from Marsden et al. (2021). Increased precision for CAMECA IMS 1280 data is due to higher ^{230}Th^{16}O count rates and a correspondingly larger sample volume.

The SBM values are more scattered than those in the low intensity beam session, reflecting some degree of instability in the primary beam during this session. At approximately 4 hours into the analytical session, the SBM readings show a drop, indicating that the primary beam was not functioning at that point. The affected spot that it affects was removed from any further calculations.
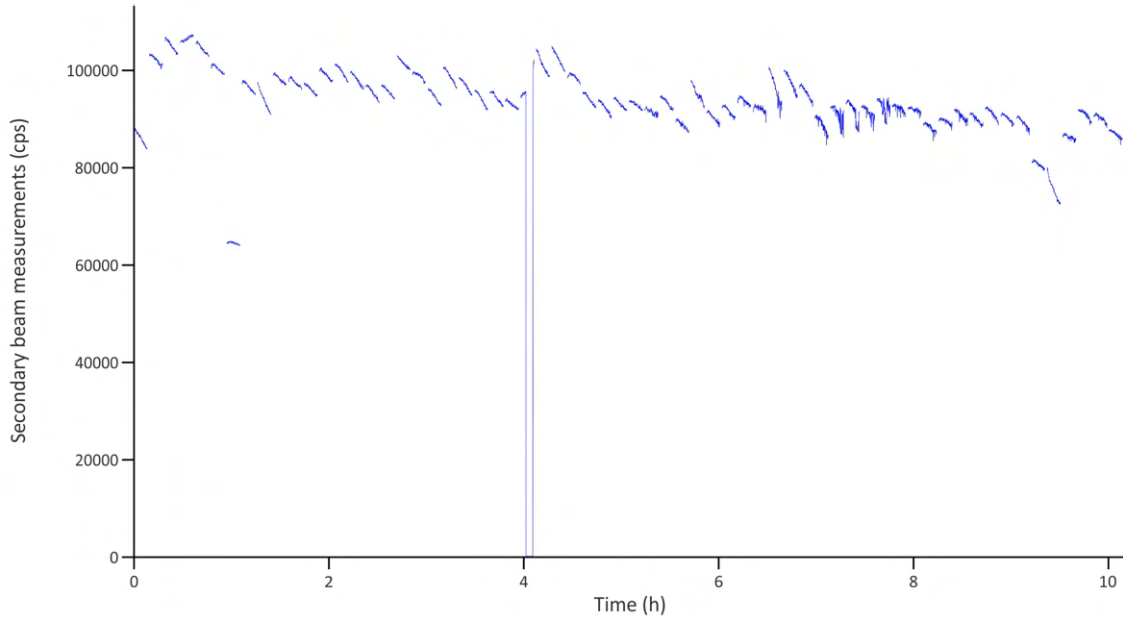
Figure 3.5: SBM measurements for the high intensity beam U-Th disequilibrium work session – screenshot taken from the Crayfish program. The drop to 0 cps at approximately 4 hours indicates a primary beam dropout at this point and the spot that this affected was removed from all further calculations.

The constant background-corrected results are shown in Figure 3.4. The ages for samples SS14-28 range from 25 ± 121 to 158 ± 155 ka (or secular equilibrium if low U cps data used). Due to high uncertainties, a weighted mean was taken giving 95.9 ± 9.6 ka, MSWD = 0.33 using IsoplotR (Vermeesch, 2018).

3.6 Discussion

3.6.1 Comparison of values to previously derived U-Th disequilibrium ages.

The same samples that were analysed in the low intensity beam session in this work have been dated by Marsden et al. (2021) using the CAMECA IMS 1280 in the Heidelberg Ion Probe laboratory at Heidelberg University. Thirty two of the 52 spots measured in the present study yielded SHRIMP II ages within uncertainty of the CAMECA IMS 1280 ages for the same crystals, however, it is understood that while age homogeneity was hypothesised for these samples (not including SS18-12), this may not reflect reality. For

the low intensity primary beam session, the age determined were overall generally older than those determined on the CAMECA IMS 1280, especially if the U cps were low (Figure 7). The dates are interpreted to reflect the age of crystallisation of the zircon on the basis of the closure temperature of the zircon U-Th disequilibrium system (∼900 °C; Lee et al., 1997). The U-Th disequilibrium ages should be older than (or within uncertainty of) the (U-Th)/He age because the (U-Th)/He age represents the eruption age (zircon (U-Th)/He system closure temperature is ∼180°C; Reiners et al., 2004) and crystallisation occurred before eruption. While the high intensity beam session uncertainties were large, the weighted mean of 95.9 ± 9.6 ka is within uncertainty of the weighted mean of the ages measured in Heidelberg of 92.0 ± 1.7 ka and shows the analytical method and Crayfish are capable of accurately replicating the results of existing methods.

Sample	Eruption age (ka)	Minimum U-Th disequilibrium age (ka) (not using values calculated from U <25,000 cps spots))
SS14-28	62 ± 6	52 ± 23 (low intensity session)
SS15-45	28 ± 1	10 ± 27
SS15-66	78 ± 5	45 ± 79
SS18-12	31 ± 2	8 ± 26
SS36-6	24 ± 1	27 ± 23

Table 3.4: Eruption ages from Marsden et al. (2021) compared to youngest crystallisation age for samples using the low intensity primary beam data

3.6.2 Large uncertainties

As expected, there is a correlation between the uncertainty in the Crayfish ages and U cps (Figure 3.6). It is hypothesised this is due to low ^{230}Th^{16}O counts as the number of ^{230}Th atoms is directly linked to concentration of U as it is a daughter product of ^{238}U decay. Due to uncertainties > 100% for samples containing ^{238}U cps < 25,000 (Supplementary Material IV, Figure 3.1a) or ^{235}U cps < 400 (Supplementary Material IV, Figure 3.1b), standards and samples with low U cps were culled from the standard line calculation.

However, not only did U concentration correlate with uncertainty, but also with the accuracy of determined ages. Figure 3.7 compares the Heidelberg ages and the ages generated on the same samples during the low intensity primary beam session in this work. The U content is represented by the circle size, and shows higher deviation from the Heidelberg ages with lower U content. This is most likely due to low ^{230}Th^{16}O counts and relatively complex background peaks/corrections (i.e., ^{230}Th^{16}O counts that are so close to background levels that the uncertainty in the background correction causes considerable deviation from true values). When originally designing the experiments, it was expected that an increase in the primary beam intensity would lead to an increase in ^{230}Th^{16}O counts relative to the background and would, therefore, significantly reduce the associated
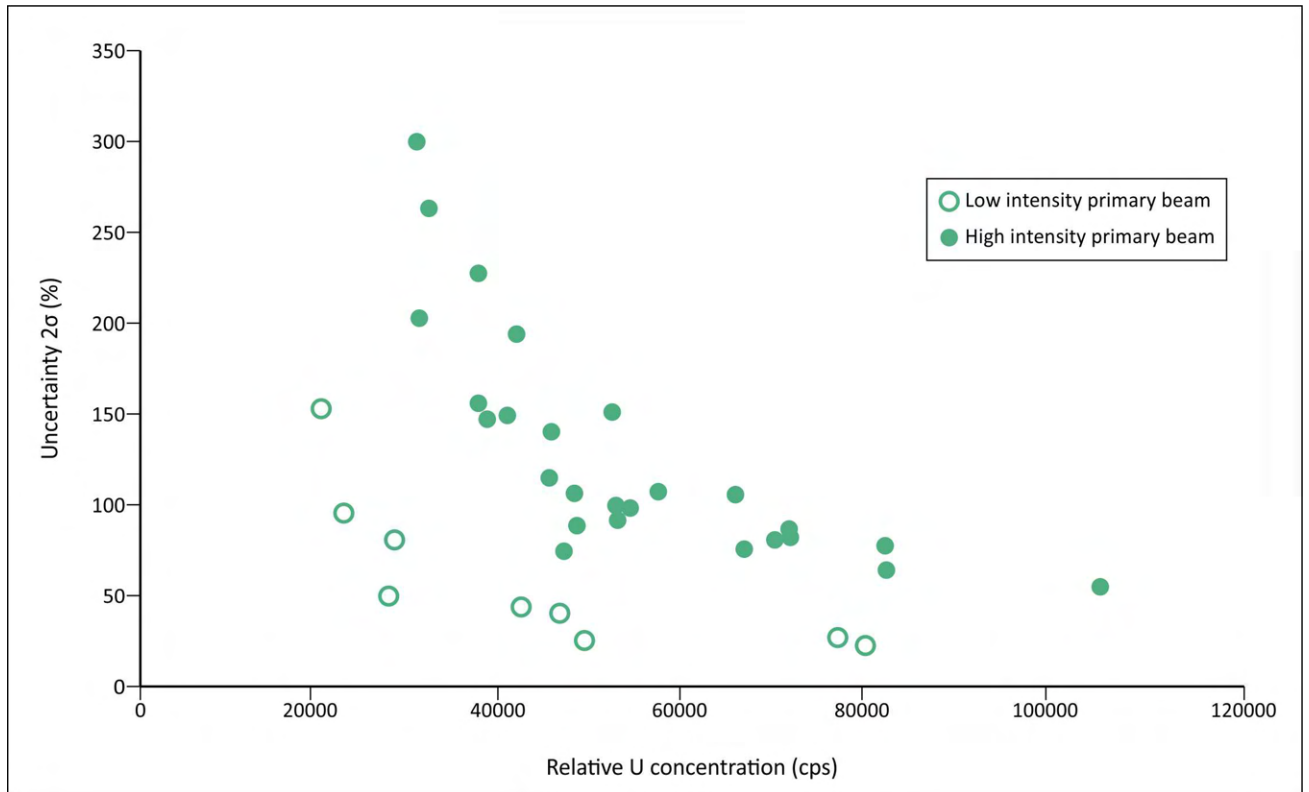
Figure 3.6: Uncertainties for sample SS14-28 compared between the high and low primary beam intensity methods.
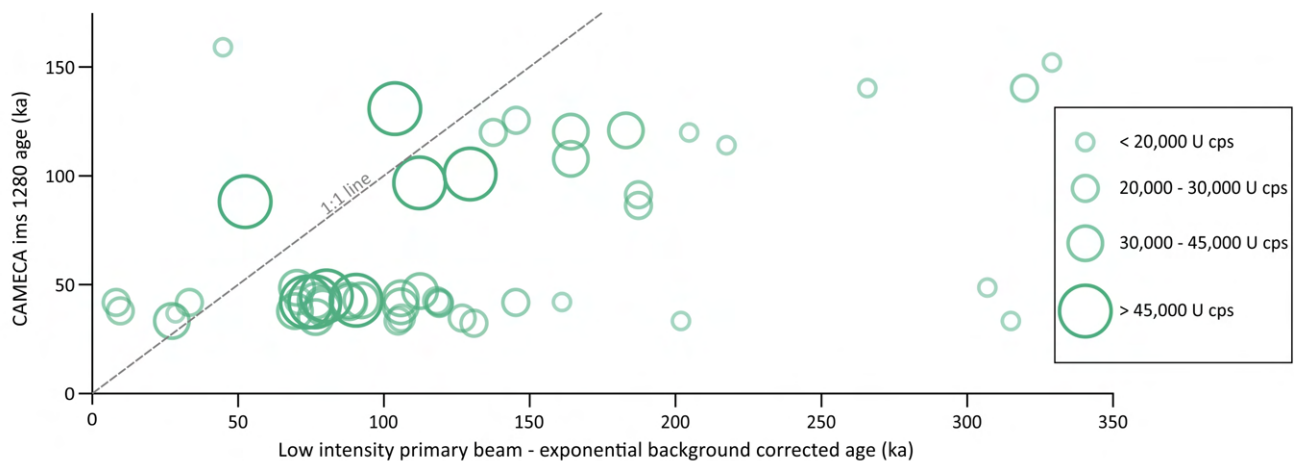
Figure 3.7: Comparison between the CAMECA IMS 1280 ages and the SHRIMP II Crayfish ages for the low intensity primary beam session. Ages that agree lie on the 1:1 line. [238]U concentration in cps for each spot on the SHRIMP II is represented by the size of the circle. Uncertainties are not represented.

uncertainties. Figure 3.6 shows a comparison between uncertainties measured on the low intensity primary beam session and those measured during the high intensity primary beam session. This comparison is for sample SS14-28 and is shown relative to U content. Against predictions, uncertainty is generally higher in the high intensity primary beam session, which may be explained due to reduced count times on the higher intensity primary beam session increasing the uncertainty on low count rates.

3.6.3   Recommendations for future experiments

- Continue to use an inverted run table (i.e., measuring the masses in reverse mass order) due to the ^{232}Th^{16}O peak being preferable to the ^{90}Zr^{92}Zr^{16}O$_4$ peak on the SHRIMP II.

- There is no discernible reduction on the uncertainty of the age using the higher intensity primary beam, however the low intensity primary beam has overall potentially lower accuracy which can be seen in the systematically older ages measured on all samples, especially if low ^{238}U concentration analyses occur. Therefore two alternative suggestions are made: either increase the count times on background peaks and the ^{230}Th^{16}O peak on a high intensity primary beam, or run low intensity primary beam analyses on samples with high ^{238}U concentration only.

- SBM normalised age results should be used because the extremely long counts on the ^{230}Th^{16}O peak cause significant variability of secondary counts which can be normalised via the use of the SBM throughout an individual scan. This is particularly relevant if the low intensity beam method is used.

- For low intensity and high intensity primary beam sessions model the background correction on the ^{230}Th^{16}O peak from observations made over an initial slow mass scan as seen in Figure 3.1.

- Measure more than 2 background points in order to better estimate the exponential background models on the ^{230}Th^{16}O peak.

- Perform a slow scan over both a reference zircon and an unknown zircon in order to check that the background model is valid in all cases.

3.7   Conclusion

The new analytical and data reduction protocols presented in this work demonstrate that complex background corrections and low ^{230}Th^{16}O counts are not an obstacle to performing U-Th disequilibrium measurements on the SHRIMP II. The obtained ages

and their associated uncertainties are comparable to those from a previous study where the CAMECA IMS 1280 was utilised, where the U cps were sufficient. However, the results show that the approach is better suited to samples which have relatively high U (approximately 200 ppm), as high U results in higher ^{230}Th^{16}O counts and therefore reduced uncertainty in the final age. The crystallisation ages for trachyte samples from Jeju Island, South Korea range from 8 ± 26 ka to $\lesssim 350$ ka and are older than, or equal within analytical uncertainty of, previously calculated eruption ages, supporting the conclusions of Marsden et al. (2021).

3.8 References

Andersen, N.L., Singer, B.S., Coble, M.A., 2019. Repeated Rhyolite Eruption From Heterogeneous Hot Zones Embedded Within a Cool, Shallow Magma Reservoir. Journal of Geophysical Research: Solid Earth 124, 2582–2600. https://doi.org/10.1029/2018JB016418

Bacon, C.R., Lowenstern, J.B., 2005. Late Pleistocene granodiorite source for recycled zircon and phenocrysts in rhyodacite lava at Crater Lake, Oregon. Earth and Planetary Science Letters 233, 277–293. https://doi.org/10.1016/j.epsl.2005.02.012

Black, L.P., Kamo, S.L., Allen, C.M., Davis, D.W., Aleinikoff, J.N., Valley, J.W., Mundil, R., Campbell, I.H., Korsch, R.J., Williams, I.S., Foudoulis, C., 2004. Improved 206Pb/^{238}U microprobe geochronology by the monitoring of a trace-element-related matrix effect; SHRIMP, ID–TIMS, ELA–ICP–MS and oxygen isotope documentation for a series of zircon standards. Chemical Geology 205, 115–140. https://doi.org/10.1016/j.chemgeo.2004.01.003

Bodorkos, S., Bowring, J.F., Rayner, N.M., 2020. Squid3: next-generation data processing software for sensitive high-resolution ion microprobe (SHRIMP). Geoscience Australia. https://doi.org/10.11636/133870

Danišík, M., Schmitt, A.K., Stockli, D.F., Lovera, O.M., Dunkl, I., Evans, N.J., 2017. Application of combined U-Th-disequilibrium/U-Pb and (U-Th)/He zircon dating to tephrochronology. Quaternary Geochronology, Advancing tephrochronology as a global dating tool: applications in volcanology, archaeology, and palaeoclimatic research 40, 23–32. https://doi.org/10.1016/j.quageo.2016.07.005

Freeman, N.J., Daly, N.R., Powell, R.E., 1967. Retardation Lens Used to Improve the Abundance Sensitivity of a Mass Spectrometer. Review of Scientific Instruments 38, 945–948. https://doi.org/10.1063/1.1720931

Hubert M. and Van der Veeken S. (2008) Outlier detection for skewed data. Journal of Chemometrics: A Journal of the Chemometrics Society 22, 235–246.

Jackson, S.E., Pearson, N.J., Griffin, W.L., Belousova, E.A., 2004. The application of laser ablation-inductively coupled plasma-mass spectrometry to in situ U–Pb zircon geochronology. Chemical Geology 211, 47–69. https://doi.org/10.1016/j.chemgeo.2004.06.017

Kaiser, K.A., Stevens, C.M., 1969. Ion-retarding lens improves the abundance sensitivity of tandem mass spectrometers.

Lee, J.K.W., Williams, I.S., Ellis, D.J., 1997. Pb, U and Th diffusion in natural zircon. Nature 390, 159–162. https://doi.org/10.1038/36554

Ludwig, K.R., 2009. SQUID 2: a user's manual. Berkeley Geochronology Center Special Publication 5, 110.

Marsden, R.C., Danišík, M., Ahn, U.-S., Friedrichs, B., Schmitt, A.K., Kirkland, C.L., McDonald, B., Evans, N.J., 2021. Zircon double-dating of Quaternary eruptions on Jeju Island. Journal of Volcanology and Geothermal Research 107171.

Nasdala, L., Reiners, P.W., Garver, J.I., Kennedy, A.K., Stern, R.A., Balan, E., Wirth, R., 2004. Incomplete retention of radiation damage in zircon from Sri Lanka. American Mineralogist 89, 219–231. https://doi.org/10.2138/am-2004-0126

Reid, M.R., Coath, C.D., Mark Harrison, T., McKeegan, K.D., 1997. Prolonged residence times for the youngest rhyolites associated with Long Valley Caldera: ^{230}Th—^{238}U ion microprobe dating of young zircons. Earth and Planetary Science Letters 150, 27–39. https://doi.org/10.1016/S0012-821X(97)00077-0

Reid, M.R., Vazquez, J.A., 2017. Fitful and protracted magma assembly leading to a giant eruption, Youngest Toba Tuff, Indonesia. Geochemistry, Geophysics, Geosystems 18, 156-177. https://doi.org/10.1002/2016GC006641

Reiners, P.W., Spell, T.L., Nicolescu, S., Zanetti, K.A., 2004. Zircon (U-Th)/He thermochronometry: He diffusion and comparisons with 40Ar/39Ar dating. Geochimica et Cosmochimica Acta 68, 1857–1887. https://doi.org/10.1016/j.gca.2003.10.021

Schmitt, A.K., 2011. Uranium Series Accessory Crystal Dating of Magmatic Processes. Annu. Rev. Earth Planet. Sci. 39, 321–349. https://doi.org/10.1146/annurev-earth-040610-133330

Schmitt, K.A., 2009. Chapter 5: Quaternary Geochronology by SIMS. Mineralogical Association of Canada Short Course 41, 109–131.

Schmitt, A.K., 2006. Laacher See revisited: High-spatial-resolution zircon dating indicates rapid formation of a zoned magma chamber. Geology 34, 597–600. https://doi.org/10.1130/G22533.1

Schmitt, A.K., Klitzke, M., Gerdes, A., Schäfer, C., 2017. Zircon Hafnium–Oxygen Isotope and Trace Element Petrochronology of Intraplate Volcanic Rocks from the Eifel (Germany) and Implications for Mantle versus Crustal Origins of Zircon Megacrysts. Journal of Petrology 58, 1841–1870. https://doi.org/10.1093/petrology/egx075

Schmitt, A.K., Stockli, D.F., Niedermann, S., Lovera, O.M., Hausback, B.P., 2010a. Eruption ages of Las Tres Vírgenes volcano (Baja California): A tale of two helium isotopes. Quaternary Geochronology 5, 503–511. https://doi.org/10.1016/j.quageo.2010.02.004

Schmitt, A.K., Wetzel, F., Cooper, K.M., Zou, H., Wörner, G., 2010b. Magmatic Longevity of

Laacher See Volcano (Eifel, Germany) Indicated by U–Th Dating of Intrusive Carbonatites. J Petrology 51, 1053–1085. https://doi.org/10.1093/petrology/egq011

Sláma, J., Košler, J., Condon, D.J., Crowley, J.L., Gerdes, A., Hanchar, J.M., Horstwood, M.S.A., Morris, G.A., Nasdala, L., Norberg, N., Schaltegger, U., Schoene, B., Tubrett, M.N., Whitehouse, M.J., 2008. Plešovice zircon — A new natural reference material for U–Pb and Hf isotopic microanalysis. Chemical Geology 249, 1–35. https://doi.org/10.1016/j.chemgeo.2007.11.005

Storm, S., Schmitt, A.K., Shane, P., Lindsay, J.M., 2014. Zircon trace element chemistry at sub-micrometer resolution for Tarawera volcano, New Zealand, and implications for rhyolite magma evolution. Contrib Mineral Petrol 167, 1–19. https://doi.org/10.1007/s00410-014-1000-z

Tierney, C.R., Reid, M.R., Vazquez, J.A., Chesner, C.A., 2019. Diverse late-stage crystallization and storage conditions in melt domains from the Youngest Toba Tuff revealed by age and compositional heterogeneity in the last increment of accessory phase growth. Contrib Mineral Petrol 174, 31. https://doi.org/10.1007/s00410-019-1566-6

Vermeesch, P., 2018. IsoplotR: A free and open toolbox for geochronology. Geoscience Frontiers, SPECIAL ISSUE: Frontiers in geoscience:A tribute to Prof. Xuanxue Mo 9, 1479–1493. https://doi.org/10.1016/j.gsf.2018.04.001

Zimmerer, M.J., Lafferty, J., Coble, M.A., 2016. The eruptive and magmatic history of the youngest pulse of volcanism at the Valles caldera: Implications for successfully dating late Quaternary eruptions. Journal of Volcanology and Geothermal Research 310, 50–57. https://doi.org/10.1016/j.jvolgeores.2015.11.021

Zou, H., Fan, Q., Schmitt, A.K., Sui, J., 2010. U–Th dating of zircons from Holocene potassic andesites (Maanshan volcano, Tengchong, SE Tibetan Plateau) by depth profiling: Time scales and nature of magma storage. Lithos 118, 202–210. https://doi.org/10.1016/j.lithos.2010.05.001

3.9 Author contributions

Ruby C. Marsden: Methodology (lead), Software (lead), Validation, Formal analysis, Investigation, Data Curation, Writing – Original Draft, Visualisation
Christopher L. Kirkland: Methodology, Investigation, Writing - Review & Editing
Martin Danišík: Conceptualisation, Writing - Review & Editing, Supervision, Funding acquisition
Matthew L. Daggitt: Methodology, Software, Formal analysis, Writing - Review & Editing, Visualisation
Ung-San Ahn: Resources
Bjarne Friedrichs: Methodology, Writing - Review & Editing
Noreen J. Evans: Writing - Review & Editing

3.10 Appendices

Supplementary Material I

Eliminating outliers via medcouple

Outlier range calculation

Given a set of counts, X, it is routine to eliminate outliers due to high instrument variability (Ludwig, 2009). Traditionally for a non-skewed distribution outliers are defined as being outside the following range:

$$\text{Outlier range} = [Q1 - 1.5 \times IQR, Q3 + 1.5 \times IQR] \tag{3.10}$$

where $Q1$ and $Q3$ are the first and third quartiles of X respectively and $IQR = Q3 - Q1$ is the interquartile range.

However, the mass peak counts measured by the SHRIMP are assumed to follow a Poisson(λ) distribution. This means the distributions for mass peaks with a small value of λ are heavily positively skewed. Therefore an alternative method is required to calculate the outlier range.

An alternative method for calculating outlier ranges for skewed distributions is described by (Hubert and Van der Veeken, 2008). This method modifies the IQR using an extra factor named the medcouple, $MC(X)$, which captures the skew of the data.

The medcouple is calculated as follows. Firstly, the set X is split into two sets, X^- and X^+, which contain the values smaller and larger than the median of X respectively. Next, the medcouple set, H, is defined as:

$$H = \left\{ \frac{(x^+ - \text{median}(X)) - (\text{median}(X) - x^-)}{x^+ - x^-} \;\middle|\; x^- \in X^-, \, x^+ \in X^+ \right\} \tag{3.11}$$

Finally, the medcouple is defined as:

$$MC(X) = \text{median}(H) \tag{3.12}$$

For a skewed distribution outliers are defined using the following equations:

$$\text{Outlier range} = \begin{cases} [Q1 - 1.5e^{-4MC} \times IQR, Q3 + 1.5e^{3MC} \times IQR] & \text{if } MC(X) > 0 \\ [Q1 - 1.5e^{-3MC} \times IQR, Q3 + 1.5e^{4MC} \times IQR] & \text{otherwise} \end{cases}$$

$$\tag{3.13}$$

Note that if $MC(X) = 0$ the outlier range will revert to that of an unskewed distribution.

Outlier removal

Given an outlier range for the set X as calculated above the following procedure is taken. If two or fewer values like outside the outlier range these values are removed as outliers. Otherwise no values are considered to be outliers and the original set X is used.

Supplementary Material II

Background correction models

Here the mathematical models for both exponential and linear backgrounds are outlined.

Exponential background

An exponential function has the format:

$$y = ae^{bx} \tag{3.14}$$

Using two points in x, y space with known values (x_1, y_1) and (x_2, y_2) both a and b can be found for the exponential function which connects these two points.

$$y_1 = ae^{bx_1} \text{ and } y_2 = ae^{bx_2}$$

The value of b can be calculated by dividing the first equation by the second:

$$\frac{y_1}{y_2} = \frac{e^{bx_1}}{e^{bx_2}}$$
$$= e^{b(x_1 - x_2)}$$
$$\ln \frac{y_1}{y_2} = b(x_1 - x_2)$$
$$b = \frac{\ln y_1 - \ln y_2}{x_1 - x_2}$$

The value of a can then be calculated using substitution:

$$a = \frac{y_1}{e^{bx_1}}$$

Linear background

If a linear background correction is used for correcting the $^{230}\text{Th}^{16}\text{O}$ mass peak then the uncertainty is propagated as follows. The model for the background is:

$$f(x) = mx + c \tag{3.15}$$

The gradient, m and the y-intercept, c are functions of the background measurements, (x_1, y_1) and (x_2, y_2).

$$m(y_1, y_2) = \frac{y_2 - y_1}{x_2 - x_1} \tag{3.16}$$
$$c(y_1, y_2) = y_1 - m(y_1, y_2) \times x_1 \tag{3.17}$$

Supplementary Material III

Uncertainty propagation in Crayfish data reduction scheme

The general equation for the first-order propagation of uncertainty for a function $f(x, y, \ldots, z)$ where variables $x, y, \ldots z$ have associated uncertainties $\sigma_x, \sigma_y, \ldots, \sigma_z$ is as follows:

$$\sigma_f = \sqrt{\left|\frac{\partial f}{\partial x}\right|^2 \sigma_x^2 + \left|\frac{\partial f}{\partial y}\right|^2 \sigma_y^2 + \ldots + \left|\frac{\partial f}{\partial z}\right|^2 \sigma_z^2} \qquad (3.18)$$

Steps 1-3

For steps 1 - 3 in there are no uncertainties.

Step 4

Step 4 is where uncertainties are first introduced. These uncertainties are the standard deviation of the 10 'block' measurements taken per scan.

Step 5

Step 5 calculates the weighted mean of the measurements for each background AMU per spot. The uncertainty in the weighted mean is calculated as follows:

$$\sigma = \sqrt{\frac{1}{\sum_{i=1}^{n} \frac{1}{\sigma_i}}} \qquad (3.19)$$

where σ_i is the uncertainty of the ith variable in mean.

Step 6

Step 6 corrects the mass peak measurements for background. Let (x_1, y_1) be the location and measurement for background 1 and (x_2, y_2) be the location and measurement for background 2. There is assumed to be no uncertainty in the AMU values x_1 and x_2. The uncertainties σ_{y_1} and σ_{y_2} for y_1 and y_2 are calculated as described in the previous step. There are three different background models: constant, linear and exponential. All mass peaks apart from $^{230}\text{Th}^{16}\text{O}$ use a constant background model.

As the value predicted by the background model is simply subtracted from the measurement at the mass peak, the uncertainty in the final corrected value for the mass peak is:

$$\sigma = \sqrt{\sigma_m^2 + \sigma_b^2} \qquad (3.20)$$

where σ_m is the uncertainty of the mass peak measurement and σ_b is the uncertainty in the

value predicted by the background model at the mass peak. The methods for calculating σ_b for the different models are now described below.

Constant background

If a constant background correction is used then the background measurement is simply the measured value y_1 and therefore

$$\sigma_b = \sigma_{y_2} \tag{3.21}$$

Linear background

If a linear background correction is used for correcting the $^{230}\text{Th}^{16}\text{O}$ mass peak then the model for the background is:

$$f(x) = mx + c \tag{3.22}$$

where the gradient, m, and the y-intercept, c, are calculated from the background measurements (x_1, y_1) and (x_2, y_2). As there are no uncertainties on x_1 or x_2 they are assumed to be constants, only the uncertainties on y_1 and y_2 need to be taken into account:

$$m(y_1, y_2) = \frac{y_2 - y_1}{x_2 - x_1} \tag{3.23}$$

$$c(y_1, y_2) = y_1 - m(y_1, y_2) \times x_1 \tag{3.24}$$

In order to calculate the uncertainty using Equation 3.18 the partial derivatives of f must be calculated with respect to y_1 and y_2:

$$\frac{\partial m}{\partial y_1} = \frac{-1}{x_2 - x_1} \tag{3.25}$$

$$\frac{\partial m}{\partial y_2} = \frac{1}{x_2 - x_1} \tag{3.26}$$

$$\frac{\partial c}{\partial y_1} = 1 - \frac{\partial m}{\partial y_1} x_1 \tag{3.27}$$

$$\frac{\partial c}{\partial y_2} = -\frac{\partial m}{\partial y_2} x_1 \tag{3.28}$$

Using Equations 3.25 & 3.27:

$$\begin{aligned}
\frac{\partial f}{\partial y_1} &= \frac{\partial m}{\partial y_1} \times x + \frac{\partial c}{\partial y_1} \\
&= \left(\frac{-1}{x_2 - x_1}\right) \times x + \left(1 - \frac{-x_1}{x_2 - x_1}\right) \\
&= \frac{x_2 - x}{x_2 - x_1}
\end{aligned} \tag{3.29}$$

Using Equations 3.26 & 3.28

$$\frac{\partial f}{\partial y_2} = \frac{\partial m}{\partial y_2} \times x + \frac{\partial c}{\partial y_2} \qquad (3.30)$$

$$= \left(\frac{1}{x_2 - x_1}\right) \times x + \left(-\frac{x_1}{x_2 - x_1}\right)$$

$$= \frac{x - x_1}{x_2 - x_1}$$

Using the Equations 3.29 & 3.30 in Equation 3.18:

$$\sigma_b = \sqrt{\left(\frac{x_2 - x}{x_2 - x_1}\right)^2 \sigma_{y_1}^2 + \left(\frac{x - x_1}{x_2 - x_1}\right)^2 \sigma_{y_2}^2} \qquad (3.31)$$

Exponential background

If an exponential background correction is used for correcting the $^{230}\text{Th}^{16}\text{O}$ mass peak then the model for the background is:

$$f(x) = ae^{bx} \qquad (3.32)$$

where the value of a and b are calculated from the background measurements (x_1, y_1) and (x_2, y_2). Again, as there are no uncertainties on x_1 or x_2 they are assumed to be constants and only the uncertainties on y_1 and y_2 need to be taken into account. From supplementary material II:

$$b(y_1, y_2) = \frac{\ln y_1 - \ln y_2}{x_1 - x_2} \qquad (3.33)$$

$$a(y_1, y_2) = y_1 e^{-b(y_1, y_2)x_1} \qquad (3.34)$$

In order to calculate the uncertainty using Equation 3.18, the partial derivatives of f must be calculated with respect to y_1 and y_2:

$$\frac{\partial b}{\partial y_1} = \frac{1}{(x_2 - x_1)} \times \frac{\partial}{\partial y_1}(\ln(y_2) - ln(y_1)) \tag{3.35}$$

$$= \frac{1}{(x_2 - x_1)} \times \frac{-1}{y_1}$$

$$= \frac{1}{y_1(x_1 - x_2)}$$

$$\frac{\partial b}{\partial y_2} = \frac{-1}{y_2(x_1 - x_2)} \tag{3.36}$$

$$\frac{\partial a}{\partial y_1} = e^{-b(y_1,y_2)x_1} - y_1 x_1 \frac{\delta b(y_1, y_2)}{\delta y_1} e^{-b(y_1,y_2)x_1} \tag{3.37}$$

$$= e^{-b(y_1,y_2)x_1}\left(1 - \frac{x_1}{x_1 - x_2}\right)$$

$$= \frac{-x_2}{x_1 - x_2} e^{-b(y_1,y_2)x_1}$$

$$\frac{\partial a}{\partial y_2} = -y_1 \frac{\partial b}{\partial y_2} e^{-b(y_1,y_2)x_1}$$

$$= -y_1\left(\frac{-1}{y_2(x_1 - x_2)}\right) e^{-b(y_1,y_2)x_1}$$

$$= \frac{y_1}{y_2(x_1 - x_2)} e^{-b(y_1,y_2)x_1}$$

Using the product rule for differentiation, $(uv)' = u'v + v'u$, we can separate out the exponential model into several sections where:

$$u = a \qquad\qquad u' = a'$$
$$v = e^{bx} \qquad\qquad v' = b'xe^{bx}$$

Therefore for any $y \in \{y_1, y_2\}$:

$$\frac{\delta f}{\delta y} = a(y_1, y_2)x\frac{\partial b}{\partial y}e^{b(y_1,y_2)x} + \frac{\partial a}{\partial y}e^{b(y_1,y_2)x} \tag{3.38}$$

Therefore for $y = y_1$:

$$\frac{\delta f}{\delta y_1} = a(y_1, y_2)x\left(\frac{1}{y_1(x_1 - x_2)}\right)e^{b(y_1,y_2)x} + \left(\frac{-x_2}{x_1 - x_2}e^{-b(y_1,y_2)x_1}\right)e^{b(y_1,y_2)x}$$

$$= \frac{e^{b(y_1,y_2)x}}{y_1(x_1 - x_2)}\left(a(y_1, y_2)x - x_2 y_1 e^{-b(y_1,y_2)x_1}\right)$$

and similarly for $y = y_2$:

$$\frac{\partial f}{\partial y_2} = \frac{e^{b(y_1, y_2)x}}{y_2(x_2 - x_1)} \left(a(y_1, y_2)x - x_1 y_1 e^{-b(y_1, y_2)x_1} \right)$$

Using the Equations 3.29 & 3.30 in Equation 3.18:

$$\sigma_b = \sqrt{\left(\frac{\delta f}{\delta y_1} \right)^2 \sigma_{y_1}^2 + \left(\frac{\partial f}{\partial y_2} \right)^2 \sigma_{y_2}^2} \tag{3.39}$$

Step 7

Step 7 is the calculation of activity ratios from the mass peak background corrected data. For the two counts of the mass peaks values m_1 and m_2 with associated uncertainties of σ_{m_1} and σ_{m_2}, the percentage background corrected uncertainties are summed in quadrature as the calculation involves division.

$$\sigma = \sqrt{\left(\frac{\sigma_{m_1}}{m_1} \right)^2 + \left(\frac{\sigma_{m_2}}{m_2} \right)^2} \tag{3.40}$$

Step 8

Step 8 uses the activity ratios for reference zircon analyses to calculate the 'standard line'. The uncertainties on this standard line are calculated following York (2004).

Step 9

Step 9 calculates the gradient for each two-point isochron formed from a zircon crystal and from the whole rock - this step must propagate the uncertainty in the activity ratios for the whole rock and the zircon crystals into the uncertainty on the gradient. The age for each gradient is then calculated using a logarithmic formula and the uncertainty must be propagated here as well. This calculation was combined into a single uncertainty propagation. The age formula (Schmitt, 2011) is:

$$\text{age} = \frac{-\ln \left(1 - s \left(\frac{y - w}{x - w} \right) \right)}{\lambda_{230}} \tag{3.41}$$

where s is the standard line constant, (x, y) are the activity ratios for the analysis, (w, w) are the activity ratios of the whole rock (and has the same value for both ratios) and λ_{230} is the ^{230}Th decay constant. The age function is partially derived in order to propagate

uncertainties an example of this using the chain method is outlined below:

$$\frac{\partial \text{age}}{\partial s} = \frac{\partial \text{age}}{\partial u} \times \frac{\partial u}{\partial s} \tag{3.42}$$

where:

$$u = 1 - s\left(\frac{y - w}{x - w}\right)$$

and:

$$\frac{\partial \text{age}}{\partial u} = \frac{-1}{\lambda_{230} u}$$

$$\frac{\partial u}{\partial s} = -\left(\frac{y - w}{x - w}\right)$$

therefore:

$$\frac{\partial \text{age}}{\partial s} = \frac{-1}{\lambda_{230}\left(1 - s\left(\dfrac{y - w}{x - w}\right)\right)} \times -\left(\frac{y - w}{x - w}\right)$$

$$= \frac{y - w}{\lambda_{230}(s - 1)w - sy + x}$$

The partial derivatives for the remaining variables are as follows, for λ_{230}:

$$\frac{\partial \text{age}}{\partial \lambda_{230}} = \frac{\ln\left(\dfrac{s(y - w)}{w - x} + 1\right)}{(\lambda_{230})^2} \tag{3.43}$$

$$\frac{\partial \text{age}}{\partial x} = \frac{s(y - w)}{\lambda_{230}((s - 1)w - sy + x)} \tag{3.44}$$

$$\frac{\partial \text{age}}{\partial y} = \frac{s}{\lambda_{230}((s - 1)w - sy + x)} \tag{3.45}$$

$$\frac{\partial \text{age}}{\partial w} = \frac{s(x - y)}{\lambda_{230}(w - x)((s - 1)w - sy + x)} \tag{3.46}$$

$$\frac{\partial \text{age}}{\partial s} = \frac{y - w}{\lambda_{230}(s - 1)w - sy + x} \tag{3.47}$$

The uncertainty for the scan age is then calculated as in Equation 3.18.

Step 10

In step 10 the ages calculated for each scan are averaged to a spot age using a weighted mean and the uncertainty is calculated as in Equation 3.19.

Supplementary Material IV
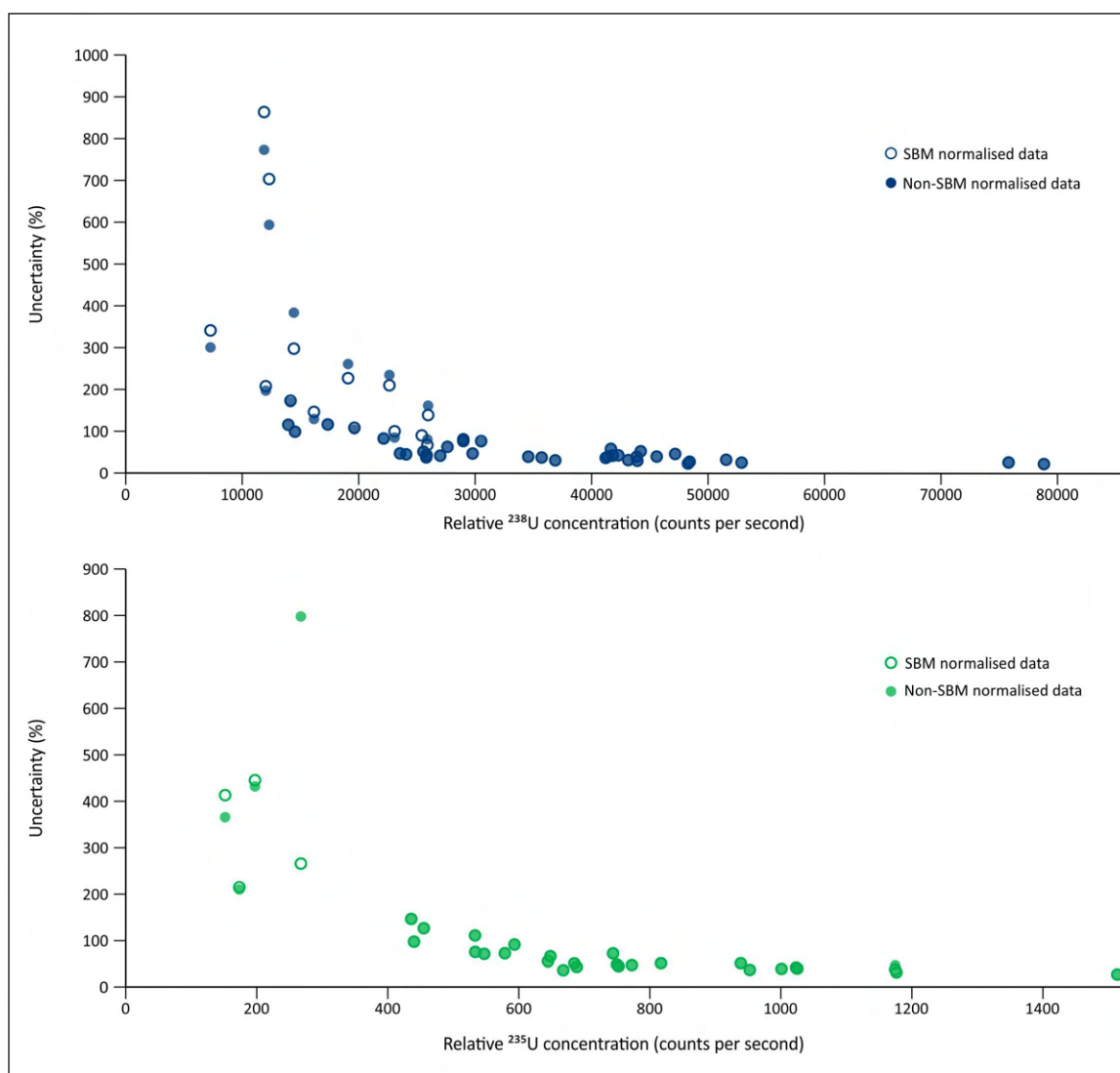
Figure 3.i: Uncertainty against relative U concentration for all data both with and without SBM normalisation for a) the low intensity primary beam session (blue) and b) the high intensity primary beam session (green).

Supplementary Material V
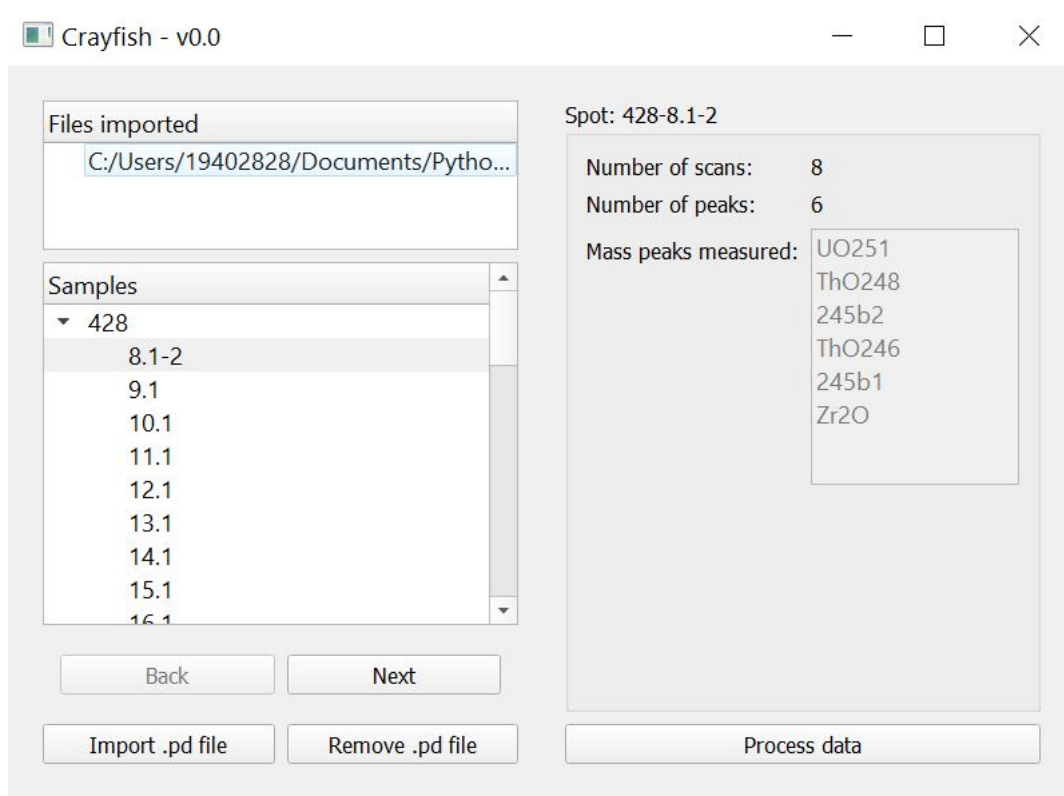
Figure 3.ii: Screenshot of Crayfish computer program file selection window
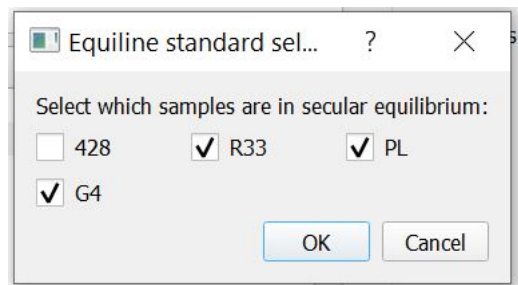
Figure 3.iii: Screenshot of Crayfish computer program secular equilibrium reference material selection window
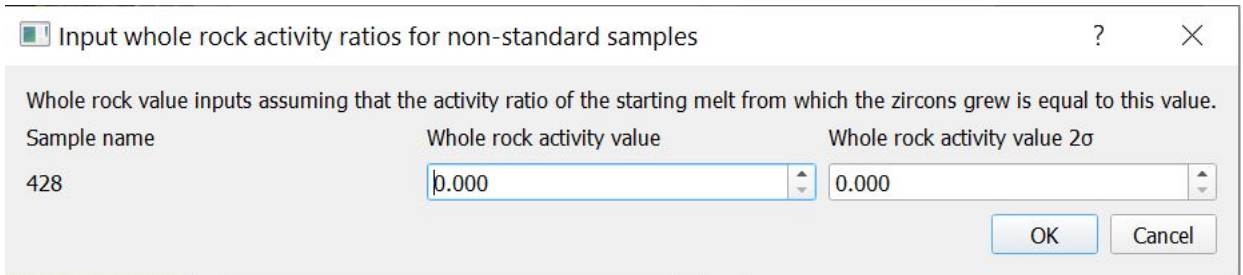
Figure 3.iv: Screenshot of Crayfish computer program whole rock activity value input window
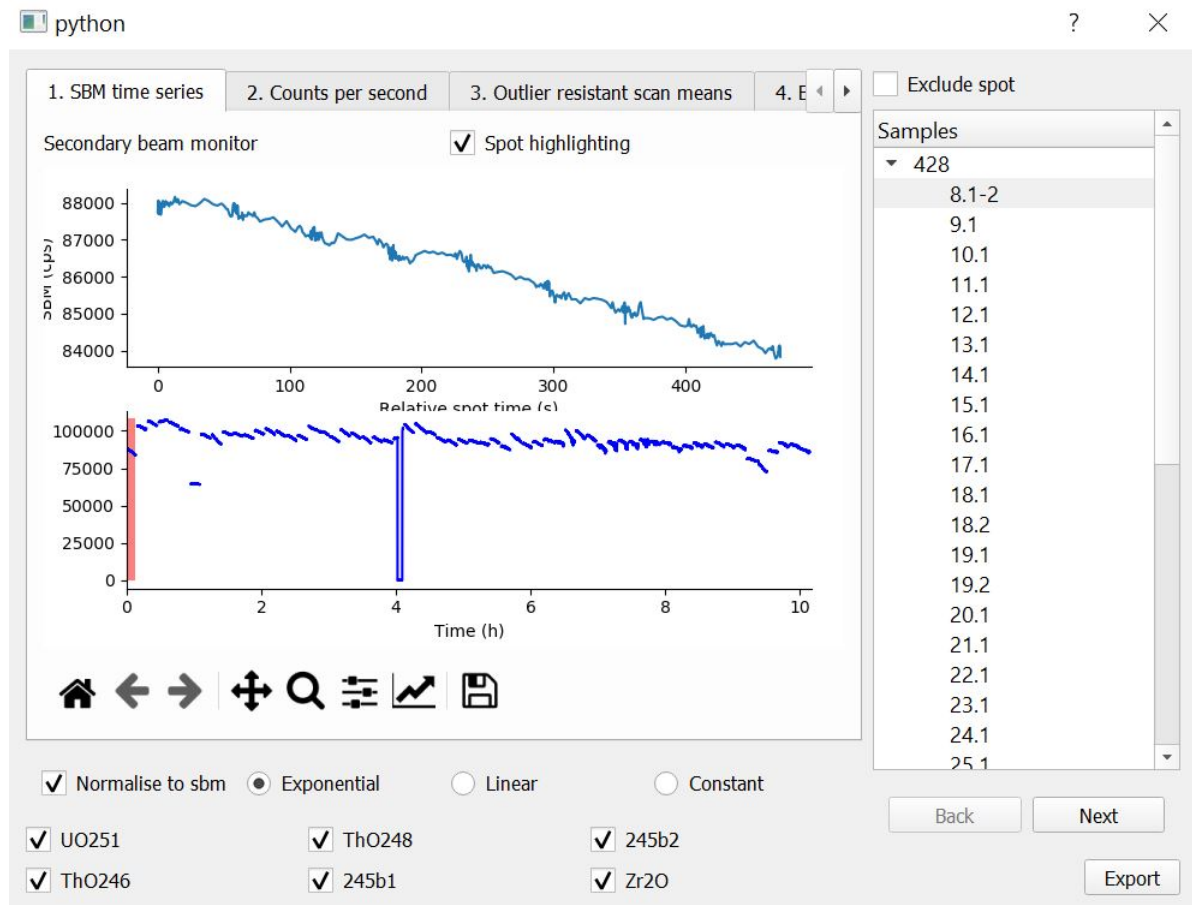
Figure 3.v: Screenshot of Crayfish computer program main data reduction process window SBM tab.
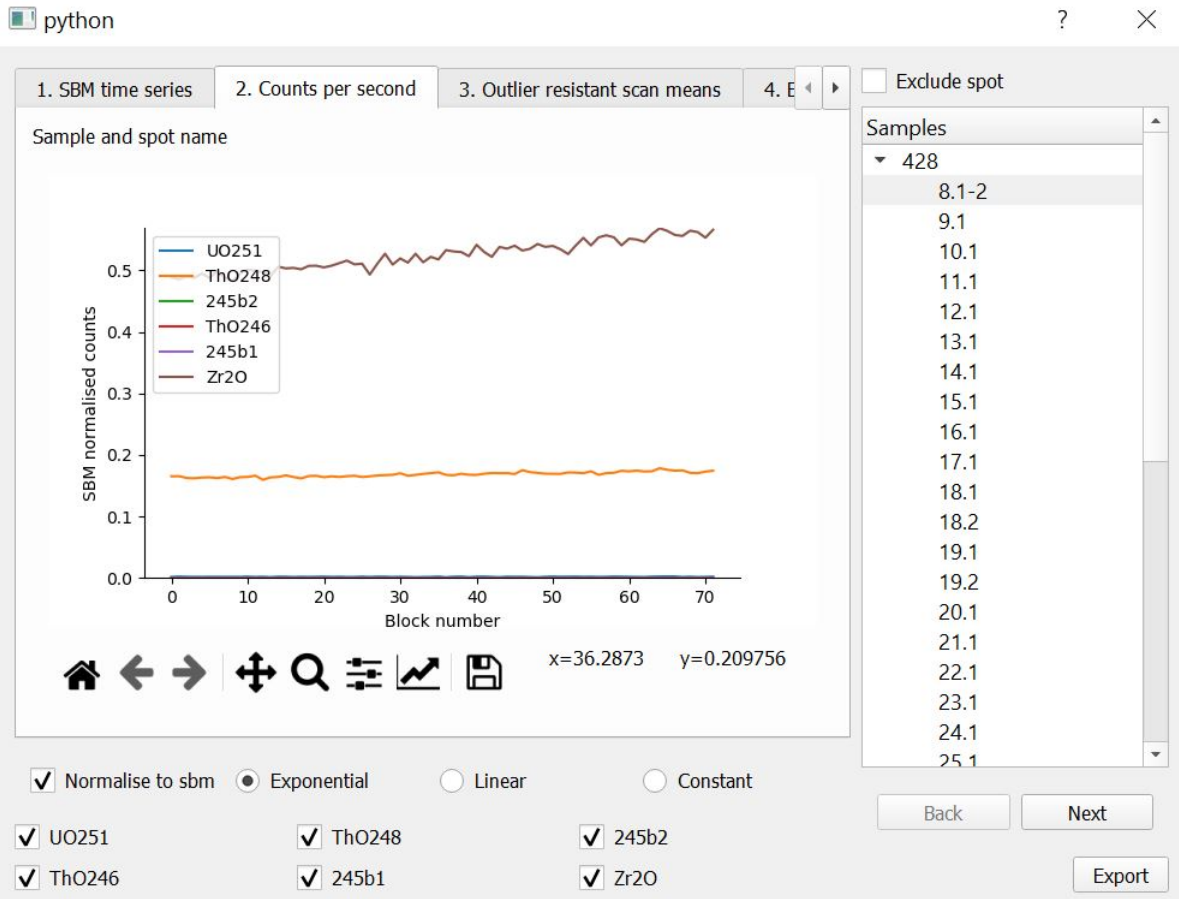
Figure 3.vi: Screenshot of Crayfish computer program main data reduction process window counts per second tab.
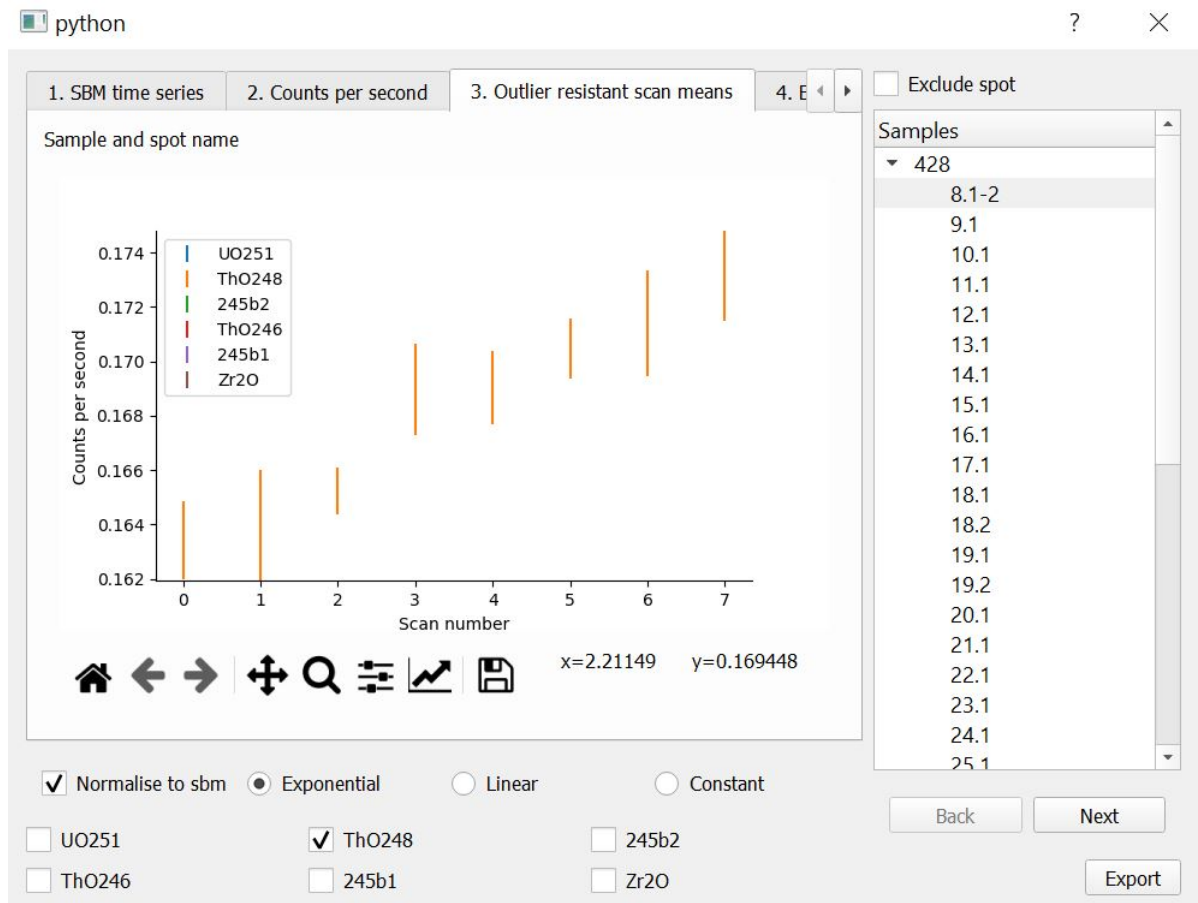
Figure 3.vii: Screenshot of Crayfish computer program main data reduction process window outlier resistant mean tab.
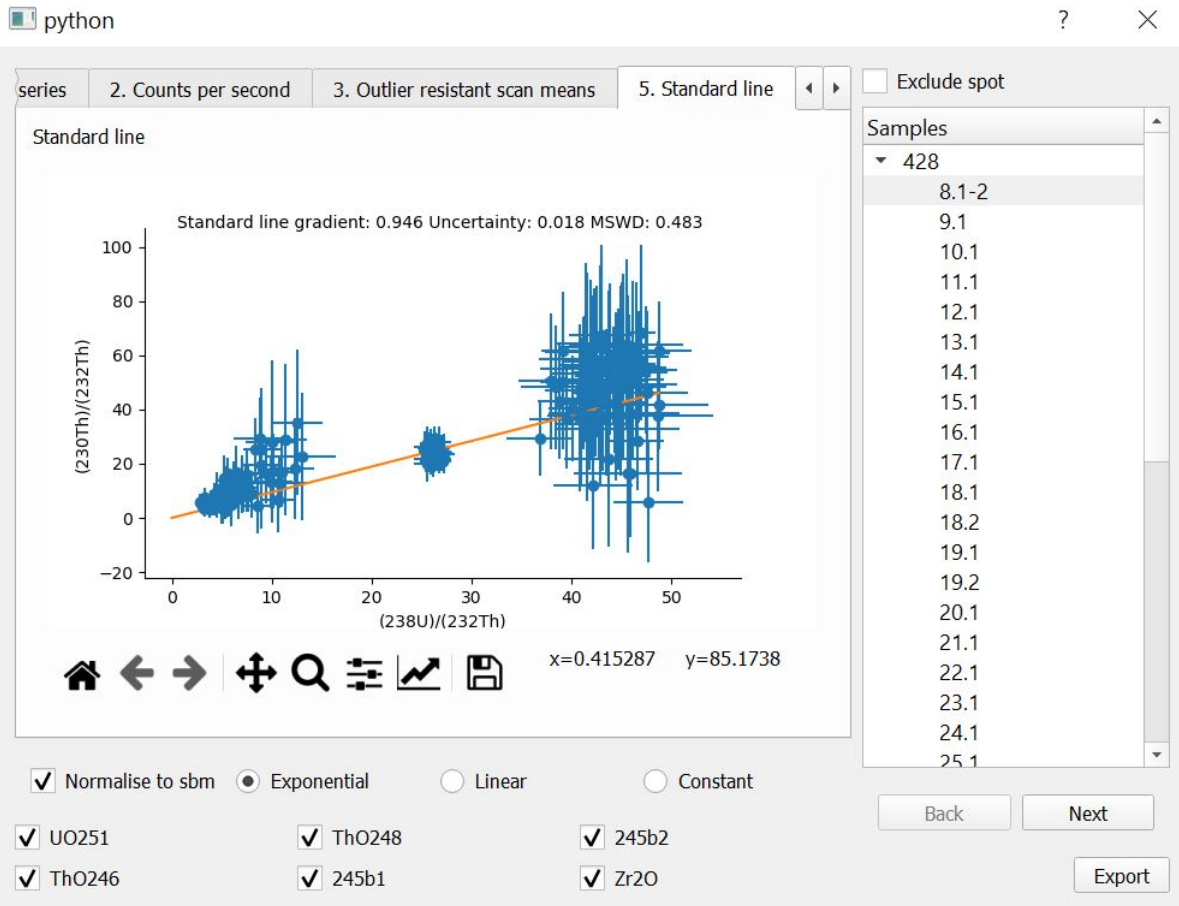
Figure 3.viii: Screenshot of Crayfish computer program main data reduction process window reference material equiline plot tab.
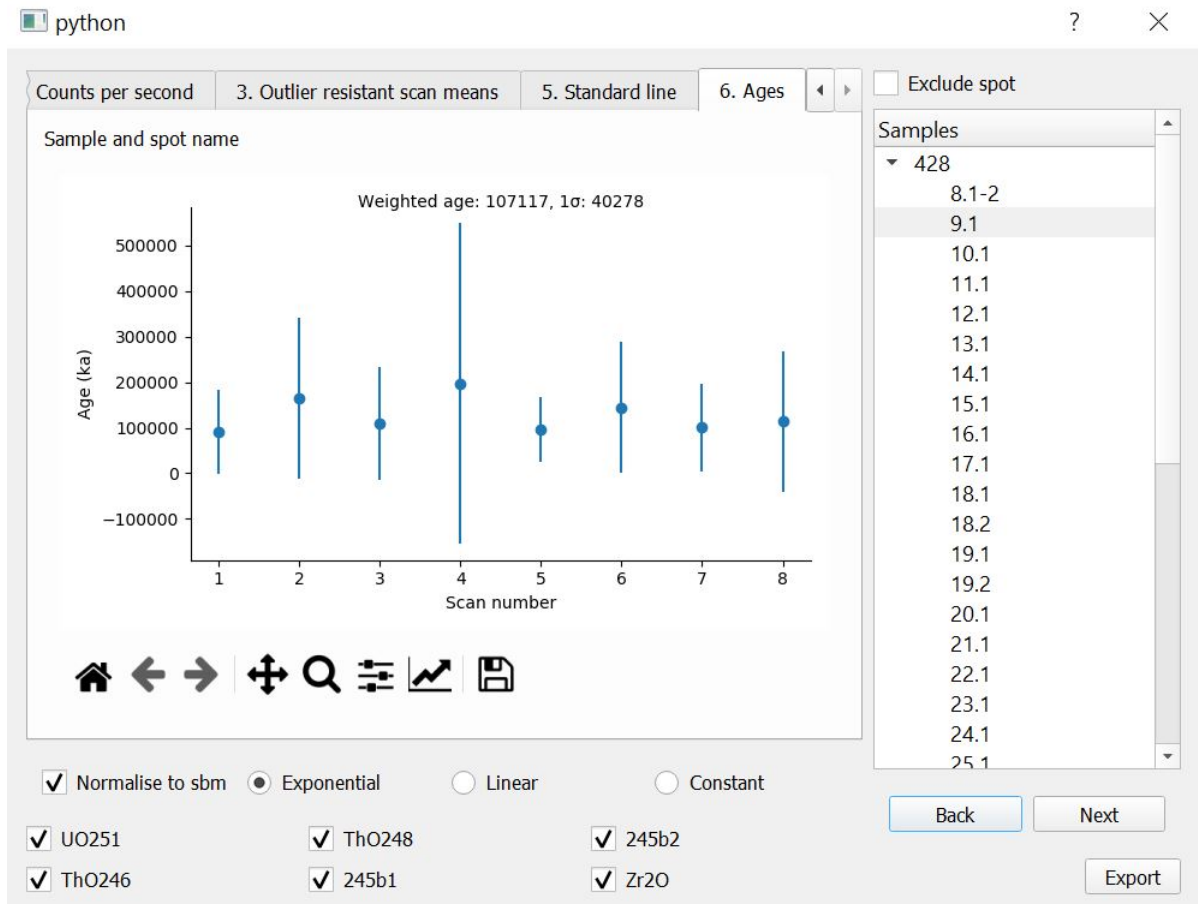
Figure 3.ix: Screenshot of Crayfish computer program main data reduction process window age results tab.

Supplementary Material VI

High intensity primary beam

Sample name	Age (years)	Uncertainty (1σ)
428-8.1-2	96840	167242
428-9.1	115801	41197
428-10.1	91071	28701
428-11.1	154139	74992
428-12.1	157710	77541
428-13.1	331793	2298368
428-14.1	154205	90687
428-15.1	91665	120164
428-16.1	64397	29543
428-17.1	150699	73218
428-18.1	135477	71459
428-18.2	118068	29582
428-19.1	68935	107019
428-19.2	60443	56041
428-22.1	87351	68835
428-23.1	149466	94339
428-24.1	155516	84061
428-25.1	115986	62129
428-26.1	77465	51061
428-27.1	83400	28796
428-28.1	150165	78163
428-28.2	119060	99837
428-30.1	95505	36639
428-30.2	97882	40388
428-31.1	58058	36452
428-32.1	132222	218572
428-33.1	130958	60043
428-34.1	112675	108140
428-34.2	25147	60345
428-35.1	195617	381703

Low intensity primary beam

Sample name	Age (years)	Uncertainty (1σ)
545-h.1	77709	11529
545-i.2	71844	14189
545-i.3	119416	28135
545-g.2	60378	15398
545-f.1	80067	10852
545-k.1	76656	13979
545-o.1	89665	14429
545-o.2	165041	87435
545-o.3	74337	9266
545-n.1	335754	462630
545-n.2	208871	245968
545-n.3	106413	25397

545-l.1	9693	13781
545-l.2	47404	10464
545-l.3	47642	10849
545-l.4	326451	750301
428-a.1	114478	15724
428-b.1	53237	11785
428-2.1	105868	10727
428-17.1	87433	36573
428-19.1	130949	17469
428-24.1	139615	30520
428-24.2	208445	163540
428-l.2	168121	23344
428-u1	167535	70578
428-u2.1	153607	101890
428-k.2	192943	60973
566-b.1	360784	789762
566-g.1	187053	44212
566-i.1	74528	29371
566-23.1	346944	556855
566-23.2	277895	401838
566-22.1	45076	40302
566-26.1	242101	306081
366-a.1	81392	8751
366-b.1	66001	16595
366-b.2	84855	22988
366-d.1	63342	13833
366-e.1	114853	14146
366-g.1	131762	26426
366-g.2	27155	11898
812-12.1	91633	12973
812-12.2	92173	20390
812-12.3	61835	10862
812-16.1	28761	71696
812-17.1	57667	16684
812-17.2	6650	12415
812-17.3	33777	15159

Chapter 4

SS14-28: an age reference material for zircon U-Th disequilibrium dating

Abstract

U-Th disequilibrium dating uses the ratio of the intermediate ^{230}Th daughter isotope to the ^{238}U parent isotope to date zircon crystallisation for volcanic and plutonic rocks in Pleistocene–Holocene deposits. It is frequently used to constrain the duration and rate of magma recharge in volcanic systems. While $\lesssim$350 ka zircon is not in secular equilibrium in the ^{230}Th system, the current U-Th disequilibrium methodology uses reference materials that are >350 ka. No reference material $\lesssim$350 ka has been available to validate the accuracy of the approach and ensure methods are repeatable across laboratories. This study presents zircon SS14-28 from Jeju Island (South Korea) as a suitable reference material for U-Th disequilibrium dating.

Zircon SS14-28 was analysed using two analytical approaches (SIMS and LA-ICPMS) and four instruments: CAMECA IMS 1280, ASI SHRIMP II, sector field high resolution LA-ICPMS and multi-collector LA-ICPMS, in four laboratories. These methods each individually result in isochrons gradients within uncertainty (2σ) of each other (CAMECA: 0.532 ± 0.051 (MSWD: 0.64); SF-HR-LA-ICPMS: 0.536 ± 0.054 (MSWD: 1.3); MC-LA-ICPMS: 0.533 ± 0.041 (MSWD: 0.67); SHRIMP II: 0.68 ± 0.22 (MSWD: 0.3)). The age proposed in this study is 82 ± 6 ka calculated from a combined isochron gradient of 0.529 ± 0.025 (MSWD: 0.87, n = 132).

4.1   Introduction

U-Th disequilibrium dating of zircon is used to determine the crystallisation age of both extrusive and intrusive zircon-bearing igneous rocks (e.g., Reid et al., 1997; Schmitt et al., 2010a). Due to the half-life of ^{230}Th (ca. 75,000 years; Cheng et al., 2000) this method is

well suited for dating $\lesssim$350 ka crystallisation events (Schmitt, 2011). Therefore, it is a key tool in investigating magma accumulation and recharge in Quaternary volcanic systems (Schmitt, 2011). In addition, U-Th disequilibrium dating is an integral part of 'zircon double-dating' (ZDD) – a combined geochronology approach to date the eruption age of $\lesssim$350 ka extrusive volcanic products which uses the crystallisation age of the zircon to correct for the effect of disequilibrium on the (U-Th)/He systematics (e.g. Schmitt et al., 2006, 2010, 2011; Danišík et al., 2012, 2017; Marsden et al., 2021a).

U-Th disequilibrium dating requires measurements of the activity ratios of ^{230}Th/^{232}Th and ^{238}U/^{232}Th of zircon crystals. These measurements can be carried out using both secondary ion mass spectrometry (SIMS) and laser ablation inductively coupled plasma mass spectrometry (LA-ICPMS) using a variety of instruments including large-geometry ion probes (CAMECA IMS, SHRIMP RG, SHRIMP II) multi-collector LA-ICPMS, and sector field high resolution LA-ICPMS (Reid et al., 1997; Bacon and Lowenstern, 2005; Schmitt et al., 2006; Bernal et al., 2014; Guillong et al., 2016, Marsden et al., 2021b). To determine individual model ages, these activity ratios are then used to construct a two-point isochron through the activity ratios of whole rock, glass, or coexisting minerals (e.g., Vazquez and Lidzbarski, 2012; Burgess et al., 2019; Friedrichs et al., 2020; Popa et al., 2020), whereby the gradient of the isochron defines the age of crystallisation (Reid et al., 1997). However, if a zircon crystal is in secular equilibrium (i.e., crystallisation age $\gtrsim$350 ka), the gradient of this isochron no longer defines the age. A zircon crystal in secular equilibrium will plot upon the equiline (1:1) (Kigoshi, 1967; Allegre, 1968; Condomines, 2003; Schmitt et al., 2006) (Figure 4.1).

Some researchers have tested the accuracy of different U-Th disequilibrium dating approaches by comparing results on the same material in two laboratories (e.g., Guillong et al., 2016) and by different methods (e.g., SIMS and thermal ionisation mass spectrometry; Schmitt et al., 2010b). While these investigations yielded comparable results, the approach currently lacks a reference material that is in disequilibrium ($\lesssim$350 ka), homogeneous, and available in sufficient quantity to permit a rigorous assessment of the accuracy between different laboratories. Therefore, the development of a secondary reference material is essential for strengthening the reliability of the U-Th disequilibrium dating methodology.

This paper characterises a suitable zircon reference material in disequilibrium for the U-Th disequilibrium method. The crystallisation age of this zircon was analysed in four laboratories using both SIMS and LA-ICPMS methods to evaluate the consistency of U-Th disequilibrium dating results.

4.2 U-Th disequilibrium theory

The ^{238}U decay series is a system of radioactive elements which decay by alpha or beta decay starting at ^{238}U and ending at the stable isotope ^{206}Pb. The decay chain contains a number of intermediate daughter isotopes with a variety of half-lives. Secular equilibrium is the state in which one ^{238}U atom decays and simultaneously one ^{206}Pb atom is produced from a decay. Consequently, in secular equilibrium, the activity (abundance decay rate) of all the intermediate daughter isotopes is equal to the activity of ^{238}U. Disequilibrium, therefore, means that the activity of ^{238}U does not equal the activity of the intermediate daughter isotopes within a closed system. U-Th disequilibrium dating analyses the activity of the ^{230}Th isotope compared to ^{238}U. The disequilibrium in igneous zircon crystals is caused by the different zircon/melt partition coefficients of U and Th, leading to their fractionation during crystallisation.

The extent of the disequilibrium of the U-Th system can be used to understand the age of zircon crystallisation. Figure 4.1 shows how ^{238}U/^{232}Th and ^{230}Th/^{232}Th activity ratios change during crystallisation of a mineral from the melt and then, given time, how the system reverts to secular equilibrium. It also shows how whole rock concentrations of Th and U are important for calculation of the age. The approach assumes that the whole rock composition represents the melt from which the zircon crystallised and that it is in secular equilibrium.
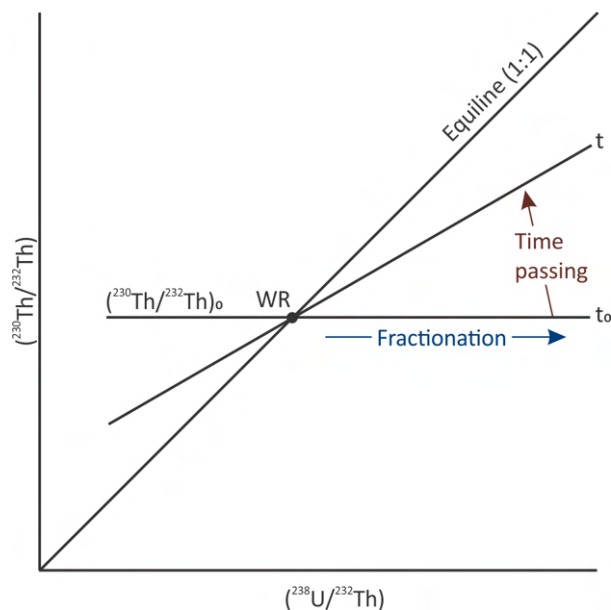
Figure 4.1: Activity ratio variation with processes for a hypothetical zircon crystal. Modified from Schmitt (2011). Arrows indicating time are schematic. WR indicates the whole rock measurements.

The measured activity values from a zircon crystal and the whole rock are then used to define a two-point isochron. The time, t, since crystallisation can be calculated using

Equation 1 where m is the isochron gradient and λ_{230} is the ^{230}Th decay constant.

$$t = \frac{ln(m-1)}{\lambda_{230}}$$

When the age of crystallisation is greater than approximately 350 ka (equivalent to ca. five half-lives of ^{230}Th) sufficient time has passed for the system to effectively having attained secular equilibrium. The current dating approach uses reference materials which are $\gg$350 ka, and thus in secular equilibrium, with their activity ratios expected to define the 1:1 equiline in (^{238}U/^{232}Th) - (^{230}Th/^{232}Th) space (Figure 4.1; Bacon and Lowenstern, 2005; Schmitt et al., 2006; Schmitt, 2011; Guillong et al., 2016; Mucek et al., 2017; Marsden et al., 2021a). Deviation of zircon measurements with crystallisation ages $\gg$ 350 ka from the equiline may indicate isotopic disturbance or, more commonly, instrumental fractionation that requires correction. If this is the case, the measured activity ratios are corrected using a factor derived from the calculated gradient of the standard line whose crystals are in secular equilibrium (e.g., Guillong et al., 2016; Friedrichs et al., 2020).

4.2.1 Challenges in measuring ^{230}Th

In secular equilibrium, because the decay constant of ^{238}U is ca. 59,000 times larger than that of ^{230}Th, for their activities to be equal the abundance of ^{230}Th must be ca. 59,000 lower than the abundance of ^{238}U. As shown in Figure 4.1 in disequilibrium, (^{230}Th) < (^{238}U) and therefore the relative abundance of ^{230}Th is even smaller in practise. This low abundance is a considerable challenge when measuring ^{230}Th (or its associated oxides).

Additional challenges occur depending on the instrumentation used. For example, use of a primary oxygen beam in SIMS causes the most abundant ^{230}Th-bearing species to be ^{230}ThO$^+$ peak. In contrast, ^{230}Th$^+$ is the most abundant ^{230}Th-bearing species in the LA-ICP-MS method because the argon plasma primarily produces atomic ions. Fully understanding possible interferences on these peaks and the required background corrections is critical, especially due to the low abundance of ^{230}Th. For example, interference correction for LA-ICPMS is affected by the ^{232}Th peak and zirconium oxides (Guillong et al., 2016). Similarly, a zirconium oxide peak interference with the ^{230}ThO peak occurs when SIMS analysis are carried out using the SHRIMP II (Marsden et al., 2021b). In constrast, when analysed on the CAMECA 1280 IMS, interferences of 232Th2CO2+ on the ^{230}ThO peak can occur (Schmitt et al., 2006). This methodological variation in U-Th disequilibrium dating introduces potential uncertainty between different procedures and it is therefore crucial that a secondary reference material for crystallisation age is developed.

4.3   Materials and methods

4.3.1   Materials

The zircon analysed in this study was separated from a trachyte sample (SS14-28) out-cropping in the Hallasan UNESCO World Heritage site on Jeju Island, South Korea (Figure 4.2a). Jeju Island is a cumulative volcanic field located 90 km south of the Korean Peninsula (Brenna et al., 2012b). The island is predominately composed of Quaternary high-Al and low-Al alkali basaltic to trachytic lava (Tatsumi et al., 2005; Brenna et al., 2012b, 2012a). The sampled outcrop is at least 15 m high and exposed for more than 30 m (Figure 4.2c). Material for analyses was collected from the base of the exposure from a section with minimal weathering. Sample SS14-28 was sampled from the same locality twice to ensure enough zircon crystals were collected; the two samples are denoted using 'a' and 'b'. Texturally, both samples are porphyritic trachytes in which millimetre size phenocrysts of K-feldspar are surrounded by a fine-grained matrix mainly composed of K-feldspar and quartz. A more detailed petrological characterisation of sample SS14-28a is provided in Supplementary material 1. Previous analytical work on SS14-28a indicates that the trachyte has an eruption age of 62 ± 6 ka (2σ) as determined by zircon double-dating (Marsden et al., 2021a).

Zircon crystals from sample SS14-28a were separated from the whole rock in the Geology Science Laboratory (South Korea) while zircon crystals from SS14-28b were separated at the John de Laeter Centre (JdLC) at Curtin University (Australia). For each kg of rock, approximately 400 zircon crystals were separated.

4.3.2   U-Th disequilibrium dating

4.3.2.1   Sample preparation for geochronology

Zircon crystals were either pressed into indium mounts for rim analysis or mounted in epoxy resin, ground to expose the interiors and then polished. This variation in mount preparation allows for both the youngest part of the crystal – the rim, and the oldest part of the crystal – the interior, to be analysed (Friedrichs et al., 2021). Additionally, prior to in situ analyses, cathodoluminescence (CL) imaging of the zircon crystals mounted in epoxy resin were acquired on a TESCAN MIRA 3 at the JdLC, Curtin University (Perth, Australia). Rim analyses were performed on the CAMECA IMS 1280 SIMS at the Heidelberg Ion Probe (HIP) Laboratory (Heidelberg, Germany). Interior analyses were undertaken on four instruments across four laboratories: CAMECA IMS 1280 SIMS (Heidelberg), SHRIMP II (JdLC), sector field high resolution (SF-HR) LA-ICPMS (ETH Zurich) and multi-collector (MC) LA-ICPMS (GeoHistory Facility, JdLC).
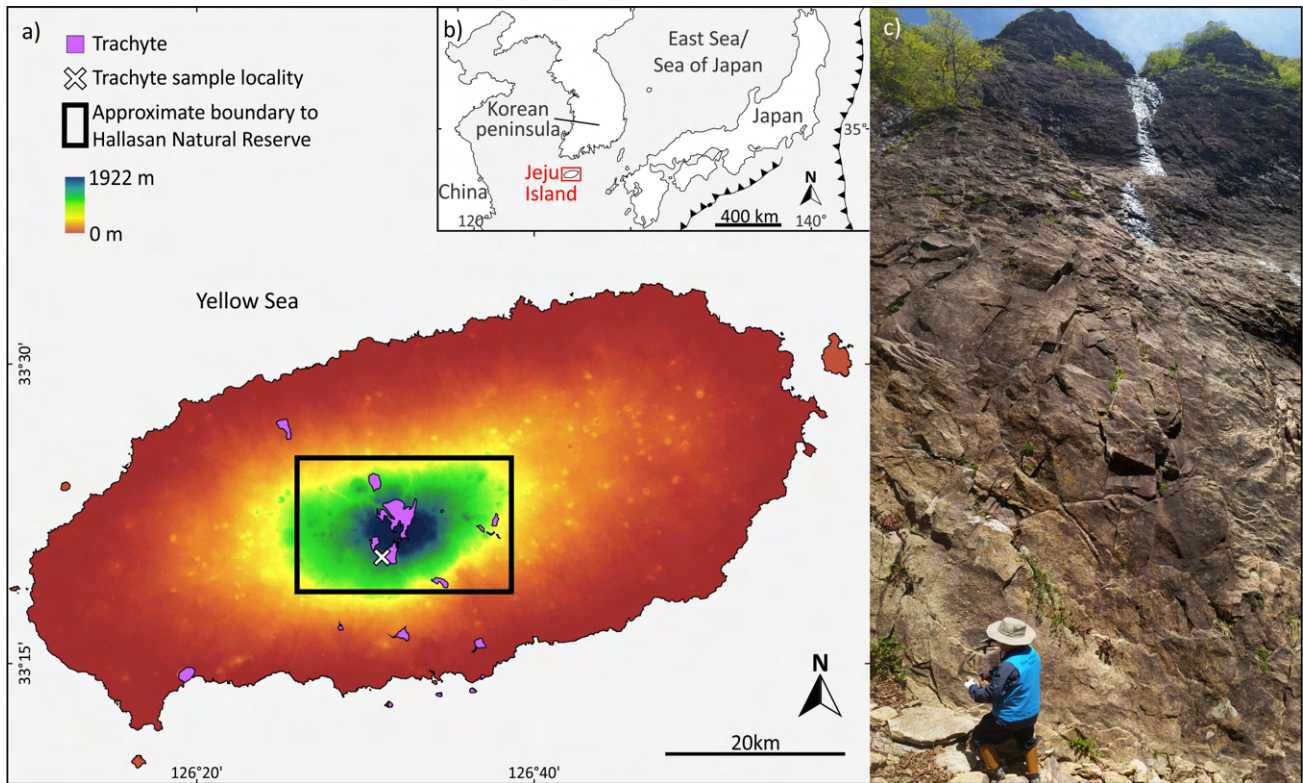
Figure 4.2: a) Digital elevation model (DEM) of Jeju Island, trachyte and boundary of the Hallasan Natural Reserve indicated (modified from Marsden et al., 2021a) b) inset shows Jeju Island geological location c) SS14-28 field locality.

4.3.2.2 U-Th disequilibrium dating using the CAMECA IMS 1280

As reported in Marsden et al. (2021a), the CAMECA 1280-HR instrument at the HIP Laboratory was utilised for U-Th disequilibrium dating of SS14-28a zircon following the procedure described in Schmitt et al. (2006, 2011) and Schmitt (2011) with the background correction described in Friedrichs et al. (2020). A 40 nA O^- primary beam defined by a 40 μm Kohler aperture was used to ionise the sample. Mass resolution was ca. 4800. The 91500 zircon (Wiedenbeck et al., 1995) was used for calibration and as a relative sensitivity standard for U abundance. AS3 zircon (Paces and Miller, 1993) was used as a secular equilibrium standard with a measured $(^{230}Th)/(^{238}U)$ ratio of 1.014 ± 0.006 (2σ, MSWD = 0.86, n = 119), and all activity ratios were standardised using this value. Data reduction was undertaken using the ZIPS 3.1.1 software and an in-house excel spreadsheet.

4.3.2.3 U-Th disequilibrium dating using SHRIMP II

As reported in Marsden et al. (2021b) SS14-28 zircons were measured using the SHRIMP II in the JdLC, Curtin University. The set of analyses were completed using a 6 nA primary beam. This primary beam was focussed through a 200 μm Kohler aperture onto the sample. Mass resolution was ca. 5000. Reference secular equilibrium zircons came

from reference materials GJ-1 (Jackson et al., 2004), Plešovice (Sláma et al., 2008), R33 (Black et al., 2004) and from sample G4 (Nasdala et al., 2004). Data was reduced using the Crayfish program (Marsden et al., 2021b), developed to manage complex background corrections and mass peaks were cycled in reverse mass order to conventional U-Th-Pb geochronology for ^{230}Th disequilibrium dating.

4.3.2.4 U-Th disequilibrium dating using sector field high resolution LA-ICPMS

U-Th disequilibrium dating using SF-HR-LA-ICPMS in pseudo-high resolution mode was conducted at ETH Zurich and followed the procedure of Guillong et al. (2016). Samples were ablated with a Resonetics RESOlution S155 laser ablation system which ablated spots of a diameter of 29 μm using a repetition rate of 5 Hz and a fluence of 2.5 Jcm^{-2}. Each ablation had a duration of 40 s and a gas blank was carried out for 30 s prior to each ablation. The isotopes were then measured on a Thermo Element XR sector-field mass spectrometer. Derivation of blank-corrected activity ratios and uncertainties utilised the SILLS software (Guillong et al., 2008). Correction for zirconium oxide (Zr2O3+) interferences on ^{230}Th, the abundance sensitivity effect of ^{232}Th on ^{230}Th and the relative sensitivity factor were carried out using in-house Excel spreadsheet following the procedure described in Guillong et al. (2016). The secular equilibrium reference materials, including 91500 (Wiedenbeck et al., 1995), G4 (Nasdala et al., 2004), GJ-1 (Jackson et al., 2004), GHR1 (Eddy et al., 2019), Fish Canyon Tuff (Schmitz and Bowring, 2001), RAK-17 (Webb et al., 2020) and Plešovice zircon (Sláma et al., 2008), were measured throughout the session and treated as unknowns during data processing. Verification of the accuracy of the measurements was undertaken by ensuring the activity ratios of these reference materials fell on the 1:1 line indicating secular equilibrium.

4.3.2.5 U-Th disequilibrium dating using multi-collector LA-ICPMS

Zircon U–Th isotopic analyses on a MC-LA-ICP-MS were carried out at Geohistory Facility in the JdLC, Curtin University. Zircon crystals were ablated using a Resonetics RESOlution SE 193nm laser, incorporating a S155 cell, coupled to a Nu Plasma II multi-collector ICPMS with a nominal resolution of ca. 300. Following two cleaning pulses and a 30 s period of background analysis, samples were spot ablated for 40 s at 5 Hz repetition rate using a 38 μm beam and laser energy at the sample surface of 2.8 J cm^{-2}. The sample cell was flushed with ultrahigh purity He (320 mL min^{-1}) and N2 (1.2 mL min^{-1}) and high purity Ar was employed as the plasma carrier gas. Signal intensities were measured simultaneously with Faraday collectors (^{232}Th, ^{235}U, ^{238}U) and ion counters (229 background (m/z), ^{230}Th, 231 background (m/z)). The raw data was processed for baseline subtraction and calculation of raw ratios using Iolite 3.7 running within Igor

Pro 6.37 software (Paton et al., 2011). The activity ratios were calculated using the decay constants proposed by Jaffey et al. (1971) for ^{238}U, Le Roux and Glendenin, (1963) for ^{232}Th; and Cheng et al. (2000) for ^{230}Th. These decay constants were chosen to maintain consistency across all techniques. Further data reduction was performed using an in-house Excel spreadsheet. Standard reference zircons 91500 (Wiedenbeck et al., 1995), GJ-1 (Jackson et al., 2004), Plešovice (Sláma et al., 2008), and R33 (Black et al., 2004) were interspersed with the samples in each session. These standards were expected to be in secular equilibrium (Schmitt, 2011) and were used to correct samples for abundance sensitivity, instrumental drift and mass bias, and relative sensitivity.

Data uncorrected for Th/U relative sensitivity was plotted in Isoplot 3.75 (Ludwig, 2012). Reference materials in secular equilibrium yielded a slope of 0.7183 (MSWD = 0.57, n = 69). The factor by which the (^{238}U/^{232}Th) ratio was multiplied to correct these reference materials to the equiline, was used to correct all data for Th/U relative sensitivity. Zirconium oxide interferences on the 230 mass/charge were assumed common to all zircon crystals measured and corrected for within the standard correction. Further data reduction was, however, necessary due to the ^{232}Th low energy tail interfering on the ^{230}Th mass. In this case, a simple background correction was performed by subtracting the measurement taken at mass 229 from the 230 measurement. This background correction is believed sufficient for this data due to the resultant background corrected activity ratios being within uncertainty of activity ratios calculated using a linear model of background (which would over-estimate a low energy tail) modelled using the mass 231 and the mass 229 measurements.

For all four instruments, model U-Th disequilibrium ages were calculated for each individual analysis. Model ages were either calculated using a two-point isochron with whole rock Th and U activity values or as isochrons for the whole sample plotted using Isoplot 3.75 (Ludwig, 2012) without using whole rock values.

4.3.3 Pit volume measurements

Secondary electron images of laser ablation pits and SHRIMP II sputtering craters were taken using a TESCAN VEGA3 SEM (JdLC). Subsequently, a Zeta 20 optical profiler was employed to measure the 3D topography and volume laser ablation pits from MC- and SF-HR-LA-ICPMS and sputtering craters from the CAMECA 1280 IMS and the SHRIMP II. The pit volume was calculated from the topography measurements using ProfilmOnline software (ProfilmOnline, 2021).

4.3.4 Whole rock trace elements and petrology

Whole rock chemistry was obtained by solution ICPMS at Labwest Minerals Analysis Pty Ltd (Perth). This analysis was carried out on pulverised samples dissolved using a proprietary methodology which includes microwave-assisted digestion in sealed Teflon pressure vessels at high pressure ($\sim$20 bar) and temperature ($\sim$180 °C) in a solution containing HNO3, HCl and HF. Isotope abundances were analysed on a Perking Elmer NexION 300Q ICPMS using external calibration (Danišík et al., 2020). The elements measured are as follows: Ag, Al, As, Ba, Be, Bi, Ca, Cd, Ce, Co, Cr, Cs, Cu, Dy, Er, Eu, Fe, Ga, Gd, Ge, Hf, Hg, Ho, In, K, La, Li, Lu, Mg, Mn, Mo, Na, Nb, Nd, Ni, P, Pb, Pr, Rb, Re, S, Sb, Sc, Se, Sm, Sn, Sr, Ta, Tb, Te, Th, Ti, Tl, Tm, U, V, W, Y, Yb, Zn, Zr. However, only the REEs (La, Ce, Pr, Nd, Sm, Eu, Gd, Tb, Dy, Ho, Er, Tm, Yb, Lu) and U and Th abundances were utilised in this study.

A 30 μm-thick thin section was prepared from representative part of SS14-28a by Minerex Services Ltd, Esperance, Western Australia. Transmitted light microscopy images in plane and polarised light were taken using a Zeiss Axio Imager 2 in the School of Earth and Planetary Sciences (EPS), Curtin University. The thin section was subsequently carbon coated and analysed using a TESCAN Integrated Mineral Analyser (TIMA) at the JdLC, Curtin University, to aid in mineral identification. A TIMA (a field emission gun scanning electron microscopy) is equipped with four electron dispersive X-ray spectrometers (EDS), capable of recording 420k X-ray counts per second. The thin section was analysed in 'dot-mapping' mode with a rectangular mesh at a step-size of 3 μm for backscattered electron (BSE) imaging. One thousand EDS counts are collected every 9th step (i.e., 27 μm) or when the BSE contrast changes (i.e., a change in mineral phase). For a given mineral grain, EDS counts are integrated across the entire grain. TIMA analyses used an accelerating voltage of 25 kV, a beam intensity of 18.78, a probe current of 5.31 nA, a spot size of 74 nm and a nominal working distance of 15 mm. After imaging and EDS collection, BSE signals and EDS peaks are referenced to a mineral library for automatic mineral classification.

4.3.5 Trace element analysis

Trace element data collection was performed using LA-ICPMS at the GeoHistory Facility in the JdLC, Curtin University, Perth, Australia. Individual zircon grains (mounted and polished in 1" epoxy rounds) were ablated using a Resonetics RESOlution M-50A-LR, incorporating a Compex 102 excimer laser. Following a 30 s period of background analysis, samples were spot ablated for 30 s at a 7 Hz repetition rate using a 30 μm beam and laser energy of 2.0 J cm^{-2}. The sample cell was flushed by ultrahigh purity He (320 mL min-1) and N2 (1.2 mL min-1). Isotopic intensities were measured using an Agilent 8900

QQQ ICP-MS, with high purity Ar as the plasma gas (flow rate 1 L min-1). The following isotopes were monitored for 0.01–0.02 s each: ^{29}Si, ^{44}Ca, ^{49}Ti, ^{89}Y, ^{91}Zr, ^{139}La, ^{140}Ce, ^{141}Pr, ^{146}Nd, ^{147}Sm, ^{153}Eu, ^{157}Gd, ^{159}Tb, ^{163}Dy, ^{165}Ho, ^{166}Er, ^{169}Tm, ^{173}Yb, ^{175}Lu, ^{178}Hf, ^{208}Pb, ^{232}Th, and ^{238}U. Zircon standard GJ-1 (Liu et al., 2010) was used as the primary standard to calculate elemental concentrations for most elements (^{91}Zr as the internal reference element, 43.14% Zr assumed in unknowns), with NIST 610 used as the primary reference material for Zr and Ca (^{29}Si reference isotope assuming 14.76% Si in unknowns). During the time-resolved analysis, short time duration spikes resulting from inclusions and compositional zoning were monitored and only the relevant part of the signal was integrated. The trace element results for NIST 612 (secondary standard) using NIST 610 as the reference material and assuming 33.7% Si, indicate that the accuracy was better than 3% for all isotopes. The time-resolved mass spectra were reduced using the 'Trace Elements' data reduction scheme in Iolite3.7 (Paton et al., 2011).

4.4 Results

4.4.1 Grain morphology and internal texture

Zircon grains are heterogeneous in shape, ranging from euhedral tetrahedrons with bipyramidal terminations to crystals which have had one or both terminations removed. The size of crystals ranges from 60 μm to 100 μm in width and from 60 μm to 200 μm in length. In crystals where both terminations are preserved, the width- to length-ratio ranges from approximately 1.7 to 2.5. Under plane polarised light microscopy needle-like inclusions can be observed. These inclusions, here interpreted as apatite, take up a minor volume ($\ll 0.1\%$) of the crystal. Oscillatory zoning patters are commonly observed varying from high levels of zonation to more homogeneous textural zoning (Figure 4.i). Over 90% of crystals show evidence of a magmatic overgrowth, with some showing potential resorption patterns.

4.4.2 U-Th disequilibrium age data

The data produced from all four instruments from zircon SS14-28 were plotted as (^{230}Th/^{232}Th) - (^{238}U/^{232}Th) isochrons (Figure 4.3) and in rank order plots of U-Th disequilibrium age (Figure 4.4). All results are tabulated in Supplementary Material 2. All uncertainties are reported at the 2σ level.

CAMECA IMS 1280 (HIP) – The age data previously calculated from two-point isochrons utilising whole rock and individual zircon activity ratios range from 71.8 $\pm$ 22.8 ka to 130.9 $\pm$ 69.4 ka (Marsden et al., 2021a) and the ages have weighted mean of 92.0 $\pm$ 3.3 ka (MSWD = 0.62). The gradient for the isochron defined by the data in activity ratio

space was calculated as 0.532 ± 0.051 (MSWD = 0.64). U concentrations for analyses are tabulated in Supplementary Material 2.

Sector field high resolution LA-ICPMS (ETH) – The age data calculated from the two-point isochrons range from 61.1 ± 21.3 ka to 104.0 ± 37.5 ka and has a weighted mean of 85.0 ± 4.0 (MSWD = 0.50). The gradient for the isochron defined by the data in activity ratio space was calculated as 0.536 ± 0.054 (MSWD = 1.3, this lies on the acceptable range for MSWD calculated from Wendt and Carl (1991).
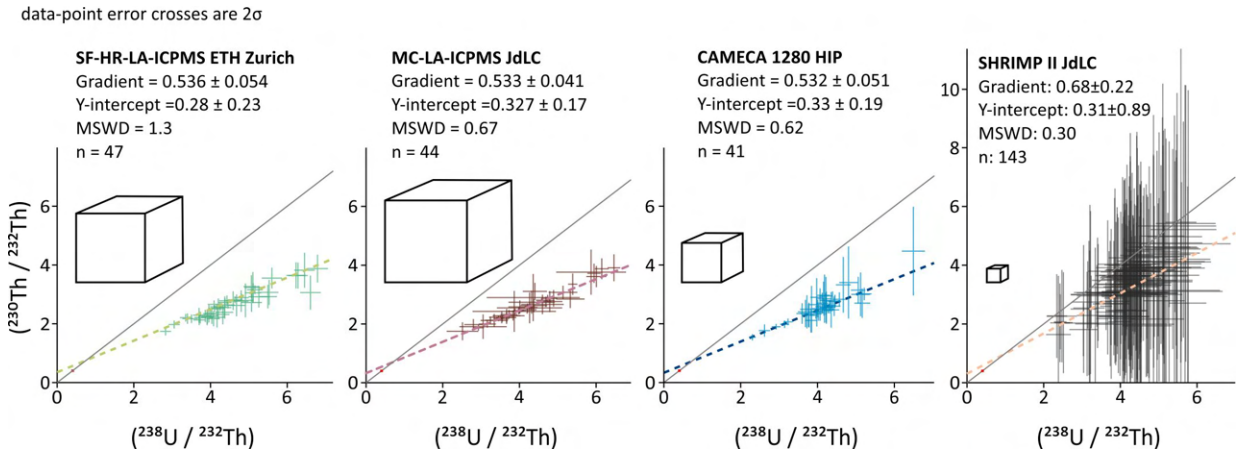
Figure 4.3: Isochrons using activity ratios for four U-Th disequilibrium techniques. The whole rock activity ratios are plotted in red. Activity ratios of SHRIMP II data are plotted per SHRIMP scan rather than per spot, this is due to variation in the method of age calculation and contributes to the increased uncertainties, furthermore, uncertainties should be considered in the context of the sample volume which are indicated using relatively sized cubes.

Multi-collector LA-ICPMS (JdLC) – The age data calculated from two-point isochrons utilising whole rock and individual zircon activity ratios range from 74.9 ± 19.3 ka to 123.2 ± 40.6 ka and has a weighted mean of 92.0 ± 3.6 ka (MSWD = 0.31, n = 44). The gradient for the isochron defined by the data in activity ratio space was calculated as 0.533 ± 0.041 (MSWD = 0.67, n = 44).

SHRIMP II (JdLC) – The age data calculated from two-point isochrons utilising whole rock and individual zircon activity ratios range from 25 ± 121 to 158 ± 155 ka and has a weighted mean of 95.9 ± 9.6 ka (MSWD = 0.33, n = 30) from Marsden et al. (2021b). The gradient for the isochron defined by the data in activity ratio space was calculated as 0.68 ± 0.22 (MSWD = 0.3, n = 143).

4.4.3 Pit volume results, whole rock U and Th activity ratios and petrology

Pit volumes were measured for all analyses made in this paper and mean pit volumes for SHRIMP, CAMECA, SF-HR LA-ICPMS and MC LA-ICPMS spots are as follows: 665.0
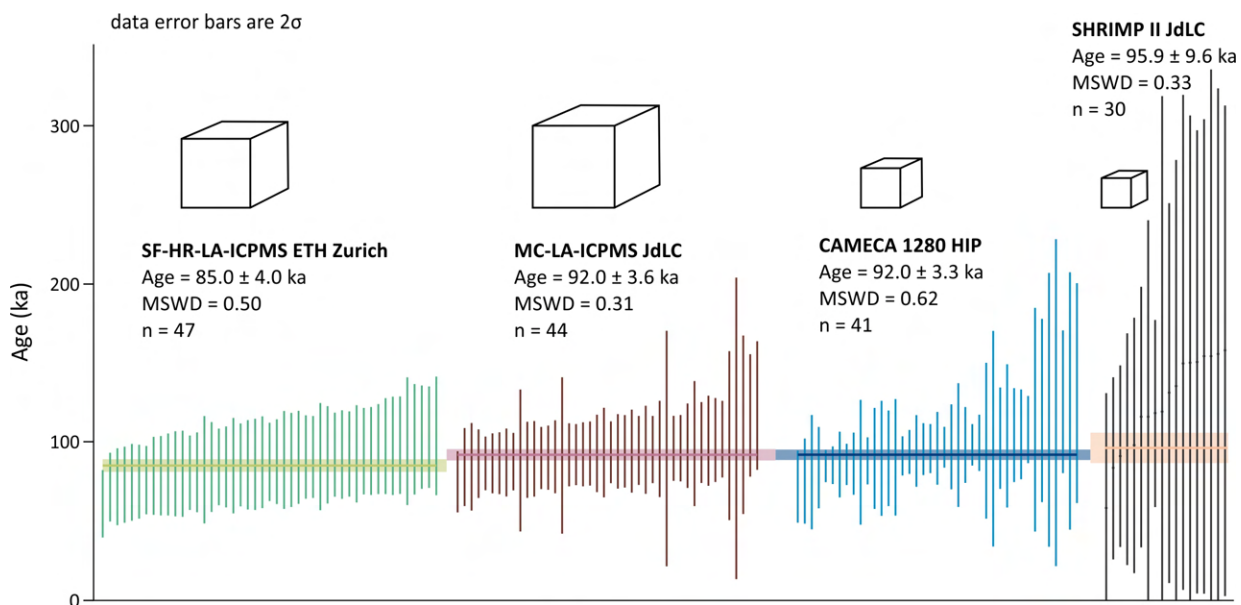
Figure 4.4: Model U-Th disequilibrium ages and their weighted mean ages and MSWDs. CAMECA 1280 data replotted from Marsden et al. (2021a). SHRIMP II data replotted from Marsden et al. (2021b). The relative volumes are indicated by cubes, with the SHRIMP II cube being larger than in Figure 4.3 because in this case as the SHRIMP age is by spot not by scan, whereas the activity measurements are taken scan by scan.

μm3 (n=4), 1631.8 μm3 (n=4), 8675.5 μm3 (n=4), and 14390.0 μm3 (n=6). The raw data is available in Supplementary Material 2.

The petrographic thin section and TIMA map of the porphyritic trachyte are provided in Supplementary Material 1. Whole rock U and Th measurements were made on whole rock samples SS14-28a and b. The (^{238}U/^{232}Th) and (^{230}Th/^{232}Th) activity ratios were calculated to be 0.404 ± 0.035 for SS14-28a and 0.437 for SS14-28b from ppm measurements of Th: 13.6, U: 1.81 (a) and Th: 14.8, U: 2.13 (b). The whole rock U and Th activity ratios were calculated from the concentration (ppm) of U and Th, assuming that the whole rock was in secular equilibrium. The activity ratios used in all further calculations are those from field session 1 to allow for comparison between session measurements.

4.4.4 Trace elements

Whole rock rare earth element (REE) and 35 individual zircon REE measurements (made on 34 crystals) are plotted on chondrite-normalised REE plots in Figure 4.ii. The full range of acquired trace element concentration are given in Supplementary Material 2. In the chondrite-normalised patterns, the majority of analysed zircon grains are characterized by low-LREE and a gradual increase from intermediate to heavy lanthanides. In seven of the single zircon grain analyses, the REE patters show higher LREE values. However, these patters correlates with analyses with high 44Ca counts and laser ablation pits which are likely to have included the needle-shaped inclusions of apatite mentioned in Section

4.1 . These mixtures are therefore not considered further. When compared with the whole rock, zircon grains show the lowest concentrations of LREE whereas enriched for middle- to heavy-REE. Both the whole rock and individual zircon REE patters are characterized by a negative Eu anomaly. The Th/U ratios for the individual zircon crystals analysed by LA-ICPMS fell in the range between 0.50 and 1.63 with a mean of 1.13 and a standard deviation of 0.27. The Th/U ratio of the whole rock was measured twice as 7.5 (SS14-28a) and 6.9 (SS14-28b).

4.5 Discussion

4.5.1 U-Th disequilibrium ages

The four methods in this study applied to trachyte samples SS14-28a and SS14-28b each result in an isochron gradient that is within uncertainty of each other (Figure 4.3). Each method also has a calculated weighted mean U-Th disequilibrium age (calculated from individual ages for each analysis), within uncertainty for all methods. This demonstrates that the U-Th disequilibrium method is repeatable across different instruments and different laboratories. The consistency of the isochron gradients implies that SS14-28 has a single crystallisation age within the uncertainty of the methods used, making it suitable as an age reference material.

Three of the four techniques employed in this study - CAMECA and both LA-ICPMS techniques - have similar uncertainties when calculating the isochron gradient (10%) and when calculating ages. While this may not be a highly precise result, it does not diminish the value of SS14-28 as a potential age reference material for U-Th disequilibrium dating as U-Th disequilibrium dating at high spatial resolution is an inherently imprecise technique due to the low levels of ^{230}Th in the zircon crystals. Indeed the multi-collector LA-ICPMS weighted age MSWD value (0.31, n = 44) indicates over-estimation of uncertainty (Wendt and Carl, 1991). SHRIMP II methods are discussed in Section 5.3.

The ages measured on the CAMECA IMS 1280 were determined on both the rim of the crystal and the interior of the crystal (Marsden et al., 2021a). The approximate U concentrations of rims ranged from 46 ppm to 1434 ppm with an average of 212 ppm over 25 measurements. The approximate U concentrations of interiors ranged from 42 ppm to 1233 ppm with an average of 467 ppm over 16 measurements. The calculated ages for these two subpopulations have weighted means within uncertainty 94.1 ± 5.6 ka (rims, MSWD = 0.59, n = 25) and 90.8 ± 4.1 ka (interiors, MSWD = 0.66, n = 16). This consistency in age, combined with U concentration heterogeneity, means that the zircon crystals from sample SS14-28 are highly suited to be a U-Th disequilibrium dating reference material.

4.5.2 Pit volumes

The homogeneous age profile of zircon crystals from sample SS14-28 is maintained regardless of the technique used to measure isotopic concentrations or the volume of analyte. LA-ICPMS often utilises a significantly higher volume of zircon than SIMS methodologies. A visual comparison of LA-ICPMS ablation pits, CAMECA IMS 1280 pits and SHRIMP II pits (Figure 4.5) shows that LA-ICPMS ablation samples more crystal volume than SIMS methods with the smallest LA-ICPMS volume (≈ 8676 μm^3) still being a factor of 5 higher than that of the CAMECA pits (≈ 1632 μm^3). The volume of the pit measured by the SHRIMP II is a factor of 2.5 smaller than the CAMECA pits and a factor of 13 smaller than the smallest LA-ICPMS pits. Regardless of the volume analysed, the SS14-28 ages remain reproducible. This indicates that the crystallisation age is homogenous across crystal scales, further supporting the results from the interior of crystals measured on the CAMECA 1280 IMS and showing that SS14-28 is a viable reference material for age regardless of the volume of crystal analysed.
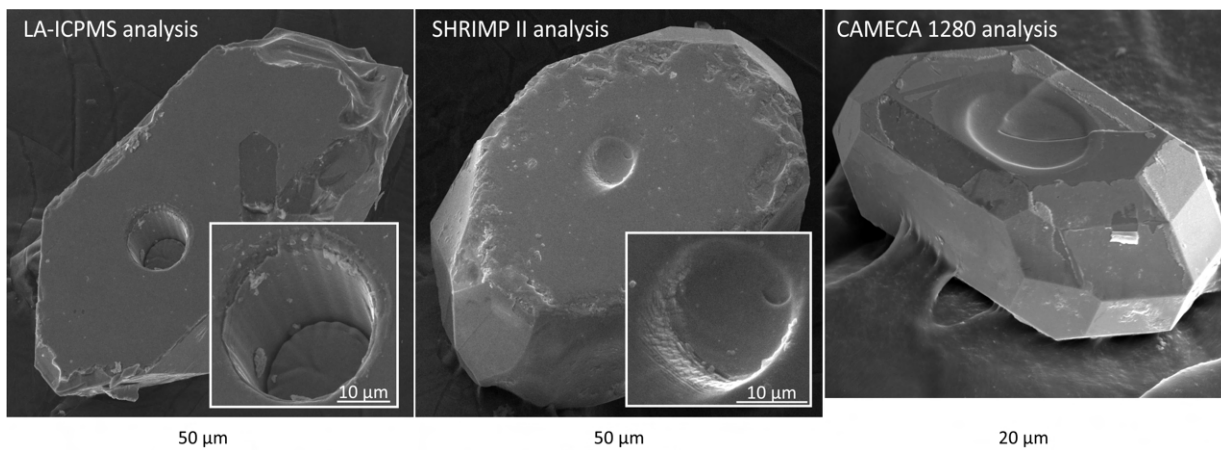
Figure 4.5: SEM images of pits in zircon crystals after U-Th disequilibrium dating analysis, insets are close-ups of pits. LA-ICPMS images are post analyses in the JdLC LA-ICPMS laboratory, ablation conditions for the SF-HR-LA-ICPMS are assumed similar to this one. The CAMECA image is from Danišík et al. (2020) which uses the same methodology as this paper.

4.5.3 SHRIMP discussion

It should be noted that despite being within uncertainty of the others, the isochron gradient calculated from the results of the SHRIMP II study of Marsden et al. (2021b) is noticeably larger than those obtained using the other methods. Marsden et al. (2021b), showed this was due to the background correction for the ^{230}ThO peak. Despite being noticeably larger, the weighted mean of the age population is within uncertainty of the other methods (Figure 4.4). Additionally, the SHRIMP II results are significantly less precise than the

other 3 methodologies with the uncertainty on ages reaching 100% in some cases. The lower primary beam used on the SHRIMP II (compared to the CAMECA) yields high uncertainty on the ^{230}ThO measurement, when corrected for background (see Marsden et al., 2021b for more detail). The extremely low pit volumes for the SHRIMP II spots reflect this lower primary beam. This means that the abundances of ^{230}Th measured were significantly lower than those measured in other methods.

4.5.4 Calculation of final isochron age

Due to the low sample volume of the SHRIMP II dating of SS14-28 and the corresponding high uncertainties, SHRIMP II data was not utilised for calculation of the 'average' isochron age. The JdLC MC-LA-ICPMS, ETH SF-HR-LA-ICPMS and CAMECA IMS 1280 activity ratios were plotted together on a single isochron (Figure 4.6) that yielded a gradient of 0.529 ± 0.025 (MSWD = 0.87, n = 132). This MSWD is consistent with a single age population meaning that no additional external uncertainty is required between techniques. The resultant crystallisation age based on the three methods is 82 ± 6 ka. This gradient and resultant crystallisation age is proposed as a representative reference age for sample SS14-28.
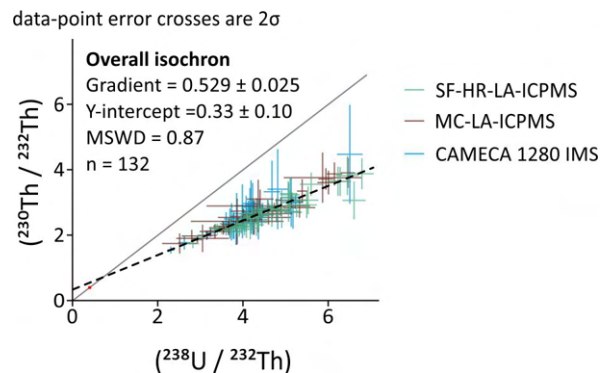
Figure 4.6: Overall isochron with data from different instruments indicated by colour.

4.5.5 Heterogeneity of trace elements

The heterogeneous trace element data for U and Th and REEs for the zircon crystals could be due to disequilibrium growth, perhaps as imaged in the oscillatory zoning of the zircon crystals (Watson, 1996; Hoksin, 2000). The patterns for individual analyses follow a typical igneous zircon REE profile. A positive slope from La (which is under the limit of detection) to Lu with a positive Ce anomaly and a negative Eu anomaly. Similar patterns are reported by for example: Nagasawa (1970) and Heaman et al. (1990). Additionally, the negative Eu anomaly indicates that feldspar crystallised before zircon in the melt (Schnetzler and Philpotts, 1970; Hoskin and Schaltegger, 2003; Claiborne et al.,

2006; Rollinson and Pease, 2021). This is consistent with the observation, both in thin section and associated TIMA phase map, of feldspar phenocrysts and the feldspar rich groundmass (Figure 4.i). All of these trace element results imply typical igneous zircon crystallisation from the melt.

Zircon crystals from sample SS14-28 have heterogeneous REE, U and Th distributions. The REEs are plotted for a selection of zircon grains in Figure 4.ii. The observed range of $(^{238}U/^{232}Th)$ and $(^{230}Th/^{232}Th)$ activity ratios measured for zircons from sample SS14-28 is the result of U and Th heterogeneity. Fortuitously, this range allows an isochron to be calculated, indicative of a single crystallisation age within uncertainty. The age determined on different zones yields the same age within uncertainty, there is no correlation of $(^{238}U/^{232}Th)$ with age.

4.6   Conclusions

This paper has shown that current techniques for U-Th disequilibrium dating give the same result for sample SS14-28, in multiple laboratories, using multiple instruments that measure different volumes of material. This study proposes that the age homogeneity and U-Th concentration heterogeneity makes sample SS14-28 a suitable secondary age reference material for U-Th disequilibrium dating. The proposed isochron age for SS14-28 is 82 ± 6 ka as calculated from an isochron gradient of 0.529 ± 0.025 (MSWD = 0.87, n = 132)), about 20 kyrs older than the eruption age measured by zircon double-dating (ZDD).

Availability of samples

Crystal aliquots can be obtained by emailing the author. As the sample locality is within the Hallasan UNESCO World Heritage Site samples may not be taken from the locality without permission of the World Heritage Office, Jeju Special Self-Governing Provincial Government, Republic of Korea.

4.7   References

Allegre, C.L., 1968. ^{230}Th dating of volcanic rocks: A comment. Earth and Planetary Science Letters 5, 209-210. https://doi.org/10.1016/S0012-821X(68)80042-1

Bacon, C.R., Lowenstern, J.B., 2005. Late Pleistocene granodiorite source for recycled zircon and phenocrysts in rhyodacite lava at Crater Lake, Oregon. Earth and Planetary Science Letters 233, 277–293. https://doi.org/10.1016/j.epsl.2005.02.012

Bernal, J.P., Solari, L.A., Gómez-Tuena, A., Ortega-Obregón, C., Mori, L., Vega-González, M., Espinosa-Arbeláez, D.G., 2014. In-situ ^{230}Th/U dating of Quaternary zircons using LA-MCICPMS. Quaternary Geochronology 23, 46–55. https://doi.org/10.1016/j.quageo.2014.06.003

Black, L.P., Kamo, S.L., Allen, C.M., Davis, D.W., Aleinikoff, J.N., Valley, J.W., Mundil, R., Campbell, I.H., Korsch, R.J., Williams, I.S., Foudoulis, C., 2004. Improved 206Pb/^{238}U microprobe geochronology by the monitoring of a trace-element-related matrix effect; SHRIMP, ID–TIMS, ELA–ICP–MS and oxygen isotope documentation for a series of zircon standards. Chemical Geology 205, 115–140. https://doi.org/10.1016/j.chemgeo.2004.01.003

Brenna, M., Cronin, S.J., Smith, I.E.M., Maas, R., Sohn, Y.K., 2012a. How Small-volume Basaltic Magmatic Systems Develop: a Case Study from the Jeju Island Volcanic Field, Korea. J Petrology 53, 985–1018. https://doi.org/10.1093/petrology/egs007

Brenna, M., Cronin, S.J., Smith, I.E.M., Sohn, Y.K., Maas, R., 2012b. Spatio-temporal evolution of a dispersed magmatic system and its implications for volcano growth, Jeju Island Volcanic Field, Korea. Lithos 148, 337–352. https://doi.org/10.1016/j.lithos.2012.06.021

Burgess, S.D., Coble, M.A., Vazquez, J.A., Coombs, M.L., Wallace, K.L., 2019. On the eruption age and provenance of the Old Crow tephra. Quaternary Science Reviews 207, 64–79. https://doi.org/10.1016/j.quascirev.2018.12.026

Cheng, H., Edwards, R.L., Hoff, J., Gallup, C.D., Richards, D.A., Asmerom, Y., 2000. The half-lives of uranium-234 and thorium-230. Chemical Geology 169, 17–33. https://doi.org/10.1016/S0009-2541(99)00157-6

Claiborne, L.L., Miller, C.F., Walker, B.A., Wooden, J.L., Mazdab, F.K., Bea, F., 2006. Tracking magmatic processes through Zr/Hf ratios in rocks and Hf and Ti zoning in zircons: An example from the Spirit Mountain batholith, Nevada. Mineralogical Magazine 70, 517–543. https://doi.org/10.1180/0026461067050348

Condomines, M., Gauthier, P.-J., Sigmarsson, O., 2003. Timescales of Magma Chamber Processes and Dating of Young Volcanic Rocks. Reviews in Mineralogy and Geochemistry 52, 125-174. https://doi.org/10.2113/0520125

Danišík, M., Shane, P., Schmitt, A.K., Hogg, A., Santos, G.M., Storm, S., Evans, N.J., Keith Fifield, L., Lindsay, J.M., 2012. Re-anchoring the late Pleistocene tephrochronology of New Zealand based on concordant radiocarbon ages and combined ^{238}U/^{230}Th disequilibrium and (U–Th)/He zircon ages. Earth and Planetary Science Letters 349–350, 240–250. https://doi.org/10.1016/j.epsl.2012.06.041

Danišík, M., Schmitt, A.K., Stockli, D.F., Lovera, O.M., Dunkl, I., Evans, N.J., 2017. Application of combined U-Th-disequilibrium/U-Pb and (U-Th)/He zircon dating to tephrochronology. Quaternary Geochronology, Advancing tephrochronology as a global dating tool: applications in volcanology, archaeology, and palaeoclimatic research 40, 23–32. https://doi.org/10.1016/j.quageo.2016.07.005

Danišík, M., Lowe, D.J., Schmitt, A.K., Friedrichs, B., Hogg, A.G., Evans, N.J., 2020. Sub-millennial eruptive recurrence in the silicic Mangaone Subgroup tephra sequence, New Zealand, from Bayesian modelling of zircon double-dating and radiocarbon ages. Quaternary Science Reviews 246, 106517.
https://doi.org/10.1016/j.quascirev.2020.106517

Eddy, M.P., Ibañez-Mejia, M., Burgess, S.D., Coble, M.A., Cordani, U.G., DesOrmeau, J., Gehrels, G.E., Li, X., MacLennan, S., Pecha, M., Sato, K., Schoene, B., Valencia, V.A., Vervoort, J.D., Wang, T., 2019. GHR1 Zircon – A New Eocene Natural Reference Material for Microbeam U-Pb Geochronology and Hf Isotopic Analysis of Zircon. Geostandards and Geoanalytical Research 43, 113–132. https://doi.org/10.1111/ggr.12246

Friedrichs, B., Schmitt, A.K., McGee, L., Turner, S., 2020. U–Th whole rock data and high spatial resolution U–Th disequilibrium and U–Pb zircon ages of Mt. Erciyes and Mt. Hasan Quaternary stratovolcanic complexes (Central Anatolia). Data in Brief 29, 105113. https://doi.org/10.1016/j.dib.2020.105113

Friedrichs, B., Atıcı, G., Danišík, M., Yurteri, E., Schmitt, A.K., 2021. Sequence modeling in zircon double-dating of early Holocene Mt. Erciyes domes (Central Anatolia). Quaternary Geochronology 61, 101129. https://doi.org/10.1016/j.quageo.2020.101129

Guillong, M., Meier, D.L., Allan, M.M., Heinrich, C.A., Yardley, B.W., 2008. Appendix A6: SILLS: A MATLAB-based program for the reduction of laser ablation ICP-MS data of homogeneous materials and inclusions. Mineralogical Association of Canada Short Course 40, 328–333.

Guillong, M., Sliwinski, J.T., Schmitt, A., Forni, F., Bachmann, O., 2016. U-Th Zircon Dating by Laser Ablation Single Collector Inductively Coupled Plasma-Mass Spectrometry (LA-ICP-MS). Geostandards and Geoanalytical Research 40, 377–387. https://doi.org/10.1111/j.1751-908X.2016.00396.x

Heaman, L.M., Bowins, R., Crocket, J., 1990. The chemical composition of igneous zircon suites: implications for geochemical tracer studies. Geochimica et Cosmochimica Acta 54, 1597–1607. https://doi.org/10.1016/0016-7037(90)90394-Z

Hoskin, P.W.O., 2000. Patterns of chaos: fractal statistics and the oscillatory chemistry of zircon. Geochimica et Cosmochimica Acta 64, 1905–1923. https://doi.org/10.1016/S0016-7037(00)00330-6

Hoskin, P.W.O., Schaltegger, U., 2003. The Composition of Zircon and Igneous and Metamorphic Petrogenesis. Reviews in Mineralogy and Geochemistry 53, 27–62. https://doi.org/10.2113/0530027

Jackson, S.E., Pearson, N.J., Griffin, W.L., Belousova, E.A., 2004. The application of laser ablation-inductively coupled plasma-mass spectrometry to in situ U–Pb zircon geochronology. Chemical Geology 211, 47–69. https://doi.org/10.1016/j.chemgeo.2004.06.017

Jaffey, A.H., Flynn, K.F., Glendenin, L.E., Bentley, W.C., Essling, A.M., 1971. Precision

Measurement of Half-Lives and Specific Activities of ^{235}U and ^{238}U. Phys. Rev. C 4, 1889–1906. https://doi.org/10.1103/PhysRevC.4.1889

Kigoshi, K., 1967. Ionium Dating of Igneous Rocks. Science 156, 932-934. https://doi.org/10.1126/science.156.3777.932

Le Roux, L.J., and Glendenin, L.E., 1963. Half-life of ^{232}Th, in: Proceedings of the National Meeting on Nuclear Energy, Pretoria, South Africa. p. 94.

Liu, Y., Hu, Z., Zong, K., Gao, C., Gao, S., Xu, J., Chen, H., 2010. Reappraisement and refinement of zircon U-Pb isotope and trace element analyses by LA-ICP-MS. Chin. Sci. Bull. 55, 1535–1546. https://doi.org/10.1007/s11434-010-3052-4

Ludwig, K.R., 2012. Isoplot 3.75: A geochronological toolkit for Excel: Berkeley Geochronology Center Special Publication No. 5 75.

Marsden, R.C., Danišík, M., Ahn, U.-S., Friedrichs, B., Schmitt, A.K., Kirkland, C.L., McDonald, B., Evans, N.J., 2021a. Zircon double-dating of Quaternary eruptions on Jeju Island. Journal of Volcanology and Geothermal Research 107171.

Marsden, R.C., Kirkland, C.L., Danišík, M., Daggitt, M.L., Ahn, U.-S., Friedrichs, B., Evans, N.J., 2021b. A new approach to SHRIMP II zircon U-Th disequilibrium dating. Computers and Geosciences, https://doi.org/10.1016/j.cageo.2021.104947

Mucek, A.E., Danišík, M., Silva, S.L. de, Schmitt, A.K., Pratomo, I., Coble, M.A., 2017. Post-supereruption recovery at Toba Caldera. Nature Communications 8, 15248. https://doi.org/10.1038/ncomms15248

Nagasawa, H., 1970. Rare earth concentrations in zircons and apatites and their host dacites and granites. Earth and Planetary Science Letters 9, 359–364. https://doi.org/10.1016/0012-821X(70)90136-6

Nasdala, L., Reiners, P.W., Garver, J.I., Kennedy, A.K., Stern, R.A., Balan, E., Wirth, R., 2004. Incomplete retention of radiation damage in zircon from Sri Lanka. American Mineralogist 89, 219–231. https://doi.org/10.2138/am-2004-0126

Paces, J.B., Miller, J.D., 1993. Precise U-Pb ages of Duluth Complex and related mafic intrusions, northeastern Minnesota: Geochronological insights to physical, petrogenetic, paleomagnetic, and tectonomagmatic processes associated with the 1.1 Ga Midcontinent Rift System. Journal of Geophysical Research: Solid Earth 98, 13997–14013. https://doi.org/10.1029/93JB01159

Paton, C., Hellstrom, J., Paul, B., Woodhead, J., Hergt, J., 2011. Iolite: Freeware for the visualisation and processing of mass spectrometric data. Journal of Analytical Atomic Spectrometry 26, 2508–2518. https://doi.org/10.1039/C1JA10172B

Popa, R.-G., Guillong, M., Bachmann, O., Szymanowski, D., Ellis, B., 2020. U-Th zircon dating reveals a correlation between eruptive styles and repose periods at the Nisyros-Yali volcanic area, Greece. Chemical Geology 555, 119830. https://doi.org/10.1016/j.chemgeo.2020.119830

ProfilmOnline - Surface Imaging, Analysis, and Measurement Software for 3D Profilometers and AFMs [WWW Document], n.d. . ProfilmOnline. URL https://www.profilmonline.com/ (accessed 6.9.21).

Reid, M.R., Coath, C.D., Mark Harrison, T., McKeegan, K.D., 1997. Prolonged residence times for the youngest rhyolites associated with Long Valley Caldera: ^{230}Th—^{238}U ion microprobe dating of young zircons. Earth and Planetary Science Letters 150, 27–39. https://doi.org/10.1016/S0012-821X(97)00077-0

Rollinson, H., Pease, V., 2021. Using Geochemical Data: To Understand Geological Processes, 2nd ed. Cambridge University Press, Cambridge. https://doi.org/10.1017/9781108777834

Schmitt, A.K., Stockli, D.F., Hausback, B.P., 2006. Eruption and magma crystallization ages of Las Tres Vírgenes (Baja California) constrained by combined ^{230}Th/^{238}U and (U–Th)/He dating of zircon. Journal of Volcanology and Geothermal Research 158, 281–295. https://doi.org/10.1016/j.jvolgeores.2006.07.005

Schmitt, A.K., Wetzel, F., Cooper, K.M., Zou, H., Wörner, G., 2010a. Magmatic Longevity of Laacher See Volcano (Eifel, Germany) Indicated by U–Th Dating of Intrusive Carbonatites. J Petrology 51, 1053–1085. https://doi.org/10.1093/petrology/egq011

Schmitt, A.K., Stockli, D.F., Niedermann, S., Lovera, O.M., Hausback, B.P., 2010b. Eruption ages of Las Tres Vírgenes volcano (Baja California): A tale of two helium isotopes. Quaternary Geochronology 5, 503–511. https://doi.org/10.1016/j.quageo.2010.02.004

Schmitt, A., Danisik, M., Evans, N., Siebel, W., Kiemele, E., Aydin, F., C. Harvey, J., 2011. Acigöl rhyolite field, Central Anatolia (part 1): High-resolution dating of eruption episodes and zircon growth rates. Contributions to Mineralogy and Petrology 162, 1215–1231. https://doi.org/10.1007/s00410-011-0648-x

Schmitt, A.K., 2011. Uranium Series Accessory Crystal Dating of Magmatic Processes. Annu. Rev. Earth Planet. Sci. 39, 321–349. https://doi.org/10.1146/annurev-earth-040610-133330

Schmitz, M.D., Bowring, S.A., 2001. U-Pb zircon and titanite systematics of the Fish Canyon Tuff: an assessment of high-precision U-Pb geochronology and its application to young volcanic rocks. Geochimica et Cosmochimica Acta 65, 2571–2587. https://doi.org/10.1016/S0016-7037(01)00616-0

Schnetzler, C.C., Philpotts, J.A., 1970. Partition coefficients of rare-earth elements between igneous matrix material and rock-forming mineral phenocrysts—II. Geochimica et Cosmochimica Acta 34, 331–340. https://doi.org/10.1016/0016-7037(70)90110-9

Sláma, J., Košler, J., Condon, D.J., Crowley, J.L., Gerdes, A., Hanchar, J.M., Horstwood, M.S.A., Morris, G.A., Nasdala, L., Norberg, N., Schaltegger, U., Schoene, B., Tubrett, M.N., Whitehouse, M.J., 2008. Plešovice zircon — A new natural reference material for U–Pb and Hf isotopic microanalysis. Chemical Geology 249, 1–35. https://doi.org/10.1016/j.chemgeo.2007.11.005

Tatsumi, Y., Shukuno, H., Yoshikawa, M., Chang, Q., Sato, K., Lee, M.W., 2005. The Petrology

and Geochemistry of Volcanic Rocks on Jeju Island: Plume Magmatism along the Asian Continental Margin. J Petrology 46, 523–553. https://doi.org/10.1093/petrology/egh087

Vazquez, J.A., Lidzbarski, M.I., 2012. High-resolution tephrochronology of the Wilson Creek Formation (Mono Lake, California) and Laschamp event using ^{238}U-^{230}Th SIMS dating of accessory mineral rims. Earth and Planetary Science Letters 357–358, 54–67. https://doi.org/10.1016/j.epsl.2012.09.013

Watson, E.B., 1996. Surface enrichment and trace-element uptake during crystal growth. Geochimica et Cosmochimica Acta 60, 5013–5020. https://doi.org/10.1016/S0016-7037(96)00299-2

Webb, P., Wiedenbeck, M., Glodny, J., 2020. G-Chron 2019 – Round 1: An International Proficiency Test for U-Pb Geochronology Laboratories; Report on the 2019 Round of G-Chron based on Palaeozoic Zircon Rak-17 (Distribution: September 2019). https://doi.org/10.48440/GFZ.B103-21061

Wendt, I., Carl, C., 1991. The statistical distribution of the mean squared weighted deviation. Chemical Geology: Isotope Geoscience section 86, 275–285. https://doi.org/10.1016/0168-9622(91)90010-T

Wiedenbeck, M., Allé, P., Corfu, F., Griffin, W.L., Meier, M., Oberli, F., Quadt, A.V., Roddick, J.C., Spiegel, W., 1995. Three Natural Zircon Standards for U-Th-Pb, Lu-Hf, Trace Element and Ree Analyses. Geostandards Newsletter 19, 1–23. https://doi.org/10.1111/j.1751-908X.1995.tb00147.x

4.8 Author contributions

Ruby C. Marsden: Investigation, Data Curation, Writing – Original Draft, Visualisation, Methodology

Martin Danišík: Conceptualisation, Writing - Review & Editing, Supervision, Funding acquisition

Axel K. Schmitt: Conceptualisation, Writing - Review & Editing

Kai Rankenburg: Methodology, Investigation, Writing - Review & Editing

Marcel Guillong: Investigation, Writing - Review & Editing

Ung-San Ahn: Resources, Writing - Review & Editing

Christopher L. Kirkland: Writing - Review & Editing

Noreen J. Evans: Writing - Review & Editing

Olivier Bachmann: Writing - Review & Editing, Supervision

Tommaso Tacchetto: Investigation, Writing - Review & Editing

Bradley McDonald: Investigation

Hugo K. H. Olierook: Investigation, Writing - Review & Editing

4.9 Appendices

Supplementary material I

Sample description - SS14-28

SS14-28 is a porphyritic trachyte collected at Lat/Long: 33.35550/126.50042 (WGS-84). In thin section the rock is mainly composed of millimetre size phenocrysts of K-feldspar (ca. 80 vol. %). Plagioclase, rounded hornblende with plagioclase cores rimmed by clinopyroxene and glomerocrysts comprising of aggregations of augite, Ti-rich magnetite (titanomagnetite), apatite and zircon are also distinguishable as phenocrysts. The groundmass comprises predominantly both feldspars, quartz, augite and Fe-rich chlorite (chamosite). Zircon crystals appear to have grown in conjunction with augite and titanomagnetite (Figure 4.iiib, c, d) at eutectic conditions. This correlates with the negative Eu anomaly in the zircon crystals (whereby all the feldspar crystallisation has taken up the Eu) and indicates that there was only a small gap between the zircon crystallisation and volcanic eruption (20 kyrs). Plagioclase is occasionally rimmed by K-feldspar, potentially representing a resorption of Ca rich-plagioclase into the melt. This phenomenon can be seen in Figures 4.iiie, f, g and h for a single plagioclase crystal.
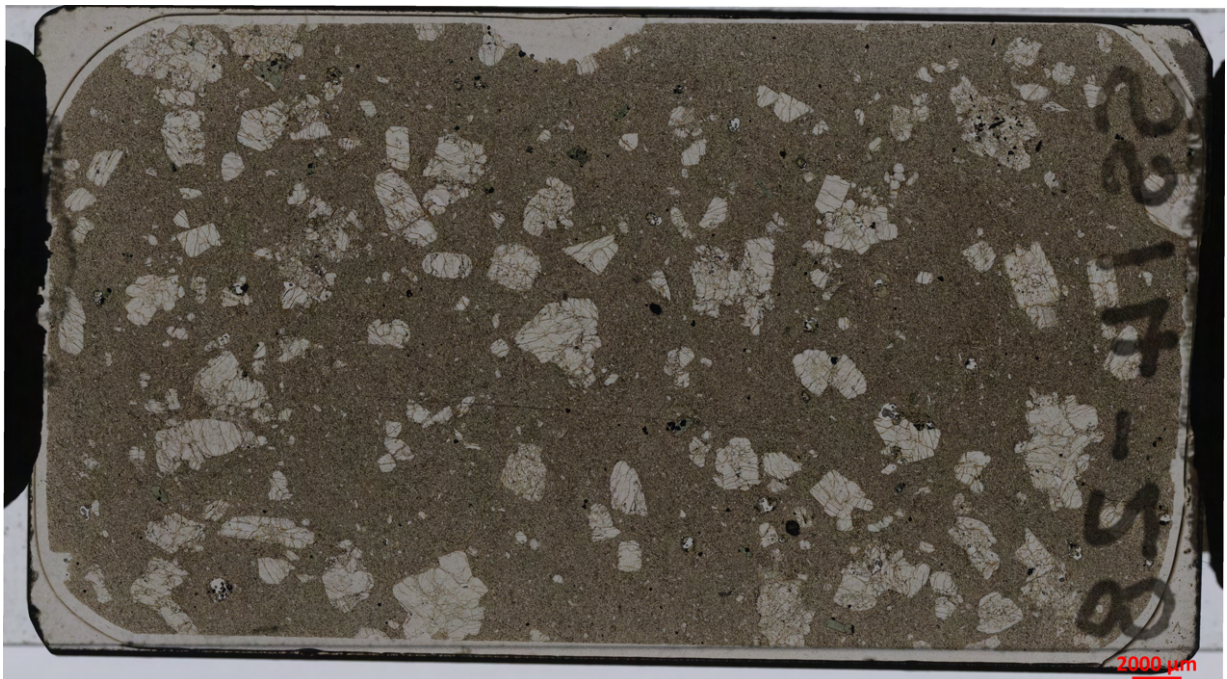
Figure 4.i: Plane polarised light microscope image of SS14-28a thin section.
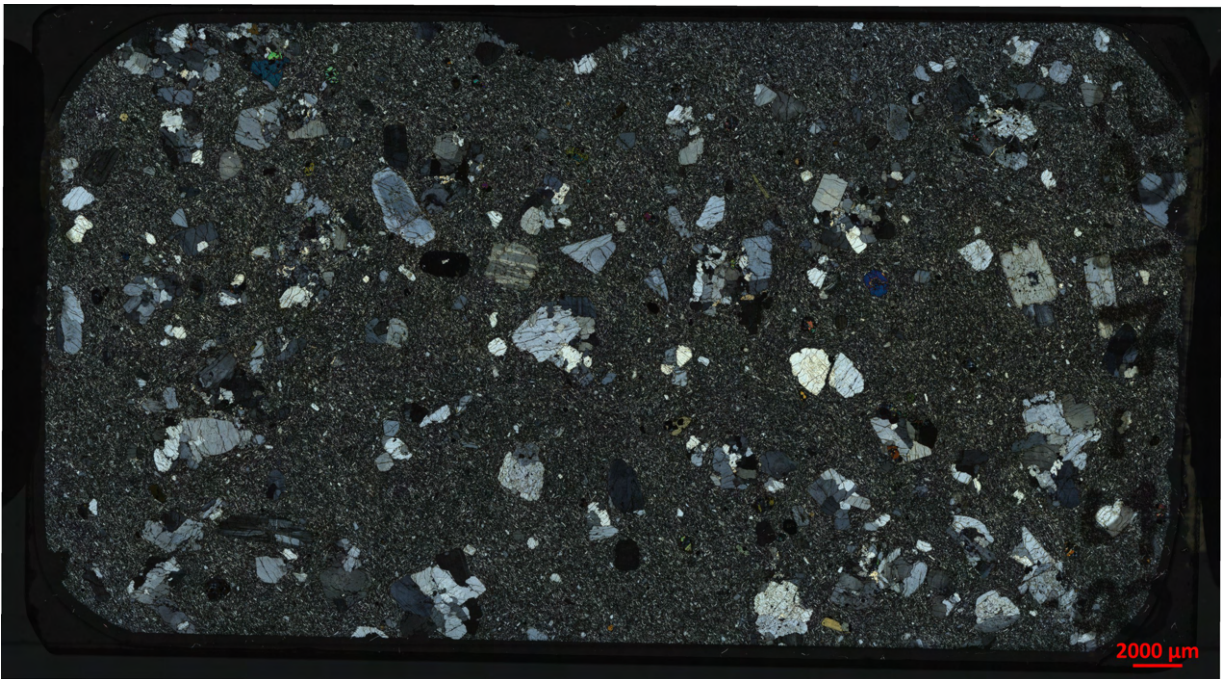
Figure 4.ii: Cross polarised light microscope image of SS14-28a thin section.
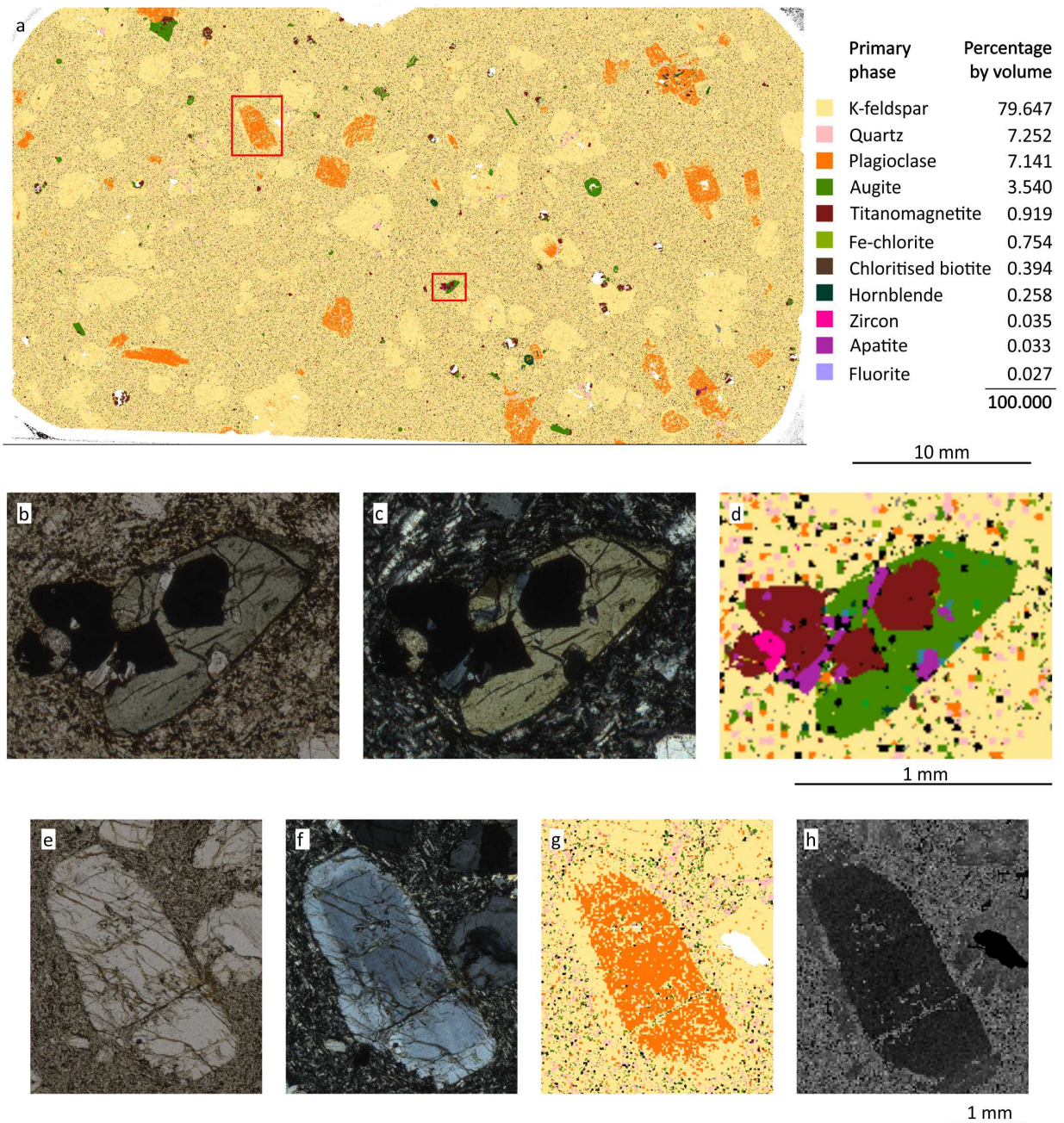
Figure 4.iii: a) TIMA phase map of thin section of SS14-28a (red boxes indicate the positions of scaled up sections shown in b, c, d, e, f, g and h); b-c) Plane polarised and cross polarised light image of an augite crystal with associated titanomagnetite, zircon and apatite; d) TIMA phase map of the section shown in b-c; e-h) plane polarised light, cross polarised light, TIMA phase map and K element map of plagioclase respectively. In h, lighter areas correspond to higher concentrations of K.

Supplementary Material II

U-Th disequilibrium dating - CAMECA 1280 IMS

Sample	Crystal identifier	Spot number	Core/Rim	(238U/232Th)	1s	(230Th/232Th)	1s	m	1s	Th age (ka)	1s+ (ka)	1s- (ka)	Average 2s (ka)	Isochron age (ka)	2s (ka)	U (ppm)
SS14-28	1		Rim	5.121	0.122	2.999	0.372	0.550	0.080	87.2	21.5	-17.9	39.4	83	9	83
SS14-28	2		Rim	3.977	0.081	2.899	0.326	0.698	0.093	130.9	40.1	-29.3	69.4	83	9	84
SS14-28	3		Rim	4.181	0.092	2.852	0.411	0.648	0.110	114.1	40.9	-29.7	70.6	83	9	58
SS14-28	4		Rim	4.390	0.097	2.768	0.167	0.593	0.044	98.1	12.6	-11.3	23.9	83	9	266
SS14-28	5		Rim	4.230	0.081	2.547	0.273	0.560	0.072	89.7	19.6	-16.6	36.3	83	9	111
SS14-28	6		Rim	4.356	0.105	2.473	0.303	0.524	0.078	81.0	19.5	-16.6	36.1	83	9	65
SS14-28	7		Rim	3.845	0.151	2.494	0.397	0.607	0.119	102.1	39.2	-28.8	68.1	83	9	64
SS14-28	8		Rim	3.599	0.074	2.348	0.176	0.609	0.057	102.4	17.2	-14.8	32.0	83	9	154
SS14-28	9		Rim	4.066	0.137	2.652	0.276	0.614	0.079	103.9	24.9	-20.3	45.2	83	9	118
SS14-28	10		Rim	2.620	0.073	1.768	0.104	0.616	0.052	104.4	15.8	-13.8	29.6	83	9	301
SS14-28	11		Rim	3.831	0.076	2.112	0.206	0.498	0.061	75.3	14.3	-12.6	26.9	83	9	114
SS14-28	12		Rim	5.164	0.103	2.699	0.251	0.482	0.054	71.8	12.0	-10.8	22.8	83	9	119
SS14-28	13		Rim	4.806	0.121	3.403	0.612	0.681	0.140	124.8	63.4	-39.8	103.2	83	9	46
SS14-28	14		Rim	4.568	0.084	2.831	0.119	0.583	0.031	95.5	8.5	-7.9	16.4	83	9	1434
SS14-28	15		Rim	4.671	0.097	3.324	0.474	0.684	0.112	125.9	48.0	-33.2	81.2	83	9	47
SS14-28	16		Rim	4.161	0.110	2.578	0.150	0.579	0.043	94.4	11.9	-10.7	22.6	83	9	192
SS14-28	17		Rim	4.155	0.083	2.965	0.235	0.683	0.065	125.4	24.8	-20.2	45.1	83	9	109
SS14-28	18		Rim	4.453	0.083	2.770	0.108	0.584	0.029	95.9	8.0	-7.5	15.5	83	9	401
SS14-28	19		Rim	3.725	0.119	2.406	0.283	0.603	0.088	100.8	27.3	-21.9	49.2	83	9	71
SS14-28	20		Rim	3.768	0.089	2.289	0.196	0.560	0.060	89.7	16.1	-14.0	30.2	83	9	120
SS14-28	21		Rim	2.922	0.058	1.898	0.048	0.593	0.024	98.2	6.7	-6.3	13.1	83	9	878
SS14-28	22		Rim	3.779	0.072	2.294	0.211	0.560	0.064	89.6	17.1	-14.8	31.9	83	9	112
SS14-28	23		Rim	3.980	0.079	2.417	0.256	0.563	0.073	90.3	19.9	-16.8	36.8	83	9	134
SS14-28	24		Rim	4.218	0.085	2.946	0.324	0.666	0.086	119.9	32.7	-25.1	57.9	83	9	72
SS14-28	25		Rim	4.224	0.078	2.451	0.203	0.536	0.054	83.8	13.6	-12.1	25.7	83	9	137
SS14-28	a	2	Core	3.232	0.059	2.065	0.057	0.588	0.024	96.7	6.6	-6.2	12.9	83	9	1233
SS14-28	b	1	Core	4.313	0.079	2.568	0.109	0.554	0.030	88.1	7.7	-7.2	14.8	83	9	381
SS14-28	c	1	Rim (Polished)	5.058	0.094	3.143	0.227	0.589	0.050	97.0	14.2	-12.6	26.8	83	9	147

SS14-28	c	2 Core	2.306	0.043	1.541	0.054	0.598	0.033	99.5	9.2	-8.5	17.8	83	9	648
SS14-28	d	1 Rim (Polished)	4.124	0.078	2.699	0.177	0.617	0.049	104.8	15.1	-13.3	28.3	83	9	187
SS14-28	d	2 Core	4.009	0.076	2.513	0.150	0.585	0.043	96.0	12.1	-10.9	23.0	83	9	235
SS14-28	e	1 Core	4.273	0.078	2.494	0.069	0.540	0.021	84.8	5.2	-5.0	10.2	83	9	891
SS14-28	f	1 Core	3.143	0.058	1.982	0.064	0.576	0.027	93.7	7.2	-6.7	13.9	83	9	639
SS14-28	g	1 Core	3.957	0.075	2.339	0.086	0.545	0.027	85.9	6.7	-6.3	13.0	83	9	935
SS14-28	h	1 Core	4.433	0.082	2.596	0.167	0.544	0.043	85.8	10.9	-9.9	20.7	83	9	197
SS14-28	k	1 Rim (Polished)	4.023	0.074	2.382	0.140	0.546	0.041	86.3	10.2	-9.4	19.6	83	9	226
SS14-28	k	2 Core	4.324	0.079	2.624	0.084	0.566	0.025	91.2	6.4	-6.0	12.4	83	9	709
SS14-28	l	1 Rim (Polished)	6.495	0.150	4.471	0.755	0.668	0.125	120.3	51.5	-34.9	86.4	83	9	42
SS14-28	l	2 Core	4.210	0.078	2.792	0.127	0.628	0.036	107.9	11.1	-10.1	21.2	83	9	320
SS14-28	m	1 Core	5.216	0.095	3.014	0.107	0.542	0.025	85.3	6.1	-5.8	11.9	83	9	566
SS14-28	n	1 Core	3.688	0.068	2.350	0.233	0.593	0.072	98.1	21.3	-17.8	39.1	83	9	110

Whole rock activity values for all age calculations are (238U/232Th): 0.404, 2σ: 0.014, (230Th/232Th): 0.404, 2σ:0.014; from Marsden et al. (2021).

Sector field, high resolution LA-ICPMS results

Sample ID	(238U)/(232Th)	±1s	(230Th)/(232Th)	±1s	m	±1s	Age (ka)	+1s (ka)	-1s (ka)	Average 2s (ka)
SS14-28 - 1	6.28	0.13	3.64	0.22	0.551	0.059	87.3	15.5	13.5	29.0
SS14-28 - 10	3.86	0.08	2.27	0.10	0.538	0.054	84.4	13.5	12.0	25.6
SS14-28 - 11	3.35	0.08	2.21	0.07	0.611	0.058	103.2	17.5	15.1	32.6
SS14-28 - 12	4.64	0.09	2.82	0.06	0.570	0.052	92.1	14.1	12.5	26.6
SS14-28 - 13	4.68	0.11	2.63	0.19	0.520	0.060	80.1	14.4	12.8	27.2
SS14-28 - 14	5.16	0.10	3.16	0.07	0.579	0.053	94.5	14.8	13.0	27.8
SS14-28 - 15	4.04	0.08	2.27	0.14	0.514	0.056	78.8	13.3	11.8	25.1
SS14-28 - 16	4.81	0.10	2.89	0.06	0.564	0.051	90.6	13.7	12.2	25.9
SS14-28 - 17	5.07	0.14	2.72	0.16	0.497	0.054	75.0	12.3	11.1	23.4
SS14-28 - 18	4.09	0.08	2.66	0.07	0.611	0.057	103.2	17.2	14.9	32.1
SS14-28 - 2	4.00	0.08	2.34	0.08	0.538	0.051	84.4	12.8	11.4	24.2
SS14-28 - 20	4.38	0.09	2.72	0.07	0.584	0.054	95.6	15.1	13.3	28.4
SS14-28 - 21	2.83	0.07	1.74	0.07	0.552	0.055	87.7	14.2	12.6	26.8
SS14-28 - 22	3.92	0.08	2.24	0.12	0.524	0.055	81.0	13.3	11.9	25.2
SS14-28 - 23	3.91	0.08	2.21	0.13	0.514	0.055	78.7	13.0	11.6	24.6
SS14-28 - 24	4.08	0.08	2.17	0.13	0.481	0.051	71.6	11.4	10.3	21.7
SS14-28 - 25	6.79	0.14	3.88	0.24	0.544	0.059	85.7	15.0	13.2	28.2
SS14-28 - 26	4.80	0.10	2.77	0.18	0.538	0.060	84.3	15.1	13.3	28.4
SS14-28 - 27	5.53	0.12	3.07	0.21	0.520	0.059	80.0	14.3	12.6	26.9
SS14-28 - 28	4.20	0.09	2.52	0.17	0.556	0.062	88.8	16.6	14.4	30.9
SS14-28 - 29	3.70	0.08	2.29	0.13	0.572	0.060	92.6	16.5	14.3	30.7
SS14-28 - 3	5.11	0.10	3.05	0.16	0.563	0.058	90.4	15.7	13.7	29.4
SS14-28 - 30	3.70	0.08	2.13	0.09	0.522	0.051	80.7	12.4	11.1	23.5
SS14-28 - 31	4.46	0.09	2.64	0.06	0.552	0.051	87.6	13.1	11.7	24.8
SS14-28 - 32	3.96	0.08	2.34	0.15	0.545	0.060	86.0	15.3	13.5	28.8
SS14-28 - 33	4.32	0.09	2.32	0.17	0.488	0.056	73.1	12.7	11.4	24.0
SS14-28 - 34	4.43	0.10	2.78	0.09	0.591	0.056	97.5	16.2	14.1	30.3
SS14-28 - 35	4.37	0.09	2.55	0.19	0.542	0.063	85.2	16.1	14.0	30.2
SS14-28 - 36	6.45	0.13	3.82	0.30	0.565	0.067	90.9	18.2	15.6	33.9
SS14-28 - 37	5.11	0.11	3.23	0.26	0.602	0.073	100.6	22.0	18.3	40.4
SS14-28 - 38	5.49	0.11	2.51	0.21	0.414	0.050	58.4	9.8	9.0	18.8

SS14-28 - 39	6.58	0.13	3.24	0.27	0.459	0.056	67.1	11.9	10.8	22.7
SS14-28 - 4	3.05	0.07	1.97	0.07	0.593	0.057	98.1	16.5	14.3	30.8
SS14-28 - 40	4.17	0.10	2.22	0.17	0.482	0.057	71.8	12.8	11.5	24.3
SS14-28 - 41	5.07	0.10	3.27	0.19	0.614	0.066	104.0	20.3	17.1	37.5
SS14-28 - 42	3.40	0.07	2.18	0.09	0.591	0.058	97.7	16.6	14.4	31.1
SS14-28 - 43	6.61	0.13	3.06	0.29	0.428	0.056	61.1	11.2	10.1	21.3
SS14-28 - 44	4.16	0.08	2.58	0.05	0.578	0.053	94.3	14.5	12.8	27.4
SS14-28 - 45	3.50	0.09	2.17	0.07	0.570	0.055	92.2	14.9	13.1	28.0
SS14-28 - 46	4.36	0.12	2.39	0.09	0.502	0.049	76.0	11.3	10.3	21.6
SS14-28 - 47	4.25	0.09	2.57	0.07	0.564	0.052	90.6	14.0	12.4	26.4
SS14-28 - 48	4.11	0.08	2.52	0.06	0.571	0.053	92.5	14.3	12.6	26.9
SS14-28 - 49	5.50	0.12	2.93	0.20	0.495	0.056	74.6	12.8	11.5	24.3
SS14-28 - 5	5.26	0.13	2.92	0.18	0.518	0.057	79.6	13.7	12.2	25.9
SS14-28 - 50	4.91	0.11	2.80	0.29	0.531	0.072	82.6	18.3	15.7	33.9
SS14-28 - 6	3.73	0.07	2.21	0.10	0.544	0.054	85.7	13.9	12.3	26.2
SS14-28 - 7	5.60	0.13	3.56	0.18	0.606	0.062	101.8	18.9	16.1	34.9
SS14-28 - 8	4.59	0.09	2.79	0.16	0.569	0.060	92.0	16.5	14.3	30.8
SS14-28 - 9	6.23	0.13	3.65	0.22	0.557	0.060	88.8	15.9	13.9	29.8

Whole rock activity values for all age calculations are (238U/232Th): 0.404, 2σ: 0.014, (230Th/232Th): 0.404, 2σ:0.014; from Marsden et al. (2021).

Sector field, high resolution LA-ICPMS operating parameters

Laboratory and Sample Preparation	
Laboratory name	Department of Earth Science, ETH Zurich
Sample type/mineral	Zircon
Sample preparation	Conventional mineral separation, 1 inch epoxy resin mount, 1 um polish

Laser ablation system	
Make, Model and type	Resonetics Resolution 155
Ablation cell and volume	Laurin Technics 155, constant geometry, aerosol dispersion volume < 1 cm3
Laser wavelength	193 nm
Pulse width	25 ns
Energy density/Fluence	~ 2.5 J cm-2
Repetition rate	5 Hz
Spot size	29 µm
Ablation rate	~ 75 nm pulse-1
Sampling mode/pattern	Single hole drilling, 3 cleaning pulses
Carrier gas and flow	100% He, 0.7 l min-1
Ablation duration	40 s

ICP-MS Instrument	
Make, Model and type	Thermo Element XR SF-ICP-MS
Sample introduction	Ablation aerosol only, squid aerosol homogenisation device
RF power	1550 W
Make-up gas flow	~ 0.95 l min-1 Ar (gas mixed to He carrier inside ablation cell funnel)
Detection system	Detection system Single detector triple mode SEM, analogue, Faraday
Masses monitored	228, 230, 232, 235, 238 amu
Integration time per peak	150 ms (mass 230), 50 ms (mass 228), 25 ms (mass 235), 20 ms (mass 232), 11 ms (mass 238)
Total integration time per reading	0.25 s
Dead time	19 ns
Typical oxide rate (ThO/Th)	0.18%
Typical doubly charged rate (Ba2+/Ba+)	3.50%

Data Processing	
Gas blank	30 s prior to each ablation spot
Calibration strategy	91500 used as primary ref. material to correct for mass bias and relative sensitivity
Reference Material information	91500 with U = 81.2 and Th = 28.6 lg g-1 (Wiedenbeck et al. 1995)
Data processing package used	SILLS (Guillong et al. 2008), Excel, IsoplotR (Vermeesch, 2018)
Mass discrimination	Mass bias correction for all ratios normalised to primary reference material
Uncertainty level and propagation	Uncertainty level and propagation 230Th counts, ratios and ages are given as combined standard uncertainty
Quality control/Validation	Based on zircon age > 4 Ma, reference materials in secular equilibrium

References used in this table:

Vermeesch, P., 2018. IsoplotR: A free and open toolbox for geochronology. Geoscience Frontiers, 9(5), pp.1479-1493.
Wiedenbeck, M.A.P.C., Alle, P., Corfu, F., Griffin, W.L., Meier, M., Oberli, F.V., Quadt, A.V., Roddick, J.C. and Spiegel, W., 1995. Three natural zircon standards for U-Th-Pb, Lu-Hf, trace element and REE analyses. Geostandards newsletter, 19(1), pp.1-23.

Multi collector LA-ICPMS results

Sample ID	(238U)/(232Th)	2s	(230Th)/(232Th)	2s	m	2s	Age (ka)	2s
SS14-28-u8 - 1	3.50	0.12	2.22	0.08	0.585	0.077	96.1	20.6
SS14-28-u7 - 2	3.54	0.33	2.23	0.21	0.582	0.104	95.2	27.8
SS14-28-u7 - 1	4.20	0.25	2.48	0.13	0.548	0.080	86.7	19.6
SS14-28-u6 - 2	3.55	0.17	2.17	0.10	0.561	0.078	90.0	19.6
SS14-28-u6 - 1	4.00	0.17	2.45	0.10	0.569	0.078	92.0	19.9
SS14-28-u5 - 4	6.01	0.26	3.61	0.36	0.573	0.094	92.9	24.5
SS14-28-u5 - 3	6.47	0.17	3.91	0.46	0.579	0.099	94.4	26.2
SS14-28-u5 - 2	5.95	0.18	3.72	0.33	0.599	0.092	99.8	25.6
SS14-28-u5 - 1	6.15	0.18	3.88	0.36	0.605	0.094	101.4	26.5
SS14-28-u4 - 3	4.38	0.35	2.63	0.23	0.559	0.095	89.5	23.9
SS14-28-u4 - 2	4.40	0.32	3.11	0.29	0.676	0.115	123.2	40.6
SS14-28-u4 - 1	4.79	0.33	2.76	0.36	0.538	0.103	84.3	24.6
SS14-28-u2 - 2	5.33	0.37	2.85	0.31	0.497	0.088	74.9	19.3
SS14-28-u2 - 1	4.69	0.14	2.75	0.18	0.548	0.078	86.6	18.9
SS14-28-u1 - 1	4.27	0.13	2.61	0.14	0.571	0.079	92.3	20.2
SS14-28-m - 1	3.67	0.36	2.28	0.23	0.575	0.108	93.4	28.3
SS14-28-l - 2	2.80	0.24	1.98	0.19	0.657	0.117	116.9	38.7
SS14-28-l - 1	3.66	0.26	2.22	0.22	0.557	0.096	88.9	24.0
SS14-28-k - 2	4.32	0.60	2.74	0.39	0.597	0.140	99.1	39.5
SS14-28-k - 1	5.14	0.38	3.08	0.23	0.565	0.091	90.8	23.1
SS14-28-h - 1	4.74	0.13	2.87	0.12	0.570	0.075	92.1	19.3
SS14-28-e - 1	3.73	0.22	2.33	0.15	0.578	0.087	94.2	22.9
SS14-28-d - 3	3.86	1.09	2.43	0.70	0.585	0.246	96.0	74.4
SS14-28-d - 2	4.36	1.21	2.90	0.80	0.631	0.260	108.7	95.3
SS14-28-d - 1	5.87	0.91	3.76	0.77	0.615	0.175	104.1	53.4
SS14-28-c - 2	2.51	0.41	1.75	0.31	0.638	0.172	111.0	56.4
SS14-28-c - 1	5.39	0.12	3.35	0.37	0.592	0.098	97.8	26.7
SS14-28-b - 2	4.60	0.55	2.66	0.33	0.539	0.114	84.4	27.7
SS14-28-b - 1	3.45	0.12	2.19	0.09	0.586	0.079	96.2	21.0
SS14-28-a - 1	3.34	0.36	2.12	0.22	0.584	0.113	95.7	30.4
SS14-28-3 - 1	3.98	0.13	2.45	0.13	0.573	0.078	92.8	20.3
SS14-28-24 - 2	2.93	0.14	1.87	0.10	0.580	0.083	94.8	21.8
SS14-28-24 - 1	3.83	0.30	2.28	0.16	0.547	0.089	86.4	21.7
SS14-28-20 - 2	4.89	0.10	2.87	0.29	0.550	0.087	87.2	21.5
SS14-28-20 - 1	4.01	0.30	2.58	0.22	0.603	0.101	100.9	28.5
SS14-28-2 - 2	4.79	0.12	2.81	0.07	0.548	0.070	86.6	17.0
SS14-28-2 - 1	4.31	0.16	2.56	0.10	0.552	0.074	87.7	18.2
SS14-28-19 - 1	3.88	0.18	2.43	0.10	0.582	0.080	95.3	21.2
SS14-28-17 - 3	4.21	0.18	2.55	0.15	0.562	0.080	90.2	20.3
SS14-28-17 - 2	3.05	0.62	1.91	0.42	0.568	0.183	91.6	49.4
SS14-28-17 - 1	3.24	0.14	2.13	0.12	0.607	0.086	101.9	24.2
SS14-28-1 - 3	4.26	0.85	2.55	0.52	0.555	0.173	88.4	44.9
SS14-28-1 - 2	4.58	0.15	2.81	0.09	0.576	0.075	93.6	19.5
SS14-28-1 - 1	3.16	0.23	2.00	0.12	0.578	0.090	94.2	23.5

Whole rock activity values for all age calculations are (238U/232Th): 0.404, 2σ: 0.014, (230Th/232Th): 0.404, 2σ:0.014; from Marsden et al. (2021).

Multi-collector LA-ICPMS operating parameters

Laboratory and Sample Preparation	
Laboratory name	GeoHistory Facility, JdLC
Sample type/mineral	Zircon
Sample preparation	Conventional mineral separation, 1 inch epoxy resin mount

Laser ablation system	
Make, Model and type	Resonetics Resolution SE
Ablation cell and volume	S155
Laser wavelength	193 nm
Pulse width	20 ns
Energy density/Fluence	~ 2.8 J cm-2
Repetition rate	5 Hz
Spot size	38 μm
Ablation rate	depends on repetition rate, laser fluence and ablated material
Sampling mode/pattern	Single hole drilling, 2 cleaning pulses
Carrier gas and flow	Ar ~1 l/min, He 320 ml/min, N2 1.2 ml/min
Ablation duration	40 s

ICP-MS Instrument	
Make, Model and type	NU Plasma II MC-ICPMS
Sample introduction	Laser ablation
RF power	1300 W
Make-up gas flow	0.8 l/min
Detection system	Faraday cups
Masses monitored	229, 230, 231, 232, 235, 238 amu
Integration time per peak	1s
Total integration time per reading	40s
Dead time	n/a
Typical oxide rate (ThO/Th)	n.m.
Typical doubly charged rate (Ba2+/Ba+)	n.m.

Data Processing	
Gas blank	n/a
Calibration strategy	NIST 612 glass (Pearce et al., 1997)
Reference Material information	NIST 612 glass for U concentration
Data processing package used	Iolite 3.7 running within Igor Pro 6.37 software (Paton et al., 2011), Excel, Isoplot 3.75 (Ludwig, 2012)
Mass discrimination	Mass bias correction for all ratios normalised to materials in secular equilibrium
Uncertainty level and propagation	Uncertainty level and propagation 230Th counts, ratios and ages are given as combined standard uncertainty
Quality control/Validation	Based on zircon age > 4 Ma, reference materials in secular equilibrium

References used in this table:

Ludwig, K.R., 2012. Isoplot 3.75: A geochronological toolkit for Excel: Berkeley Geochronology Center Special Publication No. 5 75.

Paton, C., Hellstrom, J., Paul, B., Woodhead, J., Hergt, J., 2011. Iolite: Freeware for the visualisation and processing of mass spectrometric data. Journal of Analytical Atomic Spectrometry 26, 2508–2518.

Pearce N. J. G., Perkins W. T., Westgate J. A., Gorton M. P., Jackson S. E., Neal C. R. and Chenery S. P. (1997) A Compilation of New and Published Major and Trace Element Data for NIST SRM 610 and NIST SRM 612 Glass Reference

SHRIMP II results - Individual scan activity ratios

(238U)/(232Th)	2s	(230Th)/(232Th)	2s
4.75	0.38	3.04	2.88
4.16	0.53	2.46	0.82
4.44	0.59	4.04	3.95
3.42	0.32	3.07	1.65
5.10	0.57	5.00	4.04
4.18	0.38	3.53	3.89
3.71	0.31	3.34	1.14
4.13	0.33	3.67	2.23
3.92	0.61	3.36	2.39
4.31	0.35	3.66	3.50
5.01	0.54	4.29	4.25
4.69	0.43	3.95	2.45
4.15	0.63	3.11	2.29
3.41	0.54	3.06	1.88
4.87	0.79	4.31	4.81
4.52	0.53	3.89	2.82
3.67	0.45	3.25	2.29
4.10	0.76	3.65	3.26
4.60	0.45	3.90	2.47
4.26	0.78	3.77	3.95
3.99	0.31	2.08	1.85
4.13	0.63	3.61	3.36
4.11	0.52	2.98	2.84
3.15	0.44	2.99	1.15
4.43	0.44	4.34	4.21
4.54	0.62	3.52	4.02
5.28	0.78	3.66	1.09
4.72	0.61	3.33	3.01
4.24	0.43	3.80	3.24
2.48	0.39	2.27	1.57
4.33	0.49	3.72	1.97
5.11	0.89	4.62	5.57
5.06	0.78	4.37	3.04
4.29	0.78	2.99	2.20
3.74	0.37	2.70	2.14
4.06	0.80	3.49	3.52
5.12	1.02	4.76	3.83
5.37	0.73	4.56	3.41
4.35	0.65	4.26	1.14
5.41	0.66	4.42	4.69
3.89	0.37	3.10	2.38
3.23	0.43	3.07	2.78
4.51	0.58	3.34	3.43
4.54	0.86	3.84	2.31
5.24	0.97	3.91	1.88
5.58	0.41	5.47	5.91
4.26	0.47	3.83	3.71
4.30	0.52	2.95	2.03

2.43	0.26	2.04	1.34
4.37	0.45	4.14	2.48
3.39	0.52	2.96	1.06
4.87	0.49	4.12	3.61
3.76	0.48	2.69	2.56
5.16	0.94	3.94	4.72
5.65	0.86	5.22	3.68
3.88	0.51	2.18	1.59
4.19	0.60	4.01	1.33
4.17	0.76	4.04	2.22
3.14	0.31	2.00	1.78
4.48	0.26	4.11	3.30
5.42	0.71	4.98	2.57
4.54	0.44	3.02	1.64
4.15	0.29	2.48	2.14
2.44	0.16	2.08	0.94
4.42	0.65	3.30	2.16
3.21	0.50	3.01	3.05
5.14	0.47	3.00	2.36
4.99	0.44	3.85	2.27
3.76	0.39	2.41	1.13
5.71	0.78	5.43	4.71
4.23	0.59	3.15	2.37
4.01	0.55	3.57	2.25
5.58	1.02	3.14	2.46
4.17	0.47	3.99	2.08
3.18	0.41	2.54	2.29
4.55	0.58	3.38	3.50
4.62	0.48	4.53	2.12
5.19	0.69	3.49	4.83
4.52	0.49	3.62	2.27
4.23	0.63	3.83	2.86
2.35	0.27	2.27	1.43
4.28	0.71	3.27	2.94
4.97	0.70	2.17	1.39
5.01	0.74	3.63	2.66
4.33	0.94	3.08	2.63
3.63	0.16	2.61	0.81
5.47	1.20	3.11	4.56
5.48	0.64	4.06	4.41
4.09	0.38	3.78	1.87
4.05	0.54	3.52	1.90
5.77	0.58	4.21	5.76
4.10	0.37	3.35	2.74
3.86	0.34	3.64	2.98
3.85	0.69	3.80	2.50
3.24	0.50	2.75	0.90
4.21	0.51	2.45	1.32
4.70	0.65	1.94	1.71
5.27	0.93	4.13	4.10

4.44	1.05	3.04	3.30
5.69	1.19	4.74	5.41
4.50	0.29	3.05	2.62
4.22	0.25	3.44	2.27
2.39	0.32	1.64	2.00
4.35	0.52	3.44	2.17
3.20	0.64	2.03	2.47
4.79	0.95	3.79	2.66
4.41	0.66	3.56	2.48
3.83	0.25	2.88	1.95
4.40	1.00	1.99	2.07
5.14	0.54	2.79	3.74
5.46	0.58	4.59	3.33
4.52	0.99	3.06	3.70
4.09	0.65	2.25	2.67
5.76	0.49	2.71	3.97
4.00	0.55	2.27	1.47
3.92	0.32	3.61	2.37
4.37	0.85	2.94	3.15
3.05	0.34	2.51	2.18
4.51	0.61	2.99	2.02
4.87	0.69	4.48	3.30
4.11	0.86	3.05	3.83
4.46	0.76	3.07	3.32
5.48	1.02	5.34	4.53
4.76	0.58	3.41	3.97
4.07	0.69	2.26	1.86
2.52	0.24	2.05	1.72
4.15	0.52	3.85	2.27
3.35	0.48	2.29	2.31
5.12	0.76	3.44	1.96
4.96	0.89	3.92	3.99
4.68	0.80	3.48	3.29
3.95	0.44	2.98	2.65
4.26	0.89	3.92	4.59
5.12	0.71	4.62	3.47
5.60	0.77	4.12	2.72
4.43	0.39	4.00	4.41
4.39	0.57	3.37	1.63
3.86	0.39	2.78	1.51
4.12	0.50	3.11	0.90
3.04	0.37	1.81	0.91
4.27	0.82	3.66	2.90
4.60	0.71	3.79	1.82
4.89	0.74	3.80	2.23

Pit volume results

Instrument	Pit volume (μm^3)
MC-LA-ICPMS	15450
MC-LA-ICPMS	14470
MC-LA-ICPMS	13390
MC-LA-ICPMS	15340
MC-LA-ICPMS	14380
MC-LA-ICPMS	13310
SF-HR-LA-ICPMS	8788
SF-HR-LA-ICPMS	8677
SF-HR-LA-ICPMS	8588
SF-HR-LA-ICPMS	8649
SHRIMP II	665
SHRIMP II	664
SHRIMP II	665
SHRIMP II	666
CAMECA 1280 IMS	1631
CAMECA 1280 IMS	1634
CAMECA 1280 IMS	1628
CAMECA 1280 IMS	1634

REE measurements raw data

	Source file	Date	Duration (s)	Total points	Selection type	Zr_ppm _m91 Value	2SE	LOD	Si_ppm_m29 Value	2SE
O_1_1	K6-428 - 1	13/04/2021	24.768	82	Normal	4.41E+05	6.10E+03	13	1.51E+05	2.10E+03
O_1_2	K6-428 - 2	13/04/2021	24.769	82	Normal	4.51E+05	5.80E+03	16	1.47E+05	1.90E+03
O_1_3	K6-428 - 3	13/04/2021	24.769	82	Normal	4.51E+05	5.50E+03	0.015	1.46E+05	1.80E+03
O_1_4	K6-428 - 4	13/04/2021	24.769	82	Normal	4.45E+05	5.30E+03	0.016	1.49E+05	1.70E+03
O_1_5	K6-428 - 5	13/04/2021	24.769	82	Normal	4.40E+05	6.40E+03	0.026	1.50E+05	2.10E+03
O_1_6	K6-428 - 6	13/04/2021	24.768	82	Normal	4.51E+05	6.50E+03	0.015	1.46E+05	2.10E+03
O_1_7	K6-428 - 7	13/04/2021	24.768	82	Normal	4.25E+05	6.00E+03	0.041	1.55E+05	2.20E+03
O_1_8	K6-428 - 8	13/04/2021	24.769	82	Normal	4.55E+05	5.90E+03	0.025	1.45E+05	1.90E+03
O_1_9	K6-428 - 9	13/04/2021	24.768	82	Normal	4.44E+05	5.10E+03	0.026	1.48E+05	1.70E+03
O_1_10	K6-428 - 10	13/04/2021	24.769	82	Normal	4.49E+05	6.10E+03	0.025	1.47E+05	1.90E+03
O_1_11	K6-428 - 11	13/04/2021	24.768	82	Normal	4.57E+05	5.60E+03	0.025	1.43E+05	1.60E+03
O_1_12	K6-428 - 12	13/04/2021	24.769	82	Normal	4.50E+05	5.50E+03	0.015	1.46E+05	1.80E+03
O_1_13	K7-428 - 1	13/04/2021	24.768	82	Normal	4.59E+05	5.60E+03	0.015	1.43E+05	1.70E+03
O_1_14	K7-428 - 2	13/04/2021	24.768	82	Normal	4.56E+05	7.30E+03	0.025	1.45E+05	2.30E+03
O_1_15	K7-428 - 3	13/04/2021	24.769	82	Normal	4.50E+05	7.50E+03	0.015	1.47E+05	2.50E+03
O_1_16	K7-428 - 4	13/04/2021	24.768	82	Normal	4.52E+05	6.50E+03	0.015	1.45E+05	2.10E+03
O_1_17	K7-428 - 5	13/04/2021	24.769	82	Normal	4.57E+05	6.20E+03	0.05	1.44E+05	1.90E+03
O_1_18	K7-428 - 6	13/04/2021	23.824	79	Normal	4.50E+05	7.40E+03	0.026	1.46E+05	2.40E+03
O_1_19	K7-428 - 7	13/04/2021	24.769	82	Normal	4.28E+05	8.10E+03	0.017	1.54E+05	2.80E+03
O_1_20	K7-428 - 8	13/04/2021	24.768	82	Normal	4.56E+05	6.00E+03	0.015	1.45E+05	1.90E+03
O_1_21	K7-428 - 9	13/04/2021	24.768	82	Normal	4.20E+05	7.60E+03	0.043	1.57E+05	2.80E+03
O_1_22	K7-428 - 10	13/04/2021	24.768	82	Normal	4.42E+05	5.30E+03	0.016	1.50E+05	1.80E+03
O_1_23	K7-428 - 11	13/04/2021	24.769	82	Normal	4.62E+05	7.10E+03	0.015	1.43E+05	2.20E+03
O_1_24	K7-428 - 12	13/04/2021	24.768	82	Normal	4.55E+05	7.70E+03	0.025	1.46E+05	2.40E+03
O_1_25	K7-428 - 13	13/04/2021	24.768	82	Normal	4.50E+05	5.30E+03	0.015	1.48E+05	1.80E+03
O_1_26	K7-428 - 14	13/04/2021	24.769	82	Normal	4.56E+05	6.20E+03	0.015	1.46E+05	1.90E+03
O_1_27	K7-428 - 15	13/04/2021	24.768	82	Normal	4.56E+05	8.00E+03	0.036	1.46E+05	2.60E+03
O_1_28	K7-428 - 16	13/04/2021	24.768	82	Normal	4.47E+05	6.80E+03	0.025	1.49E+05	2.30E+03
O_1_29	K7-428 - 17	13/04/2021	24.769	82	Normal	4.58E+05	7.70E+03	0.015	1.46E+05	2.30E+03
O_1_30	K7-428 - 18	13/04/2021	24.769	82	Normal	4.59E+05	6.90E+03	0.025	1.46E+05	2.20E+03
O_1_31	K7-428 - 19	13/04/2021	24.769	82	Normal	4.63E+05	6.00E+03	0.015	1.45E+05	1.80E+03
O_1_32	K7-428 - 20	13/04/2021	24.768	82	Normal	4.64E+05	7.10E+03	0.036	1.46E+05	2.30E+03
O_1_33	K7-428 - 21	13/04/2021	24.768	82	Normal	4.59E+05	7.40E+03	0.1	1.47E+05	2.50E+03
O_1_34	K7-428 - 22	13/04/2021	24.769	82	Normal	4.61E+05	6.90E+03	0.015	1.46E+05	2.10E+03
O_1_35	K7-428 - 23	13/04/2021	24.768	82	Normal	4.66E+05	7.10E+03	0.026	1.45E+05	2.10E+03
Z_GJ1_1	Gj1 - 1	13/04/2021	24.769	82	Normal	4.51E+05	7.50E+03	0.0015	1.48E+05	2.30E+03
Z_GJ1_2	Gj1 - 2	13/04/2021	24.768	82	Normal	4.51E+05	8.20E+03	0.002	1.48E+05	2.70E+03
Z_GJ1_3	Gj1 - 3	13/04/2021	24.768	82	Normal	4.46E+05	7.50E+03	NaN	1.48E+05	2.50E+03
Z_GJ1_4	Gj1 - 4	13/04/2021	24.768	82	Normal	4.46E+05	7.50E+03	NaN	1.48E+05	2.40E+03
Z_GJ1_5	Gj1 - 5	13/04/2021	24.769	82	Normal	4.49E+05	8.40E+03	NaN	1.47E+05	2.70E+03
Z_GJ1_6	Gj1 - 6	13/04/2021	24.769	82	Normal	4.48E+05	7.70E+03	NaN	1.48E+05	2.50E+03
Z_GJ1_7	Gj1 - 7	13/04/2021	24.768	82	Normal	4.60E+05	8.90E+03	NaN	1.47E+05	2.80E+03
Z_GJ1_8	Gj1 - 8	13/04/2021	24.768	82	Normal	4.56E+05	8.00E+03	NaN	1.48E+05	2.60E+03

Zircon traces, 8900 QQQ, 30 micron spot, 30s ablation, 35s baseline, 2J/cm2, 5 Hz

Primary reference zircon GJ-1 (91Zr reference isotope, 43.14 wt % Zr in unknowns), except for Zr and Ca for which NIST 610 was the primary reference material (29Si, assuming 14.76 wt % Si in unknowns)

Limit of detection (LOD) calculated using the Longerich et al., 1996 method but replacing background 1 sigma with 7 for all channels with zero variation in the baseline counts.

Longerich, H. P., S. E. Jackson, et al. (1996). "Laser Ablation Inductively Coupled Plasma Mass Spectrometric Transient Signal Data Acquisition and Analyte Concentration Calculation." Journal of Analytical Atomic Spectrometry 11 (9) pp. 899 - 904.

Measurements coloured grey are inclusion/zircon mixtures

	Ca_ppm_m44			Ti_ppm_m49			Y_ppm_m89			La_ppm_m139		
LOD	Value	2SE	LOD	Value	2SE	LOD	Value	2SE	LOD	Value	2SE	LOD
380	< LOD	< LOD	18	3.47	0.57	0.48	2553	17	0.004	< LOD	< LOD	too low to be calculated
390	101	32	20	4.69	0.58	0.18	2426	35	0.0028	< LOD	< LOD	too low to be calculated
370	< LOD	< LOD	21	9.67	0.91	0.24	421.7	4.4	0.0064	< LOD	< LOD	too low to be calculated
440	< LOD	< LOD	23	3.46	0.57	0.21	1538	32	0.0019	< LOD	< LOD	too low to be calculated
370	49	20	23	15.8	2	0.2	793	19	0.0068	< LOD	< LOD	too low to be calculated
410	40	18	18	10.6	1.7	0.3	2264	34	0.003	< LOD	< LOD	too low to be calculated
460	13040	950	25	6.36	0.85	0.21	2014	53	0.006	< LOD	< LOD	too low to be calculated
360	< LOD	< LOD	24	4.94	0.64	0.19	2464	33	0.0016	< LOD	< LOD	too low to be calculated
390	< LOD	< LOD	21	6.79	0.71	0.28	1237	43	0.0018	< LOD	< LOD	too low to be calculated
340	< LOD	< LOD	20	6.37	0.83	0.23	1508	13	0.0028	< LOD	< LOD	too low to be calculated
330	< LOD	< LOD	21	14.2	1	0.24	594	16	0.0016	< LOD	< LOD	too low to be calculated
390	587	71	22	3.58	0.57	0.21	2954	41	0.0028	< LOD	< LOD	too low to be calculated
390	< LOD	< LOD	22	11.59	0.99	0.26	1088	13	0.0048	< LOD	< LOD	too low to be calculated
410	2770	690	20	12.15	0.95	0.26	1692	23	0.0048	< LOD	< LOD	too low to be calculated
390	94	34	19	6.12	0.78	0.26	1429	58	0.0039	< LOD	< LOD	too low to be calculated
390	2400	520	23	10.25	0.89	0.22	707.3	9.4	0.0028	< LOD	< LOD	too low to be calculated
360	< LOD	< LOD	21	11.7	1	0.42	609	18	0.0047	< LOD	< LOD	too low to be calculated
350	2050	580	21	12.8	1.1	0.37	1028.6	9.9	0.0028	< LOD	< LOD	too low to be calculated
470	60900	7200	28	18.4	5.7	0.3	4040	170	0.29	< LOD	< LOD	too low to be calculated
430	< LOD	< LOD	21	10.8	1.1	0.2	773.6	8.2	0.0027	< LOD	< LOD	too low to be calculated
460	67800	4300	28	18.6	1.9	0.38	7970	150	0.0077	< LOD	< LOD	too low to be calculated
350	19700	3000	20	16.5	4.4	0.32	1600	43	0.0094	< LOD	< LOD	too low to be calculated
350	< LOD	< LOD	21	5.9	0.65	0.22	1070	12	0.0016	< LOD	< LOD	too low to be calculated
310	< LOD	< LOD	22	8.44	0.88	0.23	1514	14	0.0061	< LOD	< LOD	too low to be calculated
340	< LOD	< LOD	18	13.5	1.1	0.26	697	15	0.004	< LOD	< LOD	too low to be calculated
410	< LOD	< LOD	22	12.64	0.94	0.34	1289	11	0.0017	< LOD	< LOD	too low to be calculated
370	< LOD	< LOD	20	12.5	1.2	0.27	609.8	6.3	0.005	< LOD	< LOD	too low to be calculated
330	< LOD	< LOD	19	3.11	0.53	0.33	2772	46	0.004	< LOD	< LOD	too low to be calculated
330	< LOD	< LOD	22	7.45	0.67	0.29	924	12	0.0069	< LOD	< LOD	too low to be calculated
410	33	14	20	10.57	0.89	0.18	620	10	0.0029	< LOD	< LOD	too low to be calculated
380	< LOD	< LOD	21	10.96	0.99	0.37	517.6	5.5	0.0041	< LOD	< LOD	too low to be calculated
370	< LOD	< LOD	23	14.2	1.1	0.3	381.7	3.5	0.0029	< LOD	< LOD	too low to be calculated
400	< LOD	< LOD	23	11.6	1	0.27	755	20	0.0029	< LOD	< LOD	too low to be calculated
410	< LOD	< LOD	24	9.19	0.94	0.41	1189	13	0.0029	< LOD	< LOD	too low to be calculated
400	< LOD	< LOD	22	12.74	0.99	0.25	618	18	0.0058	< LOD	< LOD	too low to be calculated
NaN	< LOD	< LOD	0.0015	3.37	0.53	NaN	245.9	2	NaN	0.00496	0.00014	too low to be calculated
NaN	4	7.7	0.002	3.85	0.59	NaN	247.5	2	NaN	0.00501	0.00016	too low to be calculated
NaN	< LOD	< LOD	NaN	3.53	0.53	NaN	242.1	2.2	NaN	0.00503	0.00014	too low to be calculated
NaN	5.1	8.2	NaN	3.46	0.61	NaN	246.6	2.6	NaN	0.00506	0.00016	too low to be calculated
NaN	4.4	8.8	NaN	3.57	0.54	NaN	247.7	2.2	NaN	0.00494	0.00015	too low to be calculated
NaN	5.1	8.8	NaN	3.57	0.61	NaN	249.8	1.9	NaN	0.00502	0.00015	too low to be calculated
NaN	< LOD	< LOD	NaN	3.56	0.55	NaN	240.2	1.9	NaN	0.00498	0.00016	too low to be calculated
NaN	0.21	7.99	NaN	3.54	0.51	NaN	248.3	1.9	NaN	0.00501	0.00015	too low to be calculated

Ce_ppm_m140			Pr_ppm_m141			Nd_ppm_m146			Sm_ppm_m147			Eu_ppm_m153		
Value	2SE	LOD	Value	2SE	LOD	Value	2SE	LOD	Value	2SE	LOD	Value	2SE	LOD
26.54	0.39	0.0019	0.61	0.041	0.0034	8.66	0.38	0.0091	17.83	0.4	0.01	1.242	0.065	0.0026
31	2.7	0.0018	1.49	0.35	0.002	8.4	1.1	0.009	12.79	0.49	0.01	0.544	0.041	0.0026
3.231	0.096	0.0019	0.126	0.017	0.002	1.52	0.13	0.0092	2.61	0.2	0.01	0.662	0.053	0.0027
12.84	0.45	0.0021	0.401	0.039	0.0023	5.16	0.32	0.01	10	0.46	0.011	0.733	0.063	0.003
5.14	0.2	0.002	0.433	0.043	0.0022	3.47	0.24	0.0098	5.02	0.31	0.011	1.311	0.083	0.0048
36.2	0.72	0.0033	0.639	0.06	0.0021	6.68	0.3	0.0096	13.35	0.48	0.01	0.758	0.053	0.0047
626	45	0.0023	103.5	7.2	0.0024	356	26	0.011	71.6	4.3	0.012	3.07	0.17	0.0032
22.97	0.42	0.0018	0.448	0.038	0.0019	5.98	0.28	0.009	12.08	0.49	0.0095	1.265	0.08	0.0025
13.74	0.42	0.002	0.17	0.022	0.0021	2.51	0.21	0.0097	5.46	0.38	0.01	0.643	0.05	0.0027
20.64	0.27	0.0032	0.398	0.035	0.002	4.51	0.23	0.0092	7.94	0.27	0.0097	0.741	0.052	0.0026
4.43	0.16	0.0018	0.21	0.03	0.0019	2.12	0.15	0.009	3.56	0.25	0.0095	1.02	0.056	0.0025
70.8	6	0.0019	8.5	1	0.002	33.4	3.2	0.0093	20.81	0.86	0.0097	1.218	0.08	0.0026
4.79	0.1	0.0032	0.594	0.035	0.002	6.53	0.27	0.0095	10	0.36	0.0097	2.5	0.1	0.0026
158	33	0.0018	23.9	5.9	0.002	82	19	0.0094	22.8	3.2	0.0096	1.79	0.22	0.0026
24.5	1.1	0.0018	1.22	0.27	0.002	7.06	0.78	0.0096	8.1	0.47	0.0097	0.581	0.053	0.0026
73	15	0.0019	11.9	2.6	0.0021	39	8.1	0.0097	9.6	1.3	0.0098	1.09	0.087	0.0026
3.82	0.11	0.0018	0.159	0.023	0.002	2.11	0.18	0.0095	4.22	0.28	0.0096	1.012	0.073	0.0026
31.3	7.4	0.0018	5.2	1.4	0.002	20.6	4.6	0.0097	9.73	0.9	0.0098	2.21	0.12	0.0026
4550	610	0.0022	780	110	0.0025	2830	390	0.012	540	72	0.012	14.2	1.8	0.0032
3.26	0.1	0.0018	0.365	0.031	0.002	4.02	0.25	0.0095	6.48	0.26	0.0093	1.68	0.079	0.0025
6110	450	0.0039	1049	82	0.0026	3690	280	0.012	743	52	0.012	16.4	1.1	0.0033
1250	170	0.002	214	30	0.0022	730	100	0.011	133	18	0.01	3.65	0.44	0.0028
20.33	0.38	0.0018	0.269	0.03	0.002	3.93	0.26	0.0097	7.01	0.29	0.0094	0.448	0.042	0.0026
10.29	0.28	0.0018	0.663	0.064	0.0034	7.25	0.3	0.0097	10.96	0.43	0.0094	2.03	0.087	0.0025
3.275	0.097	0.0018	0.224	0.026	0.002	2.82	0.25	0.0099	4.64	0.29	0.0097	1.534	0.087	0.0044
4.38	0.11	0.0018	0.625	0.043	0.002	7.6	0.26	0.01	11.72	0.43	0.0098	3.227	0.093	0.0026
4.5	0.13	0.0019	0.16	0.02	0.0021	1.98	0.16	0.01	3.31	0.2	0.01	0.944	0.052	0.0026
34.31	0.61	0.0018	0.401	0.04	0.002	6.55	0.31	0.01	14.33	0.45	0.0098	0.656	0.048	0.0026
8.97	0.22	0.0018	0.208	0.026	0.002	3.04	0.23	0.01	5.05	0.27	0.0099	0.578	0.048	0.0044
4.36	0.22	0.0018	0.18	0.035	0.002	1.87	0.21	0.0099	3.24	0.2	0.0099	0.887	0.06	0.0025
4.35	0.12	0.0019	0.151	0.02	0.002	1.84	0.16	0.01	3.44	0.24	0.01	0.757	0.05	0.0043
2.716	0.084	0.0019	0.102	0.018	0.002	1.48	0.14	0.01	2.42	0.19	0.01	0.801	0.053	0.0025
4.85	0.14	0.0019	0.228	0.024	0.002	3.23	0.24	0.01	5.92	0.34	0.01	0.975	0.06	0.0026
6.53	0.16	0.0019	0.287	0.029	0.0035	4.06	0.22	0.01	7.54	0.36	0.011	1.124	0.069	0.0044
5.16	0.16	0.0019	0.163	0.023	0.002	2.24	0.18	0.01	3.66	0.23	0.011	0.809	0.053	0.0025
15.94	0.23	NaN	0.0264	0.0083	NaN	0.626	0.083	NaN	1.41	0.16	NaN	0.982	0.061	NaN
16.14	0.23	NaN	0.0308	0.0098	NaN	0.568	0.085	NaN	1.42	0.15	NaN	1.016	0.065	NaN
15.85	0.25	NaN	0.0281	0.0092	NaN	0.533	0.087	NaN	1.45	0.14	NaN	0.948	0.065	NaN
16.01	0.26	NaN	0.0408	0.0099	NaN	0.636	0.092	NaN	1.39	0.12	NaN	1.075	0.068	NaN
16.04	0.22	NaN	0.029	0.0091	NaN	0.598	0.077	NaN	1.45	0.14	NaN	0.999	0.059	NaN
16.15	0.22	NaN	0.0334	0.0092	NaN	0.6	0.1	NaN	1.43	0.12	NaN	1.028	0.059	NaN
15.72	0.24	NaN	0.0233	0.0079	NaN	0.568	0.079	NaN	1.4	0.12	NaN	0.971	0.052	NaN
16.14	0.25	NaN	0.034	0.01	NaN	0.6	0.1	NaN	1.42	0.13	NaN	1	0.058	NaN

Gd_ppm_m157			Tb_ppm_m159			Dy_ppm_m163			Ho_ppm_m165			Er_ppm_m166		
Value	2SE	LOD	Value	2SE	LOD	Value	2SE	LOD	Value	2SE	LOD	Value	2SE	LOD
87.7	1.2	0.021	26.39	0.25	0.0012	276.1	2.4	0.0049	89.34	0.77	0.0029	336.2	2.8	0.0034
71.5	1.3	0.0086	23.12	0.36	0.0012	250	3.9	0.0048	84	1.2	0.0012	324	5.2	0.0034
13.87	0.45	0.0088	4.31	0.11	0.0012	44.41	0.73	0.012	14.98	0.19	0.0012	60.31	0.79	0.0035
48.8	1.2	0.0098	15.23	0.3	0.0014	159.6	3.3	0.0055	53.1	1	0.0014	205.7	4.1	0.0039
23.9	1	0.0093	7.23	0.26	0.0023	78.3	2.2	0.0053	27.2	0.69	0.0013	112.1	2.2	0.0064
66.6	1.5	0.015	22.27	0.42	0.0022	236.7	3.9	0.0051	77.6	1.3	0.0013	299.1	4.7	0.0037
102.8	3.7	0.01	24.25	0.62	0.0015	224.8	5.7	0.006	69.3	1.8	0.0015	262.1	6.6	0.0043
61.7	2	0.0082	20.87	0.6	0.0012	239.5	5	0.0048	82.6	1.2	0.0012	336.4	4.3	0.0034
27.48	0.91	0.0089	9.84	0.29	0.0013	112.1	3.6	0.0051	41.4	1.4	0.005	170.3	5.8	0.0037
40.29	0.8	0.0083	13.76	0.22	0.0012	151.1	1.5	0.0048	51.85	0.52	0.0012	207.5	2.2	0.0035
15.94	0.58	0.0081	5.15	0.12	0.0029	56.6	1.3	0.0047	19.84	0.44	0.0012	83.5	1.8	0.0034
93	2.2	0.0083	30.3	0.57	0.0012	315.1	5.5	0.0048	102.8	1.6	0.0012	388.1	5.7	0.0035
40.7	0.78	0.0083	12.22	0.18	0.0012	120.7	1.5	0.0048	38.18	0.51	0.0012	142.1	1.8	0.0035
63	3.1	0.0082	18.36	0.46	0.0012	181	3.6	0.0048	58.5	0.85	0.0012	219.8	3.6	0.0058
36.4	1.9	0.014	12.54	0.6	0.0012	134.6	6.2	0.0048	47.2	2	0.0012	191.3	8.2	0.0034
22.27	0.99	0.0084	6.65	0.15	0.002	69.25	0.99	0.0049	24.22	0.34	0.0012	99.4	1.3	0.0035
17.6	0.79	0.0081	5.85	0.19	0.0028	61.7	2.2	0.0048	21.11	0.58	0.0012	86	1.8	0.0034
34.51	0.77	0.0083	10.78	0.18	0.0012	105.3	1.3	0.0049	34.79	0.37	0.0012	134.3	1.3	0.0034
495	58	0.0099	82.6	7.5	0.0014	557	35	0.0058	143.4	6.3	0.0015	475	15	0.0041
27.19	0.59	0.008	8.51	0.15	0.0012	82.6	1	0.0047	27.27	0.3	0.0012	103.6	1.1	0.0033
776	41	0.01	148.3	5.8	0.0015	1066	29	0.0061	289.3	5.5	0.0015	940	14	0.0043
134	14	0.0089	25.5	1.8	0.0013	198.2	9.5	0.0052	56	1.7	0.0013	196.6	4.2	0.037
32.86	0.65	0.0081	10.96	0.2	0.0012	111.3	1.8	0.0047	36.45	0.45	0.0012	139.2	1.6	0.0056
49.94	0.97	0.0081	16.1	0.21	0.0021	159	1.6	0.0047	52.64	0.61	0.002	195	1.9	0.0033
20.81	0.81	0.0083	6.88	0.27	0.0013	70.2	2.2	0.0048	24.07	0.63	0.0012	98.2	1.8	0.0034
47.3	0.83	0.0084	14.56	0.2	0.0013	141.2	1.6	0.0049	44.57	0.43	0.0012	165.5	1.7	0.0034
16.3	0.45	0.0086	5.64	0.1	0.0022	60.21	0.93	0.0085	21.52	0.22	0.0012	87.44	0.9	0.0035
80.2	1.5	0.0084	26.9	0.43	0.0013	288.5	4.3	0.0049	94.4	1.6	0.0012	361.5	6	0.0034
24.55	0.59	0.0085	8.06	0.18	0.0013	88.8	1.3	0.0049	30.24	0.38	0.0012	122.7	1.9	0.0034
15.2	0.51	0.029	5.28	0.13	0.0022	59.94	0.95	0.0049	21.33	0.34	0.0012	91.3	1.5	0.0034
15.01	0.45	0.0087	4.8	0.12	0.0013	52.94	0.76	0.0084	17.88	0.23	0.0012	73.48	0.87	0.0035
11.91	0.38	0.0088	3.586	0.095	0.0013	39.35	0.59	0.0083	13.08	0.21	0.0012	54.98	0.76	0.0035
27.03	0.81	0.0089	8.14	0.24	0.0044	83.5	2.1	0.005	26	0.57	0.0012	101.9	2.2	0.0036
33.02	0.74	0.009	10.59	0.15	0.0022	114.7	1.5	0.005	38.82	0.53	0.0013	162.1	2.1	0.0036
17.76	0.63	0.0089	5.7	0.17	0.0022	62.7	1.4	0.0049	20.85	0.49	0.0012	84.5	2	0.0035
7	0.3	NaN	1.909	0.054	NaN	19.85	0.39	NaN	6.79	0.12	NaN	29.13	0.43	NaN
6.76	0.29	NaN	1.992	0.061	NaN	19.97	0.39	NaN	6.93	0.15	NaN	29.77	0.43	NaN
6.95	0.25	NaN	1.864	0.063	NaN	19.87	0.39	NaN	6.61	0.11	NaN	28.89	0.4	NaN
6.84	0.27	NaN	2.004	0.062	NaN	19.9	0.35	NaN	6.86	0.11	NaN	29.2	0.38	NaN
6.93	0.3	NaN	2.046	0.055	NaN	19.9	0.35	NaN	6.87	0.14	NaN	29.49	0.42	NaN
7.08	0.28	NaN	1.926	0.059	NaN	19.94	0.38	NaN	7.1	0.11	NaN	30.03	0.45	NaN
6.65	0.3	NaN	1.915	0.059	NaN	19.85	0.38	NaN	6.69	0.12	NaN	28.64	0.38	NaN
6.99	0.31	NaN	1.936	0.056	NaN	19.92	0.33	NaN	6.68	0.12	NaN	29.5	0.36	NaN

Tm_ppm_m169			Yb_ppm_m173			Lu_ppm_m175			Hf_ppm_m178			Pb_ppm_m208		
Value	2SE	LOD	Value	2SE	LOD	Value	2SE	LOD	Value	2SE	LOD	Value	2SE	LOD
60.47	0.59	0.0011	493	4.8	0.0077	77.86	0.64	0.0011	7917	54	0.0038	< LOD	< LOD	1.4
58.8	0.84	0.0011	478.3	5.7	0.0076	73.9	1.1	0.0011	9203	88	0.0038	< LOD	< LOD	1.6
11.69	0.14	0.0011	102.5	1.3	0.0078	17.86	0.19	0.0011	6460	48	0.0038	< LOD	< LOD	1.7
37.32	0.82	0.0013	315.8	6.4	0.0087	49.81	0.92	0.0013	8040	100	0.0043	< LOD	< LOD	1.8
20.87	0.44	0.0012	187.1	3.4	0.0084	32.38	0.55	0.0012	6197	59	0.0041	3.7	1.3	1.9
54.01	0.86	0.0012	444.5	7	0.0081	69.42	0.88	0.0012	8476	84	0.004	2.7	1.2	1.8
46.3	1.2	0.0014	387	10	0.0094	63.3	1.6	0.0014	7078	65	0.0046	< LOD	< LOD	1.8
62.31	0.85	0.0011	523.1	6.2	0.0075	84.8	0.81	0.0011	7376	73	0.0037	< LOD	< LOD	1.5
32.7	1.2	0.0012	282	10	0.014	48	1.6	0.002	7113	59	0.004	< LOD	< LOD	1.5
38.44	0.4	0.0019	323.7	4.3	0.0076	53.31	0.66	0.0011	7976	65	0.0037	< LOD	< LOD	1.8
15.96	0.31	0.0011	143.5	2.7	0.018	25.24	0.42	0.0011	6107	48	0.0037	< LOD	< LOD	1.7
68.2	1	0.0011	552.3	8.1	0.0076	85.3	1.2	0.0011	8249	60	0.0038	< LOD	< LOD	1.6
25.7	0.31	0.0011	210.8	2.4	0.0075	35.18	0.44	0.0011	6416	49	0.0038	< LOD	< LOD	1.3
39.34	0.54	0.0011	327.2	4.2	0.0074	53.23	0.73	0.0011	6750	53	0.0038	2.3	0.97	1.7
36.9	1.5	0.0011	316	12	0.0075	50.7	1.8	0.0011	8430	110	0.0038	< LOD	< LOD	1.5
19.24	0.25	0.0011	172.5	2.7	0.013	30.23	0.39	0.0011	6454	54	0.0039	< LOD	< LOD	2.2
16.66	0.35	0.0011	149	3.1	0.05	25.68	0.47	0.0011	6241	56	0.0064	< LOD	< LOD	1.9
25.24	0.32	0.0011	211.6	2.4	0.0075	35.94	0.48	0.0011	6301	46	0.0039	< LOD	< LOD	1.6
81.1	1.9	0.0014	611	12	0.009	92.6	1.4	0.0013	9062	74	0.0046	20.6	3.1	2
19.35	0.19	0.0011	162.1	1.5	0.0072	27.39	0.31	0.0011	6413	58	0.0037	< LOD	< LOD	1.7
157.9	2	0.0014	1193	14	0.0095	171.7	2	0.0014	7823	71	0.0049	37.5	3.2	2
34.97	0.72	0.0012	281.8	5.3	0.0081	44.62	0.63	0.0012	8251	78	0.0041	5.6	1.5	1.4
25.54	0.32	0.0011	208.9	3	0.012	33.74	0.46	0.0011	7304	60	0.0064	< LOD	< LOD	1.3
35.68	0.38	0.0011	292.4	3.1	0.0073	46.79	0.46	0.0011	6705	53	0.0037	< LOD	< LOD	1.3
19.29	0.31	0.0011	168.9	2.4	0.0075	30.62	0.41	0.0011	6105	47	0.0038	< LOD	< LOD	1.8
29.89	0.32	0.0011	249.8	2.3	0.0075	41.27	0.46	0.0011	6224	48	0.0038	< LOD	< LOD	1.1
16.56	0.19	0.0012	142.9	1.6	0.0076	24.62	0.27	0.0011	6245	55	0.0039	1.61	0.9	1.5
65.6	1.1	0.0011	530.1	8	0.0075	82.9	1.3	0.0011	8839	97	0.0038	< LOD	< LOD	1.3
23.38	0.31	0.0011	203.7	2.5	0.0075	34.93	0.43	0.0011	6770	53	0.0038	< LOD	< LOD	1.8
17.5	0.28	0.0011	155.9	2.8	0.0075	27.98	0.5	0.0011	6312	52	0.0037	< LOD	< LOD	1.5
14.3	0.2	0.0019	125.5	1.7	0.0076	21.94	0.26	0.0011	6287	53	0.0037	< LOD	< LOD	1.7
10.57	0.17	0.0011	95.2	1.2	0.0076	17.35	0.23	0.0038	6213	47	0.0037	< LOD	< LOD	1.6
17.97	0.34	0.0011	155.2	3	0.013	25.98	0.42	0.0011	6520	63	0.0038	< LOD	< LOD	1.5
31.08	0.36	0.0011	275.8	3.3	0.0077	48.28	0.66	0.0011	6393	50	0.0038	< LOD	< LOD	1.8
15.91	0.38	0.0011	141.5	2.8	0.0076	24.06	0.48	0.0011	6278	60	0.0037	< LOD	< LOD	2
6.247	0.096	NaN	62.25	0.81	NaN	11.77	0.17	NaN	6554	53	NaN	26.4	2	NaN
6.25	0.11	NaN	62.11	0.94	NaN	11.84	0.14	NaN	6530	48	NaN	24.6	2.3	NaN
6.12	0.11	NaN	60.74	0.91	NaN	11.77	0.13	NaN	6609	52	NaN	25.9	2.7	NaN
6.348	0.093	NaN	62.72	0.95	NaN	11.82	0.16	NaN	6555	57	NaN	25.5	2.5	NaN
6.26	0.1	NaN	62.06	0.86	NaN	11.79	0.19	NaN	6580	58	NaN	26.2	2.3	NaN
6.45	0.11	NaN	62.85	0.81	NaN	11.84	0.16	NaN	6531	45	NaN	25.6	2.7	NaN
6.056	0.095	NaN	60.72	0.88	NaN	11.75	0.15	NaN	6556	55	NaN	25.5	2.5	NaN
6.296	0.095	NaN	62.46	0.96	NaN	11.82	0.15	NaN	6567	52	NaN	25.8	2.1	NaN

Th_ppm_m232			U_ppm_m238		
Value	2SE	LOD	Value	2SE	LOD
405.5	3.4	0.002	395.8	3.9	0.0014
411.3	9.2	0.002	451.7	5.8	0.0014
38	1.1	0.002	52.1	1.1	0.0014
177.1	9.2	0.0023	260	17	0.0016
46.5	1.4	0.0022	67.1	1.3	0.0015
624	7.9	0.0021	568.4	6.4	0.0015
305	24	0.029	269	17	0.0017
309.8	3.6	0.002	363.2	3.6	0.0014
183.2	2.8	0.0021	221.4	4.9	0.0015
226.4	3.2	0.002	277.6	2.5	0.0014
97.2	4.2	0.0019	113.8	2.9	0.0023
632	26	0.002	510	13	0.0014
71.34	0.93	0.002	67.27	0.81	0.0014
465	13	0.0019	307.2	4.8	0.0014
283	15	0.002	284	11	0.0014
51.41	0.69	0.002	79.4	1.4	0.0014
43.7	0.79	0.0019	63.46	0.74	0.0014
70.31	0.92	0.002	81.86	0.9	0.0014
981	16	0.0024	878	19	0.0017
45.89	0.53	0.0019	51.3	0.58	0.0013
2724	58	0.0025	1367	22	0.0017
323	15	0.0021	310	10	0.0015
318.1	7.6	0.0019	250.4	3.7	0.0013
144.4	1.4	0.0019	141.1	1.9	0.0013
38.6	1.1	0.002	56.65	0.65	0.0014
76.28	0.74	0.002	73.97	0.77	0.0014
65.9	1.4	0.002	78.79	0.97	0.0014
473.1	8.5	0.002	555.7	9.2	0.021
120.9	3.1	0.002	138.9	2.6	0.0014
39.38	0.82	0.002	64	1.3	0.0014
71.29	0.91	0.002	81.9	1.1	0.0014
22.6	0.33	0.002	35.07	0.4	0.0014
69.1	2.1	0.002	76.7	1.5	0.0014
80.8	1.1	0.002	129.9	1.7	0.0014
133.7	6.1	0.002	124.7	3.7	0.0014
9.5	0.14	NaN	320.7	3.2	NaN
9.62	0.18	NaN	322.1	2.7	NaN
9.23	0.16	NaN	314.7	2.4	NaN
9.71	0.22	NaN	323.2	3	NaN
9.74	0.2	NaN	321.4	2.7	NaN
9.78	0.2	NaN	324.2	2.5	NaN
9.23	0.18	NaN	312.5	2.8	NaN
9.51	0.18	NaN	321.8	2.5	NaN

REE measurements normalised to Boynton (1984)

Sample	La	Ce	Pr	Nd	Sm	Eu	Gd	Tb	Dy	Ho	Er	Tm	Yb	Lu
Boynton (1984)	0.31	0.808	0.112	0.6	0.195	0.0735	0.259	0.0474	0.322	0.0718	0.21	0.0324	0.209	0.0322
K6-428 - 1		32.847	5.446	14.433	91.436	16.898	338.610	556.751	857.453	1244.290	1600.952	1866.358	2358.852	2418.012
K6-428 - 2		38.366	13.304	14.000	65.590	7.401	276.062	487.764	776.398	1169.916	1542.857	1814.815	2288.517	2295.031
K6-428 - 3		3.999	1.125	2.533	13.385	9.007	53.552	90.928	137.919	208.635	287.190	360.802	490.431	554.658
K6-428 - 4		15.891	3.580	8.600	51.282	9.973	188.417	321.308	495.652	739.554	979.524	1151.852	1511.005	1546.894
K6-428 - 5		6.361	3.866	5.783	25.744	17.837	92.278	152.532	243.168	378.830	533.810	644.136	895.215	1005.590
K6-428 - 6		44.802	5.705	11.133	68.462	10.313	257.143	469.831	735.093	1080.780	1424.286	1666.975	2126.794	2155.901
K6-428 - 7		774.752	924.107	593.333	367.179	41.769	396.911	511.603	698.137	965.181	1248.095	1429.012	1851.675	1965.839
K6-428 - 8		28.428	4.000	9.967	61.949	17.211	238.224	440.295	743.789	1150.418	1601.905	1923.148	2502.871	2633.540
K6-428 - 9		17.005	1.518	4.183	28.000	8.748	106.100	207.595	348.137	576.602	810.952	1009.259	1349.282	1490.683
K6-428 - 10		25.545	3.554	7.517	40.718	10.082	155.560	290.295	469.255	722.145	988.095	1186.420	1548.804	1655.590
K6-428 - 11		5.483	1.875	3.533	18.256	13.878	61.544	108.650	175.776	276.323	397.619	492.593	686.603	783.851
K6-428 - 12		87.624	75.893	55.667	106.718	16.571	359.073	639.241	978.571	1431.755	1848.095	2104.938	2642.584	2649.068
K7-428 - 1		5.928	5.304	10.883	51.282	34.014	157.143	257.806	374.845	531.755	676.667	793.210	1008.612	1092.547
K7-428 - 2		195.545	213.393	136.667	116.923	24.354	243.243	387.342	562.112	814.763	1046.667	1214.198	1565.550	1653.106
K7-428 - 3		30.322	10.893	11.767	41.538	7.905	140.541	264.557	418.012	657.382	910.952	1138.889	1511.962	1574.534
K7-428 - 4		90.347	106.250	65.000	49.231	14.830	85.985	140.295	215.062	337.326	473.333	593.827	825.359	938.820
K7-428 - 5		4.728	1.420	3.517	21.641	13.769	67.954	123.418	191.615	294.011	409.524	514.198	712.919	797.516
K7-428 - 6		38.738	46.429	34.333	49.897	30.068	133.243	227.426	327.019	484.540	639.524	779.012	1012.440	1116.149
K7-428 - 7		5631.188	6964.286	4716.667	2769.231	193.197	1911.197	1742.616	1729.814	1997.214	2261.905	2503.086	2923.445	2875.776
K7-428 - 8		4.035	3.259	6.700	33.231	22.857	104.981	179.536	256.522	379.805	493.333	597.222	775.598	850.621
K7-428 - 9		7561.881	9366.071	6150.000	3810.256	223.129	2996.139	3128.692	3310.559	4029.248	4476.190	4873.457	5708.134	5332.298
K7-428 - 10		1547.030	1910.714	1216.667	682.051	49.660	517.375	537.975	615.528	779.944	936.190	1079.321	1348.325	1385.714
K7-428 - 11		25.161	2.402	6.550	35.949	6.095	126.873	231.224	345.652	507.660	662.857	788.272	999.522	1047.826
K7-428 - 12		12.735	5.920	12.083	56.205	27.619	192.819	339.662	493.789	733.148	928.571	1101.235	1399.043	1453.106
K7-428 - 13		4.053	2.000	4.700	23.795	20.871	80.347	145.148	218.012	335.237	467.619	595.370	808.134	950.932
K7-428 - 14		5.421	5.580	12.667	60.103	43.905	182.625	307.173	438.509	620.752	788.095	922.531	1195.215	1281.677
K7-428 - 15		5.569	1.429	3.300	16.974	12.844	62.934	118.987	186.988	299.721	416.381	511.111	683.732	764.596
K7-428 - 16		42.463	3.580	10.917	73.487	8.925	309.653	567.511	895.963	1314.763	1721.429	2024.691	2536.364	2574.534
K7-428 - 17		11.101	1.857	5.067	25.897	7.864	94.788	170.042	275.776	421.170	584.286	721.605	974.641	1084.783
K7-428 - 18		5.396	1.607	3.117	16.615	12.068	58.687	111.392	186.149	297.075	434.762	540.123	745.933	868.944
K7-428 - 19		5.384	1.348	3.067	17.641	10.299	57.954	101.266	164.410	249.025	349.905	441.358	600.478	681.366

K7-428 - 20		3.361	0.911	2.467	12.410	10.898	45.985	75.654	122.205	182.173	261.810	326.235	455.502	538.820
K7-428 - 21		6.002	2.036	5.383	30.359	13.265	104.363	171.730	259.317	362.117	485.238	554.630	742.584	806.832
K7-428 - 22		8.082	2.563	6.767	38.667	15.293	127.490	223.418	356.211	540.669	771.905	959.259	1319.617	1499.379
K7-428 - 23		6.386	1.455	3.733	18.769	11.007	68.571	120.253	194.720	290.390	402.381	491.049	677.033	747.205
Whole rock	280.968	201.733	148.214	98.500	53.846	23.673	32.394	25.527	19.161	13.928	12.571	10.802	9.809	7.764

Measurements coloured grey are inclusion/zircon mixtures

Boynton W. V. (1984) Chapter 3 - Cosmochemistry of the Rare Earth Elements: Meteorite Studies. In Developments in Geochemistry (ed. P. Henderson). Rare Earth Element Geochemistry. Elsevier. pp. 63–114.

Supplementary material III
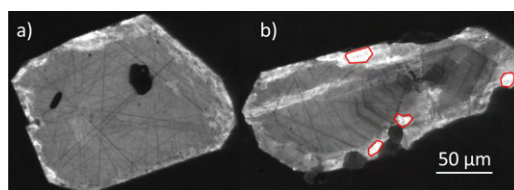
Figure 4.iv: Cathodoluminescence images of two representative crystals showing both homogeneous (left) and heterogeneous zonation (right). Note the small scratches on the surface are not intrinsic to the crystal. Very bright zones on the right image indicated with red lines are apatite inclusions.
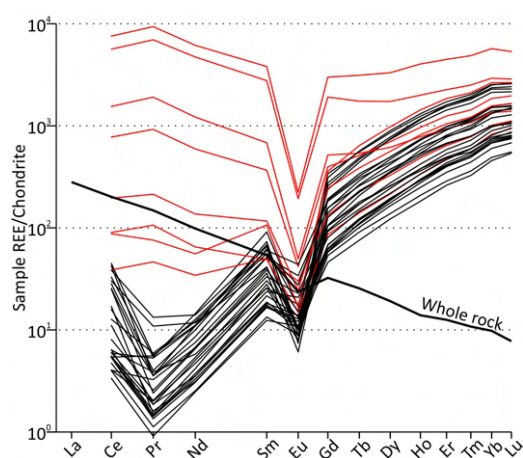
Figure 4.v: Matsuda diagram (Whitehouse and Kamber, 2002) showing REEs normalised to chondrite (Boynton, 1984) from 34 zircon crystals across samples SS14-28a and SS14-28b and SS14-28b whole rock. Red lines are analyses that ablated across apatite inclusions, and are thus not representative of the zircon chemistry.

Boynton W. V. (1984) Chapter 3 - Cosmochemistry of the Rare Earth Elements: Meteorite Studies. In Developments in Geochemistry (ed. P. Henderson). Rare Earth Element Geochemistry. Elsevier. pp. 63–114.

Whitehouse M. J. and Kamber B. S. (2002) On the overabundance of light rare earth elements in terrestrial zircons and its implication for Earth's earliest magmatic differentiation. Earth and Planetary Science Letters 204, 333–346.

Chapter 5

Zircon double-dating of Quaternary eruptions on Jeju Island, South Korea

While this chapter consists of a published paper changes in line with examiner comments have been made post-publication.

Abstract

Models of volcanic eruption periodicity are vital for hazard prediction, but require an understanding of the past pattern of melt evolution and transport within the crust. Zircon double-dating combines (U-Th)/He methods with U-Pb or U-Th disequilibrium geochronology to determine the timing of volcanic eruptions for rocks with a particular emphasis on those younger than ca. 1 Ma. This paper focuses on the Jeju Island intraplate volcano in South Korea, and compares a previously proposed model for trachyte eruption with new zircon double-dating results.The results document four episodes of trachyte eruption on Jeju. The oldest trachytes were erupted at ca.750–477 ka, followed by an episode at ca. 97–53 ka. Two further eruptive episodes occurred at ca. 31–23 ka and ca. 2 ka. This ca. 2 ka eruption age is the first geochronological documentation of such young eruptive activity from the island. In addition to the new eruption ages, there is evidence for three separate stages of zircon crystallisation, which are correlated with the three oldest eruption stages. The strong temporal correlation of zircon crystallisation and eruption on Jeju points to a simple magmatic plumbing system. These observations have important implications for hazard monitoring and mitigation on Jeju Island by highlighting the historical trachyte eruptions and the magmatic tempo for this system.

5.1 Introduction

Understanding the timelines of past volcanic eruptions and how they relate to the evolution of magma in the upper crust is vital for constructing models of magma transit from source to surface. Jeju Island,South Korea, is a Quaternary intraplate volcano of which the associated lava suite has a spectrum of chemical compositions from alkali basalt to trachyte and sub-alkali basalt to basaltic andesite extrusive products (Park et al., 1999). With a population of 700,000 and a status as a busy tourist destination, understanding the recent volcanic history of Jeju will underpin models of future volcanic risk. However, the eruption timeline and differentiation history of magma at Jeju are not yet well-constrained. Whole rock Ar-Ar age data (n= 210) has been used to constrain the eruptive ages of basaltic lava to 990–25 ka (Koh et al., 2008;Koh and Park, 2010a, 2010b; Koh et al., 2013; Koh et al., 2019). However, the analysed Ar-Ar material was collected from hydrological cores and mostly lacks stratigraphic context, particularly because single eruptive events may not be laterally continuous (Martí et al., 2018). In addition, the Ar-Ar whole rock dating approach may be problematic for young eruptions due to excess ^{40}Ar (e.g.,McDougall and Harrison, 1999; Hora et al., 2010). In such cases, verification by an independent radiometric dating method is required to provide robust eruptive recurrence intervals and to constrain rates of magmatic evolution in differentiated volcanic systems.

Combined U-Th-Pb and (U-Th)/He dating of zircon, also known as zircon double-dating (ZDD), is a relatively new geochronological method (e.g.Schmitt et al., 2006, 2011; Danišík et al., 2012, 2017, 2020) suitable for dating young (ca. <1 Ma) zircon-bearing volcanic rocks. ZDD combines either U-Th disequilibrium (for zircon with crystallisation ages ≲350 ka) or U-Pb geochronology (for older zircon),with (U-Th)/He dating. Given the different closure temperatures of these radiometric systems (>900 °C for U-Th-Pb and ~180 °C for (U-Th)/He; Cherniak and Watson, 2001; Reiners et al., 2004), ZDD yields not only the eruption age of zircon crystals, but also their crystallisation age and therefore allows the estimation of their residence time in the magma reservoir (e.g.Schmitt et al., 2013, 2014a; Danišík et al., 2020).

In this study, ZDD is applied to samples of Jeju trachytes, and to xenoliths entrained by trachybasalts or basalts that have not been previously dated but for which geological context was established by detailed field work. The aim of this research is to (i) refine existing geochronology, (ii) better constrain the timeline of Jeju volcanism by dating previously undated units, and (iii) provide constraints on the dynamics of magmatic processes in the crust beneath the Jeju volcano from zircon crystallisation ages. This improved understanding of past magmatism and volcanism informs models of melt generation and can provide insight into the likelihood of hazardous future volcanic eruptions on the island.

5.2 Geological setting

Jeju Island is a 31 km by 73 km elliptical cumulative volcanic field of Quaternary age, situated 90 km south of the Korean peninsula (Figure 5.1,Supplementary material II Figure 5.i, 5.ii) (Brenna et al., 2012a, 2012b; Woo et al., 2013a). Jeju Island is formed predominantly by lavas ranging from high-Al and low-Al alkali basalts to trachytes (Tatsumi et al., 2005; Brenna et al., 2012a, 2012b). The island comprises Jurassic to Cretaceous basement, covered by continental shelf deposits of quartzite and mud-stone, overlain by approximately 100 m of volcaniclastic deposits (Seoguipo formation). Stratigraphically overlying these rocks are lavas which form a major shield volcano (Sohn et al., 2008; Woo et al.,2013b) known as Hallasan or Mt. Halla. At the summit of Hallasan, 1950 m above sea level, is the Baengnokdam crater, which is filled by a trachyte lava dome and is thought to be the location of the source of a trachybasalt lava flow (Ahn and Hong, 2017). In addition to this summit crater, there are multiple trachyte outcrops within the elevated area of Hallasan (Figure 5.1c). Outside of this area there are multiple small trachyte outcrops which are thought to be small in situ domes or flows. Additionally, there are more than 300 monogenetic cones (although some vents sourced multiple eruptions; Brenna et al., 2011), and numerous tuff rings and tuffaceous deposits distributed across the island (Woo et al., 2013b).
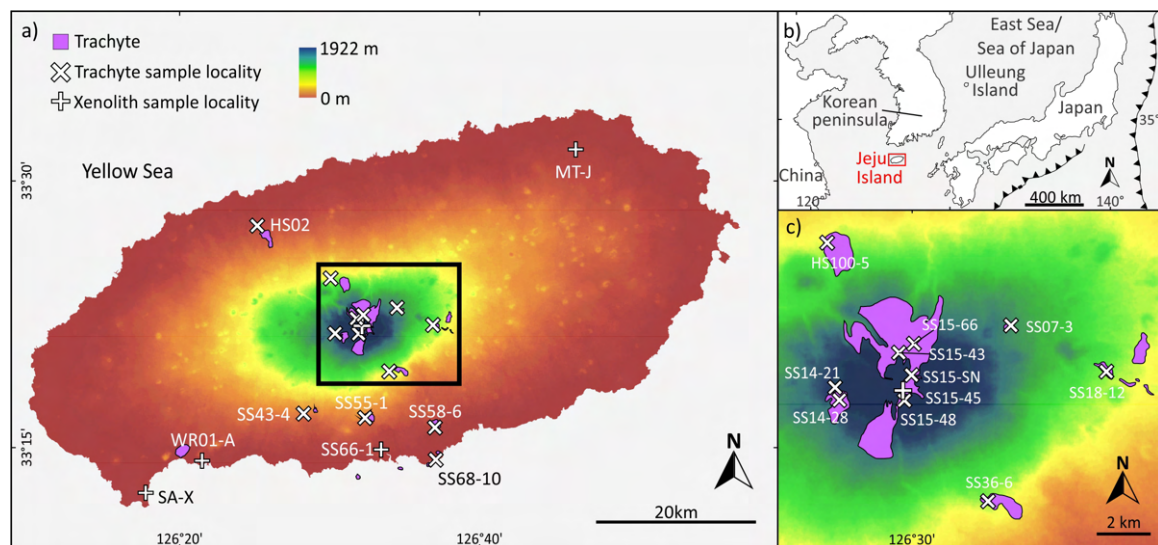
Figure 5.1: a) Digital Elevation Model of Jeju Island (NASA/METI/AIST/Japan Spacesystems, and U.S./Japan ASTER Science Team, 2019) with trachyte outcrops mapped and sample localities marked. b) Map of the region with the Japanese subduction zones indicated. c) Digital Elevation Model of the Hallasan summit area (marked on the complete map of Jeju) and sample localities. Trachyte mapping modified after (Park et al., 2000a, 2000b).

The initial evolution of Jeju Island is still a matter of some debate.The onset of volcanism at ca. 1.8 Ma is based on fossil biostratigraphic markers and Sr isotopes (Kim and Heo, 1997; Khim et al., 2001; Kanget al., 2010). In contrast, paleomagnetic data on

volcaniclastics and marine sediments suggests volcanism began much earlier during the late Pliocene (ca. 4 Ma) (Min et al., 1986;Lee, 1988). Finally, the oldest eruption age recorded on trachybasalts by whole rock Ar-Ar dating is 992 ± 21 ka (2σ)(Koh and Park, 2010b).In order to define the timing of the major stages of volcanic activity,numerous basalts (n= 203) and trachytes (n= 7) were dated using the Ar-Ar whole rock method (Koh et al., 2008; Koh and Park,2010a,2010b; Koh et al., 2013; Brenna et al., 2015).Brenna et al. (2015)summarised the existing geochronological data, combined these with geochemical data and field relationships and proposed a comprehensive model for the geological evolution of Jeju. This model defines three basaltic stages(Stage 1b at 1700–500 ka, Stage 2 at 500–250 ka and Stage 3b at 250–25 ka), and two trachytic eruptive stages (Stage 1t at 960–500 ka and Stage 3t at 25–1 ka)(Figure 5.6). In addition to whole rock Ar-Ar geochronology, optically stimulated luminescence (OSL) has been applied to sediments underlying trachyte and trachybasalt lavas at the Baengnokdam summit, suggesting the lavas' eruption at <37 ka and between 21 and 19 ka, respectively (Ahn and Hong, 2017).

Historical records suggest the youngest volcanic activity on Jeju occurred at 1002 CE and 1007 CE (Lee and Yang, 2006). The 1002 CE eruption is described in historical documents as follows: "'Red water'(lava)erupted from four orifices in Mt. Tamra (now called Mt. Hanra). Ended in 5 days. All the 'red water' turned into bricks and stones" (Lee and Yang, 2006), where Mt. Hanra is another spelling of Mt. Halla. The youngest geochronological ages related to volcanic activity were reported by Ahn (2016)who applied OSL and radiocarbon dating to under- and overlying sediments of three monogenetic cones resulting in ages of<3.8 ka, >4.5 ka, and <6–7 ka. However, previous studies have not succeeded in making a positive match between historic records and geochronological dating of volcanic products due to the difficulty of locating the volcanic products described in the historic records.

5.3   Samples and methods

Twenty samples were analysed; fourteen trachyte samples, four xenoliths, a sample from a tuff ring, and one rhyolite (Table 1). The samples were collected from a variety of eruptive products (lava flows, domes and pyroclasts) mostly from the central area of Hallasan (Figure 5.1a, c). Zircon crystals were separated at the Geology Science laboratory in South Korea using standard mineral separation procedures. A selection of zircon crystals were imaged using cathodoluminescence (CL) and the remaining crystals were dated either by the U-Th disequilibrium method (Schmitt et al., 2006, 2011; Schmitt,2011), or by the U-Pb method if it was assumed, based on previous work, that the zircon crystallisation age was $\gtrsim$350 ka. These crystallisation ages are required for disequilibrium correction of the $\lesssim$1 Ma (U-Th)/He data (Schmitt et al., 2006, 2010a). Whole rock U and Th measurements

for U-Th disequilibrium dating and corrections were analysed in the LabWest laboratory, Perth. U-Th disequilibrium dating was carried out at the Heidelberg Ion Probe (HIP) laboratory (Heidelberg University).

U-Pb dating was carried out at the HIP laboratory, and in two laboratories at the John de Laeter Centre (JdLC), Curtin University (SHRIMP II Facility and GeoHistory laser ablation inductively coupled plasma (LA-ICPMS) Facility). U-Pb ages <1 Ma were corrected for U-Th disequilibrium following the method of Sakata et al. (2017)and Sakata (2018). The initial Pb isotopic ratios from the model of Stacey and Kramers (1975)for contemporaneous Pb were used to correct all ratios using the ^{207}Pb correction method. Values were projected from common Pb onto a concordia curve that was modified to reflect U-Th disequilibrium in the system(Sakata et al., 2017; Sakata, 2018; Kirkland et al., 2020). For samples where the uncertainty (2σ) on the U-Th-Pb age was of the same order of magnitude as the maximum age difference, a weighted mean was calculated.Following U-Th-Pb analysis, the zircon crystals were (U-Th)/He dated in the JdLC Low Temperature Thermochronology Facility following the procedures outlined in Danišík et al. (2017, 2020). (U-Th)/He ages <1 Ma were corrected for U-Th disequilibrium, which occurs because not enough time has elapsed since zircon crystallisation for secular equilibrium to have been reached between ^{238}U and its long-lived intermediate daughter isotopes (most notably ^{230}Th with a 75.7 kyr half-life). The deficit or surplus in ^{230}Th causes the number of ^{4}He generated during ^{238}U decay to be lower or higher than expected. A correction has been incorporated into age calculations following the procedures of Schmitt et al. (2010a). Using the MCHeCalc program,ZDD eruption ages were calculated as MCHeCalc best-fit ages. Disequilibrium corrections were not required for zircon grains erupted >1 Ma as secular equilibrium is attained in these older crystals. In this case,sample eruption ages were calculated as weighted means using Isoplot (Ludwig, 2012). Full details on the analytical methods are provided in Supplementary material I.

5.4   Results

Average ZDD ages, including crystallisation and eruption ages, are summarised in Table 1 and Figure 5.2. Unless stated otherwise all uncertainties are 2σ. Full results are provided in Supplementary materials III, IV and V.

5.4.1   Volcanic samples

Cathodoluminescence (CL) images of zircon crystals from the trachyte samples with crystallisation ages <350 ka reveal oscillatory zoning, sharp well-defined crystal edges and bi-pyramidal terminations. Zircon crystals from >350 ka distil trachytes preserve textures such as dissolution-regrowth fronts, interpreted as evidence of zircon resorption into the

Table 5.1: Summary of results

Sample ID	Lithology/type	$n_{U\text{-}Th\text{-}Pb}$[a]	U-Th-Pb minimum age ±2σ[b] (ka)	U-Th-Pb maximum age ±2σ[b] (ka)	Mean U-Th-Pb age ±2σ (ka)	MSWD	n_{ZDD}[e]	ZDD eruption age ±2σ (ka)f	MSWD
SS55-1	trachyte/lava	7	744 ± 43	806 ± 73	768 ± 20[c]	0.7	2	**750 ± 61**	n/a
SS43-4	trachyte/lava	24	377 ± 319	988 ± 907	659 ± 55[c]	3.5	7	**651 ± 34**	n/a
SS58-6	trachyte/lava	13	350 ± 93	565 ± 30	527 ± 29[c]	2.7	6	**477 ± 23**	n/a
WR01-A	granite/ xenolith	20	73,000 ± 1,000	497,000 ± 15,000	n/a	n/a	7	**740 ± 66**	2.4
SA-X	quartzite/xenolith	21	104,000 ± 2,000	2,537,000 ± 31,000	n/a	n/a	9	**3.6 ± 0.7**	3.4
MT-J	quartzite/xenolith	n/a	n/a	n/a	n/a	n/a	6	**7.2 ± 1.4**	0.6
SS66-1	???/ xenolith	20	71,300 ± 5,000	2,160,000 ± 84,000	n/a	n/a	n/a	**n/a**	n/a
HS100-5	trachyte/lava	41	87 ± 23	168 ± 117	111 ± 14[d]	1.1	7	**97 ± 7**	n/a
SS15-66	trachyte/lava	40	94 ± 30	168 ± 137	110 ± 7[d]	0.7	14	**78 ± 5**	n/a
HS02	trachyte/lava	16	91 ± 26	> 350	n/a	n/a	9	**71 ± 4**	n/a
SS15-43	trachyte/lava	44	91 ± 15	196 ± 108	n/a	n/a	12	**71 ± 6**	n/a
SS68-10	trachyte/lava	7	99 ± 26	> 350	n/a	n/a	3	**67 ± 9**	n/a
SS14-28	trachyte/lava	41	72 ± 22	131 ± 67	83 ± 9[d]	0.7	6	**62 ± 6**	n/a
SS14-21	trachyte/lava	20	81 ± 21	235 ± 191	n/a	n/a	7	**53 ± 6**	n/a
SS18-12	trachyte/lava	20	36 ± 20	50 ± 9	44 ± 3[d]	0.8	8	**31 ± 2**	n/a
SS15-SN	trachyte/lava	42	31 ± 9	100 ± 112	n/a	n/a	10	**25 ± 2**	n/a
SS36-6	trachyte/lava	49	24 ± 44	100 ± 114	n/a	n/a	10	**24 ± 1**	n/a
SS15-48	rhyolite	19	28 ± 9	184 ± 116	n/a	n/a	8	**23 ±2**	n/a
SS07-3	trachyte/lava	16	4.6 ± 9	24 ± 15	n/a	n/a	11	**2.0 ± 1.0**	n/a
SS15-45	trachyte/xenolith	49	28 ± 11	57 ± 17	31 ± 4[d]	0.7	14	**28 ± 1**	n/a

[a] Number of U-Th-Pb dated crystals
[b] 2σ values for U-Th disequilibrium data are the mean of the positive and negative uncertainties
[c] Calculated as error weighted mean using Isoplot v.3.75 (Ludwig, 2012)
[d] Calculated as isochron age using Isoplot v. 3.75 (Ludwig, 2012)
[e] Number of crystals analysed by ZDD
[f] Eruption age calculated as ZDD using MCHeCalc (Schmitt et al., 2010a), or as error weighted mean using Isoplot v. 3.75 (Ludwig, 2012)
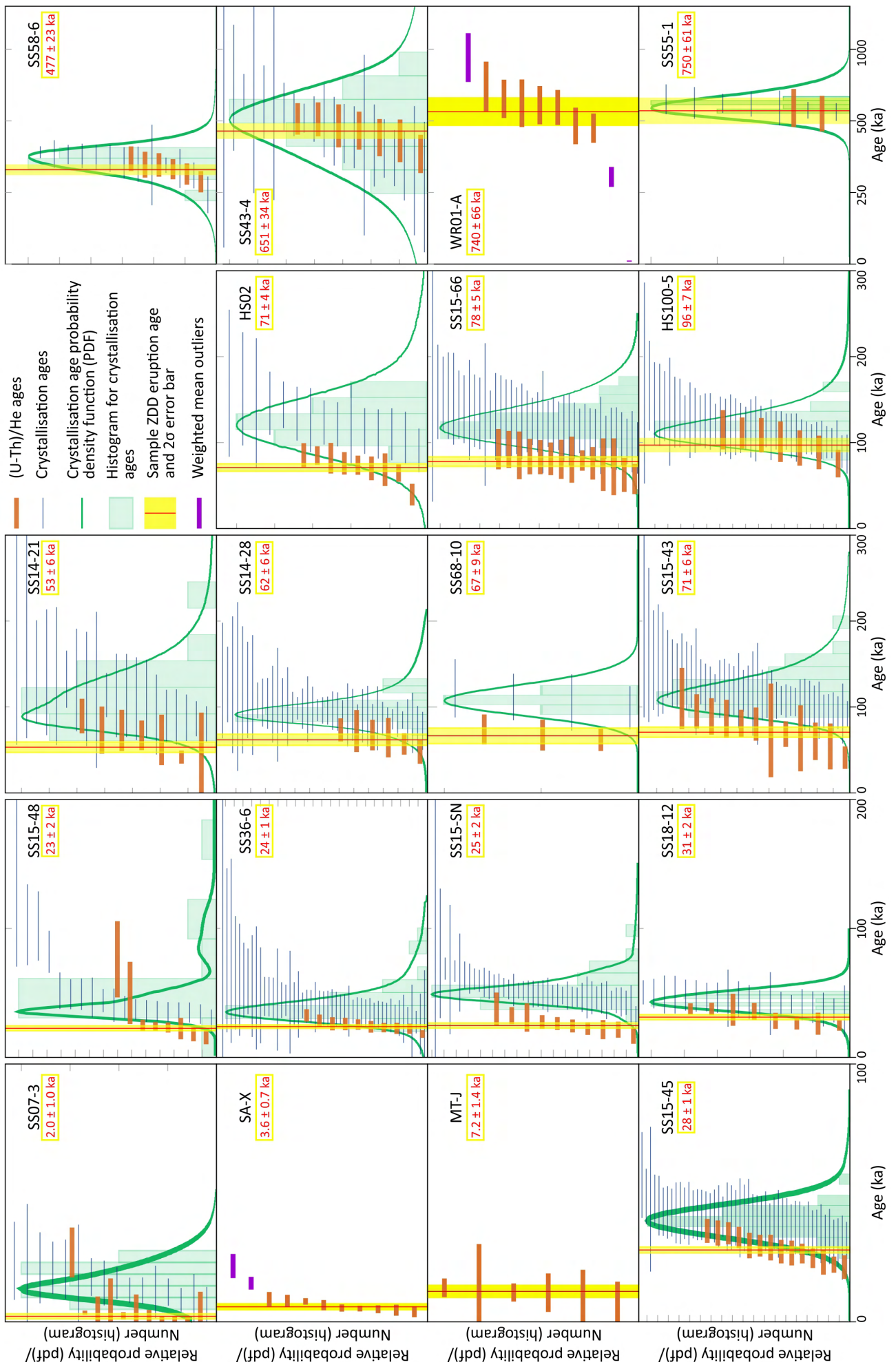
Figure 5.2: ZDD ages combined with crystallisation ages for trachyte eruptions <100 ka.

magma (Figure 5.3c, d, e).
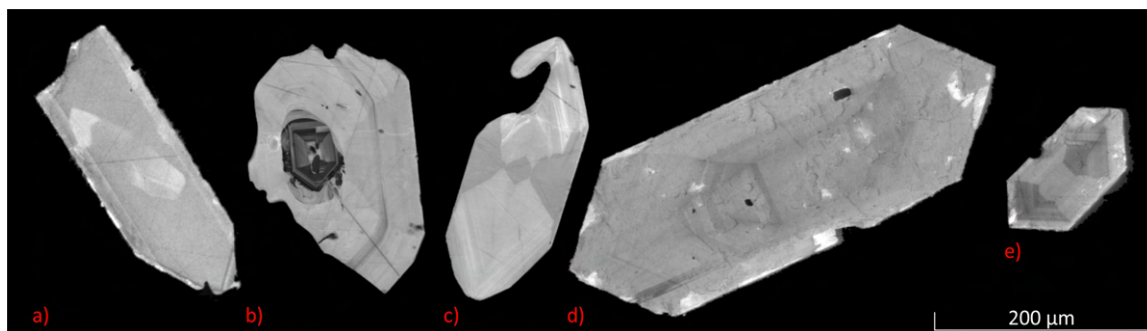
Figure 5.3: Cathodoluminescence of zircons crystallised in Jeju trachytes (c, d and e) and xenoliths (a and b).

5.4.1.1   U-Pb and U-Th disequilibrium zircon crystallisation ages

Zircon U-Pb ages were determined for samples SS55–1, SS43–4 and SS58–6 (Table 1). The younger ages do not correlate with enhanced U concentration and therefore there is no evidence of radiation damage-driven radiogenic-Pb loss. The single grain age ranges for samples SS55-1, SS43-4 and SS58-6 are 744–806 ka, 457–988 ka and 350–565 ka respectively.

Zircon U-Th disequilibrium ages were calculated for 13 samples (Table 1). U-Th disequilibrium model ages for single crystals were calculated as two-point isochrons between the whole rock and the crystal measurements. Five trachyte samples yielded U-Th disequilibrium activity ratios that define an isochron in $(^{230}\text{Th})/(^{232}\text{Th}) - (^{230}\text{Th})/(^{238}\text{U})$ space (Figure 5.4). For these samples, an isochron age was calculated using a York-fit regression as implemented in Isoplot (Ludwig, 2012).

Samples dated by U-Th disequilibrium were categorised into three groups: Samples HS02, HS100-5, SS68-10, SS14-21, SS14-28, SS15-66 and SS15-43 have U-Th disequilibrium crystallisation ages between 80 ± 51 and 169 ± 91 ka. Samples SS15-48, SS15-SN, SS18-12 and SS36-6 have U-Th disequilibrium crystallisation ages between 26 ± 24 and 69 ± 8 ka (93% of the data fall in this range). Sample SS07–3 has the youngest crystallisation ages, ranging between 5 ± 9 and 24 ± 15 ka. A total of four grains in samples HS02 and SS68–10 yielded analyses in secular equilibrium ($\gtrsim$350 ka).

The duration of crystallisation for each sample was estimated using a Monte Carlo implementation of a Bayesian approach (Isoplot; Ludwig, 2012) which takes the youngest and oldest crystallisation age of the sample and the sample ZDD eruption age as inputs. This approach incorporates the a-priori knowledge that the eruption age is the lower bound for crystallisation ages. The shortest crystallisation duration on Jeju is 12.2 +11.7/-10.9 ka (SS18-12) and the longest is 260 +940/-240 ka (SS43-4).

154
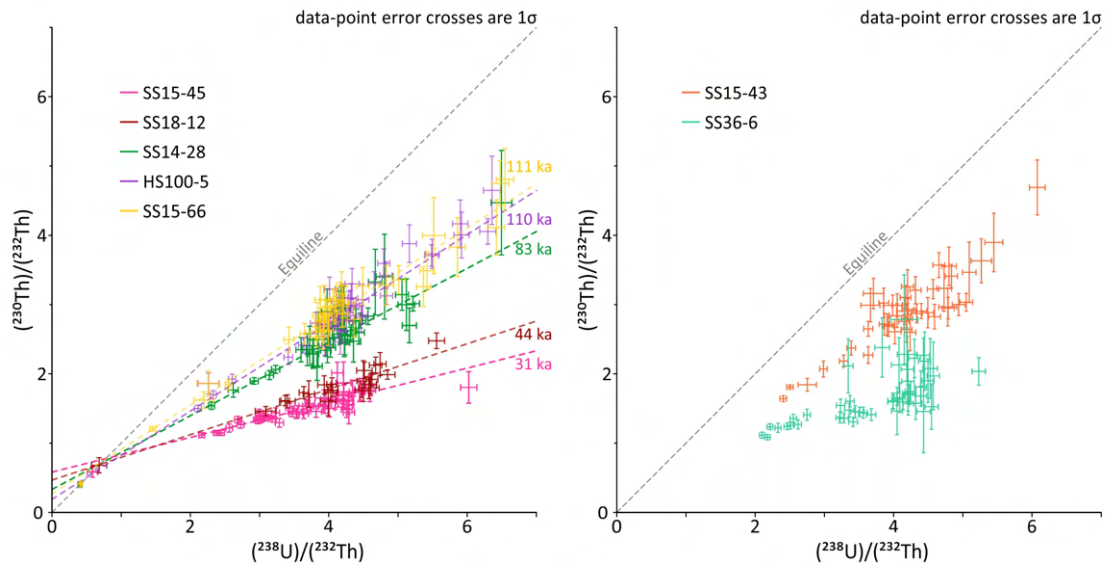
Figure 5.4: U-Th disequilibrium results for seven example samples. Left: Isochrons calculated from U-Th disequilibrium measurements for five samples. Right: for comparison two samples with no isochrons ages calculated due to scatter.

5.4.1.2 ZDD data

The ZDD eruption ages (Table 1) range from 750 ± 61 to 2 ± 1 ka and define groups as follows: the oldest group contains three trachyte samples with eruption ages ranging from 750 ± 61 to 477 ± 23 ka, which are ca. 400 ka older than the other samples. The second oldest group contains seven samples with eruption ages of 96 ± 7 to 53 ± 6 ka. The next youngest group is ca. 22 ka younger, ranging from 31 ± 2 to 23 ± 2 ka. The youngest eruption age is from sample SS07–3 at 2.0 ± 1.0 ka.

5.4.2 Xenolithic samples

From the CL images it can be seen that the shapes of xenolith zircon grains vary from sharp well-defined euhedral crystals, to rounded grains. There are also crystals with clear cores and rims and grains with no apparent zoning (3a, b).

5.4.2.1 U-Pb and U-Th disequilibrium zircon crystallisation ages

Three samples yielded U-Pb ages >1 Ma. Two of these were xenoliths and the other, SS66-1, was a clast from a tuff ring (Table 1). Twenty zircon crystals from sample WR01-A were analysed and the concordant U-Pb ages range from 73 ± 1 to 81 ± 1 Ma with a single outlier at 497 ± 15 Ma. Nine zircon crystals from sample SA-X were analysed 21 times with 11 concordant zircon U-Pb ages which range from 104 ± 2 Ma to 2537 ± 31 Ma, including three older ages at 1734 ± 94, 2389 ± 60, and 2537 ± 31 Ma. SS66–1 was analysed 20 times on 20 zircon crystals, but only yielded four concordant ages. The

discordant zircon U-Pb ages range from 71 ± 5 to 2160 ± 84 Ma, concordant ages range from 464 ± 22 to 1860 ± 86 Ma.

Only one trachyte xenolith entrained in trachybasalt, SS15–45, was found to have a crystallisation age of <350 ka and was thus amenable for U-Th disequilibrium geochronology. This sample has a U-Th disequilibrium isochron age of 31 ± 4 ka (MSWD = 0.72, n = 49) and a range of U-Th disequilibrium model ages of 27.8 ± 10.9 ka to 56.8 ± 16.7 ka from 49 spots on 45 crystals. A field photo of SS15–45 can be found in Supplementary material II (Figure 5.iv).

Sample MT-J was not measured for zircon crystallisation ages as it is a quartzite xenolith. In this case, the crystallisation age must be significantly older than the eruption age and the sample can be dated using the (U-Th)/He method without disequilibrium correction.

5.4.2.2 (U-Th)/He and ZDD data

The range of xenolith (U-Th)/He ages is 740 ± 66 to 3.6 ± 0.7 ka covering the whole range of ages seen in the trachyte data. Samples WR01-A, MT-J and SA-X ages were calculated as weighted means, at respectively 740 ± 66 ka (MSWD = 2.4, n = 7), 7.2 ± 1.4 ka (MSWD = 3.4, n = 9) and 3.6 ± 0.7 ka (MSWD = 0.6, n = 6). SS15–45 has a ZDD eruption age of 28 ± 1 ka calculated using MCHeCalc. SS66–1 is an outlier because of much older (U-Th)/He ages that range from 72 ± 4 Ma to 284 ± 15 Ma and are uniformly distributed across this range and do not record a meaningful geological event.

5.5 Discussion

5.5.1 Interpretation of results

5.5.1.1 Volcanic samples

Two samples, SS43–4 and SS58–6, yielding <1 Ma U-Pb ages, had broad age spectra (457–988 ka and 350–565 ka). We interpret these broad spectra to indicate a protracted zircon crystallisation interval. However, in contrast sample SS55-1 yielded a MSWD value from the weighted mean (Table 1; 768 ± 20, MSWD = 0.69, n = 7) consistent with a single population grown over a short crystallisation period.

The presence of four grains in secular equilibrium (one from HS02, three from SS68–10) indicates these samples either underwent a period of protracted crystallisation of zircon in the magma, or inherited older zircon from other sources, which were entrained in the melt. The large age gap (HS02: 181 ka; SS68–10: 228 ka) between the age of the oldest grain and the next oldest crystallisation age suggests that inheritance is the more likely explanation.

Only one sample, SS15–48, contains crystals which are both in disequilibrium and are outliers from the other crystallisation ages obtained on the same sample. The 29 kyr gap between the youngest outlier and the oldest age of the non-outlier grains is longer than the entire age range of the younger population (23 ka). This suggests that the outliers represent grains inherited during magma mixing or grains entrained in the melt at the time of eruption (i.e. xenocrysts).

The ZDD ages are interpreted as the age at which the samples were cooled through ∼180 °C (i.e. during or shortly after eruption; Reiners et al., 2002). Under this interpretation, all eruption ages are either slightly younger than the corresponding crystallisation ages or overlap these ages within uncertainty (barring a single crystallisation age in sample SS58–6). This suggests that zircon crystallisation continued right up until eruption, within the uncertainty of single crystal ages.

5.5.1.2 Xenolithic samples

Three samples have U-Pb ages ranging from 73 Ma to 2537 Ma. Jeju Island basement rock is thought to consist of quartzite and granitic plutons of Jurassic and Cretaceous ages and Precambrian gneisses similar to the South East of the Korean peninsula (Kim et al., 2002). These xenoliths are therefore interpreted to be derived from these basement rocks. This interpretation is supported by the diverse crystal shapes of zircon from sample SA-X and MT-J, reflecting a likely detrital origin of this zircon in the quartzite (images in Supplementary material II, Figure 5.v). In the case of WR01-A, which has only one U-Pb crystallisation age outlier, a granitic origin is proposed because of the regular appearance of the zircon crystals and the aforementioned basement ages, which are comparable with the crystallisation ages. Sample SS15–45 has a young crystallisation age (31 ± 4 ka) and is thought to be a trachyte xenolith from the Jeju volcanic field, entrained in a trachybasalt. This crystallisation age is interpreted as the maximum eruption age of the trachyte because the crystallisation of zircon must have occurred either prior to (or simultaneously with) trachyte eruption and entrainment. This also constrains the maximum eruption age of the trachybasalt, as it must have erupted after trachyte zircon crystallisation.

The (U-Th)/He ages of xenolith samples should be interpreted with caution because the zircon crystals within the xenoliths may not have been fully reset (i.e. the zircon may not have been held at a high enough temperature for a sufficient period of time for He to fully diffuse out of the crystal; Reiners et al., 2002).

Samples WR01-A, SA-X, MT-J and SS15–45 are all small xenoliths (< 15 cm diameter) entrained in basaltic lavas. The temperature of basaltic lava is estimated to be 1150–1250°C (Blondes et al., 2007). The minimum duration for xenoliths up to 10 cm in diameter (and their composite zircon grains) to reset >99.99% of the inherited ^{4}He at this temperature is ca. 1 h (Blondes et al., 2007). Samples MT-J, SA-X and WR01-A are assumed to

have been entrained in magma at depth, due to their U-Pb ages. These ages suggest they are from the basement, rather than being formed within the lifetime of volcanism on Jeju, and are therefore assumed to have undergone the conditions necessary for their zircons to be fully reset. Consequently their (U-Th)/He ages are interpreted as fully reset eruption ages. SS15–45 is a trachyte formed in the Hallasan summit area and may have been entrained in the eruptive product at any stage of eruption. Therefore the ZDD age for SS15–45 is interpreted as a maximum eruption age of the trachybasalt. The eruption age of the trachyte cannot be measured as the He concentration is thought to be reset by reheating. This maximum eruption age of the trachybasalt can simultaneously be the minimum eruption age of the trachyte. Additionally, as SS15–45 is interpreted as a product of Jeju volcanism, it is redefined as a cognate inclusion.

Sample SS66–1 was found in a tuff ring and there is no evidence that this xenolith was significantly heated in contact with magma for any period of time. This, alongside the extremely old and variable (U-Th)/He ages measured (>72 Ma), suggests that it is a basement xenolith that was not heated for a long enough time to reset the zircons.

5.5.2 Comparison of eruption ages with previously published ages

5.5.2.1 Ar-Ar whole rock

Seven samples measured in this study have been dated by whole rock Ar-Ar (and K-Ar) methods: SS55–1 (799 ± 6 ka; Koh et al., 2013), SS43–4 (765 ± 5 ka; Koh et al., 2013), SS58–6 (542 ± 6 ka; Koh et al., 2013), SS68–10 (288 ± 1 ka; Koh et al., 2013), HS02 (128 ± 4; Koh et al., 2013), SS15–66 (102 ± 1; Koh et al., 2019), and SS15-SN (25 ± 8; Won et al., 1986; 70 ± 10; Tamanyu, 1990). The resulting ages have been interpreted to indicate the timing of eruption (Won et al., 1986; Tamanyu, 1990; Koh et al., 2013; Koh et al., 2019). All Ar-Ar whole rock ages are older than the ZDD eruption ages determined on the same localities in this study. Sample SS55–1 and SS15-SN are exceptions. SS55–1's Ar-Ar whole rock age is older but within uncertainty of the ZDD eruption age. In the case of SS15-SN, Won et al. (1986) obtained a K-Ar age within error of the ZDD eruption age while Tamanyu (1990) measured a significantly older age. Five samples also have U-Th disequilibrium or U-Pb zircon crystallisation ages which are younger than the whole rock Ar-Ar eruption age, including SS55–1 (Figure 5.5).

We place greater confidence in the ZDD eruption ages obtained in this work than in the previous whole rock Ar-Ar ages because ZDD uses two independent geochronological methods, both of which yielded younger ages than those determined by whole rock Ar-Ar analysis. Previous work has indicated that Ar-Ar whole rock ages may be compromised by low radiogenic Ar, excess radiogenic Ar, and/or preferential weathering of crystals that
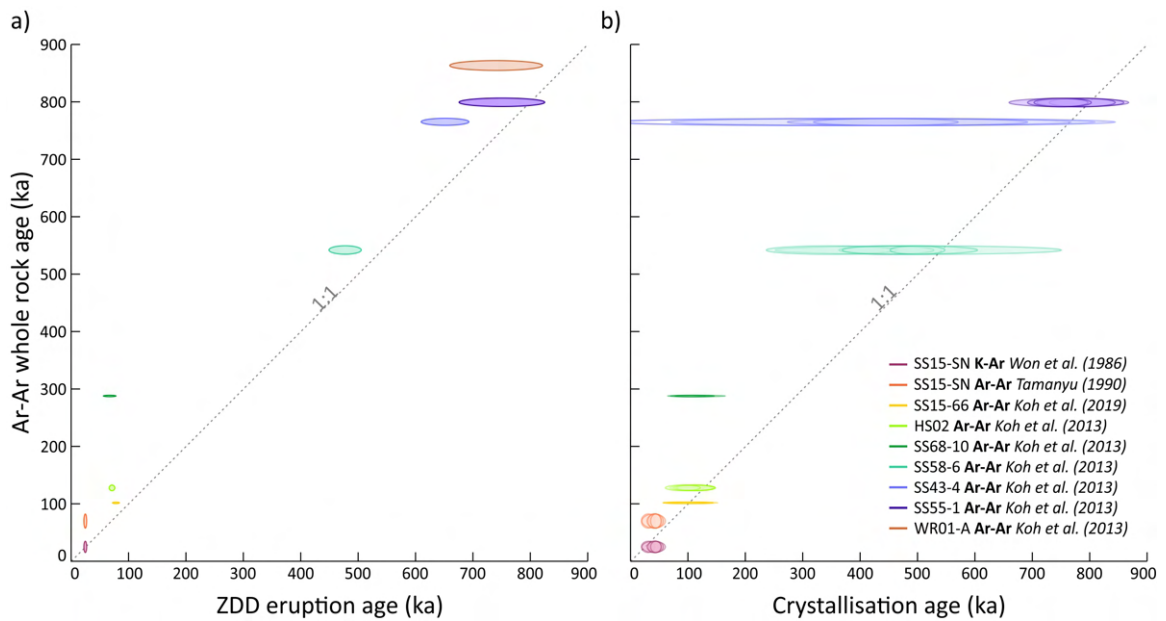
Figure 5.5: Comparison of previous Ar-Ar whole rock ages with a) ZDD eruption ages and b) U-Th disequilibrium and U-Pb crystallisation ages. SS15-SN is comparing this study's data with Won et al. (1986) and to Tamanyu (1990), SS15-66 is comparing this study's data with Koh et al. (2019) and the remaining samples are comparing this study's data with Koh et al. (2013).

lowers Ar retentivity (McDougall and Harrison, 1999; Kelley, 2002).

The sample SS15–66 has an Ar-Ar whole rock age of 102 ± 1 ka (Koh et al., 2019) within error of the youngest crystallisation age (94 ± 30 ka). Additionally, this sample has such a narrow age range that it can be represented by a U-Th disequilibrium isochron age of 110 ± 7 ka, which is older than the whole rock Ar-Ar age. Therefore, for this sample it is less clear whether the whole rock Ar-Ar eruption age or ZDD eruption age (78 ± 5 ka) is more accurate.

The age of xenolith sample WR01-A has indirectly been constrained by whole rock Ar-Ar because the trachyandesite flow stratigraphically above it yielded an Ar-Ar whole rock age of 863 ± 7 (Koh et al., 2013). However, WR01-A has a (U-Th)/He age of 740 ± 66 ka, interpreted as an eruption age, which is younger than the minimum age constraint given by the whole rock Ar-Ar age. A further dating effort is required to confirm the eruption age of this flow as WR01-A does not have an independent zircon crystallisation age which can be used as an eruption age maximum.

The discrepancies in the majority of samples between our U-Th disequilibrium ages and ZDD eruption ages versus some previously published whole rock Ar-Ar ages raises concerns about the interpretation of whole rock Ar-Ar data as eruption ages. Additionally, it is difficult to assess the reliability of the whole rock K-Ar and Ar-Ar dates in Won et al. (1986), Tamanyu (1990), Koh et al. (2013) and Koh et al. (2019) as no detailed data tables were provided. Moreover, the new ZDD chronology raises some questions on the timing of the trachyte evolutionary model presented by Brenna et al. (2015) for Jeju

159

(Figure 5.6) as that model was developed using whole rock Ar-Ar geochronology.

5.5.2.2 OSL and radiocarbon ages

OSL and radiocarbon have been used to date the sediments underlying or overlying two samples from which we dated xenoliths (Ahn, 2016; Ahn et al., 2017) and two eruptive products from the Baengnokdam summit (Ahn and Hong, 2017). Sample MT-J had OSL and radiocarbon ages which suggested that the lava flow erupted at <8 ka and <12 ka respectively (Ahn et al., 2017). The (U-Th)/He age was determined as 7.2 ± 1.4 ka (Table 1), consistent with OSL and radiocarbon results. SA-X is a xenolith from the Songaksan Tuff Ring and Songaksan is estimated to have erupted at <3.8 ka (OSL; Ahn, 2016). The xenolith (U-Th)/He age of 3.6 ± 0.7 ka determined in this work is consistent with this previous interpretation.

OSL and radiocarbon results for the Hallasan trachyte (SS15-SN) indicate an eruption at <38 ± 3.2 ka (Ahn and Hong, 2017). Our results give a (U-Th)/He age of 25 ± 2 ka. The difference in these dates is consistent with OSL and radiocarbon dating being applied to the underlying sediments rather than to the eruptive products themselves. SS15–45 is a trachyte xenolith in a trachybasalt flow which Ahn and Hong (2017) dated as 19–21 ka. However, our results give an age of 28 ± 1 ka. We hypothesise that this difference could be due to incomplete resetting of the (U-Th)/He system in xenolith zircon crystals, if the xenolith was entrained at a late stage of trachybasalt eruption.

5.5.3 Eruption ages and Jeju evolutionary model for trachytes

The new ZDD data allow us to better constrain the existing evolutionary model for trachytes on Jeju Island. Brenna et al. (2015) defined a model from whole rock Ar-Ar data with two comparatively compositionally evolved eruption stages: Stage 1t at 960–500 ka (which includes trachyandesite ages) and Stage 3t at 25–1 ka. Three of the trachytes measured in this study yielded eruption ages of 750 ka, 651 ka, and 477 ka, which fit into Stage 1t within error. Four of the remaining trachyte eruptions fit within Stage 3t, but the majority of the ZDD ages obtained in this study do not fit the model.

Analysis of the probability density function (PDF) (Vermeesch, 2012) of all trachyte eruption ages has been used to propose a new model (Figure 5.6). This visualisation highlights three distinct episodes of volcanism for Jeju's recent trachytic eruptive history (97–53 ka, 31–23 ka and 2 ka) which should be added to Brenna's model in place of Stage 3t. These episodes appear to have spatial relevance with the 97–53 ka episode outcropping to the NW of the Hallasan summit, the 31–23 ka episode outcropping at the summit and to the SE, and to the 2 ka episode outcropping ENE of the Hallasan summit. Further field and sample location images are found in Supplementary material II.
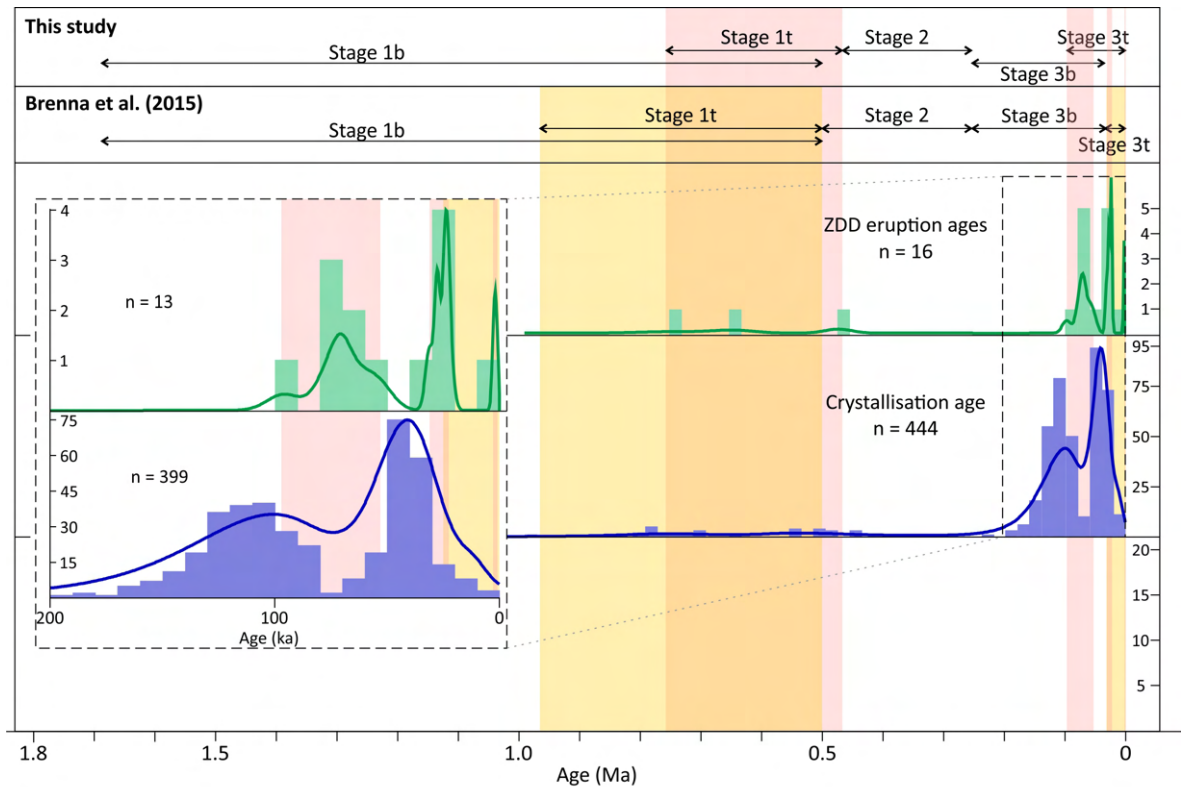
Figure 5.6: Brenna et al. (2015)'s model for trachytic and basaltic stages with the probability density functions for three datasets: ZDD eruption ages (this study), crystallisation ages of zircons (this study) and Ar-Ar whole rock ages (Koh and Park, 2010b; Koh et al., 2013; Brenna et al., 2015) shown below. The inset shows histograms for eruption and crystallisation ages at a higher resolution, measured for the <200 ka ages only.

Furthermore, Stage 1t, if not altered to 740–477 ka based on our data, should at a minimum, be extended from 960 to 500 ka to 960–477 ka, acknowledging that further work should be done to ascertain the most accurate temporal constraints. Finally, the oldest trachyte eruption age of 960 ka in the Brenna et al. (2015) model should be investigated further using ZDD because: i) this age is currently only supported by whole rock Ar-Ar data, and ii) the crystallisation age of the oldest trachyte zircon on Jeju would give information about the time trachyte first started to evolve underneath the island.

5.5.4 Crystallisation ages and Jeju evolutionary model for trachytes

All crystallisation ages for Jeju trachytes have been used to construct a probability density function (Figure 5.6). This function suggests there were three episodes of crystallisation. The first was >350 kyr and was a prolonged period of zircon crystallisation with the least zircon crystallisation ages measured in this study. The second was at approximately 100 ka (range from ca. 80–200 ka). The youngest episode had the greatest number of zircons measured crystallising at around 45 ka (within a range from ca. 0–70 ka).

5.5.4.1 Implications of crystallisation and eruption ages for the dynamics of the Jeju magma reservoir

The crystallisation and eruption ages of zircon crystals in trachyte measured by ZDD provides insight into the dynamics of the Jeju magmatic system. Trachyte is hypothesised to develop in sills in the upper crust as trachybasalt fractionates (Brenna et al., 2012b, Brenna et al., 2014; Jeffery and Gertisser, 2018). Zircon does not crystallise until alkaline melts become sufficiently silica saturated (Hanchar and Watson, 2003) and it is thought that zircon will not start to form until trachyte begins to evolve from trachyandesite. This growth pattern is reflected in our zircon separation observations: less evolved melts, sub-alkali basalts, trachybasalts and trachyandesites on Jeju Island yielded no zircon. Therefore, the age of zircon crystallisation can be used as a proxy for the timing of trachyte evolution, but because some trachytes that are not as Si-saturated might not crystallise zircon, this proxy may not be ubiquitously accessible. Alongside the eruption ages, these crystallisation ages can help to better constrain the time between trachyte differentiation and eruption.

The different peaks of zircon crystallisation (Figure 5.6) suggest that there are distinct episodes of trachyte evolution on Jeju Island. As discussed, the crystallisation patterns and eruption ages of individual samples give us further information about Jeju's magmatic system. However, before analysis in undertaken it is necessary to identify xenocrysts and antecrysts.

Discerning the presence of xenocrysts and antecrysts

When a population of zircon crystals is dated, it can be challenging to distinguish between grains crystallised in the melt associated with the eruption product and those reworked from previous magmas and entrained during an eruption (i.e. distinguishing between autocrysts and antecrysts) and those reworked from the country rock (i.e. distinguishing between autocrysts and xenocrysts).

There are five trachyte samples (SS15-45, SS18-12, SS14-28, SS15-66, and HS100-5) with U-Th disequilibrium data which can be fitted to an isochron with an MSWD value of less than 1 (Figure 5.4) (Ludwig, 2012). This suggests that there are no xenocrysts and antecrysts of different ages in these samples. There is additionally a single $\gtrsim$350 ka sample, SS55–1, with an age range which is statistically indistinguishable from a single age of crystallisation of 768 ± 20 ka (MSWD = 0.7, n = 7).

The remaining samples have a broader range of crystallisation ages and most have a simple distribution, with zircon crystallisation occurring continually until eruption. Multiple reworking of some trachyte melt containing zircon is a possible explanation for the broader distribution of ages. This means that the older ages could either be due to extended duration of crystallisation in a single melt or the incorporation of antecrysts from an older melt. The age distributions for these samples must therefore be used with caution when describing the length of zircon crystallisation or pre-eruptive crystallisation times.

Samples HS02 and SS68-10 are exceptions because in these samples there is a clear distinction between a group of younger crystallisation ages (<350 ka) and an older group of crystals in secular equilibrium ($\gtrsim$350 ka). The older group of crystals have unknown ages and therefore are not plotted on Figure 5.2. Therefore, it is likely that xenocrysts or antecrysts are present in these samples.

Individual age spectra and overall age spectra analysis – what does it mean?

The individual zircon crystallisation ages for Jeju Island range from coeval with eruption to over 600 kyr before eruption. While zircon clearly formed long before eruption in some cases, every trachyte sample on Jeju Island has a youngest crystallisation age that is coeval with the eruption age (Figure 5.2). This suggests that zircon crystallisation, and therefore trachyte evolution, continued until eruption. The oldest five crystallisation ages for zircons in Jeju trachyte measured were >800 ka. This implies that zircon crystallisation, and therefore trachyte evolution, has been occurring on Jeju for at least 800 kyrs.

Well-constrained crystallisation and eruption ages can be obtained for the samples with U-Th disequilibrium isochron ages (five samples SS15-66, HS100-5, SS14-28, SS18-12, SS15-45; Figure 5.4). The time between an isochron crystallisation age and eruption age for these five samples varies from coeval within error to 32 ± 9 ka. These mean pre-eruptive

163

ages can be used to constrain the magma stalling model proposed by Brenna et al., 2012a, Brenna et al., 2012b. Assuming the pre-eruptive age is the time for magma stalling then trachytes of Jeju have a range of magma stalling durations from no stalling to stalling for 32 ± 9 kyr. This variety of trachyte magma stalling and evolution pattern which exists on Jeju Island is still unexplained and is an area for further investigation. HS100-5 and SS15-66 have isochron ages which are within error at 110 ± 7 and 111 ± 14 ka and so these eruptions may potentially have sampled the same melt body. This would need to be confirmed using zircon geochemistry.

For sample SS55–1, the weighted mean crystallisation age of 768 ± 20 ka (MSWD = 0.7, n = 7) and the ZDD eruption age of 750 ± 61 ka, are coeval within error. This suggests that the period of time between trachyte evolution and eruption did not significantly vary over time.

The remaining samples, with broader crystallisation timescales, have a range of crystallisation durations (the difference between the oldest and youngest crystallisation ages) of 16 +17/-13 kyr (SS07-3) to 260 +940/-240 kyr (SS43-4). However, as discussed in Section 5.4.1.1, these ages cannot be distinguished from xenocrysts and as such it is preferable to compare the probability density functions of crystallisation ages. The probability density functions (Figure 5.7a, b, c) are smooth and unimodal, except in the single case of SS15-48 which has a long tail represented by four zircon crystals which are thought to be antecrysts.

Samples HS02 and SS68–10, the two samples with clear distinctions between significantly older zircons ($\gtrsim$350 ka) and a younger population (maximum ages 168.9 ± 90.5 and 122.4 ± 34.6 ka respectively), are both distal from the central volcanic edifice. The only other samples which contain >350 ka zircons (SS43-4, SS58-6 and SS55-1) are from the small volume trachyte domes. We hypothesise that the distal trachytes (HS02 and SS68-10) recycled zircon from the >350 ka trachytes that crop out over the entire island (from Stage 1t). In the central regions it is possible that these older trachytes are so volumetrically insignificant when compared to the <350 ka trachytes that their zircons have been diluted in the <350 ka zircon population to the point where they were not sampled, which was suggested as a mechanism for rhyolites in the Taupo Volcanic Zone by (Charlier and Wilson, 2010).

Sample SS07–3 has a crystallisation age range that is significantly younger than the other crystallisation ages (4.6 ± 8.8 to 23.6 ± 15.2 ka compared to the youngest other crystallisation age – 24.4 ± 44.3 ka). We hypothesise that a new influx of trachyandesite melt evolved and erupted as trachyte within the last 24 ka and either the older zircons were diluted, indicating a large volume of young melt, or a separate melt system developed.

Taken together, the well-defined crystallisation events (Figure 5.6) and the smooth and simple distribution of the individual crystallisation age spectra (Figure 5.7) suggest

that the melt system under Jeju Island is simple, with clear episodes of trachyte evolution and few remobilised zircon crystals.

5.5.5 Comparison with other volcanic systems

The Jeju volcanic system is an intraplate, alkaline system, with melt thought to be produced from decompression melting (Fukao et al., 2001; Huang and Zhao, 2006; Song et al., 2018). The new ZDD data permit comparison with other studies globally where a similar approach has been used to study the magmatic and eruptive history. This approach can help understanding the relative complexities of different magma systems. In the following discussion we compare Jeju Island with a selection of other Quaternary volcanic systems from different geological settings. Various alkaline volcanic systems are used for comparison, with two additional non-alkaline systems briefly examined for interest.

5.5.5.1 Jeju

As discussed in the previous section (5.4.1.2), the individual crystallisation age spectra from Jeju Island (Figure 5.7a, b, c) are smooth with a single peak and the individual spectrum peaks occur shortly before or coeval with the ZDD eruption age. The overall crystallisation age spectrum (Figure 5.6) shows three age ranges for crystallisation: the oldest >350 ka is coeval with the oldest eruption ages, while the younger two peaks of crystallisation show ages at approximately 100 ka and 45 ka. These appear 40 and 20 kyr before the two eruption peaks at approximately 60 ka and 25 ka. Both of these observations suggest that Jeju Island has a simple plumbing system.

5.5.5.2 Alkaline systems

Zou et al. (2014) studied the U series zircon ages for the caldera forming eruption at 1 ka, as well as post- and pre-caldera eruptions, at the Changbai volcano on the Chinese/North Korean border. While Jeju has never recorded such a large-scale eruption, Changbai is similar in terms of eruption products and geological setting, and is situated 1500 km from the Japan Trench subduction zone which is thought to influence the volcanism there (Tang et al., 2014). Jeju Island volcanism is also thought to be influenced by this subduction zone (Brenna et al., 2015). The three Changbai eruptions studied (Figure 5.7d) had eruption ages of ca. 4 ka, 1 ka and 0.3 ka, with the first two being comenditic and the last trachytic. The two comendite eruptions have crystallisation patterns which are similar to the Jeju volcanics as they fall on an isochron at 12.2 ka. This 8.2 kyr and 11.2 kyr pre-eruptive time is similar to that measured on Jeju. The Changbai trachyte, however, has a more complex crystallisation age spectrum with two peaks (2.6 and 130 ka), the first peak being narrow and the second, broad. The trachyte is therefore thought to have
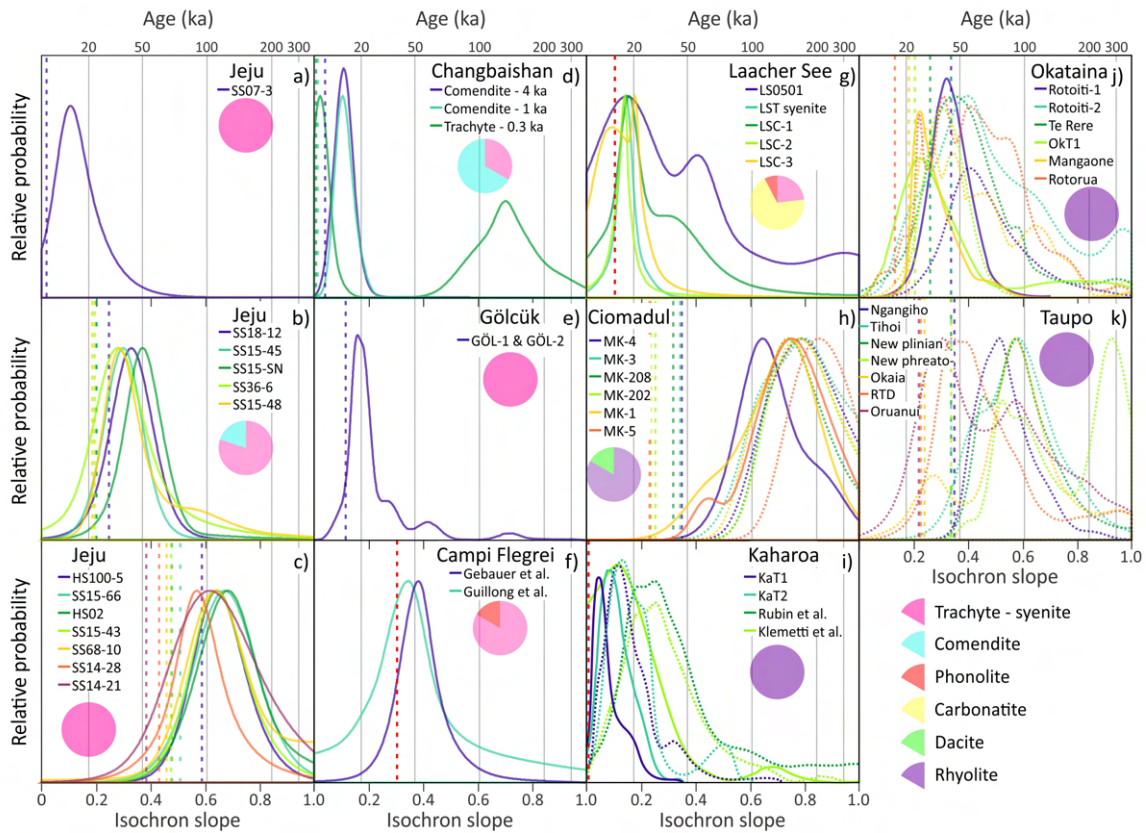
Figure 5.7: Probability density functions which show a variation of complexities of crystallisation age spectra across a selection of volcanic regions both similar and different to Jeju Island. The associated pie charts show the proportions of lithologies making up the samples from which zircons were extracted and analysed. Probability density functions of U-Th disequilibrium isochron model slope values and eruption ages for: a), b), and c) Jeju Island (this study); d) Changbaishan recalculated from Zou et al. (2014); e) Gölcük redrawn from Schmitt et al. (2014b); f) Breccia Museo, Campi Flegrei recalculated from (Gebauer et al., 2014; Guillong et al., 2016); g) Laacher See Tephra and Carbonatites recalculated from Schmitt (2006) and Schmitt et al. (2010); h) Ciomadul recalculated from Harangi et al. (2015); i) samples from Kaharoa eruption re-drawn from Storm et al. (2011, 2012) (KaT1 and KaT2 and Rubin et al. (2015) and re-calculated from Klemetti et al. (2011); j) selected samples from the Okataina Volcanic Centre re-calculated from Charlier and Wilson (2010) (Rotoiti 1, Mangaone and Rotorua) and re-drawn from Rubin et al. (2015) (Rotoiti 2, Te Rere) and Okareka (OkT1) re-drawn from Storm et al. (2012) and k) selected samples from the Oruanui super-eruption and pre-cursors re-calculated from Wilson and Charlier (2009). Colouration of probability density curves show the relative eruption ages (dark blue – oldest, teal, dark green, light green, yellow, orange, dark red – youngest).

sampled a different melt to the two comendite eruptions. While on Jeju each age spectrum has a different peak value, for the Changbai volcanics, two spectra are similar and one is different. This suggests that while Changbaishan is in a similar geological setting, the melt system is larger and more complex than that at Jeju Island.

Schmitt et al., 2014a, Schmitt et al., 2014b investigated a 13 ka eruption in the Gölcük caldera, a 100 km2 area in SW Anatolia, Turkey. The majority of zircon crystals from the two samples gave crystallisation ages between ca. 15–25 ka with minor crystallisation, as described in the study, up to 136 ka (Figure 5.7e). The Jeju probability density functions (PDFs) do not have minor peaks, while the PDF for the samples studied by Schmitt et al., 2014a, Schmitt et al., 2014b show minor peaks at ca. 37, 59, and 136 ka.

The crystallisation ages of zircons from syenite (trachyte) and foid-syenite (phonolite) clasts in the Breccia Museo deposit from the Campi Flegrei caldera, Italy were measured by Gebauer et al. (2014); Guillong et al. (2016) and isochron ages were reported as 50 ± 5 ka and 42 ± 4 ka respectively. Additionally, Gebauer et al. (2014) measured ZDD ages for a selection of zircon crystals and proposed an eruption age of 41.7 ± 1.8 ka. These analyses show a simple PDF similar to those of Jeju (Figure 5.7a, b, c, f).

The Lower Laacher See Tephra (LLST) and the Laacher See Carbonatites (LSC) plutonic clasts, sampled from the Middle and Upper Laacher See Tephras (MLST, ULST), were measured for U-Th disequilibrium by Schmitt (2006) and Schmitt et al. (2010b). In Figure 5.7g, the complexities of the LLST crystallisation age spectra can be seen (LS0501) and compared with the various LSC clast age spectra. Schmitt et al. (2010b) suggested that the complex zircon crystallisation age histories imply onset of phonolite differentiation 10–20 kyr before eruption. This is dissimilar to the simple probability density functions for Jeju Island.

5.5.5.3   Silica saturated volcanism

Harangi et al. (2015) used ZDD to measure the crystallisation and eruption ages of zircon from six of the youngest dacitic and andesitic units from the Ciomadul volcano in the Carpathian–Pannonian region, Romania. The main difference between the ages from Ciomadul and Jeju is the time gap between the peak of the crystallisation age spectra and eruption ages (Figure 5.7h). Additionally, the youngest crystallisation age of the Ciomadul samples is not within error of the eruption age, whereas for all Jeju samples, the youngest crystallisation age is within error of the eruption age.

The age spectra of selected eruptions from the Taupo and Okataina Volcanic Centres can be seen in Figure 5.7i, j, k (Wilson and Charlier, 2009; Charlier and Wilson, 2010; Klemetti et al., 2011; Storm et al., 2011, Storm et al., 2012; Rubin et al., 2015). Charlier and Wilson (2010) suggest that the relative simplicity of the Taupo model age spectra compared to the Okataina age spectra is due to additional complexity in the Okataina

magma chamber (Shane et al., 2005; Smith et al., 2002, Smith et al., 2005).

It is possible that the simple age spectra defined by Jeju trachytes are due to a differentiated magmatic system with small volume, reducing the compositional complexity of the silicic eruptive products. The larger scale chemistry of Jeju Island shows a maximum silica content of 66 wt% (with one exception – sample SS15-48–70 wt%), compared to the melts from Taupo Volcanic Centre and Okataina Volcanic Centre which both have a maximum silica content of 78.5 wt% (Smith et al., 2005). Potentially the less developed, volumetrically small characteristics of the Jeju melts are reflected in the simple age spectra. Alternatively, the Si-undersaturation of alkaline systems could cause suppression of zircon crystallisation until the later stages of evolution (Hanchar and Watson, 2003). This would lead to simpler age variations in zircon from Si-undersaturated suites compared to Si-saturated suites. While this is certainly true for the New Zealand volcanics, the volcanics of Ciomadul and Changbaishan challenge this idea. Ciomadul is a Si-saturated suite, but has simple crystallisation age spectra, while the zircon measured from the trachyte from Changbaishan have a clear bimodal age distribution of older and younger zircons, which would not be expected if zircon crystallisation was suppressed. The simplicity of the age spectra of zircon from trachyte crystallised over the last 200 kyrs could suggest zircon crystallisation suppression until late stage melt evolution and a relatively simple process of melt evolution.

5.5.6   Active volcanism on Jeju

The new geochronology presented herein also has implications for the status of Jeju Island as an active volcano. The Smithsonian Institute's Global Volcanism Program defines volcanoes as 'historically active' where humans have observed eruptions, or as Holocene volcanoes (Smithsonian Institution and Venzke, 2013). It defines Jeju as historically active due to the historical records of volcanism on the coast and supporting OSL and radiocarbon data obtained on bracketing sediments (Ahn, 2016).

The youngest eruption ages measured in this work are 7.2 ± 1.4, 3.6 ± 0.7 and 2.0 ± 1.0 ka. As far as we are aware these are the youngest isotopic ages directly measured on Jeju Island. The first two of these young eruptive ages (xenolith samples MT-J and SA-X) are from a sub-alkali basalt lava flow in Majanggul lava cave on the NE of the island, and a basaltic trachyandesite tuff ring (Songaksan), respectively.

The youngest eruption age of 2.0 ± 1.0 ka is of particular significance as it dates a trachyte eruption. As an evolved, silicic melt, trachyte can erupt both effusively and explosively. It is also the first eruption age recorded from the central area of Hallasan during this historically active period of volcanism. This eruption age may indicate that previously unverified historical events at 1002 CE (Lee and Yang, 2006) were accurately recorded. Understanding that trachyte recently erupted in the centre of Jeju Island may

improve the accuracy of hazard assessments about the potential for future eruptions on the island.

5.6 Conclusions

This work applied the ZDD method to trachyte samples obtained from Jeju Island in an attempt to refine its eruptive chronology. This new analysis revealed four stages of trachyte volcanism which has significantly refined the previous evolutionary model. The first stage was a long, low volume stage from ca. 750 ka to 477 ka. The two middle stages span ca. 97–53 ka and 32–23 ka respectively. The youngest stage is represented by a single eruption age of 2 ± 1 ka, the youngest radiometric age measured on Jeju. These data add to a wealth of evidence indicating recent active volcanism on Jeju Island and has implications for hazard management on Jeju Island as a populous island and tourist destination.

The age ranges of zircon magmatic residence time inferred from crystallisation and eruption ages are varied. However, compared to crystallisation patterns determined in young volcanic systems from other geologic settings, they are much simpler. This suggests that the magma chamber dynamics beneath Jeju Island are simpler than many others globally.

Both zircon crystallisation ages as well as zircon eruption ages provided by the ZDD approach indicate that some of the previously published Ar-Ar whole rock ages may be erroneously old.

5.7 References

Ahn, U.S., 2016. Study of the Last Volcanic Activity on Historical Records on Jeju Island, Korea. The Journal of the Petrological Society of Korea 25, 69–83. https://doi.org/10.7854/JPSK.2016.25.1.69

Ahn, U.S., Choi, J.-H., Yeo, E.-Y., 2017. Eruption timing of the Geomun Oreum through the comparison of radiocarbon and quartz OSL ages (translated to English from Korean). Journal of the Geological Society of Korea 53, 367–376. https://doi.org/10.14770/jgsk.2017.53.3.367

Ahn, U.S., Hong, S.S., 2017. Volcanological History of the Baengnokdam Summit Crater Area, Mt. Halla in Jeju Island, Korea. The Journal of the Petrological Society of Korea 26, 221–234. https://doi.org/10.7854/JPSK.2017.26.3.221

Blondes, M.S., Reiners, P.W., Edwards, B.R., Biscontini, A., 2007. Dating young basalt eruptions by (U-Th)/He on xenolithic zircons. Geology 35, 17–20. https://doi.org/10.1130/G22956A.1

Brenna, M., Cronin, S.J., Kereszturi, G., Sohn, Y.K., Smith, I.E.M., Wijbrans, J., 2015. Intraplate

volcanism influenced by distal subduction tectonics at Jeju Island, Republic of Korea. Bull Volcanol 77, 7. https://doi.org/10.1007/s00445-014-0896-5

Brenna, M., Cronin, S.J., Németh, K., Smith, I.E.M., Sohn, Y.K., 2011. The influence of magma plumbing complexity on monogenetic eruptions, Jeju Island, Korea. Terra Nova 23, 70–75. https://doi.org/10.1111/j.1365-3121.2010.00985.x

Brenna, M., Cronin, S.J., Smith, I.E.M., Maas, R., Sohn, Y.K., 2012a. How Small-volume Basaltic Magmatic Systems Develop: a Case Study from the Jeju Island Volcanic Field, Korea. J Petrology 53, 985–1018. https://doi.org/10.1093/petrology/egs007

Brenna, M., Cronin, S.J., Smith, I.E.M., Sohn, Y.K., Maas, R., 2012b. Spatio-temporal evolution of a dispersed magmatic system and its implications for volcano growth, Jeju Island Volcanic Field, Korea. Lithos 148, 337–352. https://doi.org/10.1016/j.lithos.2012.06.021

Brenna, M., Price, R., Cronin, S.J., Smith, I.E.M., Sohn, Y.K., Kim, G.B., Maas, R., 2014. Final Magma Storage Depth Modulation of Explosivity and Trachyte–Phonolite Genesis at an Intraplate Volcano: a Case Study from Ulleung Island, South Korea. J Petrology 55, 709–747. https://doi.org/10.1093/petrology/egu004

Charlier, B.L.A., Wilson, C.J.N., 2010. Chronology and Evolution of Caldera-forming and Post-caldera Magma Systems at Okataina Volcano, New Zealand from Zircon U–Th Model-age Spectra. J Petrology 51, 1121–1141. https://doi.org/10.1093/petrology/egq015

Cherniak, D.J., Watson, E.B., 2001. Pb diffusion in zircon. Chemical Geology, What are we dating? Understanding the Crystallogernesis of U-Pb 172, 5–24. https://doi.org/10.1016/S0009-2541(00)00233-3

Danišík, M., Shane, P., Schmitt, A.K., Hogg, A., Santos, G.M., Storm, S., Evans, N.J., Fifield, L.K., Lindsay, J.M., 2012. Re-anchoring the late Pleistocene tephrochronology of New Zealand based on concordant radiocarbon ages and combined ^{238}U/^{230}Th disequilibrium and (UeTh)/He zircon ages. Earth Planet Sci. Lett. 349-350, 240-250.

Danišík, M., Schmitt, A.K., Stockli, D.F., Lovera, O.M., Dunkl, I., Evans, N.J., 2017. Application of combined U-Th-disequilibrium/U-Pb and (U-Th)/He zircon dating to tephrochronology. Quaternary Geochronology, Advancing tephrochronology as a global dating tool: applications in volcanology, archaeology, and palaeoclimatic research 40, 23–32. https://doi.org/10.1016/j.quageo.2016.07.005

Danišík, M., Lowe, D. J., Schmitt, A. K., Friedrichs, B., Hogg, A. G., Evans, N. J. (2020). Sub-millennial eruptive recurrence in the silicic Mangaone Subgroup tephra sequence, New Zealand, from Bayesian modelling of zircon double-dating and radiocarbon ages. Quaternary Science Reviews, 246, 106517.

Fukao, Y., Widiyantoro, S., Obayashi, M., 2001. Stagnant slabs in the upper and lower mantle transition region. Reviews of Geophysics 39, 291–323. https://doi.org/10.1029/1999RG000068

Gebauer, S.K., Schmitt, A.K., Pappalardo, L., Stockli, D.F., Lovera, O.M., 2014. Crystallization

and eruption ages of Breccia Museo (Campi Flegrei caldera, Italy) plutonic clasts and their relation to the Campanian ignimbrite. Contrib Mineral Petrol 167, 953. https://doi.org/10.1007/s00410-013-0953-7

Guillong, M., Sliwinski, J.T., Schmitt, A., Forni, F., Bachmann, O., 2016. U-Th Zircon Dating by Laser Ablation Single Collector Inductively Coupled Plasma-Mass Spectrometry (LA-ICP-MS). Geostandards and Geoanalytical Research 40, 377–387. https://doi.org/10.1111/j.1751-908X.2016.00396.x

Hanchar, J.M., Watson, E.B., 2003. Zircon Saturation Thermometry. Reviews in Mineralogy and Geochemistry 53, 89–112. https://doi.org/10.2113/0530089

Harangi, S., Lukács, R., Schmitt, A.K., Dunkl, I., Molnár, K., Kiss, B., Seghedi, I., Novothny, Á., Molnár, M., 2015. Constraints on the timing of Quaternary volcanism and duration of magma residence at Ciomadul volcano, east–central Europe, from combined U–Th/He and U–Th zircon geochronology. Journal of Volcanology and Geothermal Research 301, 66–80. https://doi.org/10.1016/j.jvolgeores.2015.05.002

Hora, J.M., Singer, B.S., Jicha, B.R., Beard, B.L., Johnson, C.M., de Silva, S., Salisbury, M., 2010. Volcanic biotite-sanidine 40Ar/39Ar age discordances reflect Ar partitioning and pre-eruption closure in biotite. Geology 38, 923–926. https://doi.org/10.1130/G31064.1

Huang, J., Zhao, D., 2006. High-resolution mantle tomography of China and surrounding regions. Journal of Geophysical Research: Solid Earth 111. https://doi.org/10.1029/2005JB004066

Jeffery, A.J., Gertisser, R., 2018. Peralkaline Felsic Magmatism of the Atlantic Islands. Front. Earth Sci. 6. https://doi.org/10.3389/feart.2018.00145

Kang, S., Lim, D., Kim, S.-Y., 2010. Benthic foraminiferal assemblage of Seogwipo Formation in Jeju Island, South Sea of Korea: Implication for late Pliocene to early Pleistocene cold episode in the northwestern Pacific margin. Quaternary International, Palaeobotanical and Palynological Records from Italy 225, 138–146. https://doi.org/10.1016/j.quaint.2010.04.009

Kelley, S., 2002. Excess argon in K–Ar and Ar–Ar geochronology. Chemical Geology 188, 1–22. https://doi.org/10.1016/S0009-2541(02)00064-5

Khim, B.K., Woo, K.S., Sohn, Y.K., 2001. Sr isotopes of the Seoguipo Formation (Korea) and their application to geologic age. Journal of Asian Earth Sciences 19, 701–711. https://doi.org/10.1016/S1367-9120(01)00008-6

Kim, J.-Y., Heo, W.-H., 1997. Shell beds and trace fossils of the Seogwipo Formation (Early Pleistocene), Jeju Island, Korea. Ichnos 5, 89–99. https://doi.org/10.1080/10420949709386408

Kim, K.H., Tanaka, T., Suzuki, K., Nagao, K., Park, E.J., 2002. Evidences of the presence of old continental basement in Cheju volcanic Island, South Korea, revealed by radiometric ages and Nd-Sr isotopes of granitic rocks. GEOCHEMICAL JOURNAL 36, 421–441. https://doi.org/10.2343/geochemj.36.421

Kirkland, C.L., Danišík, M., Marsden, R., Piilonen, P., Barham, M., Sutherland, L., 2020. Dating

young zircon: A case study from Southeast Asian megacrysts. Geochimica et Cosmochimica Acta 274, 1–19. https://doi.org/10.1016/j.gca.2020.01.013

Klemetti, E.W., Deering, C.D., Cooper, K.M., Roeske, S.M., 2011. Magmatic perturbations in the Okataina Volcanic Complex, New Zealand at thousand-year timescales recorded in single zircon crystals. Earth and Planetary Science Letters 305, 185–194. https://doi.org/10.1016/j.epsl.2011.02.054

Koh, G.-W., Park, J.-B., 2010a. The Study on Geology and Volcanism in Jeju Island (II): Petrochemistry and 40Ar/39Ar Absolute Ages of the Volcanic Rocks in Gapado-Marado, Jeju Island. Economic and Environmental Geology 43, 53–66.

Koh, G.-W., Park, J.-B., 2010b. The Study on Geology and Volcanism in Jeju Island (III): Early Lava Effusion Records in Jeju Island on the Basis of 40Ar/39Ar Absolute Ages of Lava Samples. Economic and Environmental Geology 43, 163–176.

Koh, G.W., Park, J.B., Hong, S.S., Ko, I.J., Kim, T.H., 2019. Multiple volcanic eruption episodes in the highlands of Mt. Halla (Hallasan), Jeju Island, Korea: 40Ar/39Ar ages of lava flows. Journal of the Geological Society of Korea 55, 71-86. https://doi.org/10.14770/jgsk.2019.55.1.71

Koh, G.-W., Park, J.B., Kang, B.-R., Kim, G.-P., Moon, D.C., 2013. Volcanism in Jeju Island. Journal of the Geological Society of Korea 49, 209–230. https://doi.org/10.14770/jgsk.2013.49.2.209

Koh, G.-W., Park, J.-B., Park, Y.-S., 2008. The Study on Geology and Volcanism in Jeju Island (I): Petrochemistry and 40Ar/39Ar Absolute ages of the Subsurface Volcanic Rock Cores from Boreholes in the Eastern Lowland of Jeiu Island. Economic and Environmental Geology 41, 93–113.

Lee, K., Yang, W.-S., 2006. Historical Seismicity of Korea. Bulletin of the Seismological Society of America 96, 846–855. https://doi.org/10.1785/0120050050

Lee, D.Y., 1988. Quaternary geology of the Jeju Island. Korea Institute of Energy and Resources Report 87, 233–278.

Ludwig, K.R., 2012. Isoplot 3.75: A geochronological toolkit for Excel: Berkeley Geochronology Center Special Publication No. 5 75.

Martí, J., Groppelli, G., Brum da Silveira, A., 2018. Volcanic stratigraphy: A review. Journal of Volcanology and Geothermal Research 357, 68–91. https://doi.org/10.1016/j.jvolgeores.2018.04.006

McDougall, I., Harrison, T.M., 1999. Geochronology and Thermochronology by the 40Ar/39Ar Method. Oxford University Press on Demand.

Min, K.D., Won, J.S., Hwang, S.Y., 1986. Paleomagnetic Study on the Volcanic and Sedimentary Rocks of Jeju Island. Economic and Environmental Geology 19, 153–163.

NASA/METI/AIST/Japan Spacesystems, and U.S./Japan ASTER Science Team, 2019. ASTER Global Digital Elevation Model V003 [Data set]. NASA EOSDIS Land Processes DAAC.

Park, J.B., Park, K.H., Cho, D.L., Koh, G.W., 1999. Petrochemical classification of the Quaternary volcanic rocks in Cheju Island. Korea. Journal of the Geological Society of Korea 35, 253–264.

Park, K.H., Cho, D.L., Kim, Y.B., Kim, J.C., Cho, B.W., Jang, Y.N., Lee, B.J., Lee, S.R., Son, B.K., Cheon, H.Y., 2000a. Geologic report of the Seogwipo-Hahyori sheet (1:50,000). Jeju Provincial Government 163.

Park, K.H., Lee, B.J., Kim, J.C., Cho, D.L., Lee, S.R., Choi, H.I., Park, D.W., Lee, S.R., Choi, Y.S., Yang, D.Y., 2000b. Explanatory note of the Jeju (Baekado, Jinnampo) sheet (1:250,000). Korea Institute of Geoscience and Mineral Resources, Taejon.

Reiners, P.W., Farley, K.A., Hickes, H.J., 2002. He diffusion and (U–Th)/He thermochronometry of zircon: initial results from Fish Canyon Tuff and Gold Butte. Tectonophysics 349, 297–308.

Reiners, P.W., Spell, T.L., Nicolescu, S., Zanetti, K.A., 2004. Zircon (U-Th)/He thermochronometry: He diffusion and comparisons with 40Ar/39Ar dating. Geochimica et Cosmochimica Acta 68, 1857–1887. https://doi.org/10.1016/j.gca.2003.10.021

Rubin, A., Cooper, K.M., Leever, M., Wimpenny, J., Deering, C., Rooney, T., Gravley, D., Yin, Q., 2015. Changes in magma storage conditions following caldera collapse at Okataina Volcanic Center, New Zealand. Contrib Mineral Petrol 171, 4. https://doi.org/10.1007/s00410-015-1216-6

Sakata, S., 2018. A practical method for calculating the U-Pb age of Quaternary zircon: Correction for common Pb and initial disequilibria. Geochem. J. 52, 281–286. https://doi.org/10.2343/geochemj.2.0508

Sakata, S., Hirakawa, S., Iwano, H., Danhara, T., Guillong, M., Hirata, T., 2017. A new approach for constraining the magnitude of initial disequilibrium in Quaternary zircons by coupled uranium and thorium decay series dating. Quaternary Geochronology 38, 1–12. https://doi.org/10.1016/j.quageo.2016.11.002

Schmitt, A., Danišík, M., Evans, N., Siebel, W., Kiemele, E., Aydin, F., C. Harvey, J., 2011. Acigöl rhyolite field, Central Anatolia (part 1): High-resolution dating of eruption episodes and zircon growth rates. Contributions to Mineralogy and Petrology 162, 1215–1231. https://doi.org/10.1007/s00410-011-0648-x

Schmitt, A.K., 2011. Uranium Series Accessory Crystal Dating of Magmatic Processes. Annual Review of Earth and Planetary Sciences 39, 321–349. https://doi.org/10.1146/annurev-earth-040610-133330

Schmitt, A.K., 2006. Laacher See revisited: High-spatial-resolution zircon dating indicates rapid formation of a zoned magma chamber. Geology 34, 597–600. https://doi.org/10.1130/G22533.1

Schmitt, A.K., Danišík, M., Aydar, E., Şen, E., Ulusoy, İ., Lovera, O.M., 2014a. Identifying the Volcanic Eruption Depicted in a Neolithic Painting at Çatalhöyük, Central Anatolia, Turkey. PLOS ONE 9, e84711. https://doi.org/10.1371/journal.pone.0084711

Schmitt, A.K., Danišík, M., Siebel, W., Elitok, Ö., Chang, Y.-W., Shen, C.-C., 2014b. Late

Pleistocene zircon ages for intracaldera domes at Gölcük (Isparta, Turkey). Journal of Volcanology and Geothermal Research 286, 24–29. https://doi.org/10.1016/j.jvolgeores.2014.08.027

Schmitt, A.K., Martín, A., Stockli, D.F., Farley, K.A., Lovera, O.M., 2013. (U-Th)/He zircon and archaeological ages for a late prehistoric eruption in the Salton Trough (California, USA). Geology 41, 7–10. https://doi.org/10.1130/G33634.1

Schmitt, A.K., Stockli, D.F., Hausback, B.P., 2006. Eruption and magma crystallization ages of Las Tres Vírgenes (Baja California) constrained by combined ^{230}Th/ ^{238}U and (U-Th)/He dating of zircon. Journal of Volcanology and Geothermal Research 158, 281–295. https://doi.org/10.1016/j.jvolgeores.2006.07.005

Schmitt, A.K., Stockli, D.F., Niedermann, S., Lovera, O.M., Hausback, B.P., 2010a. Eruption ages of Las Tres Vírgenes volcano (Baja California): A tale of two helium isotopes. Quaternary Geochronology 5, 503–511. https://doi.org/10.1016/j.quageo.2010.02.004

Schmitt, A.K., Wetzel, F., Cooper, K.M., Zou, H., Wörner, G., 2010b. Magmatic Longevity of Laacher See Volcano (Eifel, Germany) Indicated by U–Th Dating of Intrusive Carbonatites. J Petrology 51, 1053–1085. https://doi.org/10.1093/petrology/egq011

Shane, P., Nairn, I.A., Smith, V.C., 2005. Magma mingling in the ∼50 ka Rotoiti eruption from Okataina Volcanic Centre: implications for geochemical diversity and chronology of large volume rhyolites. Journal of Volcanology and Geothermal Research 139, 295–313. https://doi.org/10.1016/j.jvolgeores.2004.08.012

Smith, V.C., Shane, P., Nairn, I.A., 2005. Trends in rhyolite geochemistry, mineralogy, and magma storage during the last 50 kyr at Okataina and Taupo volcanic centres, Taupo Volcanic Zone, New Zealand. Journal of Volcanology and Geothermal Research 148, 372–406. https://doi.org/10.1016/j.jvolgeores.2005.05.005

Smith, V.C., Shane, P., Smith, I.E.M., 2002. Tephrostratigraphy and geochemical fingerprinting of the Mangaone Subgroup tephra beds, Okataina Volcanic Centre, New Zealand. New Zealand Journal of Geology and Geophysics 45, 207–219. https://doi.org/10.1080/00288306.2002.9514969

Smithsonian Institution, Venzke, E., 2013. Volcanoes of the World, v. 4.3.4.

Sohn, Y.K., Park, K.H., Yoon, S.-H., 2008. Primary versus secondary and subaerial versus submarine hydrovolcanic deposits in the subsurface of Jeju Island, Korea. Sedimentology 55, 899–924. https://doi.org/10.1111/j.1365-3091.2007.00927.x

Song, J.-H., Kim, S., Rhie, J., Lee, S.-H., Kim, Y., Kang, T.-S., 2018. Imaging of Lithospheric Structure Beneath Jeju Volcanic Island by Teleseismic Traveltime Tomography. Journal of Geophysical Research: Solid Earth 123, 6784–6801. https://doi.org/10.1029/2018JB015979

Stacey, J.S., Kramers, J.D., 1975. Approximation of terrestrial lead isotope evolution by a two-stage model. Earth and planetary science letters 26, 207–221.

Storm, S., Shane, P., Schmitt, A.K., Lindsay, J.M., 2012. Decoupled crystallization and eruption histories of the rhyolite magmatic system at Tarawera volcano revealed by zircon ages and growth

rates. Contrib Mineral Petrol 163, 505–519. https://doi.org/10.1007/s00410-011-0682-8

Storm, S., Shane, P., Schmitt, A.K., Lindsay, J.M., 2011. Contrasting punctuated zircon growth in two syn-erupted rhyolite magmas from Tarawera volcano: Insights to crystal diversity in magmatic systems. Earth and Planetary Science Letters 301, 511–520. https://doi.org/10.1016/j.epsl.2010.11.034

Tamanyu, S., 1990. The K-Ar ages and their stratigraphic interpretation of the Cheju Island volcanics, Korea. Chishitsu Chosajo Geppo 41, 527–537.

Tang, Y., Obayashi, M., Niu, F., Grand, S.P., Chen, Y.J., Kawakatsu, H., Tanaka, S., Ning, J., Ni, J.F., 2014. Changbaishan volcanism in northeast China linked to subduction-induced mantle upwelling. Nature Geoscience 7, 470–475. https://doi.org/10.1038/ngeo2166

Tatsumi, Y., Shukuno, H., Yoshikawa, M., Chang, Q., Sato, K., Lee, M.W., 2005. The Petrology and Geochemistry of Volcanic Rocks on Jeju Island: Plume Magmatism along the Asian Continental Margin. J Petrology 46, 523–553. https://doi.org/10.1093/petrology/egh087

Vermeesch, P., 2012. On the visualisation of detrital age distributions. Chemical Geology 312–313, 190–194. https://doi.org/10.1016/j.chemgeo.2012.04.021

Wilson, C.J.N., Charlier, B.L.A., 2009. Rapid Rates of Magma Generation at Contemporaneous Magma Systems, Taupo Volcano, New Zealand: Insights from U–Th Model-age Spectra in Zircons. J Petrology 50, 875–907. https://doi.org/10.1093/petrology/egp023

Won, J.K., Matsuda, J., Nagao, K., Kim, K.H., Lee, M.W., 1986. Paleomagnetism and Radiometric Age of Trachytes in Jeju Island, Korea. Economic and Environmental Geology 19, 25–33.

Woo, K.S., Sohn, Y.K., Ahn, U.S., Yoon, S.H., Spate, A., 2013a. Geographic Setting, in: Woo, K.S., Sohn, Y.K., Yoon, S.H., Ahn, U.S., Spate, A. (Eds.), Jeju Island Geopark - A Volcanic Wonder of Korea, Geoparks of the World (Closed). Springer Berlin Heidelberg, Berlin, Heidelberg, pp. 3-6. https://doi.org/10.1007/978-3-642-20564-4_2

Woo, K.S., Sohn, Y.K., Ahn, U.S., Yoon, S.H., Spate, A., 2013b. Geology of Jeju Island, in: Woo, K.S., Sohn, Y.K., Yoon, S.H., Ahn, U.S., Spate, A. (Eds.), Jeju Island Geopark - A Volcanic Wonder of Korea, Geoparks of the World (Closed). Springer Berlin Heidelberg, Berlin, Heidelberg, pp. 13–14. https://doi.org/10.1007/978-3-642-20564-4_5

Zou, H., Fan, Q., Zhang, H., Schmitt, A.K., 2014. U-series zircon age constraints on the plumbing system and magma residence times of the Changbai volcano, China/North Korea border. Lithos 200–201, 169–180. https://doi.org/10.1016/j.lithos.2014.04.0

5.8 Author contributions

Ruby C. Marsden: Investigation, Writing - Original Draft
Martin Danišík: Conceptualisation, Investigation, Visualization, Supervision, Writing-

Reviewing and Editing

Ung-San Ahn: Conceptualisation, Resources, Writing-Reviewing and Editing

Bjarne Friedrichs: Investigation, Writing-Reviewing and Editing

Axel K. Schmitt: Investigation, Writing-Reviewing and Editing

Christopher L. Kirkland: Investigation, Writing-Reviewing and Editing

Bradley McDonald: Investigation

Noreen J. Evans: Investigation, Writing-Reviewing and Editing

5.9 Appendices

Supplementary Material I

Supplementary methods for zircon double-dating of Quaternary eruptions on Jeju Island

Zircon U-Th-Pb (Heidelberg Ion Probe, Heidelberg University)

Zircon U-Th disequilibrium measurements were carried out on a CAMECA 1280-HR instrument at the Heidelberg Ion Probe Laboratory (Heidelberg, Germany) following the procedure in Schmitt et al. (2006, 2011), Schmitt (2011), and Friedrichs et al. (2020). Calibration and standard work was carried out using 91500 zircon (Wiedenbeck et al., 1995) as a relative sensitivity standard for U abundances and AS3 (Paces and Miller, 1993) as a secular equilibrium standard. The measured $(^{230}\text{Th})/(^{238}\text{U})$ ratio for the AS3 reference zircon in this study was 1.014 ± 0.006 (2σ, MSWD = 0.86, n = 119), and all data were re-calculated for AS3 to match unity. Model U-Th disequilibrium ages were calculated either using a two-point isochron with whole rock Th and U activity values or additionally as isochrons (Ludwig, 2012) without whole rock values used.

Zircon U-Pb measurements were carried out following the procedure in Friedrichs et al. (2020). Positive ion species $^{204}\text{Pb}+$, $^{206}\text{Pb}+$, $^{207}\text{Pb}+$, $^{208}\text{Pb}+$, $^{232}\text{Th}+$, $^{238}\text{U}+$, $^{238}\text{U}^{16}\text{O}+$, and $^{238}\text{U}^{16}\text{O}2+$ were analysed sequentially in a single-collection mode using a 10 – 40 nA ion beam focused to a 20 μm diameter beam on the sample surface. The primary reference for the U-Pb relative sensitivity calibration was AS3, resulting in a self-normalized age of 1104 ± 9 Ma (2σ, MSWD = 0.64, n = 21) assuming an age of 1099.1 ± 0.5 Ma (Paces and Miller, 1993). 91500 zircon was employed as secondary reference material, and yielded a discordant $^{206}\text{Pb}/^{238}\text{U}$ age of 1114 ± 44 Ma (2σ, n = 1) not within uncertainty of the crystallisation age of 1065 Ma (Wiedenbeck et al., 1995). $^{206}\text{Pb}/^{238}\text{U}$ ratios were corrected for common Pb using a ^{204}Pb correction. U-Pb age analysis was further investigated in Isoplot v3.75 (Ludwig, 2012) and discordant data were discarded based on a lead-loss hypothesis.

Zircon U-Pb (SHRIMP II, JdLC, Curtin University)

U-Pb work was undertaken on the SHRIMP II in two sessions following the methods of Compston et al. (1984); Claoué-Long et al. (1995) and Williams (1998). The primary ion beam was composed of O_2- ions at 10 keV and had a 30 μm diameter with an ion current between 2.5 and 3.0 nA. The first session measured samples SS43-4, SS55-1 and SS58-6 using the following isotopic mass measurements (the extended count times are due to expected young ages as Jeju Island is <1.8 Ma): 196 (species $^{90}Zr_2^{16}O+$, count time 2 s), 204 ($^{204}Pb+$, 10 s), 204.1 (background, 10 s), 206 ($^{206}Pb+$, 30 s), 207 ($^{207}Pb+$, 50 s), 208 ($^{208}Pb+$, 10 s), 238 ($^{238}U+$, 10 s), 248 ($[^{232}Th^{16}O]+$, 5 s), and 254 ($[^{238}U^{16}O]+$, 5 s). FCT was utilized as the primary reference material (28.4 $\pm$ 0.02 Ma, Schmitz and Bowring, 2001; 27.52 $\pm$ 0.09 Ma, Lanphere and Baadsgaard, 2001) with maximum uncertainty on the reference of 1.7%. PL1 (in-house Penglai zircon; Yu et al., 2020) was treated as a secondary reference material and the ^{207}Pb corrected $^{206}Pb/^{238}U$ PL1 age was 4.3 $\pm$ 0.4 Ma, identical within uncertainty to the accepted age of 4.1 $\pm$ 0.2 Ma to 4.3 $\pm$ 0.1 Ma (Yu et al., 2020) for Penglai megacrysts. The ages for unknowns were <1 Ma and were corrected for disequilibrium (Sakata et al., 2017; Sakata, 2018; Kirkland et al., 2020).

The second session utilized the same primary ion beam settings and measured sample SA-X using R33 (Black et al., 2004) as the primary reference material and FCT as a secondary reference material. The isotopes measured and count times are as follows: 196 ($^{90}Zr_2^{16}O+$, 2 s), 204 ($^{204}Pb+$, 10 s), 204.1 (background, 10 s), 206 ($^{206}Pb+$, 20 s), 207 ($^{207}Pb+$, 20 s), 208 ($^{208}Pb+$, 10 s), 238 ($^{238}U+$, 5 s), 248 ($[^{232}Th^{16}O]+$, 5 s), and 254 ($[^{238}U^{16}O]+$, 2 s). Moderately long count times on ^{206}Pb and ^{207}Pb were utilized given the relatively young expected age of unknown zircons. The uncertainty on the primary reference materal was 1.4%.The secondary reference material yielded a ^{204}Pb corrected $^{206}Pb/^{238}U$ age of 26.0 $\pm$ 1.6 Ma, within error of accepted $^{206}Pb/^{238}U$ ages at 28.4 $\pm$ 0.02 Ma (Schmitz and Bowring, 2001) or 27.5 $\pm$ 0.1 Ma (Lanphere and Baadsgaard, 2001).

Zircon U-Pb (LA-MC-ICP-MS, GeoHistory Facility, JdLC, Curtin University)

Single stream laser ablation U-Pb dates were measured on sample WR01-A following protocols described in Spencer et al. (2019). Instrumentation included a Resonetics RESOlution M-50A-LR incorporating a Compex 102 excimer laser and an Agilent 7700s quadrupole ICP-MS. Following two cleaning pulses, the laser settings specific to the run were: spot size - 33 μm; frequency - 5 Hz; fluence - 2 J cm^{-2}; ablation time - 40 s and total baseline acquisition time - 75 s. High purity Ar was employed as the carrier gas. Unknowns were bracketed by standard blocks containing the primary standard (91500; Wiedenbeck et al., 1995) and secondary standards GJ-1 and FCT. GJ-1 yielded a weighted mean ^{207}Pb corrected $^{206}Pb/^{238}U$ age of 609.8 $\pm$ 2.2 Ma, within error of the expected age of 609 Ma (Jackson et al., 2004). FCT yielded a weighted mean ^{207}Pb corrected $^{206}Pb/^{238}U$

age of 27.9 ± 0.3 Ma, within error of the recommended value 27.5 ± 0.1 Ma (Lanphere and Baadsgaard, 2001).

Zircon (U-Th)/He (JdLC, Curtin University)

Zircon (U-Th)/He analysis was carried out in the JdLC Low Temperature Thermochronology Facility and followed the procedure of Danišík et al. (2017). For majority of the samples, zircon crystals were selected for (U-Th)/He from zircon mineral concentrate based on their size, morphology and U concentration determined during U-Th-Pb dating. Crystals from samples SS43-4, SS55-1 and SS58-6 were embedded into epoxy and their facets were gently polished for U-Pb dating before (U-Th)/He dating without grinding away a portion of crystal that could potentially affect Ft correction factor calculation. To ensure that a correct Ft factor was applied to these crystals, optical microscope photographs were taken before mounting in epoxy and after the crystals were plucked out. Only crystals which had a negligible difference in width after polishing were chosen for (U-Th)/He dating. Selected crystals were photographed under an optical microscope along two axes, loaded into niobium tubes and analysed for He using an AlphachronTM II instrument. Zircon crystals were degassed in an ultra-high vacuum using a 970 nm diode laser at $1250°C$ for 15 minutes and the extracted gas was spiked with ^{3}He and then measured for ^{4}He by isotope dilution on a quadrupole PrismaPlus QMG 220. After analysis each crystal was re-heated in a re-extraction step to confirm full removal of the He in the first heating cycle.

The ^{4}He results were blank corrected using measurements made on empty niobium tubes. The niobium tubes containing zircon were then spiked with 235U and ^{230}Th and dissolved in 350 μl of HF and HNO3 in Parr pressure vessels at $240°C$ for 60 h (Evans et al. 2005). Solutions were then removed from the pressure vessels and dried for 2 d to remove HF. 300 μl of HCl was then added to dissolve the remaining fluoride salts and the samples were returned to the pressure vessels for a further dissolution cycle of $200°C$ for 24 h. Final solutions were then diluted with Milli-Q water and analysed by isotope dilution for ^{238}U and ^{232}Th, and by external calibration for 147Sm on an Element XR^{TM} High Resolution ICP-MS. The total analytical uncertainty (TAU) was calculated as a square root of sum of squares of uncertainty on He and weighted uncertainties on U, Th, and Sm measurements. The zircon (U-Th)/He ages were corrected for alpha ejection (Ft-correction) after Farley et al. (1996), whereby homogenous distributions of U, Th, and Sm were assumed for the crystals and crystal surface and volume estimations were calculated from optical microscope images.

The Ft-corrected (U-Th)/He ages were then corrected for U-series disequilibrium and pre-eruptive crystal residence time (Farley et al., 2002) using MCHeCalc software (Schmitt et al., 2010). In addition to the Ft-corrected (U-Th)/He ages and U-Th crystallization ages (with their associated uncertainties), the software also requires D230 and D231 parameters

which describe zircon-melt fractionation of Th and Pa relative to U. Calculation of D230 (Farley et al. 2002) was made by dividing zircon Th/U values by whole-rock Th/U, whereby we assume that the magma was in secular equilibrium and that the measured whole-rock values are representative for the magma from which the zircons originated. For D231 a value of 3.3 was adopted based on an average of published Pa/U zircon-rhyolite melt partition coefficient values (Schmitt, 2007, 2011; Sakata et al., 2017) (Schmitt, 2007, 2011; Sakata et al., 2017). MCHeCalc outputs a best-fit eruption age which is here termed a ZDD age.

For samples where pre-eruptive crystal time was great enough that the disequilibrium correction was unnecessary (SA-X, MT-J, WR01-A), Ft corrected (U-Th)/He ages (6 to 9 replicates per sample) were then used to calculate mean value using the error-weighted mean with 95% confidence intervals function in Isoplot v.4.15 Excel add-in (Ludwig, 2012), which is interpreted as the representative eruption age of each sample.

References

Black, L.P., Kamo, S.L., Allen, C.M., Davis, D.W., Aleinikoff, J.N., Valley, J.W., Mundil, R., Campbell, I.H., Korsch, R.J., Williams, I.S., Foudoulis, C., 2004. Improved ^{206}Pb/^{238}U microprobe geochronology by the monitoring of a trace-element-related matrix effect; SHRIMP, ID–TIMS, ELA–ICP–MS and oxygen isotope documentation for a series of zircon standards. Chemical Geology 205, 115-140. https://doi.org/10.1016/j.chemgeo.2004.01.003

Claoué-Long, J.C., Compston, W., Roberts, J., Fanning, C.M., 1995. Two Carboniferous Ages: A Comparison of Shrimp Zircon Dating with Conventional Zircon Ages and 40Ar/39Ar Analysis.

Compston, W., Williams, I.S., Meyer, C., 1984. U-Pb geochronology of zircons from lunar breccia 73217 using a sensitive high mass-resolution ion microprobe. Journal of Geophysical Research: Solid Earth 89, B525-B534. https://doi.org/10.1029/JB089iS02p0B525

Danišík, M., Schmitt, A.K., Stockli, D.F., Lovera, O.M., Dunkl, I., Evans, N.J., 2017. Application of combined U-Th-disequilibrium/U-Pb and (U-Th)/He zircon dating to tephrochronology. Quaternary Geochronology, Advancing tephrochronology as a global dating tool: applications in volcanology, archaeology, and palaeoclimatic research 40, 23-32. https://doi.org/10.1016/j.quageo.2016.07.005

Friedrichs, B., Schmitt, A.K., McGee, L., Turner, S., 2020. U–Th whole rock data and high spatial resolution U-Th disequilibrium and U–Pb zircon ages of Mt. Erciyes and Mt. Hasan Quaternary stratovolcanic complexes (Central Anatolia). Data in Brief 29, 105113. https://doi.org/10.1016/j.dib.2020.105113

Jackson, S.E., Pearson, N.J., Griffin, W.L., Belousova, E.A., 2004. The application of laser ablation-inductively coupled plasma-mass spectrometry to in situ U-Pb zircon geochronology. Chemical Geology 211, 47–69. https://doi.org/10.1016/j.chemgeo.2004.06.017

Kirkland, C.L., Danišík, M., Marsden, R., Piilonen, P., Barham, M., Sutherland, L., 2020. Dating young zircon: A case study from Southeast Asian megacrysts. Geochimica et Cosmochimica Acta 274, 1–19. https://doi.org/10.1016/j.gca.2020.01.013

Lanphere, M.A., Baadsgaard, H., 2001. Precise K–Ar, 40Ar/39Ar, Rb–Sr and U/Pb mineral ages from the 27.5 Ma Fish Canyon Tuff reference standard. Chemical Geology 175, 653-671. https://doi.org/10.1016/S0009-2541(00)00291-6

Ludwig, K.R., 2012. Isoplot 3.75: A geochronological toolkit for Excel: Berkeley Geochronology Center Special Publication No. 5 75.

Paces, J.B., Miller, J.D., 1993. Precise U-Pb ages of Duluth Complex and related mafic intrusions, northeastern Minnesota: Geochronological insights to physical, petrogenetic, paleomagnetic, and tectonomagmatic processes associated with the 1.1 Ga Midcontinent Rift System. Journal of Geophysical Research: Solid Earth 98, 13997–14013. https://doi.org/10.1029/93JB01159

Sakata, S., 2018. A practical method for calculating the U-Pb age of Quaternary zircon: Correction for common Pb and initial disequilibria. Geochem. J. 52, 281–286. https://doi.org/10.2343/geochemj.2.0508

Sakata, S., Hirakawa, S., Iwano, H., Danhara, T., Guillong, M., Hirata, T., 2017. A new approach for constraining the magnitude of initial disequilibrium in Quaternary zircons by coupled uranium and thorium decay series dating. Quaternary Geochronology 38, 1-12. https://doi.org/10.1016/j.quageo.2016.11.002

Schmitt, A., Danisik, M., Evans, N., Siebel, W., Kiemele, E., Aydin, F., C. Harvey, J., 2011. Acigöl rhyolite field, Central Anatolia (part 1): High-resolution dating of eruption episodes and zircon growth rates. Contributions to Mineralogy and Petrology 162, 1215–1231. https://doi.org/10.1007/s00410-011-0648-x

Schmitt, A., Stockli, D., Niedermann, S., Lovera, O., P. Hausback, B., 2010. Eruption ages of Las Tres Vírgenes volcano (Baja California): A tale of two helium isotopes. Quaternary Geochronology - QUAT GEOCHRONOL 5, 503–511. https://doi.org/10.1016/j.quageo.2010.02.004

Schmitt, A.K., 2011. Uranium Series Accessory Crystal Dating of Magmatic Processes. Annual Review of Earth and Planetary Sciences 39, 321–349. https://doi.org/10.1146/annurev-earth-040610-133330

Schmitt, A.K., 2007. Ion microprobe analysis of (231Pa)/(235U) and an appraisal of protactinium partitioning in igneous zircon. American Mineralogist 92, 691–694. https://doi.org/10.2138/am.2007.2449

Schmitt, A.K., Stockli, D.F., Hausback, B.P., 2006. Eruption and magma crystallization ages of Las Tres Vírgenes (Baja California) constrained by combined ^{230}Th/ ^{238}U and (U-Th)/He dating of zircon. Journal of Volcanology and Geothermal Research 158, 281–295. https://doi.org/10.1016/j.jvolgeores.2006.07.005

Schmitz, M.D., Bowring, S.A., 2001. U-Pb zircon and titanite systematics of the Fish Canyon

Tuff: an assessment of high-precision U-Pb geochronology and its application to young volcanic rocks. Geochimica et Cosmochimica Acta 65, 2571–2587. https://doi.org/10.1016/S0016-7037(01)00616-0

Spencer, C.J., Danišík, M., Ito, H., Hoiland, C., Tapster, S., Jeon, H., McDonald, B., Evans, N.J., 2019. Rapid Exhumation of Earth's Youngest Exposed Granites Driven by Subduction of an Oceanic Arc. Geophysical Research Letters 46, 1259–1267. https://doi.org/10.1029/2018GL080579

Wiedenbeck, M., Allé, P., Corfu, F., Griffin, W.L., Meier, M., Oberli, F., Quadt, A.V., Roddick, J.C., Spiegel, W., 1995. Three Natural Zircon Standards for U-Th-Pb, Lu-Hf, Trace Element and Ree Analyses. Geostandards Newsletter 19, 1–23. https://doi.org/10.1111/j.1751-908X.1995.tb00147.x

Williams, I.S., 1998. U-Th-Pb geochronology by ion microprobe. Reviews in economic geology 7, 1–35.

Yu, S., Sun, J., Evans, N.J., Danišík, M., Wu, L., Tian, Y., Shen, Z., 2020. Further Evaluation of Penglai Zircon Megacrysts as a Reference Material for (U-Th)/He Dating. Geostandards and Geoanalytical Research May 2020. https://doi.org/10.1111/ggr.12331

Supplementary Material II
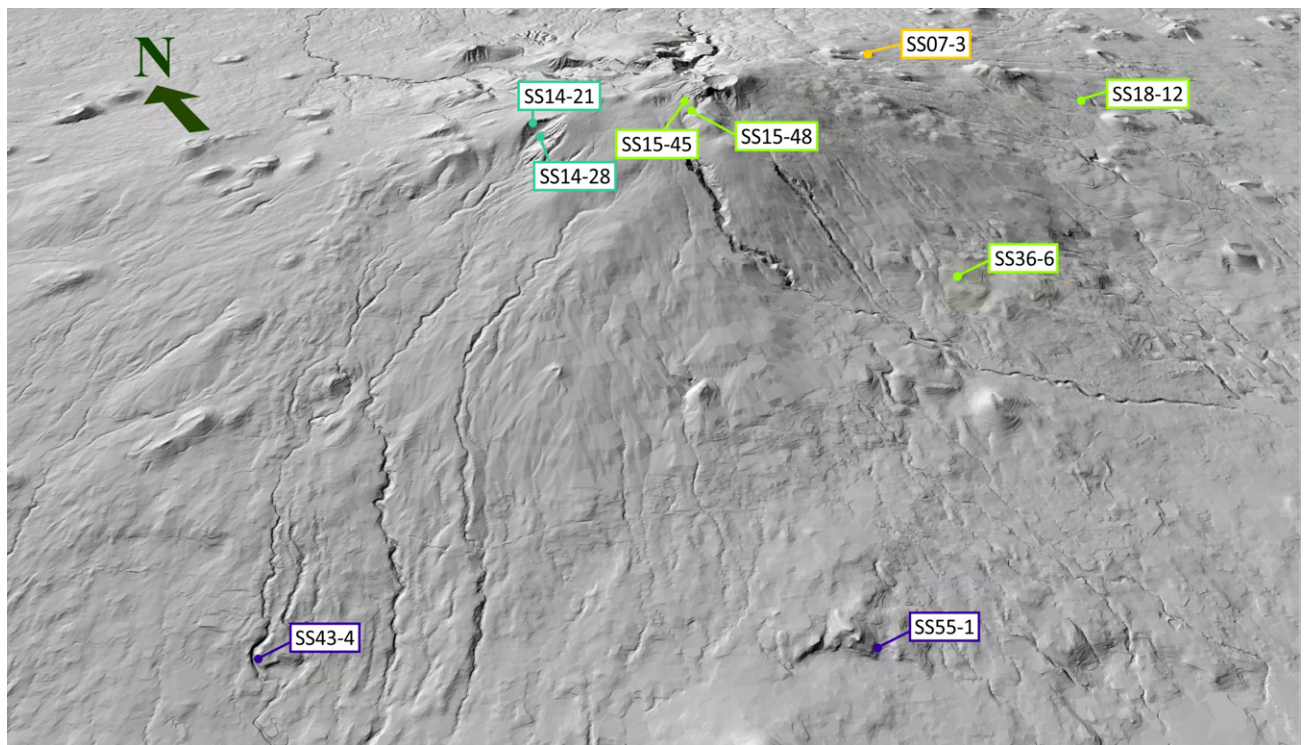
Figure 5.i: Southern flank of Hallasan with sample locations
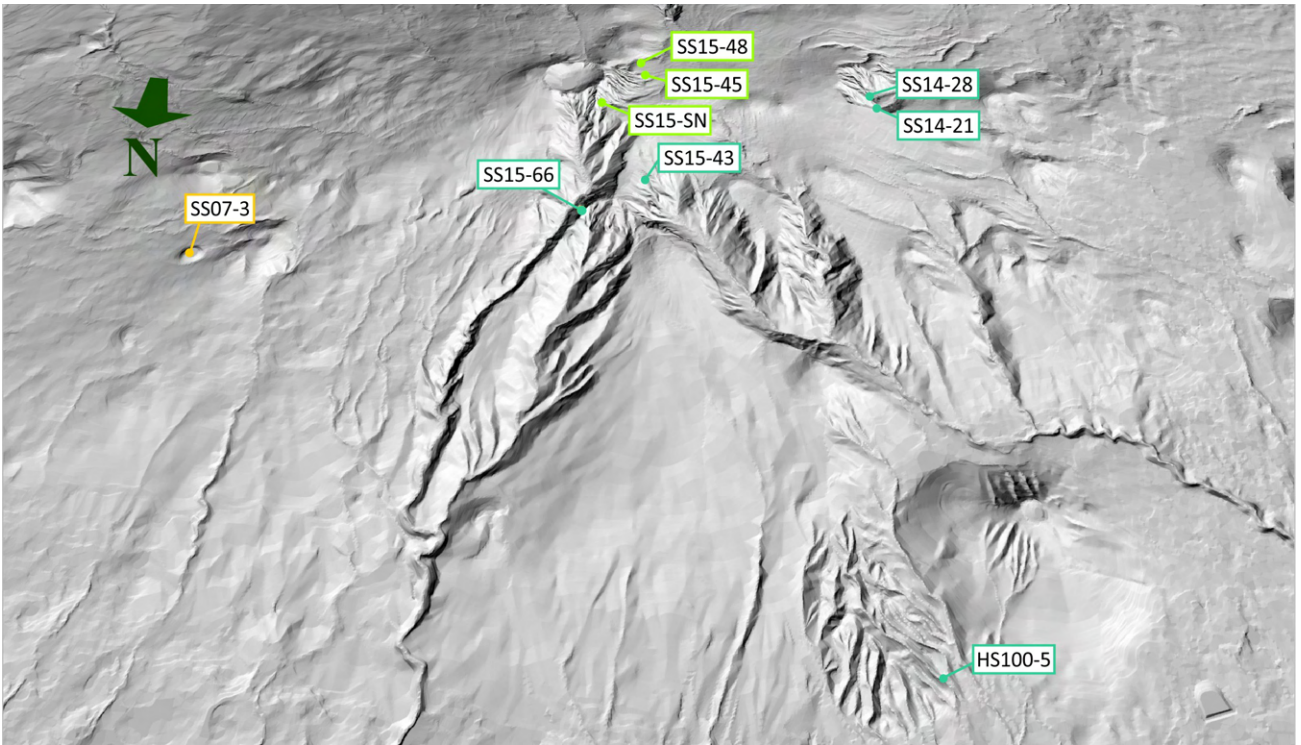
Figure 5.ii: Northern flank of Hallasan with sample locations

Figure 5.iii: Samples SS14-21 and SS14-28 field relations

Figure 5.iv: Sample SS15-45 xenolith within the Baekrockdam trachybasalt
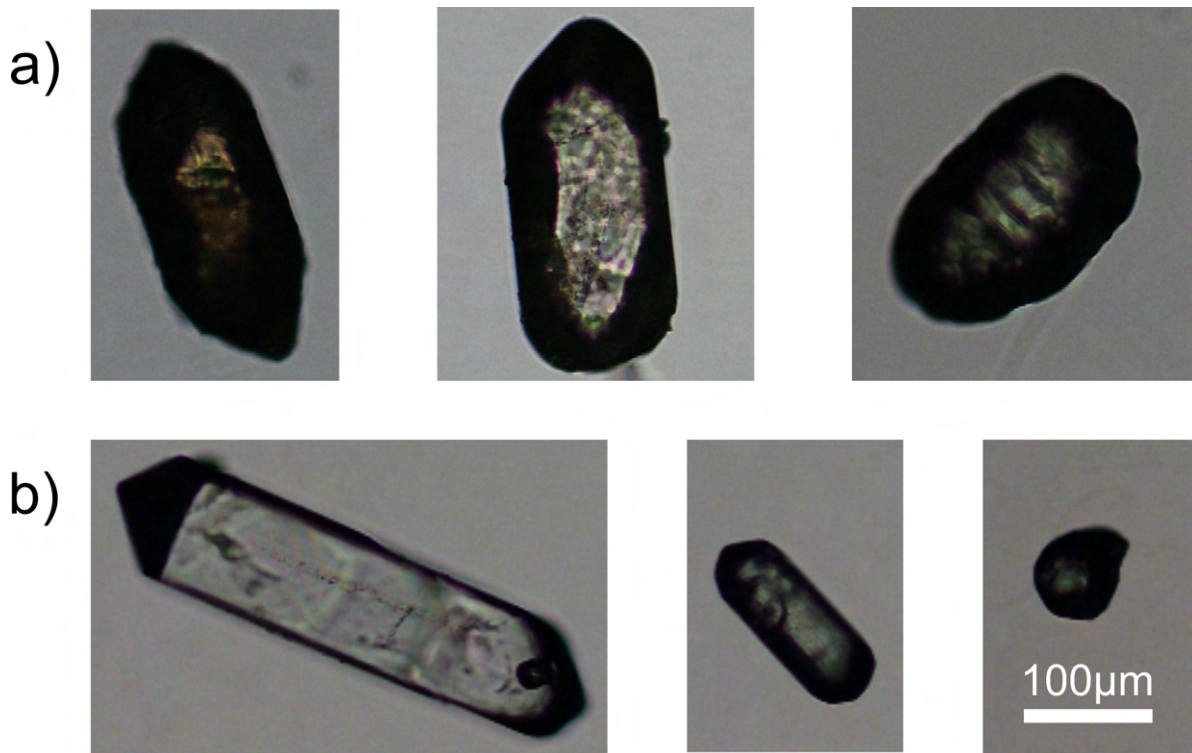
Figure 5.v: a) Sample SA-X crystal shape variation from bi-pyramidal crystal terminations to rounded grains. b) Sample MT-J crystal shape variation from bi-pyramidal crystal terminations to rounded grains. The white bar is the 100 um scale bar for all images

Supplementary Material III

U-Th disequilibrium data

Sample	Crystal identifier	Spot number	Core/Rim	(238U/232Th)	1s	(230Th/232Th)	1s	m	1s	Th age (ka)	1s + (ka)	1s - (ka)	Isochron age (ka)	2s (ka)	U (ppm)
HS-02	1	1	Rim	3.868	0.076	2.473	0.154	0.566	0.051	91.1	13.8	-12.2	n/a[b]	n/a[b]	188
HS-02	2	1	Rim	3.493	0.078	2.571	0.085	0.675	0.038	122.9	13.7	-12.1	n/a[b]	n/a[b]	488
HS-02	3	1	Rim	4.396	0.112	3.599	0.297	0.787	0.084	168.9	54.4	-36.1	n/a[b]	n/a[b]	98
HS-02	4	1	Rim	3.742	0.164	2.947	0.239	0.743	0.088	148.2	45.7	-32.1	n/a[b]	n/a[b]	128
HS-02	5	1	Rim	3.980	0.073	2.998	0.123	0.705	0.042	133.2	16.9	-14.6	n/a[b]	n/a[b]	313
HS-02	6	1	Rim	4.307	0.103	3.008	0.138	0.645	0.043	112.9	14.2	-12.6	n/a[b]	n/a[b]	296
HS-02	7	1	Rim	3.966	0.084	2.704	0.161	0.619	0.053	105.4	16.3	-14.2	n/a[b]	n/a[b]	185
HS-02	8	1	Rim	2.587	0.066	2.070	0.054	0.733	0.044	144.2	19.5	-16.6	n/a[b]	n/a[b]	807
HS-02	9	1	Rim	4.869	0.091	4.729	0.291	0.967	0.073	372.0	∞[a]	-127.1	n/a[b]	n/a[b]	132
HS-02	10	1	Rim	2.873	0.057	2.273	0.042	0.730	0.033	142.8	14.2	-12.6	n/a[b]	n/a[b]	1620
HS-02	11	1	Rim	3.315	0.064	2.357	0.114	0.640	0.048	111.6	15.6	-13.7	n/a[b]	n/a[b]	670
HS-02	12	1	Rim	4.092	0.079	3.008	0.170	0.685	0.053	126.1	20.3	-17.1	n/a[b]	n/a[b]	218
HS-02	13	1	Rim	3.255	0.060	2.682	0.162	0.780	0.067	165.3	39.7	-29.0	n/a[b]	n/a[b]	177
HS-02	14	1	Rim	3.648	0.068	2.662	0.099	0.671	0.039	121.3	13.8	-12.2	n/a[b]	n/a[b]	427
HS-02	15	1	Rim	3.845	0.148	2.793	0.197	0.670	0.070	121.2	26.2	-21.1	n/a[b]	n/a[b]	163
HS-02	16	1	Rim	3.398	0.062	2.399	0.127	0.636	0.051	110.4	16.4	-14.3	n/a[b]	n/a[b]	326
HS100-5	1	1	Rim	4.132	0.077	2.867	0.182	0.660	0.051	118.0	17.7	-15.2	111.0	14.0	162
HS100-5	2	1	Rim	3.900	0.074	2.713	0.173	0.660	0.052	117.9	18.0	-15.4	111.0	14.0	159
HS100-5	3	1	Rim	4.012	0.075	2.665	0.153	0.626	0.045	107.5	13.9	-12.3	111.0	14.0	193
HS100-5	4	1	Rim	3.811	0.077	2.732	0.155	0.683	0.048	125.5	18.0	-15.4	111.0	14.0	202
HS100-5	5	1	Rim	4.313	0.083	2.985	0.223	0.660	0.059	117.8	20.8	-17.4	111.0	14.0	147
HS100-5	6	1	Rim	4.204	0.100	2.775	0.174	0.624	0.049	106.7	15.2	-13.3	111.0	14.0	211
HS100-5	7	1	Rim	4.336	0.103	3.300	0.222	0.736	0.060	145.6	28.1	-22.3	111.0	14.0	140
HS100-5	8	1	Rim	4.121	0.079	3.046	0.189	0.711	0.053	135.4	22.2	-18.4	111.0	14.0	146
HS100-5	9	1	Rim	3.943	0.077	2.399	0.130	0.564	0.039	90.5	10.2	-9.3	111.0	14.0	220
HS100-5	10	1	Rim	4.290	0.081	2.989	0.201	0.665	0.054	119.4	19.1	-16.2	111.0	14.0	148
HS100-5	11	1	Rim	4.488	0.093	3.070	0.224	0.653	0.057	115.4	19.6	-16.6	111.0	14.0	130

HS100-5	12	1 Rim	4.012	0.079	3.221	0.176	0.781	0.052	165.6	29.4	-23.1	111.0	14.0	168
HS100-5	13	1 Rim	4.124	0.083	2.850	0.161	0.657	0.046	116.9	15.7	-13.7	111.0	14.0	171
HS100-5	14	1 Rim	4.350	0.088	2.965	0.130	0.649	0.036	114.3	11.8	-10.7	111.0	14.0	285
HS100-5	15	1 Rim	2.261	0.151	1.862	0.151	0.785	0.104	167.9	72.0	-43.0	111.0	14.0	208
HS100-5	16	1 Rim	4.192	0.083	3.100	0.198	0.711	0.055	135.7	22.9	-18.9	111.0	14.0	162
HS100-5	17	1 Rim	4.167	0.077	2.459	0.175	0.546	0.048	86.2	12.2	-11.0	111.0	14.0	157
HS100-5	18	1 Rim	4.324	0.093	3.092	0.207	0.685	0.055	126.3	21.1	-17.7	111.0	14.0	132
HS100-5	19	1 Rim	3.937	0.079	2.710	0.181	0.653	0.053	115.4	18.2	-15.6	111.0	14.0	172
HS100-5	20	1 Rim	4.468	0.095	2.816	0.209	0.593	0.053	98.3	15.4	-13.5	111.0	14.0	125
HS100-5	a	1 Core	4.141	0.076	2.626	0.113	0.594	0.033	98.5	9.2	-8.4	111.0	14.0	376
HS100-5	b	1 Rim (Polished)	5.919	0.111	4.004	0.332	0.653	0.062	115.5	21.3	-17.8	111.0	14.0	111
HS100-5	b	2 Core	4.835	0.089	3.127	0.128	0.614	0.032	104.0	9.3	-8.6	111.0	14.0	416
HS100-5	c	1 Rim (Polished)	2.330	0.045	1.699	0.059	0.672	0.035	121.7	12.3	-11.0	111.0	14.0	653
HS100-5	c	2 Core	2.603	0.050	1.925	0.069	0.691	0.036	128.3	13.4	-12.0	111.0	14.0	511
HS100-5	d	1 Core	4.826	0.090	3.423	0.194	0.682	0.046	125.3	17.2	-14.8	111.0	14.0	273
HS100-5	e	1 Rim (Polished)	5.899	0.111	4.165	0.344	0.684	0.064	125.9	24.8	-20.2	111.0	14.0	108
HS100-5	e	2 Core	4.023	0.074	2.755	0.122	0.649	0.036	114.4	12.0	-10.8	111.0	14.0	364
HS100-5	f	1 Rim (Polished)	6.357	0.123	4.649	0.493	0.713	0.084	136.3	37.9	-28.1	111.0	14.0	74
HS100-5	f	2 Core	4.795	0.088	3.595	0.210	0.727	0.050	141.6	22.1	-18.3	111.0	14.0	311
HS100-5	g	1 Core	3.415	0.063	2.241	0.105	0.610	0.037	102.7	11.0	-10.0	111.0	14.0	349
HS100-5	h	1 Core	6.297	0.116	4.055	0.184	0.619	0.034	105.5	10.1	-9.2	111.0	14.0	320
HS100-5	i	1 Rim (Polished)	4.258	0.080	2.758	0.149	0.611	0.041	103.0	12.1	-10.9	111.0	14.0	229
HS100-5	i	2 Core	2.109	0.049	1.501	0.047	0.643	0.034	112.5	10.9	-9.9	111.0	14.0	1336
HS100-5	j	1 Core	5.486	0.101	3.708	0.154	0.650	0.033	114.7	10.8	-9.9	111.0	14.0	379
HS100-5	k	1 Core	5.494	0.101	3.732	0.211	0.654	0.043	115.8	14.6	-12.9	111.0	14.0	210
HS100-5	l	1 Core	3.639	0.076	2.411	0.113	0.620	0.038	105.7	11.5	-10.4	111.0	14.0	324
HS100-5	m	1 Core	4.657	0.086	3.302	0.172	0.681	0.043	124.9	15.7	-13.7	111.0	14.0	234
HS100-5	n	1 Core	4.479	0.082	2.850	0.131	0.600	0.035	100.0	9.9	-9.0	111.0	14.0	312
HS100-5	o	1 Rim (Polished)	5.164	0.103	3.879	0.271	0.730	0.059	142.9	26.9	-21.6	111.0	14.0	155
HS100-5	o	2 Core	4.075	0.076	2.805	0.134	0.654	0.039	115.9	13.1	-11.7	111.0	14.0	249
SS07-3	1	1 Rim	4.810	0.069	1.195	0.319	0.154	0.075	18.2	10.1	-9.3	n/a[b]	n/a[b]	99
SS07-3	3	1 Rim	4.641	0.075	0.947	0.085	0.099	0.022	11.4	2.7	-2.6	n/a[b]	n/a[b]	639
SS07-3	4	1 Rim	4.219	0.070	0.922	0.073	0.104	0.021	12.0	2.6	-2.5	n/a[b]	n/a[b]	844

SS07-3	5	1 Rim	4.050	0.081	1.149	0.180	0.174	0.052	20.9	7.1	-6.7	n/a[b]	n/a[b]	288
SS07-3	6	1 Rim	4.894	0.109	1.094	0.103	0.128	0.025	14.9	3.1	-3.0	n/a[b]	n/a[b]	503
SS07-3	7	1 Rim	4.753	0.049	1.155	0.117	0.146	0.029	17.3	3.7	-3.6	n/a[b]	n/a[b]	546
SS07-3	8	1 Rim	4.050	0.101	1.221	0.193	0.194	0.056	23.6	7.8	-7.3	n/a[b]	n/a[b]	171
SS07-3	9	1 Rim	4.725	0.059	0.957	0.174	0.100	0.042	11.5	5.2	-5.0	n/a[b]	n/a[b]	220
SS07-3	10	1 Rim	4.556	0.041	1.221	0.173	0.170	0.044	20.3	5.9	-5.6	n/a[b]	n/a[b]	228
SS07-3	13	1 Rim	4.697	0.235	1.261	0.153	0.174	0.039	20.8	5.2	-5.0	n/a[b]	n/a[b]	361
SS07-3	15	1 Rim	4.500	0.043	0.766	0.203	0.057	0.052	6.5	6.2	-5.8	n/a[b]	n/a[b]	168
SS07-3	17	1 Rim	4.275	0.040	0.816	0.069	0.074	0.020	8.4	2.3	-2.3	n/a[b]	n/a[b]	740
SS07-3	18	1 Rim	4.388	0.046	1.264	0.324	0.188	0.085	22.8	12.0	-10.8	n/a[b]	n/a[b]	174
SS07-3	19	1 Rim	4.388	0.065	1.031	0.131	0.128	0.035	15.0	4.4	-4.3	n/a[b]	n/a[b]	550
SS07-3	20	1 Rim	4.388	0.041	0.698	0.147	0.041	0.039	4.6	4.5	-4.3	n/a[b]	n/a[b]	212
SS07-3	21	1 Rim	4.388	0.057	0.943	0.073	0.105	0.020	12.1	2.5	-2.4	n/a[b]	n/a[b]	717
SS14-21	1	1 Rim	1.514	0.056	1.160	0.032	0.702	0.045	132.1	17.8	-15.3	n/a[b]	n/a[b]	3682
SS14-21	2	1 Rim	2.888	0.144	2.162	0.242	0.717	0.103	137.7	49.3	-33.8	n/a[b]	n/a[b]	76
SS14-21	3	1 Rim	4.198	0.079	2.505	0.353	0.563	0.092	90.3	25.8	-20.9	n/a[b]	n/a[b]	92
SS14-21	4	1 Rim	4.720	0.134	3.267	0.585	0.669	0.135	120.8	57.2	-37.3	n/a[b]	n/a[b]	51
SS14-21	5	1 Rim	4.895	0.094	3.519	0.366	0.699	0.082	131.0	34.5	-26.2	n/a[b]	n/a[b]	69
SS14-21	6	1 Rim	4.247	0.080	3.171	0.290	0.726	0.075	141.2	35.1	-26.5	n/a[b]	n/a[b]	92
SS14-21	7	1 Rim	3.312	0.129	1.975	0.149	0.552	0.056	87.7	14.5	-12.8	n/a[b]	n/a[b]	165
SS14-21	8	1 Rim	4.551	0.088	3.064	0.334	0.648	0.080	114.0	28.3	-22.5	n/a[b]	n/a[b]	83
SS14-21	9	1 Rim	3.381	0.179	2.022	0.176	0.555	0.066	88.4	17.6	-15.1	n/a[b]	n/a[b]	153
SS14-21	10	1 Rim	3.897	0.107	2.282	0.140	0.548	0.043	86.6	10.8	-9.9	n/a[b]	n/a[b]	207
SS14-21	11	1 Rim	4.645	0.090	3.127	0.171	0.648	0.042	114.1	13.9	-12.3	n/a[b]	n/a[b]	200
SS14-21	12	1 Rim	5.294	0.105	3.930	0.448	0.725	0.092	141.1	44.3	-31.4	n/a[b]	n/a[b]	57
SS14-21	13	1 Rim	3.530	0.170	2.470	0.298	0.669	0.100	120.7	39.1	-28.7	n/a[b]	n/a[b]	53
SS14-21	14	1 Rim	4.333	0.083	3.589	0.380	0.814	0.096	183.9	79.9	-45.6	n/a[b]	n/a[b]	63
SS14-21	15	1 Rim	4.287	0.080	2.393	0.179	0.522	0.047	80.6	11.2	-10.1	n/a[b]	n/a[b]	132
SS14-21	17	1 Rim	5.420	0.135	3.550	0.408	0.633	0.082	109.4	27.6	-22.0	n/a[b]	n/a[b]	72
SS14-21	18	1 Rim	3.883	0.096	2.605	0.270	0.641	0.078	111.8	26.7	-21.5	n/a[b]	n/a[b]	80
SS14-21	19	1 Rim	4.189	0.080	2.485	0.241	0.559	0.064	89.4	17.0	-14.7	n/a[b]	n/a[b]	90
SS14-21	20	1 Rim	4.221	0.081	2.791	0.297	0.633	0.077	109.4	25.9	-20.9	n/a[b]	n/a[b]	73

186

SS14-21	21	1 Rim	5.259	0.099	4.685	0.395	0.884	0.082	234.8	133.1	-58.2	n/a[b]	n/a[b]	110
SS14-28	1	1 Rim	5.121	0.122	2.999	0.372	0.550	0.080	87.2	21.5	-17.9	83	9	83
SS14-28	2	1 Rim	3.977	0.081	2.899	0.326	0.698	0.093	130.9	40.1	-29.3	83	9	84
SS14-28	3	1 Rim	4.181	0.092	2.852	0.411	0.648	0.110	114.1	40.9	-29.7	83	9	58
SS14-28	4	1 Rim	4.390	0.097	2.768	0.167	0.593	0.044	98.1	12.6	-11.3	83	9	266
SS14-28	5	1 Rim	4.230	0.081	2.547	0.273	0.560	0.072	89.7	19.6	-16.6	83	9	111
SS14-28	6	1 Rim	4.356	0.105	2.473	0.303	0.524	0.078	81.0	19.5	-16.6	83	9	65
SS14-28	7	1 Rim	3.845	0.151	2.494	0.397	0.607	0.119	102.1	39.2	-28.8	83	9	64
SS14-28	8	1 Rim	3.599	0.074	2.348	0.176	0.609	0.057	102.4	17.2	-14.8	83	9	154
SS14-28	9	1 Rim	4.066	0.137	2.652	0.276	0.614	0.079	103.9	24.9	-20.3	83	9	118
SS14-28	10	1 Rim	2.620	0.073	1.768	0.104	0.616	0.052	104.4	15.8	-13.8	83	9	301
SS14-28	11	1 Rim	3.831	0.076	2.112	0.206	0.498	0.061	75.3	14.3	-12.6	83	9	114
SS14-28	12	1 Rim	5.164	0.103	2.699	0.251	0.482	0.054	71.8	12.0	-10.8	83	9	119
SS14-28	13	1 Rim	4.806	0.121	3.403	0.612	0.681	0.140	124.8	63.4	-39.8	83	9	46
SS14-28	14	1 Rim	4.568	0.084	2.831	0.119	0.583	0.031	95.5	8.5	-7.9	83	9	1434
SS14-28	15	1 Rim	4.671	0.097	3.324	0.474	0.684	0.112	125.9	48.0	-33.2	83	9	47
SS14-28	16	1 Rim	4.161	0.110	2.578	0.150	0.579	0.043	94.4	11.9	-10.7	83	9	192
SS14-28	17	1 Rim	4.155	0.083	2.965	0.235	0.683	0.065	125.4	24.8	-20.2	83	9	109
SS14-28	18	1 Rim	4.453	0.083	2.770	0.108	0.584	0.029	95.9	8.0	-7.5	83	9	401
SS14-28	19	1 Rim	3.725	0.119	2.406	0.283	0.603	0.088	100.8	27.3	-21.9	83	9	71
SS14-28	20	1 Rim	3.768	0.089	2.289	0.196	0.560	0.060	89.7	16.1	-14.0	83	9	120
SS14-28	21	1 Rim	2.922	0.058	1.898	0.048	0.593	0.024	98.2	6.7	-6.3	83	9	878
SS14-28	22	1 Rim	3.779	0.072	2.294	0.211	0.560	0.064	89.6	17.1	-14.8	83	9	112
SS14-28	23	1 Rim	3.980	0.079	2.417	0.256	0.563	0.073	90.3	19.9	-16.8	83	9	134
SS14-28	24	1 Rim	4.218	0.085	2.946	0.324	0.666	0.086	119.9	32.7	-25.1	83	9	72
SS14-28	25	1 Rim	4.224	0.078	2.451	0.203	0.536	0.054	83.8	13.6	-12.1	83	9	137
SS14-28	a	2 Core	3.232	0.059	2.065	0.057	0.588	0.024	96.7	6.6	-6.2	83	9	1233
SS14-28	b	1 Core	4.313	0.079	2.568	0.109	0.554	0.030	88.1	7.7	-7.2	83	9	381
SS14-28	c	1 Rim (Polished)	5.058	0.094	3.143	0.227	0.589	0.050	97.0	14.2	-12.6	83	9	147
SS14-28	c	2 Core	2.306	0.043	1.541	0.054	0.598	0.033	99.5	9.2	-8.5	83	9	648
SS14-28	d	1 Rim (Polished)	4.124	0.078	2.699	0.177	0.617	0.049	104.8	15.1	-13.3	83	9	187
SS14-28	d	2 Core	4.009	0.076	2.513	0.150	0.585	0.043	96.0	12.1	-10.9	83	9	235
SS14-28	e	1 Core	4.273	0.078	2.494	0.069	0.540	0.021	84.8	5.2	-5.0	83	9	891

Sample	Spot	Analysis												
SS14-28	f	1 Core	3.143	0.058	1.982	0.064	0.576	0.027	93.7	7.2	-6.7	83	9	639
SS14-28	g	1 Core	3.957	0.075	2.339	0.086	0.545	0.027	85.9	6.7	-6.3	83	9	935
SS14-28	h	1 Core	4.433	0.082	2.596	0.167	0.544	0.043	85.8	10.9	-9.9	83	9	197
SS14-28	k	1 Rim (Polished)	4.023	0.074	2.382	0.140	0.546	0.041	86.3	10.2	-9.4	83	9	226
SS14-28	k	2 Core	4.324	0.079	2.624	0.084	0.566	0.025	91.2	6.4	-6.0	83	9	709
SS14-28	l	1 Rim (Polished)	6.495	0.150	4.471	0.755	0.668	0.125	120.3	51.5	-34.9	83	9	42
SS14-28	l	2 Core	4.210	0.078	2.792	0.127	0.628	0.036	107.9	11.1	-10.1	83	9	320
SS14-28	m	1 Core	5.216	0.095	3.014	0.107	0.542	0.025	85.3	6.1	-5.8	83	9	566
SS14-28	n	1 Core	3.688	0.068	2.350	0.233	0.593	0.072	98.1	21.3	-17.8	83	9	110
SS15-43	1	1 Rim	4.241	0.083	2.597	0.263	0.573	0.070	92.9	19.4	-16.5	n/a[b]	n/a[b]	121
SS15-43	2	1 Rim	5.271	0.148	3.629	0.318	0.664	0.068	118.9	24.8	-20.2	n/a[b]	n/a[b]	95
SS15-43	3	1 Rim	4.055	0.077	2.987	0.166	0.709	0.048	134.7	19.7	-16.7	n/a[b]	n/a[b]	182
SS15-43	4	1 Rim	4.731	0.106	3.230	0.329	0.654	0.078	115.9	27.7	-22.1	n/a[b]	n/a[b]	125
SS15-43	5	1 Rim	4.210	0.088	2.928	0.156	0.664	0.044	119.2	15.4	-13.5	n/a[b]	n/a[b]	199
SS15-43	6	1 Rim	4.189	0.077	2.638	0.186	0.591	0.051	97.8	14.5	-12.8	n/a[b]	n/a[b]	171
SS15-43	7	1 Rim	4.052	0.113	2.838	0.171	0.669	0.051	120.6	18.4	-15.8	n/a[b]	n/a[b]	174
SS15-43	8	1 Rim	4.175	0.077	3.101	0.173	0.716	0.048	137.5	20.5	-17.2	n/a[b]	n/a[b]	167
SS15-43	9	1 Rim	4.161	0.116	2.904	0.191	0.667	0.055	119.9	19.7	-16.7	n/a[b]	n/a[b]	157
SS15-43	10	1 Rim	3.668	0.138	2.989	0.240	0.793	0.081	171.9	54.1	-36.0	n/a[b]	n/a[b]	163
SS15-43	11	1 Rim	3.711	0.147	3.157	0.220	0.833	0.076	195.5	66.8	-41.2	n/a[b]	n/a[b]	117
SS15-43	12	1 Rim	4.204	0.089	3.256	0.244	0.751	0.067	152.0	34.1	-25.9	n/a[b]	n/a[b]	157
SS15-43	13	1 Rim	3.636	0.068	2.269	0.121	0.579	0.040	94.4	10.9	-9.9	n/a[b]	n/a[b]	237
SS15-43	14	1 Rim	4.786	0.131	2.963	0.274	0.585	0.065	96.1	18.6	-15.9	n/a[b]	n/a[b]	109
SS15-43	15	1 Rim	3.989	0.136	2.986	0.149	0.721	0.050	139.5	21.6	-18.1	n/a[b]	n/a[b]	296
SS15-43	16	1 Rim	2.754	0.133	1.842	0.092	0.614	0.053	103.9	16.2	-14.1	n/a[b]	n/a[b]	258
SS15-43	17	1 Rim	4.195	0.079	2.797	0.199	0.632	0.054	109.3	17.5	-15.1	n/a[b]	n/a[b]	156
SS15-43	18	1 Rim	4.020	0.091	2.607	0.176	0.611	0.051	103.0	15.4	-13.5	n/a[b]	n/a[b]	166
SS15-43	19	1 Rim	4.803	0.106	3.550	0.276	0.716	0.065	137.5	28.4	-22.5	n/a[b]	n/a[b]	103
SS15-43	20	1 Rim	3.868	0.075	2.714	0.155	0.668	0.048	120.4	16.9	-14.6	n/a[b]	n/a[b]	184
SS15-43	21	1 Rim	3.908	0.074	2.707	0.158	0.658	0.048	117.3	16.4	-14.2	n/a[b]	n/a[b]	185
SS15-43	22	1 Rim	5.451	0.130	3.894	0.422	0.692	0.085	128.7	35.5	-26.8	n/a[b]	n/a[b]	86
SS15-43	23	1 Rim	4.496	0.085	2.881	0.218	0.607	0.055	101.9	16.4	-14.3	n/a[b]	n/a[b]	161

SS15-43	a	1 Core	6.079	0.114	4.687	0.396	0.755	0.071	153.7	37.7	-28.0	n/a[b]	n/a[b]	106
SS15-43	a	2 Core	4.657	0.085	3.567	0.180	0.745	0.045	149.0	21.2	-17.8	n/a[b]	n/a[b]	449
SS15-43	b	1 Core	3.389	0.062	2.371	0.101	0.660	0.037	117.9	12.7	-11.4	n/a[b]	n/a[b]	441
SS15-43	c	1 Rim (Polished)	4.319	0.081	3.205	0.196	0.717	0.052	137.7	22.3	-18.5	n/a[b]	n/a[b]	158
SS15-43	c	2 Core	2.406	0.049	1.641	0.043	0.620	0.029	105.8	8.6	-8.0	n/a[b]	n/a[b]	1075
SS15-43	d	1 Core	5.053	0.093	3.031	0.128	0.566	0.030	91.2	7.9	-7.3	n/a[b]	n/a[b]	420
SS15-43	e	1 Rim (Polished)	4.838	0.089	3.406	0.171	0.678	0.041	123.8	14.9	-13.1	n/a[b]	n/a[b]	257
SS15-43	e	2 Core	2.988	0.055	2.068	0.115	0.646	0.047	113.4	15.7	-13.7	n/a[b]	n/a[b]	399
SS15-43	f	1 Rim (Polished)	5.096	0.098	3.463	0.435	0.653	0.094	115.6	34.3	-26.1	n/a[b]	n/a[b]	77
SS15-43	f	2 Core	3.636	0.067	2.648	0.107	0.696	0.037	129.9	14.1	-12.5	n/a[b]	n/a[b]	345
SS15-43	g	1 Rim (Polished)	4.574	0.084	3.221	0.138	0.677	0.036	123.3	13.0	-11.6	n/a[b]	n/a[b]	443
SS15-43	g	2 Core	3.929	0.074	2.685	0.146	0.649	0.044	114.2	14.6	-12.9	n/a[b]	n/a[b]	253
SS15-43	h	1 Core	4.402	0.081	2.904	0.109	0.627	0.031	107.6	9.3	-8.6	n/a[b]	n/a[b]	467
SS15-43	i	1 Core	4.594	0.087	2.824	0.178	0.579	0.044	94.4	12.2	-10.9	n/a[b]	n/a[b]	215
SS15-43	j	1 Rim (Polished)	4.152	0.076	2.755	0.095	0.628	0.029	108.1	8.9	-8.2	n/a[b]	n/a[b]	525
SS15-43	j	2 Core	4.336	0.080	2.869	0.136	0.628	0.037	108.0	11.5	-10.4	n/a[b]	n/a[b]	326
SS15-43	k	1 Core	3.280	0.062	2.184	0.084	0.621	0.033	105.9	10.0	-9.2	n/a[b]	n/a[b]	395
SS15-43	k	2 Core	2.504	0.047	1.808	0.032	0.671	0.024	121.3	8.3	-7.7	n/a[b]	n/a[b]	3188
SS15-43	l	1 Core	4.792	0.088	2.946	0.155	0.581	0.038	94.9	10.2	-9.4	n/a[b]	n/a[b]	243
SS15-43	m	1 Core	3.860	0.071	3.021	0.213	0.758	0.064	155.1	33.4	-25.5	n/a[b]	n/a[b]	212
SS15-43	n	1 Core	4.944	0.094	2.999	0.159	0.573	0.037	92.9	9.9	-9.1	n/a[b]	n/a[b]	296
SS15-45	1	1 Rim	4.215	0.080	1.739	0.129	0.318	0.038	41.8	6.2	-5.9	31	4	290
SS15-45	2	1 Rim	4.290	0.082	1.442	0.163	0.232	0.046	28.8	6.7	-6.3	31	4	125
SS15-45	3	1 Rim	4.341	0.129	1.734	0.175	0.306	0.049	39.9	8.0	-7.5	31	4	148
SS15-45	4	1 Rim	3.691	0.068	1.536	0.086	0.306	0.031	39.9	5.0	-4.8	31	4	451
SS15-45	5	1 Rim	4.445	0.082	1.738	0.138	0.299	0.038	38.8	6.0	-5.7	31	4	185
SS15-45	6	1 Rim	4.135	0.077	1.629	0.108	0.294	0.033	38.1	5.2	-5.0	31	4	230
SS15-45	7	1 Rim	3.946	0.091	1.537	0.106	0.284	0.035	36.4	5.4	-5.1	31	4	261
SS15-45	8	1 Rim	2.163	0.042	1.116	0.035	0.337	0.035	44.8	5.9	-5.6	31	4	970
SS15-45	9	1 Rim	3.676	0.109	1.536	0.092	0.308	0.034	40.2	5.5	-5.3	31	4	276
SS15-45	10	1 Rim	4.006	0.080	1.504	0.125	0.269	0.039	34.2	6.0	-5.7	31	4	212
SS15-45	11	1 Rim	4.212	0.108	1.871	0.302	0.355	0.085	47.8	15.3	-13.4	31	4	62

SS15-45	12	1 Rim	4.212	0.078	1.615	0.116	0.284	0.034	36.5	5.4	-5.1	31	4	220
SS15-45	13	1 Rim	3.183	0.059	1.350	0.048	0.295	0.025	38.1	3.9	-3.8	31	4	716
SS15-45	14	1 Rim	4.456	0.083	1.778	0.158	0.308	0.043	40.3	6.9	-6.5	31	4	157
SS15-45	15	1 Rim	4.602	0.085	1.834	0.151	0.311	0.039	40.7	6.4	-6.1	31	4	170
SS15-45	16	1 Rim	4.218	0.085	1.703	0.137	0.308	0.040	40.2	6.5	-6.1	31	4	179
SS15-45	17	1 Rim	4.258	0.078	1.486	0.114	0.246	0.033	30.8	4.9	-4.7	31	4	228
SS15-45	18	1 Rim	3.527	0.098	1.426	0.070	0.286	0.029	36.8	4.5	-4.3	31	4	476
SS15-45	20	1 Rim	3.817	0.080	1.458	0.086	0.270	0.030	34.4	4.6	-4.4	31	4	357
SS15-45	21	1 Rim	4.278	0.080	1.545	0.130	0.260	0.037	32.9	5.6	-5.3	31	4	229
SS15-45	22	1 Rim	4.124	0.082	2.015	0.153	0.404	0.046	56.5	8.7	-8.1	31	4	172
SS15-45	23	1 Rim	4.092	0.078	1.605	0.113	0.291	0.035	37.5	5.5	-5.2	31	4	269
SS15-45	24	1 Rim	6.022	0.117	1.805	0.228	0.225	0.043	27.8	6.2	-5.9	31	4	251
SS15-45	25	1 Rim	4.594	0.085	1.766	0.167	0.295	0.043	38.1	6.9	-6.5	31	4	202
SS15-45	26	1 Rim	3.929	0.127	1.652	0.114	0.319	0.038	42.0	6.3	-6.0	31	4	220
SS15-45	27	1 Rim	3.725	0.070	1.567	0.093	0.313	0.033	41.0	5.4	-5.1	31	4	469
SS15-45	28	1 Rim	4.218	0.107	1.687	0.170	0.303	0.049	39.5	8.0	-7.4	31	4	175
SS15-45	29	1 Rim	3.917	0.072	1.529	0.083	0.283	0.028	36.4	4.4	-4.2	31	4	383
SS15-45	30	1 Rim	4.278	0.080	1.623	0.120	0.281	0.035	36.1	5.4	-5.2	31	4	220
SS15-45	a	1 Core	2.968	0.054	1.341	0.060	0.317	0.031	41.7	5.1	-4.9	31	4	466
SS15-45	b	1 Core	3.473	0.064	1.456	0.076	0.302	0.030	39.3	4.8	-4.6	31	4	384
SS15-45	c	1 Core	2.997	0.055	1.434	0.056	0.352	0.030	47.4	5.1	-4.9	31	4	565
SS15-45	d	1 Core	2.561	0.047	1.218	0.058	0.321	0.037	42.2	6.0	-5.7	31	4	488
SS15-45	e	1 Rim (Polished)	7.608	0.140	2.349	0.193	0.251	0.029	31.6	4.2	-4.1	31	4	225
SS15-45	e	2 Core	3.960	0.074	1.633	0.136	0.311	0.042	40.7	6.9	-6.5	31	4	181
SS15-45	f	1 Rim (Polished)	3.020	0.055	1.349	0.054	0.314	0.029	41.2	4.6	-4.4	31	4	605
SS15-45	f	2 Core	2.445	0.046	1.149	0.037	0.304	0.030	39.5	4.8	-4.6	31	4	898
SS15-45	g	1 Rim (Polished)	2.377	0.044	1.149	0.035	0.315	0.031	41.3	5.0	-4.8	31	4	877
SS15-45	g	2 Core	2.999	0.055	1.352	0.056	0.318	0.029	41.8	4.8	-4.6	31	4	711
SS15-45	h	1 Core	2.723	0.050	1.268	0.051	0.320	0.031	42.0	5.1	-4.9	31	4	662
SS15-45	i	1 Core	3.229	0.060	1.438	0.072	0.323	0.032	42.6	5.3	-5.0	31	4	456
SS15-45	j	1 Core	3.100	0.057	1.365	0.044	0.311	0.025	40.6	4.0	-3.8	31	4	925
SS15-45	k	1 Rim (Polished)	3.639	0.067	1.425	0.070	0.275	0.027	35.2	4.1	-4.0	31	4	437
SS15-45	k	2 Core	3.438	0.063	1.507	0.070	0.323	0.029	42.6	4.8	-4.6	31	4	429

SS15-45	l	1 Rim (Polished)	3.547	0.065	1.453	0.088	0.293	0.033	37.9	5.3	-5.0	31	4	323
SS15-45	l	2 Core	2.688	0.052	1.340	0.049	0.359	0.031	48.6	5.5	-5.2	31	4	605
SS15-45	m	1 Core	2.991	0.055	1.335	0.051	0.312	0.028	40.9	4.5	-4.3	31	4	739
SS15-45	n	1 Core	3.286	0.060	1.293	0.063	0.262	0.028	33.2	4.3	-4.1	31	4	496
SS15-45	o	1 Core	3.080	0.056	1.381	0.057	0.319	0.029	42.0	4.7	-4.5	31	4	593
SS15-48	0	1 Rim	2.928	0.054	2.033	0.096	0.606	0.048	101.6	14.2	-12.6	n/a[b]	n/a[b]	536
SS15-48	1	1 Rim	2.730	0.056	1.223	0.038	0.272	0.026	34.7	4.0	-3.8	n/a[b]	n/a[b]	1139
SS15-48	2	1 Rim	6.094	0.138	5.089	0.473	0.815	0.090	184.4	72.7	-43.3	n/a[b]	n/a[b]	82
SS15-48	3	1 Rim	4.800	0.089	2.830	0.133	0.524	0.035	81.1	8.4	-7.8	n/a[b]	n/a[b]	459
SS15-48	5	1 Rim	2.041	0.037	1.158	0.027	0.361	0.034	49.0	5.9	-5.6	n/a[b]	n/a[b]	1420
SS15-48	6	1 Rim	3.240	0.064	1.551	0.112	0.346	0.046	46.3	8.0	-7.5	n/a[b]	n/a[b]	593
SS15-48	7	1 Rim	2.673	0.056	1.326	0.038	0.331	0.027	44.0	4.6	-4.4	n/a[b]	n/a[b]	1146
SS15-48	8	1 Rim	3.639	0.067	1.579	0.117	0.309	0.042	40.4	6.8	-6.4	n/a[b]	n/a[b]	644
SS15-48	10	1 Rim	2.716	0.052	1.224	0.035	0.275	0.025	35.1	3.9	-3.7	n/a[b]	n/a[b]	1009
SS15-48	11	1 Rim	2.988	0.064	1.310	0.043	0.280	0.025	35.8	3.9	-3.7	n/a[b]	n/a[b]	816
SS15-48	12	1 Rim	2.732	0.050	1.279	0.045	0.300	0.028	38.9	4.5	-4.3	n/a[b]	n/a[b]	993
SS15-48	13	1 Rim	3.229	0.060	1.402	0.055	0.289	0.026	37.3	4.1	-4.0	n/a[b]	n/a[b]	723
SS15-48	14	1 Rim	2.762	0.051	1.134	0.056	0.226	0.032	28.0	4.6	-4.4	n/a[b]	n/a[b]	1070
SS15-48	15	1 Rim	3.129	0.058	1.334	0.050	0.273	0.026	34.9	3.9	-3.8	n/a[b]	n/a[b]	723
SS15-48	16	1 Rim	4.060	0.079	2.744	0.182	0.613	0.057	103.7	17.3	-14.9	n/a[b]	n/a[b]	167
SS15-48	17	1 Rim	2.659	0.050	1.219	0.041	0.280	0.028	35.9	4.3	-4.1	n/a[b]	n/a[b]	1055
SS15-48	18	1 Rim	1.999	0.038	1.163	0.037	0.376	0.040	51.5	7.2	-6.8	n/a[b]	n/a[b]	1540
SS15-48	20	1 Rim	2.671	0.050	1.384	0.059	0.360	0.036	48.8	6.2	-5.9	n/a[b]	n/a[b]	618
SS15-48	21	1 Rim	2.733	0.051	1.206	0.037	0.264	0.025	33.5	3.8	-3.7	n/a[b]	n/a[b]	1002
SS15-66	1	1 Rim	4.161	0.077	3.152	0.172	0.731	0.048	143.3	21.7	-18.1	110	7	231
SS15-66	2	1 Rim	3.650	0.067	2.578	0.148	0.669	0.048	120.7	17.1	-14.8	110	7	233
SS15-66	3	1 Rim	4.491	0.089	3.267	0.266	0.700	0.067	131.4	27.6	-22.0	110	7	126
SS15-66	4	1 Rim	6.547	0.125	4.806	0.449	0.716	0.075	137.5	33.3	-25.5	110	7	86
SS15-66	5	1 Rim	4.829	0.106	3.278	0.284	0.649	0.066	114.2	22.8	-18.8	110	7	114
SS15-66	6	1 Rim	3.424	0.073	2.495	0.179	0.692	0.062	128.4	24.5	-20.0	110	7	146
SS15-66	7	1 Rim	4.362	0.097	2.783	0.252	0.600	0.066	100.1	19.5	-16.6	110	7	100
SS15-66	8	1 Rim	2.257	0.164	1.860	0.178	0.785	0.119	167.8	88.4	-48.2	110	7	270

SS15-66	9	1	Rim	5.517	0.162	3.996	0.550	0.702	0.110	132.2	50.4	-34.3	110	7	102
SS15-66	9	2	Rim	3.837	0.072	2.841	0.185	0.709	0.056	134.8	23.4	-19.2	110	7	190
SS15-66	10	1	Rim	1.458	0.045	1.208	0.032	0.761	0.046	156.2	23.1	-19.1	110	7	1008
SS15-66	11	1	Rim	4.083	0.076	2.919	0.200	0.683	0.056	125.3	21.3	-17.8	110	7	192
SS15-66	12	1	Rim	4.109	0.159	2.979	0.234	0.694	0.070	129.4	28.5	-22.6	110	7	217
SS15-66	13	1	Rim	4.204	0.079	3.043	0.233	0.694	0.063	129.2	25.2	-20.5	110	7	156
SS15-66	14	1	Rim	3.992	0.074	2.626	0.216	0.618	0.062	105.2	19.3	-16.4	110	7	162
SS15-66	15	1	Rim	5.858	0.116	3.828	0.426	0.627	0.079	107.7	26.1	-21.1	110	7	101
SS15-66	16	1	Rim	3.934	0.072	2.634	0.173	0.631	0.051	108.8	16.2	-14.1	110	7	174
SS15-66	17	1	Rim	3.977	0.074	2.842	0.226	0.681	0.065	124.9	24.9	-20.3	110	7	173
SS15-66	18	1	Rim	3.874	0.071	2.774	0.175	0.682	0.053	125.1	19.8	-16.7	110	7	174
SS15-66	19	1	Rim	2.193	0.140	1.620	0.119	0.678	0.086	123.8	33.8	-25.7	110	7	260
SS15-66	20	1	Rim	3.929	0.073	2.798	0.175	0.678	0.052	123.8	19.1	-16.3	110	7	191
SS15-66	21	1	Rim	4.201	0.078	2.872	0.190	0.649	0.052	114.3	17.5	-15.1	110	7	135
SS15-66	22	1	Rim	3.877	0.081	3.070	0.194	0.767	0.059	159.0	31.8	-24.6	110	7	196
SS15-66	23	1	Rim	4.063	0.075	3.052	0.177	0.723	0.051	140.2	22.1	-18.4	110	7	177
SS15-66	24	1	Rim	3.914	0.073	2.527	0.166	0.604	0.049	101.1	14.5	-12.8	110	7	169
SS15-66	25	1	Rim	4.187	0.078	3.274	0.200	0.758	0.055	155.0	28.4	-22.5	110	7	134
SS15-66	a	1	Core	3.820	0.070	2.530	0.145	0.621	0.045	106.0	13.7	-12.2	110	7	212
SS15-66	b	1	Core	3.946	0.073	3.068	0.209	0.751	0.061	152.0	30.9	-24.1	110	7	127
SS15-66	d	1	Core	4.215	0.077	3.007	0.144	0.682	0.041	125.2	14.9	-13.1	110	7	250
SS15-66	e	1	Core	6.423	0.120	4.113	0.399	0.616	0.067	104.4	21.1	-17.7	110	7	98
SS15-66	f	1	Core	4.003	0.074	2.766	0.211	0.655	0.060	116.3	21.0	-17.6	110	7	114
SS15-66	g	1	Core	2.549	0.047	1.844	0.079	0.670	0.040	120.9	14.1	-12.5	110	7	432
SS15-66	h	1	Core	6.475	0.123	4.750	0.326	0.716	0.056	137.3	23.8	-19.5	110	7	128
SS15-66	i	1	Core	4.192	0.077	2.861	0.192	0.648	0.053	113.9	17.6	-15.2	110	7	166
SS15-66	j	1	Core	3.934	0.073	2.744	0.145	0.662	0.044	118.4	15.1	-13.2	110	7	229
SS15-66	k	1	Core	5.368	0.101	3.259	0.286	0.574	0.059	93.2	16.3	-14.2	110	7	109
SS15-66	l	1	Core	5.010	0.095	3.359	0.204	0.641	0.046	111.8	15.1	-13.2	110	7	185
SS15-66	m	1	Core	3.811	0.070	2.614	0.136	0.648	0.042	113.9	13.9	-12.4	110	7	237
SS15-66	n	1	Core	5.420	0.101	3.488	0.275	0.614	0.056	104.0	17.3	-14.9	110	7	132
SS15-66	o	1	Core	4.029	0.074	2.959	0.131	0.704	0.039	132.9	15.4	-13.5	110	7	345
SS15-SN	1	1	Rim	4.086	0.081	1.566	0.108	0.322	0.030	42.4	4.9	-4.7	n/a[b]	n/a[b]	241

SS15-SN	2	1 Rim	3.900	0.103	1.543	0.102	0.332	0.030	44.1	5.1	-4.9	n/a[b]	n/a[b]	297
SS15-SN	3	1 Rim	4.287	0.092	1.578	0.204	0.309	0.053	40.3	8.6	-8.0	n/a[b]	n/a[b]	104
SS15-SN	4	1 Rim	2.644	0.048	1.161	0.052	0.348	0.024	46.7	4.1	-3.9	n/a[b]	n/a[b]	587
SS15-SN	5	1 Rim	3.871	0.093	1.584	0.115	0.347	0.034	46.5	5.9	-5.6	n/a[b]	n/a[b]	276
SS15-SN	6	1 Rim	4.063	0.076	1.572	0.129	0.325	0.036	43.0	5.9	-5.6	n/a[b]	n/a[b]	184
SS15-SN	7	1 Rim	3.929	0.159	2.508	0.681	0.601	0.193	100.3	72.3	-43.1	n/a[b]	n/a[b]	43
SS15-SN	8	1 Rim	3.404	0.091	1.562	0.084	0.393	0.030	54.5	5.6	-5.3	n/a[b]	n/a[b]	321
SS15-SN	9	1 Rim	3.688	0.120	1.561	0.126	0.359	0.040	48.5	7.1	-6.6	n/a[b]	n/a[b]	339
SS15-SN	10	1 Rim	2.492	0.048	1.161	0.048	0.373	0.024	50.9	4.3	-4.2	n/a[b]	n/a[b]	494
SS15-SN	11	1 Rim	3.243	0.104	1.324	0.055	0.332	0.023	44.1	3.8	-3.7	n/a[b]	n/a[b]	612
SS15-SN	12	1 Rim	4.382	0.085	1.712	0.182	0.335	0.046	44.5	7.8	-7.3	n/a[b]	n/a[b]	182
SS15-SN	13	1 Rim	4.026	0.075	1.662	0.116	0.354	0.033	47.6	5.7	-5.4	n/a[b]	n/a[b]	273
SS15-SN	14	1 Rim	3.828	0.078	1.572	0.167	0.348	0.049	46.6	8.5	-7.9	n/a[b]	n/a[b]	173
SS15-SN	15	1 Rim	3.263	0.060	1.376	0.062	0.348	0.023	46.7	3.9	-3.7	n/a[b]	n/a[b]	460
SS15-SN	16	1 Rim	4.872	0.096	1.917	0.169	0.344	0.038	46.0	6.6	-6.2	n/a[b]	n/a[b]	183
SS15-SN	17	1 Rim	3.920	0.077	1.657	0.105	0.363	0.031	49.2	5.4	-5.1	n/a[b]	n/a[b]	319
SS15-SN	18	1 Rim	3.355	0.164	1.394	0.093	0.343	0.036	45.9	6.2	-5.9	n/a[b]	n/a[b]	248
SS15-SN	19	1 Rim	3.834	0.129	2.173	0.375	0.521	0.110	80.3	28.5	-22.6	n/a[b]	n/a[b]	49
SS15-SN	20	1 Rim	3.189	0.072	1.574	0.081	0.427	0.031	60.8	6.0	-5.7	n/a[b]	n/a[b]	339
SS15-SN	21	1 Rim	4.390	0.087	2.194	0.306	0.454	0.077	66.0	16.5	-14.3	n/a[b]	n/a[b]	135
SS15-SN	22	1 Rim	2.962	0.056	1.303	0.071	0.360	0.029	48.7	5.0	-4.8	n/a[b]	n/a[b]	381
SS15-SN	23	1 Rim	3.487	0.134	1.558	0.101	0.381	0.036	52.4	6.6	-6.2	n/a[b]	n/a[b]	377
SS15-SN	24	1 Rim	2.704	0.051	1.199	0.043	0.355	0.020	48.0	3.5	-3.4	n/a[b]	n/a[b]	720
SS15-SN	25	1 Rim	4.622	0.096	2.347	0.545	0.465	0.129	68.3	30.0	-23.5	n/a[b]	n/a[b]	36
SS15-SN	a	1 Rim (Polished)	2.977	0.055	1.391	0.049	0.392	0.021	54.3	3.8	-3.6	n/a[b]	n/a[b]	627
SS15-SN	a	2 Core	2.056	0.038	1.088	0.032	0.426	0.021	60.6	4.2	-4.0	n/a[b]	n/a[b]	1213
SS15-SN	b	1 Core	2.849	0.052	1.391	0.073	0.412	0.031	58.0	5.8	-5.5	n/a[b]	n/a[b]	394
SS15-SN	c	1 Core	7.324	0.135	2.068	0.228	0.244	0.033	30.6	4.9	-4.7	n/a[b]	n/a[b]	172
SS15-SN	d	1 Core	1.746	0.032	1.014	0.023	0.468	0.020	68.9	4.3	-4.1	n/a[b]	n/a[b]	1301
SS15-SN	e	1 Core	3.570	0.065	1.518	0.071	0.359	0.023	48.5	4.0	-3.9	n/a[b]	n/a[b]	380
SS15-SN	f	1 Core	2.495	0.046	1.261	0.044	0.419	0.023	59.3	4.3	-4.2	n/a[b]	n/a[b]	783
SS15-SN	g	1 Core	3.567	0.066	1.513	0.106	0.358	0.034	48.3	5.9	-5.6	n/a[b]	n/a[b]	202

SS15-SN	h	1	Core	2.365	0.043	1.160	0.046	0.396	0.025	55.1	4.6	-4.4	n/a[b]	n/a[b]	513
SS15-SN	i	1	Core	2.667	0.049	1.293	0.066	0.402	0.030	56.1	5.6	-5.3	n/a[b]	n/a[b]	419
SS15-SN	j	1	Core	3.045	0.056	1.376	0.042	0.376	0.017	51.5	3.1	-3.0	n/a[b]	n/a[b]	902
SS15-SN	k	1	Core	2.440	0.045	1.161	0.041	0.382	0.022	52.6	3.9	-3.7	n/a[b]	n/a[b]	633
SS15-SN	l	1	Core	3.149	0.058	1.328	0.072	0.345	0.027	46.2	4.6	-4.4	n/a[b]	n/a[b]	323
SS15-SN	m	1	Core	3.352	0.062	1.433	0.078	0.356	0.027	48.1	4.7	-4.5	n/a[b]	n/a[b]	334
SS15-SN	n	1	Core	2.229	0.041	1.069	0.036	0.376	0.021	51.6	3.8	-3.6	n/a[b]	n/a[b]	912
SS15-SN	n	2	Core	2.156	0.040	1.159	0.044	0.442	0.026	63.7	5.3	-5.0	n/a[b]	n/a[b]	1535
SS15-SN	o	1	Core	1.755	0.033	1.004	0.024	0.458	0.021	66.9	4.2	-4.1	n/a[b]	n/a[b]	1121
SS18-12	1	1	Rim	4.058	0.075	1.762	0.089	0.320	0.032	42.1	5.3	-5.1	44	3	360
SS18-12	2	1	Rim	4.740	0.088	2.142	0.166	0.360	0.044	48.7	7.8	-7.3	44	3	173
SS18-12	3	1	Rim	4.849	0.108	1.989	0.066	0.314	0.022	41.1	3.6	-3.5	44	3	824
SS18-12	4	1	Rim	5.557	0.115	2.478	0.112	0.368	0.027	50.2	4.8	-4.6	44	3	429
SS18-12	5	1	Rim	4.605	0.085	1.853	0.147	0.299	0.041	38.7	6.5	-6.1	44	3	188
SS18-12	6	1	Rim	4.046	0.075	1.850	0.094	0.348	0.034	46.6	5.8	-5.5	44	3	351
SS18-12	7	1	Rim	3.711	0.081	1.708	0.191	0.339	0.067	45.2	11.6	-10.5	44	3	220
SS18-12	8	1	Rim	3.401	0.114	1.604	0.094	0.339	0.043	45.3	7.3	-6.9	44	3	307
SS18-12	9	1	Rim	4.677	0.091	2.125	0.118	0.361	0.034	49.0	5.9	-5.6	44	3	335
SS18-12	10	1	Rim	4.029	0.088	1.733	0.115	0.314	0.039	41.2	6.4	-6.1	44	3	280
SS18-12	11	1	Rim	3.934	0.094	1.842	0.129	0.357	0.045	48.2	7.9	-7.4	44	3	192
SS18-12	12	1	Rim	3.088	0.151	1.463	0.066	0.325	0.042	42.9	7.0	-6.5	44	3	527
SS18-12	13	1	Rim	4.622	0.087	1.920	0.099	0.314	0.030	41.2	4.9	-4.7	44	3	363
SS18-12	14	1	Rim	4.476	0.094	1.758	0.098	0.284	0.031	36.5	4.8	-4.6	44	3	507
SS18-12	15	1	Rim	3.639	0.067	1.729	0.087	0.354	0.036	47.7	6.3	-6.0	44	3	453
SS18-12	16	1	Rim	4.579	0.148	1.797	0.156	0.286	0.044	36.8	6.9	-6.5	44	3	166
SS18-12	17	1	Rim	4.499	0.094	1.895	0.295	0.318	0.079	41.8	13.5	-12.0	44	3	77
SS18-12	21	1	Rim	3.992	0.115	1.605	0.210	0.279	0.066	35.7	10.6	-9.6	44	3	154
SS18-12	22	1	Rim	4.514	0.112	2.048	0.119	0.357	0.036	48.2	6.3	-6.0	44	3	316
SS18-12	23	1	Rim	3.369	0.062	1.614	0.073	0.347	0.035	46.6	6.1	-5.8	44	3	562
SS36-6	1	1	Rim	4.081	0.111	2.127	0.393	0.421	0.118	59.6	25.0	-20.3	n/a[b]	n/a[b]	58
SS36-6	2	1	Rim	3.995	0.077	1.611	0.111	0.275	0.038	35.1	5.8	-5.5	n/a[b]	n/a[b]	297
SS36-6	3	1	Rim	4.499	0.088	1.901	0.314	0.314	0.084	41.2	14.3	-12.7	n/a[b]	n/a[b]	64
SS36-6	4	1	Rim	4.052	0.081	1.463	0.341	0.226	0.103	27.9	15.6	-13.7	n/a[b]	n/a[b]	47

SS36-6	5	1 Rim	4.433	0.089	2.265	0.251	0.418	0.070	59.1	13.9	-12.3	n/a[b]	n/a[b]	81
SS36-6	6	1 Rim	4.212	0.078	1.568	0.165	0.245	0.050	30.7	7.4	-6.9	n/a[b]	n/a[b]	129
SS36-6	7	1 Rim	4.210	0.089	1.891	0.428	0.338	0.123	45.0	22.5	-18.7	n/a[b]	n/a[b]	35
SS36-6	8	1 Rim	4.247	0.078	1.745	0.145	0.293	0.044	37.8	7.0	-6.6	n/a[b]	n/a[b]	178
SS36-6	9	1 Rim	4.201	0.090	2.064	0.476	0.388	0.138	53.6	27.8	-22.1	n/a[b]	n/a[b]	34
SS36-6	10	1 Rim	3.837	0.106	2.377	0.426	0.533	0.139	83.2	38.5	-28.4	n/a[b]	n/a[b]	37
SS36-6	11	1 Rim	3.361	0.068	1.475	0.102	0.289	0.044	37.2	6.9	-6.5	n/a[b]	n/a[b]	351
SS36-6	12	1 Rim	4.195	0.139	2.280	0.381	0.451	0.112	65.4	24.9	-20.2	n/a[b]	n/a[b]	44
SS36-6	13	1 Rim	3.992	0.073	1.592	0.103	0.269	0.036	34.2	5.4	-5.2	n/a[b]	n/a[b]	304
SS36-6	14	1 Rim	4.393	0.086	1.810	0.232	0.299	0.065	38.8	10.6	-9.7	n/a[b]	n/a[b]	102
SS36-6	15	1 Rim	3.229	0.059	1.366	0.077	0.261	0.037	33.0	5.6	-5.3	n/a[b]	n/a[b]	321
SS36-6	16	1 Rim	4.233	0.080	1.702	0.140	0.282	0.043	36.2	6.7	-6.3	n/a[b]	n/a[b]	254
SS36-6	17	1 Rim	4.138	0.076	1.595	0.109	0.258	0.036	32.6	5.4	-5.1	n/a[b]	n/a[b]	250
SS36-6	18	1 Rim	4.304	0.084	2.222	0.277	0.421	0.079	59.7	16.0	-14.0	n/a[b]	n/a[b]	79
SS36-6	19	1 Rim	4.092	0.078	1.656	0.215	0.280	0.066	35.8	10.5	-9.5	n/a[b]	n/a[b]	77
SS36-6	20	1 Rim	4.052	0.077	1.631	0.087	0.276	0.031	35.2	4.8	-4.6	n/a[b]	n/a[b]	341
SS36-6	21	1 Rim	4.436	0.096	1.456	0.594	0.200	0.160	24.4	24.4	-19.9	n/a[b]	n/a[b]	32
SS36-6	22	1 Rim	4.551	0.096	1.524	0.327	0.212	0.086	26.0	12.6	-11.3	n/a[b]	n/a[b]	81
SS36-6	23	1 Rim	4.155	0.198	2.782	0.644	0.602	0.191	100.5	71.2	-42.7	n/a[b]	n/a[b]	25
SS36-6	24	1 Rim	3.283	0.065	1.357	0.064	0.252	0.032	31.7	4.8	-4.6	n/a[b]	n/a[b]	425
SS36-6	25	1 Rim	4.450	0.089	2.182	0.420	0.394	0.114	54.6	22.6	-18.7	n/a[b]	n/a[b]	47
SS36-6	26	1 Rim	4.321	0.088	1.575	0.235	0.240	0.067	29.9	10.0	-9.2	n/a[b]	n/a[b]	114
SS36-6	27	1 Rim	4.577	0.090	1.969	0.489	0.326	0.127	43.1	22.8	-18.9	n/a[b]	n/a[b]	48
SS36-6	28	1 Rim	4.210	0.077	1.720	0.123	0.289	0.039	37.2	6.1	-5.8	n/a[b]	n/a[b]	217
SS36-6	29	1 Rim	4.531	0.106	2.075	0.433	0.358	0.114	48.3	21.4	-17.9	n/a[b]	n/a[b]	48
SS36-6	30	1 Rim	3.346	0.071	2.114	0.388	0.533	0.149	83.1	42.1	-30.3	n/a[b]	n/a[b]	33
SS36-6	a	1 Core	3.372	0.062	1.606	0.083	0.337	0.038	44.8	6.4	-6.0	n/a[b]	n/a[b]	416
SS36-6	b	1 Core	3.447	0.063	1.451	0.089	0.271	0.038	34.5	5.8	-5.5	n/a[b]	n/a[b]	338
SS36-6	c	1 Core	2.509	0.046	1.254	0.050	0.303	0.041	39.4	6.6	-6.2	n/a[b]	n/a[b]	623
SS36-6	d	1 Rim (Polished)	7.175	0.132	2.697	0.199	0.308	0.032	40.1	5.2	-5.0	n/a[b]	n/a[b]	241
SS36-6	d	2 Core	3.235	0.061	1.544	0.092	0.330	0.042	43.8	7.1	-6.7	n/a[b]	n/a[b]	299
SS36-6	e	1 Core	2.552	0.047	1.355	0.062	0.351	0.045	47.1	7.8	-7.3	n/a[b]	n/a[b]	440

Sample														
SS36-6	f	1 Core	2.215	0.041	1.235	0.042	0.349	0.045	46.9	7.9	-7.4	n/a[b]	n/a[b]	701
SS36-6	g	1 Rim (Polished)	3.562	0.065	1.438	0.079	0.256	0.034	32.2	5.0	-4.8	n/a[b]	n/a[b]	391
SS36-6	g	2 Core	4.399	0.081	1.680	0.147	0.263	0.043	33.4	6.5	-6.1	n/a[b]	n/a[b]	185
SS36-6	h	1 Core	2.180	0.040	1.086	0.039	0.256	0.044	32.3	6.7	-6.3	n/a[b]	n/a[b]	717
SS36-6	i	1 Core	2.751	0.051	1.409	0.081	0.343	0.048	45.8	8.2	-7.7	n/a[b]	n/a[b]	267
SS36-6	j	1 Rim (Polished)	5.233	0.097	2.034	0.199	0.293	0.046	37.8	7.3	-6.9	n/a[b]	n/a[b]	141
SS36-6	j	2 Core	2.621	0.048	1.270	0.066	0.294	0.044	38.0	7.1	-6.6	n/a[b]	n/a[b]	341
SS36-6	k	1 Rim (Polished)	3.513	0.065	1.450	0.068	0.264	0.031	33.5	4.7	-4.5	n/a[b]	n/a[b]	475
SS36-6	k	2 Core	3.418	0.063	1.306	0.067	0.220	0.031	27.2	4.5	-4.3	n/a[b]	n/a[b]	471
SS36-6	l	1 Core	3.679	0.067	1.410	0.085	0.236	0.034	29.4	4.9	-4.7	n/a[b]	n/a[b]	340
SS36-6	m	1 Core	2.102	0.038	1.114	0.044	0.291	0.049	37.6	7.8	-7.3	n/a[b]	n/a[b]	603
SS36-6	n	1 Core	2.464	0.045	1.241	0.048	0.303	0.041	39.4	6.6	-6.2	n/a[b]	n/a[b]	548
SS36-6	o	1 Core	2.331	0.043	1.221	0.066	0.316	0.052	41.4	8.7	-8.0	n/a[b]	n/a[b]	503
SS68-10	1	1 Rim	0.713	0.042	0.733	0.042	1.183	0.720	∞[a]	∞[a]	∞[a]	n/a[b]	n/a[b]	1498
SS68-10	2	1 Rim	3.779	0.076	2.639	0.132	0.641	0.046	111.8	14.8	-13.1	n/a[b]	n/a[b]	227
SS68-10	3	1 Rim	4.313	0.082	2.893	0.204	0.617	0.057	104.8	17.7	-15.3	n/a[b]	n/a[b]	152
SS68-10	4	1 Rim	4.752	0.098	3.084	0.186	0.598	0.048	99.5	13.8	-12.3	n/a[b]	n/a[b]	204
SS68-10	6	1 Rim	4.121	0.077	2.975	0.169	0.674	0.051	122.4	18.7	-15.9	n/a[b]	n/a[b]	186
SS68-10	7	1 Rim	1.286	0.037	1.285	0.044	0.998	0.102	689.7	∞[a]	-442.8	n/a[b]	n/a[b]	649
SS68-10	8	1 Rim	0.956	0.019	0.951	0.026	0.986	0.143	468.1	∞[a]	-265.9	n/a[b]	n/a[b]	1014

a) The infinity mark denotes samples which are in secular equilibrium or are within error of secular equilibrium

b) No isochron age calculated

Whole rock activity values for age calculations are tabulated in supplementary material VI

Supplementary Material IV

U-Pb disequilibrium corrected ages for SHRIMP II session one ages

Sample	Zircon code	Spot id	Core/ Rim	238U/206Pb	% error (2σ)	207Pb/206Pb	% error (2σ)	U ppm	Th ppm	f207% - unmodified	Th/U	$f_{Th/U}$	f207%	207Pb corrected 206Pb/238U age (Ma)	Error (2σ)	U-Th disequilibrium corrected 207Pb/206Pb age (Ma)	Error (2σ)	Notes
SS43-4	a	1	Core	2942	17	0.559	18	34	27	65.03	0.809	0.2579	64.28	0.766	0.296	0.863	0.308	
SS43-4	ab	1	Core	9225	18	0.117	36	42	31	8.98	0.738	0.2353	7.32	0.636	0.122	0.731	0.105	
SS43-4	b	1	Core	11275	22	0.186	84	29	21	17.79	0.713	0.2272	15.66	0.47	0.156	0.566	0.143	
SS43-4	d	1	Rim	14142	17	-0.339	48	15	7	-48.75	0.461	0.1470	0.05	0.678	0.15	0.548	0.078	reverse discordant (Pb/Pb -0.339)
SS43-4	d	2	Core	8951	19	0.167	36	62	37	15.30	0.591	0.1885	13.64	0.61	0.128	0.710	0.111	
SS43-4	e	1	Core	3472	17	0.719	22	18	9	85.24	0.467	0.1489		0.274	0.388	1.949	0.319	No solution for bisection method
SS43-4	f	1	Core	2295	23	0.7	16	26	20	82.88	0.756	0.2409	82.21	0.481	0.418	0.582	0.442	
SS43-4	h	1	Core	7916	17	0.178	34	50	40	16.74	0.807	0.2572	15.27	0.678	0.132	0.771	0.117	
SS43-4	h	2	Rim	6748	42	0.543	42	17	9	62.94	0.518	0.1651	61.54	0.354	0.32	0.457	0.316	
SS43-4	h	3	Core	10379	29	-0.003	212	50	40	-6.27	0.798	0.2544	0.03	0.66	0.19	0.702	0.179	reverse discordant
SS43-4	h	4	Rim	12807	28	0.186	86	34	15	17.75	0.445	0.1419	15.29	0.414	0.154	0.519	0.137	
SS43-4	i	1	Core	8762	60	0.543	50	19	8	62.89	0.423	0.1347	61.16	0.273	0.302	0.377	0.319	
SS43-4	j	1	Core	7353	18	0.207	62	29	21	20.27	0.742	0.2366	19.02	0.699	0.192	0.793	0.179	
SS43-4	k	1	Rim	4289	34	0.464	48	15	8	52.89	0.552	0.1759	52.01	0.708	0.482	0.811	0.463	
SS43-4	k	2	Core	11714	59	0.28	44	32	23	29.68	0.717	0.2284	27.47	0.387	0.244	0.482	0.171	
SS43-4	k	3	Core	18298	29	-0.256	38	37	16	-38.24	0.427	0.1361	0.07	0.487	0.146	0.445	0.103	reverse discordant (Pb/Pb -0.256)
SS43-4	k	4	Rim	7742	6	0.119	56	45	34	9.20	0.749	0.2389	7.84	0.756	0.082	0.850	0.081	
SS43-4	n	2	Core	7868	23	0.299	42	48	38	32.02	0.792	0.2523	30.57	0.557	0.182	0.650	0.168	
SS43-4	o1	1	Core	9208	11	0.145	28	54	30	56.43	0.556	0.1771	10.81	0.305	0.370	0.714	0.071	
SS43-4	o2	1	Rim	22391	121	0	0	28	12	-112.59	0.437	0.1392	0.08	0.612	0.078	0.379	0.352	reverse discordant
SS43-4	o2	2	Core	9370	31	0.227	42	40	34	22.96	0.851	0.2711	21.22	0.53	0.184	0.621	0.152	
SS43-4	p	1	Core	2489	15	0.626	22	42	32	73.43	0.762	0.2429	72.83	0.688	0.448	0.786	0.473	
SS43-4	v	1	Core	784	35	0.752	10	40	25	89.40	0.625	0.1992	89.04	0.871	0.788	0.988	0.907	
SS43-4	w	1	Core	6974	22	0.376	24	25	15	41.80	0.600	0.1912	40.41	0.538	0.158	0.639	0.145	
SS43-4	y	1	Core	718	88	0.783	8	10	7	93.30	0.700	0.2231		0.601	0.912	9.052	7.869	No solution for bisection method
SS43-4	z	1	Core	13009	40	0.001	424	30	20	-5.75	0.667	0.2125	0.04	0.524	0.210	0.581	0.201	reverse discordant

Sample		Spot	Core/Rim														Note
SS55-1	a	1 Core	9294	7	0.071	18	296	486	3.11	1.642	0.4319	1.68	0.672	0.023	0.744	0.043	
SS55-1	b	1 Core	8818	6	0.072	27	154	217	3.14	1.409	0.3706	1.77	0.708	0.025	0.787	0.047	
SS55-1	d	1 Core	8850	9	0.071	27	140	204	3.21	1.457	0.3833	1.68	0.705	0.033	0.783	0.062	
SS55-1	d	2 Core	8741	14	0.108	23	115	144	7.92	1.252	0.3294	6.39	0.679	0.048	0.763	0.085	
SS55-1	d	3 Core	9381	6	0.058	29	188	285	1.48	1.516	0.3987	0.02	0.677	0.021	0.752	0.041	
SS55-1	d	4 Core	8658	10	0.043	37	202	333	-0.47	1.649	0.4336	0.02	0.748	0.037	0.806	0.073	
SS55-1	e	1 Rim	8985	11	0.049	40	152	200	0.48	1.316	0.3461	0.03	0.714	0.04	0.789	0.077	
SS58-6	a	1 Core	13118	15	0.0952	30	273	431	6.18	1.579	0.3107	3.96	0.461	0.070	0.547	0.062	
SS58-6	b	1 Core	11910	14	0.1902	24	130	138	18.33	1.062	0.2089	16.06	0.442	0.070	0.540	0.064	
SS58-6	b	2 Core	13435	17	0.1135	34	172	203	8.50	1.180	0.2323	6.12	0.439	0.076	0.533	0.068	
SS58-6	b	3 Core	16155	24	0.0678	83	123	133	2.76	1.081	0.2128	0.05	0.388	0.098	0.484	0.099	reverse discordant
SS58-6	b	4 Rim	12975	17	0.1056	31	132	144	7.61	1.091	0.2147	5.19	0.459	0.080	0.556	0.070	
SS58-6	c	1 Core	13184	8	0.1632	24	198	333	14.92	1.682	0.3310	12.57	0.416	0.040	0.500	0.039	
SS58-6	d	1 Core	15962	19	0.3505	44	56	41	38.59	0.732	0.1441	35.52	0.248	0.092	0.350	0.093	
SS58-6	e	1 Core	14804	23	0.1024	81	80	72	7.22	0.900	0.1771	4.40	0.404	0.102	0.505	0.089	
SS58-6	f	1 Core	14635	19	0.1917	26	150	210	18.50	1.400	0.2756	15.86	0.359	0.074	0.448	0.065	
SS58-6	g	1 Rim	0.13	127	1	101	1238	1072		0.866	0.1704		0.000		14017.243	#NUM!	No solution for bisection method
SS58-6	g	2 Core	12882	11	0.0954	17	484	781	6.28	1.614	0.3176	4.03	0.469	0.054	0.554	0.049	
SS58-6	g	3 Core	13187	6	0.0581	27	447	663	1.60	1.483	0.2919	0.04	0.481	0.032	0.565	0.030	reverse discordant
SS58-6	i	1 Rim	7364	19	0.4538	7	539	815	51.68	1.512	0.2976	50.24	0.423	0.086	0.511	0.079	
SS58-6	j	1 Rim	13481	44	0.1834	143	48	32	17.40	0.667	0.1312	14.82	0.395	0.236	0.501	0.204	
SS58-6	j	2 Core	93	23	0.8152	7	93	104	97.40	1.118	0.2201		1.79	5.052	68.695	15.798	No solution for bisection method

U-Pb SHRIMP II session two ages

Sample	Zircon code	Spot id	Core/Rim	Concordant?	204 corrected $^{207}Pb^*/^{235}U$	Percentage error (1σ)	204 corrected $^{206}Pb^*/^{238}U$	Percentage error (1σ)	204 corrected $^{206}Pb/^{238}U$ age (Ma)	Error (2σ)
SA-X	2.3	1 Core	Concordant		9.4	2.4	0.411	1.8	2219	68
SA-X	2.3	2 Core/Rim	Discordant		8.5	1.7	0.379	1.7	2070	59
SA-X	2.4	1 Core	Concordant		10.0	3.9	0.449	3.0	2389	120
SA-X	2.4	2 Core/Rim	Discordant		5.1	1.7	0.323	1.5	1802	46
SA-X	2.4	3 Core/Rim	Discordant		4.5	1.5	0.290	1.5	1641	42
SA-X	2.5	1 Core	Concordant		4.8	6.2	0.309	6.2	1734	188
SA-X	2.5	2 Core/Rim	Discordant		4.5	5.6	0.289	4.0	1635	115
SA-X	2.5	3 Core/Rim	Discordant		3.9	9.6	0.248	8.7	1429	224
SA-X	2.6	1 Core	Discordant		5.1	2.5	0.321	2.4	1794	74

Sample	Zircon code	Spot id	Core/Rim							
SA-X	2.6	2	Core/Rim	Discordant	5.3	3.4	0.327	2.9	1823	94
SA-X	1.5	1	Core/Rim	Discordant	0.0	178.7	0.023	2.5	148	7
SA-X	1.5	2	Core/Rim	Concordant	0.2	14.4	0.026	2.5	165	8
SA-X	1.6	1	Core/Rim	Concordant	0.3	3.9	0.038	1.9	238	9
SA-X	1.6	2	Core	Concordant	0.2	8.3	0.037	1.8	234	8
SA-X	1.7	1	Core	Concordant	0.2	7.8	0.026	1.7	166	6
SA-X	1.7	2	Core/Rim	Concordant	0.1	14.9	0.026	2.0	163	6
SA-X	1.8	1	Core/Rim	Concordant	0.1	30.6	0.016	2.3	105	5
SA-X	1.8	2	Core/Rim	Concordant	0.1	26.5	0.017	2.0	106	4
SA-X	1.9	1	Core/Rim	Discordant	4.6	2.5	0.276	1.6	1572	45
SA-X	1.9	2	Core/Rim	Discordant	6.4	1.7	0.325	1.5	1812	47
SA-X	1.9	3	Core	Concordant	11.5	1.6	0.482	1.5	2537	62

U-Pb LA-ICP MS ages

Sample	Zircon code	Spot id	Core/Rim	^{238}U/^{206}Pb	Error (2σ)	^{207}Pb/^{206}Pb	Error (2σ)	^{207}Pb corrected ^{206}Pb/^{238}U age (Ma)	Error (2σ)	Common ^{207}Pb/^{206}Pb model value
WR01-A	1	1	Core/Rim	84.4	1.2	0.0515	0.0014	75.5	1.1	0.840
WR01-A	2	1	Core/Rim	76.9	1.2	0.0671	0.0044	81.3	1.3	0.841
WR01-A	3	1	Core/Rim	73.7	3.3	0.1150	0.0150	79.5	3.9	0.841
WR01-A	4	1	Core/Rim	85.5	1.3	0.0477	0.0004	74.9	1.1	0.840
WR01-A	5	1	Core/Rim	82.6	1.2	0.0486	0.0004	77.5	1.1	0.841
WR01-A	6	1	Core/Rim	76.3	1.5	0.1361	0.0061	74.6	1.6	0.840
WR01-A	7	1	Core/Rim	84.8	1.2	0.0479	0.0004	75.6	1.1	0.840
WR01-A	8	1	Core/Rim	82.2	1.3	0.0525	0.0011	77.5	1.2	0.841
WR01-A	9	1	Core/Rim	82.3	1.3	0.0531	0.0019	77.3	1.2	0.841
WR01-A	10	1	Core/Rim	86.8	2.2	0.0525	0.0014	73.4	1.8	0.840
WR01-A	11	1	Core/Rim	86.6	1.4	0.0510	0.0010	73.7	1.2	0.840
WR01-A	12	1	Core/Rim	82.4	1.7	0.0730	0.0100	75.2	1.8	0.840
WR01-A	13	1	Core/Rim	85.8	1.3	0.0478	0.0005	74.7	1.1	0.840
WR01-A	14	1	Core/Rim	87.3	1.4	0.0523	0.0005	72.9	1.1	0.840
WR01-A	15	1	Core/Rim	85.5	1.3	0.0690	0.0043	73.0	1.2	0.840
WR01-A	16	1	Core/Rim	86.5	1.3	0.0479	0.0004	74.1	1.1	0.840
WR01-A	17	1	Core/Rim	84.5	1.3	0.0514	0.0019	75.5	1.2	0.840
WR01-A	18	1	Core/Rim	82.3	1.4	0.0636	0.0042	76.3	1.3	0.841
WR01-A	19	1	Core/Rim	11.7	0.4	0.1113	0.0010	496.6	15.3	0.869
WR01-A	20	1	Core/Rim	87.1	1.3	0.0522	0.0013	73.2	1.1	0.840

U-Pb CAMECA ages

Sample	Spot id	Core/Rim	Concordant?	$^{206}Pb/^{238}U$	Error (1σ)	$^{207}Pb/^{235}U$	Error (1σ)	$^{204}Pb/^{206}Pb$	Error (1σ)	Th/U	U (ppm)	^{204}Pb corrected $^{206}Pb/^{238}U$ age (Ma)	Error (1σ)	% Radiogenic ^{206}Pb
SS66-1	1	Unknown	Discordant	0.3555	0.0096	5.581	0.150	0.000010	0.000004	0.035	1141	1960	46	100
SS66-1	2	Unknown	Discordant	0.0121	0.0003	0.169	0.015	0.004294	0.001020	1.110	145	71.3	2.5	91.9
SS66-1	3	Unknown	Discordant	0.1215	0.0309	2.662	0.488	0.001796	0.000705	0.222	152	715	173	96.6
SS66-1	4	Unknown	Discordant	0.3156	0.0107	4.939	0.176	0.000065	0.000011	0.07	1059	1770	52	99.9
SS66-1	5	Unknown	Discordant	0.0322	0.0007	0.230	0.006	0.000223	0.000039	0.471	1516	203	5	99.6
SS66-1	6	Unknown	Concordant	0.3350	0.0089	5.468	0.148	0.000031	0.000007	0.013	1008	1860	43	99.9
SS66-1	7	Unknown	Discordant	0.2830	0.0070	4.509	0.119	0.000257	0.000074	0.425	794	1600	35	99.5
SS66-1	8	Unknown	Discordant	0.2534	0.0070	4.047	0.116	0.000364	0.000027	0.09	767	1450	36	99.3
SS66-1	9	Unknown	Concordant	0.3306	0.0091	5.209	0.156	0.000055	0.000017	1.37	204	1840	44	99.9
SS66-1	10	Unknown	Discordant	0.1720	0.0144	2.700	0.232	0.000081	0.000036	0.094	597	1020	79	99.9
SS66-1	11	Unknown	Discordant	0.2686	0.0178	4.288	0.231	0.000541	0.000149	0.766	213	1520	90	99
SS66-1	12	Unknown	Discordant	0.3997	0.0092	9.403	0.220	0.000163	0.000034	0.325	392	2160	42	99.7
SS66-1	13	Unknown	Discordant	0.3414	0.0125	8.525	0.748	0.004716	0.000823	1.64	23	1750	62	91.1
SS66-1	14	Unknown	Discordant	0.1363	0.0127	1.837	0.193	0.000353	0.000052	0.372	458	819	72	99.3
SS66-1	15	Unknown	Discordant	0.2713	0.0120	4.299	0.187	0.000052	0.000009	0.109	955	1550	61	99.9
SS66-1	16	Unknown	Discordant	0.0947	0.0200	1.229	0.331	0.000416	0.000113	0.029	741	579	117	99.2
SS66-1	17	Unknown	Discordant	0.1687	0.0119	3.833	0.139	0.004639	0.001129	0.848	152	923	64	91.2
SS66-1	18	Unknown	Concordant	0.3286	0.0115	5.128	0.174	0.000027	0.000006	0.037	831	1830	56	100
SS66-1	19	Unknown	Discordant	0.0657	0.0060	0.909	0.076	0.002489	0.000740	0.059	918	392	35	95.3
SS66-1	20	Unknown	Concordant	0.0749	0.0018	0.591	0.015	0.000124	0.000027	0.018	786	464	11	99.8

Supplementary Material V

(U-Th)/He data

Sample code	232Th (ng)	± 1sig (%)	238U (ng)	± 1sig (%)	4He (ncc)	± 1sig (%)	TAU[a] (%)	Unc. age (ka)	± 1sig (ka)	Ft[b]	Ft-Cor. age (ka)	± 1sig (ka)	238U/230Th age (ka)	± 1sig (ka)	D230[c]	Dsq.-Cor. (ka)	± 1sig (ka)
HS02-1	0.253	2.14	0.332	2.4	0.0020	10.4	10.7	42.9	4.6	0.729	47.3	5.6	91.5	12.4	0.163	68.4	9.5
HS02-2	2.113	1.41	1.544	1.8	0.0145	3.8	4.1	58.4	2.4	0.781	60.2	3.9	124.0	12.1	0.292	74.2	5.6
HS02-5	1.047	1.97	1.185	2.3	0.0089	3.7	4.2	51.4	2.1	0.799	51.7	3.3	134.2	15.1	0.189	64.2	5.2
HS02-6	0.591	1.42	0.670	1.8	0.0055	5.9	6.1	56.0	3.4	0.846	53.3	4.2	113.9	12.9	0.189	70.9	6.9
HS02-8	0.876	1.42	0.568	1.8	0.0060	5.3	5.5	64.0	3.5	0.715	72.0	5.3	146.8	16.4	0.329	85.0	7.3
HS02-10	9.866	1.96	8.547	2.3	0.0995	0.7	2.0	75.3	1.5	0.867	69.9	3.7	144.8	11.6	0.247	85.0	5.6
HS02-13	0.423	1.54	0.426	2.1	0.0040	6.7	6.9	62.4	4.3	0.721	69.7	5.9	163.3	32.1	0.212	81.4	8.9
HS02-14	1.440	1.41	1.088	1.8	0.0101	5.2	5.4	58.3	3.2	0.767	61.2	4.5	121.8	12.2	0.283	75.9	6.6
HS02-15	0.359	1.54	0.387	2.1	0.0017	13.6	13.7	29.6	4.1	0.756	31.5	4.6	121.6	22.9	0.199	39.4	6.3
Best fit eruption age ± 2σ (both in ka)																70.9	4.3
HS100-5-1	0.661	2.46	0.816	2.6	0.0084	4.0	4.6	71.0	3.3	0.749	76.3	5.1	118.8	16.1	0.108	110.0	9.0
HS100-5-2	0.354	1.52	0.397	2.3	0.0041	8.0	8.3	70.0	5.8	0.700	80.5	7.8	118.4	16.5	0.119	115.3	11.6
HS100-5-3	0.547	1.51	0.650	2.2	0.0050	6.8	7.1	52.8	3.7	0.708	60.0	5.2	107.8	13.0	0.112	88.7	9.7
HS100-5-4	0.424	2.39	0.433	2.6	0.0032	5.8	6.2	49.6	3.1	0.709	56.3	4.4	124.5	16.4	0.131	74.1	8.0
HS100-5-6*	0.430	1.51	0.494	2.1	0.0111	4.2	4.6	153.6	7.1	0.712	173.6	11.7	105.8	14.0	0.116	n/a	n/a
HS100-5-9*	0.446	1.51	0.402	2.2	0.0068	5.5	5.8	111.0	6.4	0.708	126.1	9.6	89.4	9.5	0.148	n/a	n/a
HS100-5-12	0.348	3.44	0.426	3.4	0.0044	5.8	6.5	72.0	4.7	0.770	75.2	6.1	166.1	26.1	0.109	94.0	10.3
HS100-5-13	0.286	1.52	0.311	1.9	0.0030	8.5	8.7	64.8	5.6	0.750	69.6	7.0	117.1	14.5	0.122	101.0	11.8
HS100-5-14	0.429	1.54	0.622	2.2	0.0055	6.5	6.8	62.8	4.3	0.703	71.9	6.1	114.1	11.1	0.092	107.4	10.1
HS100-5-17*	0.531	2.26	0.786	2.5	0.0138	4.6	5.1	124.9	6.4	0.778	129.2	9.2	86.6	11.3	0.090	n/a	n/a
HS100-5-19	0.434	1.54	0.541	2.3	0.0082	2.5	3.1	104.9	3.3	0.731	115.5	6.8	116.4	16.9	0.107	n/a	n/a
Best fit eruption age ± 2σ (both in ka)																96.0	7.4
SS07-3-1a	1.219	2.62	1.468	3.4	0.0001	156.9	156.9	0.4	0.6	0.700	0.4	0.6	12.6	1.0	0.146	0.7	1.2
SS07-3-3a	1.536	1.51	1.838	1.9	0.0001	178.6	178.6	0.3	0.5	0.700	0.3	0.6	12.6	1.0	0.147	0.7	1.2
SS07-3-4a	0.137	1.55	0.137	1.9	0.0000	251.9	251.9	2.2	5.4	0.700	2.5	6.2	12.6	1.0	0.177	2.7	14.1
SS07-3-5a	0.167	2.08	0.156	2.5	0.0003	39.2	39.2	13.4	5.3	0.700	15.5	6.1	12.6	1.0	0.188	26.8	9.7
SS07-3-6a	0.153	1.55	0.266	1.9	0.0000	325.0	325.0	1.2	3.9	0.700	1.4	4.5	12.6	1.0	0.101	0.0	11.5
SS07-3-7a	1.947	1.51	2.197	1.9	0.0005	21.4	21.5	1.6	0.4	0.700	1.9	0.4	12.6	1.0	0.156	3.5	0.8
SS07-3-3b	1.079	2.46	1.189	2.9	0.0002	61.4	61.5	1.1	0.7	0.728	1.2	0.7	11.4	2.7	0.160	2.2	1.4
SS07-3-6b	1.120	1.67	1.577	2.5	0.0001	133.5	133.5	0.4	0.6	0.713	0.5	0.6	14.9	3.1	0.125	0.9	1.2
SS07-3-7b	0.412	1.68	0.564	2.4	0.0001	135.1	135.1	0.9	1.2	0.681	1.0	1.4	17.3	3.7	0.129	1.6	2.9

SS07-3-13b	0.244	2.46	0.248	2.9	0.0000	329.2	329.2	1.3	4.2	0.674	1.5	4.8	20.8	5.1	0.174	2.1	8.4
SS07-3-16b*	0.308	1.69	0.327	2.3	0.0001	197.9	197.9	1.0	2.1	0.655	1.2	2.4	n/a	n/a	0.166	n/a	n/a
SS07-3-17b*	1.819	1.67	2.309	2.3	0.1522	1.1	2.2	457.5	10.2	0.729	482.8	26.2	8.4	2.3	0.139	n/a	n/a
SS07-3-18b	0.294	2.40	0.284	2.8	0.0001	163.5	163.5	2.1	3.4	0.715	2.2	3.6	22.8	11.4	0.182	3.3	6.4
SS07-3-19b*	0.002	18.51	0.007	2.3	0.0001	125.2	125.2	71.2	89.1	LOST	LOST	LOST	15.0	4.3	LOST	n/a	n/a
Best fit eruption age ± 2σ (both in ka)																**2.0**	**1.0**
SS14-21-1	1.514	1.50	0.696	1.9	0.0041	6.4	6.5	31.7	2.1	0.740	34.5	2.8	132.1	16.5	0.232	41.5	3.8
SS14-21-6*	0.021	2.14	0.046	2.5	0.0001	267.1	267.1	11.6	31.0	0.765	12.2	32.6	141.2	30.8	0.049	11.6	40.6
SS14-21-7	0.243	1.53	0.269	2.0	0.0018	13.7	13.8	44.3	6.1	0.774	46.1	6.8	87.7	13.6	0.097	72.5	12.0
SS14-21-8*	0.553	1.51	0.522	2.0	0.0112	4.9	5.1	141.7	7.3	0.776	146.9	10.5	114.0	25.4	0.113	n/a	n/a
SS14-21-9	0.241	2.14	0.236	2.5	0.0013	19.9	20.0	36.4	7.3	0.713	41.1	8.5	88.4	16.4	0.109	61.9	14.7
SS14-21-10	0.306	1.43	0.276	1.8	0.0023	10.7	10.8	54.3	5.9	0.759	57.6	6.9	86.6	10.4	0.119	88.9	10.2
SS14-21-15*	0.103	2.38	0.133	3.1	0.0015	13.2	13.5	77.1	10.4	0.725	85.5	12.3	80.6	10.7	0.083	n/a	n/a
SS14-21-17	0.247	1.91	0.237	1.9	0.0017	14.3	14.4	46.9	6.8	0.714	52.9	8.1	109.4	24.8	0.112	72.5	13.8
SS14-21-19	0.318	1.43	0.348	1.9	0.0020	8.3	8.5	39.6	3.4	0.730	43.6	4.3	89.4	15.9	0.098	65.6	8.6
SS14-21-21*	0.102	1.49	0.100	1.9	0.0020	11.2	11.3	129.7	14.7	0.769	135.7	16.8	234.8	95.7	0.109	n/a	n/a
Best fit eruption age ± 2σ (both in ka)																**52.9**	**6.0**
SS14-28-5	0.212	2.14	0.200	2.5	0.0013	14.7	14.8	41.4	6.1	0.692	48.1	7.5	89.7	18.1	0.140	72.1	12.2
SS14-28-9	0.885	1.96	0.931	2.3	0.0055	7.8	8.0	40.0	3.2	0.665	48.4	4.5	103.9	22.6	0.126	67.1	8.9
SS14-28-11	0.807	1.89	1.051	1.9	0.0061	6.8	7.0	40.3	2.8	0.719	45.1	3.9	75.3	13.4	0.101	72.8	6.8
SS14-28-12*	1.385	1.41	1.189	1.8	0.0033	7.7	7.8	18.1	1.4	0.753	19.3	1.8	71.8	11.4	0.154	n/a	n/a
SS14-28-16	0.951	1.42	1.192	1.8	0.0059	6.9	7.1	34.4	2.4	0.713	38.8	3.3	94.4	11.3	0.105	56.9	6.3
SS14-28-23	0.205	1.56	0.265	2.0	0.0014	14.2	14.3	37.9	5.4	0.721	42.3	6.4	90.3	18.4	0.102	64.4	11.5
SS14-28-25	0.302	1.43	0.390	1.8	0.0018	10.4	10.5	31.4	3.3	0.799	31.6	3.7	83.8	12.8	0.102	47.3	6.9
Best fit eruption age ± 2σ (both in ka)																**61.6**	**6.4**
SS15-43-1	0.336	1.97	0.437	2.3	0.0034	8.5	8.7	54.3	4.7	0.700	62.4	6.2	92.9	18.0	0.098	94.9	10.0
SS15-43-7	0.848	1.42	0.757	1.8	0.0067	4.6	4.8	57.4	2.7	0.773	59.8	4.1	120.6	17.1	0.143	80.8	8.0
SS15-43-8	0.605	2.32	0.464	2.6	0.0022	13.9	14.0	29.4	4.1	0.705	33.5	5.0	137.5	18.8	0.167	41.0	6.5
SS15-43-9	0.286	1.43	0.326	1.8	0.0029	7.9	8.0	59.7	4.8	0.770	62.4	5.9	119.9	18.2	0.112	86.2	11.0
SS15-43-13	0.152	1.92	0.141	2.2	0.0008	31.4	31.4	38.2	12.0	0.631	48.7	15.5	94.4	10.4	0.137	72.7	27.0
SS15-43-14	0.223	1.91	0.185	2.0	0.0009	21.0	21.1	32.2	6.8	0.662	39.1	8.5	96.1	17.2	0.153	53.7	13.5
SS15-43-15	0.195	1.44	0.271	1.8	0.0025	12.0	12.1	65.7	8.0	0.671	78.8	10.3	139.5	19.8	0.092	108.7	17.8
SS15-43-16	0.323	1.94	0.330	2.3	0.0026	8.8	9.0	52.3	4.7	0.692	60.8	6.2	103.9	15.1	0.125	88.4	10.6
SS15-43-18	0.229	1.56	0.214	2.1	0.0011	14.4	14.5	34.6	5.0	0.644	43.2	6.6	103.0	14.5	0.137	60.2	10.9
SS15-43-19*	0.166	1.58	0.227	2.1	0.0005	39.9	39.9	16.9	6.7	0.670	20.2	8.1	137.5	25.5	0.094	n/a	n/a
SS15-43-20	0.434	1.42	0.446	1.8	0.0033	6.6	6.8	48.8	3.3	0.773	50.8	4.3	120.4	15.7	0.124	68.1	7.4
SS15-43-21	0.597	1.42	0.605	1.8	0.0048	7.4	7.6	52.6	4.0	0.733	57.7	5.2	117.3	15.3	0.126	80.0	9.6

Sample																
SS15-43-23	0.122	2.68	0.159	2.4	0.0008	24.5	24.6	36.0	8.9	0.653	44.4	11.1	101.9	15.4	0.098	63.2	19.1
Best fit eruption age ± 2σ (both in ka)																**70.5**	**5.8**
SS15-45-3	4.142	1.52	3.666	2.2	0.0087	7.9	8.1	15.4	1.2	0.836	14.8	1.4	39.9	7.7	0.216	22.9	2.4
SS15-45-4	9.409	1.50	6.927	2.0	0.0263	4.2	4.5	23.7	1.1	0.840	22.7	1.5	39.9	4.9	0.260	34.3	2.4
SS15-45-5	13.228	1.50	11.484	2.0	0.0405	1.7	2.4	22.8	0.5	0.881	20.9	1.1	38.8	5.9	0.220	32.7	2.1
SS15-45-7	5.610	2.20	4.164	2.5	0.0136	5.8	6.1	20.4	1.2	0.847	19.3	1.5	36.4	5.3	0.257	29.5	2.5
SS15-45-8	4.201	1.52	4.132	2.2	0.0090	3.6	4.0	14.4	0.6	0.814	14.3	0.9	44.8	5.7	0.194	22.0	1.6
SS15-45-9	4.248	1.50	3.139	2.1	0.0088	6.5	6.7	17.6	1.2	0.789	17.9	1.5	40.2	5.4	0.259	26.6	2.4
SS15-45-10	2.316	2.24	2.179	2.6	0.0058	6.1	6.4	17.4	1.1	0.803	17.4	1.4	34.2	5.8	0.203	28.5	2.5
SS15-45-13	6.176	1.50	5.245	2.0	0.0149	5.8	6.0	18.3	1.1	0.850	17.3	1.3	38.1	3.8	0.225	26.9	2.3
SS15-45-14	7.981	2.23	7.673	2.5	0.0274	2.7	3.4	23.6	0.8	0.877	21.6	1.3	40.3	6.7	0.199	35.1	2.3
SS15-45-16	4.733	1.50	4.547	2.0	0.0127	3.2	3.5	18.4	0.7	0.890	16.7	1.0	40.2	6.3	0.199	26.4	1.9
SS15-45-21	6.881	1.50	7.206	2.0	0.0244	3.6	4.0	22.7	0.9	0.895	20.4	1.3	32.9	5.5	0.182	34.2	2.1
SS15-45-22	1.657	1.52	1.991	1.9	0.0042	8.2	8.3	14.6	1.2	0.839	14.0	1.4	56.5	8.4	0.159	21.2	2.3
SS15-45-23	3.794	2.98	3.429	2.4	0.0087	4.4	4.8	16.5	0.8	0.858	15.4	1.1	37.5	5.4	0.211	24.6	1.9
SS15-45-24	5.950	1.89	6.396	1.9	0.0174	5.1	5.3	18.3	1.0	0.857	17.2	1.3	27.8	6.0	0.178	29.3	2.1
SS15-45-25*	3.840	1.89	3.099	1.9	0.0377	2.6	3.0	77.5	2.3	0.822	75.9	4.4	38.1	6.7	0.237	n/a	n/a
Best fit eruption age ± 2σ (both in ka)																**27.8**	**1.1**
SS15-48-2	0.130	2.68	0.192	2.5	0.0010	21.2	21.3	37.2	7.9	0.677	44.2	9.7	184.4	58.0	0.145	49.9	12.1
SS15-48-3	0.136	1.93	0.166	2.1	0.0011	18.3	18.4	44.1	8.1	0.712	49.9	9.5	81.1	8.1	0.176	76.2	14.7
SS15-48-10	3.245	1.41	2.125	1.8	0.0056	6.1	6.3	15.9	1.0	0.782	16.4	1.3	35.1	3.8	0.329	23.1	2.0
SS15-48-11	1.282	1.53	0.883	1.9	0.0016	13.7	13.8	11.0	1.5	0.703	12.6	1.8	35.8	3.8	0.313	17.8	2.7
SS15-48-12	3.910	2.00	2.588	2.4	0.0072	3.8	4.3	16.8	0.7	0.787	17.1	1.1	38.9	4.4	0.326	24.0	1.7
SS15-48-14	0.698	2.32	0.399	2.6	0.0009	16.9	17.0	13.5	2.3	0.666	16.3	2.9	28.0	4.5	0.377	22.8	4.1
SS15-48-18	2.444	1.41	1.362	1.8	0.0039	6.5	6.7	16.7	1.1	0.697	19.3	1.6	51.5	7.0	0.387	24.8	2.2
SS15-48-21	1.063	2.00	0.711	2.4	0.0012	15.8	15.9	10.3	1.6	0.723	11.5	1.9	33.5	3.8	0.322	16.3	2.8
Best fit eruption age ± 2σ (both in ka)																**22.7**	**1.9**
SS15-66-1	0.598	3.66	0.673	3.6	0.0060	7.4	8.0	60.8	4.9	0.762	64.2	6.0	143.3	19.9	0.120	83.4	10.0
SS15-66-3	0.219	2.35	0.286	3.2	0.0026	11.8	12.2	63.6	7.7	0.820	62.4	8.2	131.4	24.8	0.104	84.4	13.7
SS15-66-5	0.183	2.31	0.167	3.1	0.0012	18.8	19.0	48.3	9.2	0.724	53.7	10.5	114.2	20.8	0.149	72.0	16.7
SS15-66-6	0.142	2.36	0.161	3.6	0.0012	16.5	16.7	49.9	8.4	0.717	56.0	9.8	128.4	22.3	0.119	74.2	15.3
SS15-66-7	0.325	2.31	0.330	2.9	0.0028	10.4	10.7	56.5	6.0	0.711	63.9	7.5	100.1	18.1	0.133	93.5	11.8
SS15-66-10	8.908	2.29	6.275	3.4	0.0620	1.1	2.8	60.9	1.7	0.749	65.4	3.7	156.2	21.1	0.192	79.0	5.9
SS15-66-11	0.210	1.56	0.311	2.1	0.0020	11.6	11.8	44.7	5.3	0.830	43.3	5.5	125.3	19.6	0.091	57.5	8.8
SS15-66-12	0.425	3.73	0.522	3.6	0.0045	5.8	6.6	59.6	3.9	0.761	63.0	5.2	129.4	25.5	0.110	83.4	10.4
SS15-66-13	0.165	1.57	0.259	2.0	0.0017	11.8	11.9	46.1	5.5	0.787	47.2	6.1	129.2	22.8	0.086	62.7	9.9
SS15-66-14	0.155	1.58	0.215	2.1	0.0019	8.6	8.8	62.2	5.5	0.807	62.0	6.3	105.2	17.8	0.098	91.6	10.8

SS15-66-16	0.275	2.32	0.392	3.2	0.0028	7.0	7.6	51.0	3.9	0.781	52.5	4.8	108.8	15.2	0.095	76.4	9.5
SS15-66-17	0.146	3.75	0.197	4.5	0.0018	11.7	12.3	62.2	7.7	0.848	59.0	7.8	124.9	22.6	0.100	80.0	13.4
SS15-66-18	0.391	2.31	0.424	3.6	0.0037	6.1	6.8	58.8	4.0	0.783	60.4	5.1	125.1	18.2	0.125	80.8	9.5
SS15-66-20	0.291	2.34	0.384	3.7	0.0031	8.6	9.2	56.8	5.2	0.768	59.5	6.2	123.8	17.7	0.103	82.6	11.4
Best fit eruption age ± 2σ (both in ka)																**78.0**	**5.4**
SS15-SN-2	1.913	1.94	1.865	2.3	0.0044	6.2	6.5	15.8	1.0	0.826	15.4	1.3	44.1	5.0	0.124	26.4	2.5
SS15-SN-3	0.399	1.54	0.545	2.0	0.0012	15.7	15.8	15.9	2.5	0.766	16.7	2.8	40.3	8.3	0.089	30.7	5.5
SS15-SN-6	1.486	1.41	1.167	1.8	0.0036	7.4	7.5	19.3	1.5	0.807	19.3	1.7	43.0	5.8	0.154	32.3	3.3
SS15-SN-13	0.408	1.43	0.506	1.8	0.0015	14.3	14.4	19.8	2.9	0.769	20.8	3.2	47.6	5.5	0.098	37.6	6.3
SS15-SN-14	0.936	2.32	0.777	2.7	0.0012	16.5	16.6	10.3	1.7	0.800	10.4	1.8	46.6	8.2	0.146	16.4	3.1
SS15-SN-17	1.372	1.46	1.441	2.5	0.0028	8.2	8.5	12.9	1.1	0.765	13.5	1.3	49.2	5.3	0.115	22.4	2.4
SS15-SN-18	0.522	1.47	0.633	2.6	0.0010	15.0	15.2	10.9	1.7	0.706	12.5	2.0	45.9	6.0	0.100	21.2	3.7
SS15-SN-22	1.165	2.05	1.059	2.9	0.0020	12.6	12.8	12.1	1.6	0.747	13.1	1.8	48.7	4.9	0.133	21.2	3.1
SS15-SN-23	1.699	1.46	1.427	2.4	0.0031	7.4	7.7	14.0	1.1	0.731	15.4	1.4	52.4	6.4	0.144	24.4	2.5
SS15-SN-24	1.125	1.47	0.963	2.3	0.0023	7.0	7.2	15.6	1.1	0.747	16.8	1.5	48.0	3.4	0.141	27.5	2.6
Best fit eruption age ± 2σ (both in ka)																**24.7**	**1.9**
SS18-12-1	31.995	1.50	31.557	2.0	0.1263	1.0	1.9	26.6	0.5	0.895	23.9	1.3	42.1	5.2	0.226	37.5	2.2
SS18-12-3	0.571	1.51	0.592	1.9	0.0016	14.9	15.0	18.1	2.7	0.649	22.5	3.6	41.1	3.6	0.215	36.0	6.1
SS18-12-4	0.751	2.10	0.818	2.4	0.0021	14.3	14.5	17.1	2.5	0.788	17.5	2.7	50.2	4.7	0.205	26.9	4.3
SS18-12-6	10.642	2.09	10.341	2.4	0.0427	1.9	2.8	27.3	0.8	0.896	24.6	1.4	46.6	5.6	0.229	37.3	2.4
SS18-12-11	1.651	1.41	1.462	1.8	0.0044	8.9	9.0	19.6	1.8	0.814	19.4	2.0	48.2	7.6	0.251	28.2	3.2
SS18-12-14	1.418	1.97	1.494	2.3	0.0037	6.3	6.6	16.8	1.1	0.819	16.5	1.4	36.5	4.7	0.211	26.3	2.4
SS18-12-15	2.498	1.41	1.987	1.8	0.0055	5.7	5.9	17.4	1.0	0.807	17.4	1.3	47.7	6.2	0.280	24.6	2.1
SS18-12-23	4.059	1.50	3.037	1.9	0.0124	6.9	7.1	25.6	1.8	0.828	24.9	2.2	46.6	5.9	0.298	35.3	3.3
Best fit eruption age ± 2σ (both in ka)																**31.1**	**1.9**
SS36-6-2	3.119	2.35	3.387	2.7	0.0075	5.8	6.2	15.1	0.9	0.868	14.0	1.1	35.1	5.7	0.214	22.1	2.0
SS36-6-3	1.807	1.52	2.136	2.2	0.0050	5.3	5.6	16.0	0.9	0.851	15.1	1.1	41.2	13.5	0.196	23.3	2.3
SS36-6-5	4.169	2.29	4.952	2.8	0.0142	5.9	6.3	19.7	1.2	0.891	17.8	1.4	59.1	13.1	0.195	26.0	2.6
SS36-6-6	5.633	2.29	5.386	3.8	0.0161	5.0	5.9	19.7	1.2	0.867	18.3	1.4	30.7	7.2	0.243	28.4	2.3
SS36-6-8	8.350	2.29	8.131	3.7	0.0268	3.8	4.8	21.8	1.1	0.845	20.8	1.4	37.8	6.8	0.238	32.4	2.4
SS36-6-11	5.806	3.63	5.751	3.9	0.0155	6.1	6.9	17.9	1.2	0.861	16.7	1.4	37.2	6.7	0.234	25.8	2.4
SS36-6-14	3.843	2.29	3.983	2.9	0.0075	4.1	4.7	12.7	0.6	0.865	11.8	0.8	38.8	10.1	0.224	18.1	1.5
SS36-6-16	5.117	2.29	4.740	3.0	0.0118	7.0	7.5	16.4	1.2	0.891	14.8	1.3	36.2	6.5	0.250	22.3	2.2
SS36-6-17	6.578	2.29	6.765	3.2	0.0174	4.6	5.3	17.2	0.9	0.866	16.0	1.2	32.6	5.2	0.226	25.5	2.0
SS36-6-19	3.436	1.52	3.266	2.1	0.0082	4.2	4.5	16.6	0.7	0.876	15.2	1.0	35.8	10.0	0.244	23.0	1.8
Best fit eruption age ± 2σ (both in ka)																**23.7**	**1.3**
SS43-4-b*	0.169	1.45	0.238	1.8	0.0305	2.9	3.3	902.1	29.7	0.837	867.3	51.6	566.0	71.6	0.225	n/a	n/a

SS43-4-d	0.423	1.96	0.571	2.3	0.0597	1.3	2.4	732.2	17.3	0.867	679.6	37.1	710.3	55.5	0.234	708.5	41.6
SS43-4-h	0.177	1.45	0.217	1.8	0.0190	5.3	5.5	601.7	33.0	0.844	573.7	42.4	659.5	38.7	0.258	603.4	52.2
SS43-4i	0.058	1.77	0.085	2.1	0.0064	6.4	6.6	534.1	35.3	0.829	518.5	42.8	377.2	159.5	0.216	539.2	46.9
SS43-4j*	0.059	2.24	0.085	2.5	0.0026	13.8	13.9	216.3	30.1	0.827	210.4	31.1	793.1	89.7	0.218	n/a	n/a
SS43-4-k	0.193	1.45	0.266	1.8	0.0261	3.3	3.7	689.5	25.3	0.868	639.3	39.4	783.8	36.1	0.230	653.2	46.6
SS43-4-o1	0.110	1.97	0.158	2.3	0.0131	3.0	3.6	586.7	21.0	0.791	596.9	36.3	714.0	35.6	0.221	618.9	45.6
SS43-4-o2	0.377	1.43	0.569	1.8	0.0557	1.3	2.0	696.2	14.2	0.831	674.1	36.1	621.2	75.8	0.210	710.8	38.6
SS43-4-w	0.094	1.49	0.176	1.8	0.0156	5.6	5.8	648.9	37.6	0.806	647.9	49.4	638.8	72.5	0.169	676.4	52.6
Best fit eruption age ± 2σ (both in ka)																**651.2**	**34.2**
SS55-1-b*	0.240	1.99	0.209	2.3	0.0251	2.1	2.8	775.3	21.7	0.776	803.9	45.5	786.6	23.5	0.299	n/a	n/a
SS55-1-d	6.938	1.41	5.824	1.8	0.7014	0.6	1.6	773.4	12.0	0.874	712.0	37.0	769.0	14.5	0.311	763.7	46.5
SS55-1-e	12.432	1.41	9.569	1.9	1.1776	0.6	1.6	774.9	12.4	0.878	710.2	37.0	788.5	38.7	0.339	736.1	43.6
Best fit eruption age ± 2σ (both in ka)																**750.0**	**60.6**
SS58-6-a	4.276	1.97	3.132	2.3	0.2668	0.9	2.0	530.0	10.7	0.854	499.4	26.6	546.6	31.0	0.307	532.5	31.2
SS58-6-b	4.685	1.41	3.628	1.8	0.3017	1.1	1.8	524.2	9.4	0.900	468.7	24.7	534.8	18.1	0.290	502.6	32.7
SS58-6-c	0.568	1.42	0.520	1.8	0.0370	2.4	2.8	465.4	13.0	0.823	455.0	25.9	499.7	19.5	0.246	501.4	29.7
SS58-6-e	1.353	2.00	1.154	2.3	0.0775	1.1	2.1	432.9	9.2	0.877	397.2	21.3	505.1	44.5	0.263	416.7	27.0
SS58-6-f	1.167	1.42	1.226	1.8	0.0874	1.5	2.1	478.9	10.2	0.871	442.4	23.9	448.3	32.6	0.214	480.1	25.5
SS58-6-g	9.752	1.41	6.524	1.8	0.5048	0.6	1.5	470.6	7.1	0.858	441.4	22.9	562.3	12.9	0.336	455.1	26.8
Best fit eruption age ± 2σ (both in ka)																**477.3**	**22.9**
SS68-10-1*	12.097	1.97	4.415	2.3	0.1889	0.9	1.8	213.8	3.9	0.820	209.8	11.0	secular equilibrium		0.542	n/a	n/a
SS68-10-2*	1.129	1.42	0.517	1.8	0.0159	5.6	5.8	167.1	9.6	0.719	187.0	14.2	111.8	14.0	0.432	n/a	n/a
SS68-10-3	0.317	1.43	0.398	1.8	0.0027	9.2	9.3	47.4	4.4	0.769	49.6	5.2	104.8	16.5	0.158	68.2	9.0
SS68-10-4	0.471	1.42	0.638	1.8	0.0038	6.1	6.3	41.7	2.6	0.755	44.4	3.6	99.5	13.0	0.146	62.7	6.6
SS68-10-6	0.436	1.96	0.537	2.3	0.0042	7.7	7.9	54.3	4.3	0.779	56.1	5.2	122.4	17.3	0.161	74.3	8.7
SS68-10-8*	10.106	1.41	3.324	1.8	0.1442	0.9	1.5	207.9	3.2	0.781	214.2	11.1	secular equilibrium		0.602	n/a	n/a
Best fit eruption age ± 2σ (both in ka)																**67.2**	**9.0**
MT-J-1	0.192	2.09	1.358	2.2	0.0009	14.5	14.7	5.1	0.7	0.731	7.0	1.1	n/a	n/a	n/a	n/a	n/a
MT-J-3	0.259	1.53	0.332	1.8	0.0001	214.8	214.8	1.4	3.1	0.793	1.8	3.9	n/a	n/a	n/a	n/a	n/a
MT-J-4	1.924	1.51	1.653	1.8	0.0017	12.7	12.8	6.6	0.8	0.822	8.1	1.1	n/a	n/a	n/a	n/a	n/a
MT-J-5	0.095	2.09	0.627	2.2	0.0004	32.6	32.7	5.0	1.6	0.725	6.9	2.3	n/a	n/a	n/a	n/a	n/a
MT-J-7	0.116	1.56	0.488	1.7	0.0002	69.7	69.8	3.2	2.2	0.623	5.1	3.6	n/a	n/a	n/a	n/a	n/a
MT-J-8	0.060	1.63	0.433	1.8	0.0003	76.1	76.1	5.0	3.8	0.685	7.3	5.6	n/a	n/a	n/a	n/a	n/a
Weighted mean eruption age ± 2σ (both in ka)											**7.2**	**1.4**					
SA-X-1*	1.523	1.71	2.379	2.5	0.0039	9.3	9.6	11.7	1.1	0.886	n/a	n/a	n/a	n/a	n/a	n/a	n/a
SA-X-3*	3.477	1.25	4.621	2.0	0.0053	6.3	6.6	8.0	0.5	0.875	n/a	n/a	n/a	n/a	n/a	n/a	n/a
SA-X-4	0.815	1.26	2.979	2.0	0.0016	13.2	13.4	4.2	0.6	0.835	5.0	0.7	n/a	n/a	n/a	n/a	n/a

Sample																	
SA-X-5	4.074	1.25	8.596	2.1	0.0032	9.3	9.5	2.8	0.3	0.882	3.1	0.3	n/a	n/a	n/a	n/a	n/a
SA-X-6	1.579	1.75	1.457	2.6	0.0011	14.9	15.0	4.7	0.7	0.884	5.4	0.9	n/a	n/a	n/a	n/a	n/a
SA-X-7	2.167	1.25	6.621	2.4	0.0034	5.8	6.2	4.0	0.2	0.822	4.8	0.4	n/a	n/a	n/a	n/a	n/a
SA-X-8	2.911	1.73	5.031	1.8	0.0018	14.7	14.8	2.6	0.4	0.876	3.0	0.5	n/a	n/a	n/a	n/a	n/a
SA-X-9	1.073	2.79	4.862	2.1	0.0018	11.9	12.0	2.9	0.3	0.870	3.3	0.4	n/a	n/a	n/a	n/a	n/a
SA-X-10	0.821	1.74	3.791	1.8	0.0011	23.0	23.1	2.3	0.5	0.838	2.8	0.7	n/a	n/a	n/a	n/a	n/a
SA-X-11	0.934	1.73	3.110	1.7	0.0008	26.7	26.8	2.0	0.5	0.850	2.4	0.6	n/a	n/a	n/a	n/a	n/a
SA-X-12	0.663	1.74	4.557	1.7	0.0019	14.5	14.6	3.3	0.5	0.841	3.9	0.6	n/a	n/a	n/a	n/a	n/a
Weighted mean eruption age ± 2σ (both in ka)											**3.6**	**0.7**					
WR01-A-1*	0.351	3.43	0.336	3.5	0.0393	1.3	3.1	771.8	24.3	0.770	n/a	n/a	n/a	n/a	n/a	n/a	n/a
WR01-A-2*	4.351	2.16	3.624	3.4	0.2006	0.8	2.8	354.9	9.9	0.839	n/a	n/a	n/a	n/a	n/a	n/a	n/a
WR01-A-3	0.136	2.32	0.255	3.0	0.0222	4.7	5.4	636.9	34.7	0.816	780.5	57.7	n/a	n/a	n/a	n/a	n/a
WR01-A-4	1.286	1.33	1.231	2.2	0.1045	1.0	2.0	560.1	11.3	0.849	659.7	35.6	n/a	n/a	n/a	n/a	n/a
WR01-A-5	0.253	2.22	0.206	2.9	0.0228	4.3	4.9	704.1	34.5	0.817	861.9	60.3	n/a	n/a	n/a	n/a	n/a
WR01-A-6	0.222	1.38	0.182	1.9	0.0150	4.1	4.3	528.4	22.9	0.788	670.5	44.4	n/a	n/a	n/a	n/a	n/a
WR01-A-7*	3.856	2.06	3.258	2.3	0.0057	6.9	7.2	11.2	0.8	0.766	n/a	n/a	n/a	n/a	n/a	n/a	n/a
WR01-A-9	0.430	3.69	0.424	3.5	0.0389	1.7	3.3	608.5	20.4	0.789	771.2	46.4	n/a	n/a	n/a	n/a	n/a
WR01-A-10	0.655	2.17	0.458	3.0	0.0494	1.8	2.9	663.9	19.5	0.828	801.9	46.5	n/a	n/a	n/a	n/a	n/a
WR01-A-11	1.368	2.16	0.820	2.6	0.0808	1.5	2.5	581.6	14.5	0.765	760.3	42.5	n/a	n/a	n/a	n/a	n/a
Weighted mean eruption age ± 2σ (both in ka)											**740**	**66**					

*Zircon crystals which were not used in the final calculation of eruption age as the crystals was thought to either be inherited or contained fluid inclusions seen in a eruption age > crystallisation age or in the case of xenolith samples - not fully reset for Helium

[a]TAU - total analytical uncertainty

[b]alpha-ejection correction factor (Farley et al., 2002) with an estimated 1σ uncertainty of 5%

[c]D_{230} - melt-zircon Th-U fractionation coefficient calculated as (Th/U)zircon/(Th/U)magma, whereby a whole rock value measured externally was used for (Th/U)magma (Farley et al., 2002; Schmitt et al., 2010)

Supplementary Material VI

Sample code	Latitude	Longitude	Whole rock (238U/232Th)[a]	± 1sig	Whole rock (230Th/232Th)	± 1sig
WR-01	33.23700	126.34558	n/a	n/a	n/a	n/a
SS43-4	33.28214	126.46514	n/a	n/a	n/a	n/a
SS58-6	33.27178	126.60775	n/a	n/a	n/a	n/a
SS68-10	33.24211	126.61092	0.605	0.028	0.605	0.028
HS-02	33.45703	126.41047	0.653	0.035	0.653	0.035

SS14-28	33.35550	126.50042	0.404	0.014	0.404	0.014
SS18-12	33.36550	126.60700	0.681	0.055	0.681	0.055
SS15-66	33.37422	126.52983	0.414	0.008	0.414	0.008
SS15-43	33.37106	126.52378	0.391	0.020	0.391	0.020
SS15-45	33.35811	126.52547	0.584	0.038	0.584	0.038
SS15-48	33.35583	126.52617	0.658	0.034	0.658	0.034
SS36-6	33.32186	126.55950	0.709	0.049	0.709	0.049
SS07-3[b]	33.38050	126.56825	0.539	0.054	0.539	0.054
SS14-21	33.35875	126.49892	0.327	0.013	0.327	0.013
SS15-SN	33.36372	126.52917	0.370	0.003	0.370	0.003
SS55-1	33.27528	126.52858	n/a	n/a	n/a	n/a
HS100-5	33.40769	126.49528	0.407	0.009	0.407	0.009
SA-X	33.20619	126.29028	n/a	n/a	n/a	n/a
MT-J	33.53000	126.76472	n/a	n/a	n/a	n/a
SS66-1	33.25083	126.54917	n/a	n/a	n/a	n/a

a) Calculated from whole rock 238U and 232Th concentrations

b) Unfortunately this sample was very weathered and so a whole rock value could not be measured and an average of Mt Halla whole rock values was used uncertainty was estimated at 10% due to this lack of measurement

Chapter 6

Conclusions

Methodological improvement of geochronological techniques usually aims to increase accuracy and precision, thereby increasing confidence in the temporal resolution of geological events. Greater age resolution is required to answer important geological and archaeological questions about the nature of the planet we inhabit. These questions range from understanding the duration of magma storage in supervolcanoes (e.g., Stelten et al., 2015; Wotzlaw et al., 2015), to the onset of human expansion in Europe following the Last Glacial Maximum (Blockley et al., 2006).

Zircon double-dating (ZDD) is a geochronological method which is used to date volcanic products <1 Ma. Eruption ages of a sample are determined by combining single crystal zircon (U-Th)/He ages and U-Pb or U-Th disequilibrium crystallisation ages measured on the same grains. This thesis has contributed several methodological developments which improve the ZDD technique, with a focus on three aspects: Firstly, the work has demonstrated that zircon U-Th disequilibrium dating can be carried out on the SHRIMP II instrument, increasing the range of instruments on which the crystallisation age measurement can be performed. This allows U-Th disequilibrium dating to be undertaken in a wider range of laboratories and provides additional validation for the technique by showing that ages can be replicated using different instrument platforms. Secondly, this thesis has provided the first viable age reference material for zircon U-Th disequilibrium dating. Reference zircon SS14-28 can be used to assess the reproducibility of ages across different laboratories and provides a known age that can be used to help set up this technique in new laboratories. Finally, the theoretical accuracy of the ZDD technique for crystals with a protracted crystallisation history has been improved and the impact of the simplifying assumption of a single crystallisation age has been evaluated. While removing this assumption has decreased the precision of the ZDD technique, it is envisaged that in the future, it will result in improved mathematical models and, in turn, result in more accurate ZDD ages.

Additionally, this thesis has dated volcanic products in two case studies. One

particularly noteworthy outcome is the lowest published age determined by ZDD of 2 ± 1 ka, measured on a trachyte from Jeju Island, South Korea.

6.1 U-Th disequilibrium dating

This thesis has presented two main improvements to zircon U-Th disequilibrium dating protocols. Firstly, the research resulted in development of the first U-Th disequilibrium dating methodology for the SHRIMP II, which includes a novel background model for the SHRIMP II and an associated (freely available) computer program (Chapter 3). The methodology yielded crystallisation ages within uncertainty of those measured on the CAMECA IMS 1280, the instrument most commonly utilised for U-Th disequilibrium dating (e.g., Reid et al., 1997; Schmitt, 2006).

Secondly, this work has provided an age reference material, SS14-28, for the zircon U-Th disequilibrium dating method (Chapter 4). This sample fulfils the necessary requirements of an age reference material: it is young (<350 ka) and in secular disequilibrium, is homogenous in terms of age (i.e., every crystal yields the same age within uncertainty) and it is available in abundance. SS14-28 was dated using four separate instrument platforms (SHRIMP II, CAMECA IMS 1280, sector field high resolution LA-ICPMS and MC-LA-ICPMS) and the crystallisation age was found to be 82 ± 6 ka (2σ). This reference material will allow external calibration for individual runs in laboratories around the world and make it easier to develop the U-Th disequilibrium technique in new laboratories.

Although ages measured on the SHRIMP II and CAMECA IMS 1280 were coeval within uncertainty, the uncertainties measured on the SHRIMP II (20% to ca. 250%), are significantly larger than those obtained using the CAMECA IMS 1280 (12% to ca. 190%). This difference is due to the lower intensity of the primary beam on the SHRIMP II compared to the CAMECA IMS 1280 and consequently a much smaller sample volume on the SHRIMP (665.0 μm^3) compared to the CAMECA (1631.8 μm^3). It is hypothesised that the SHRIMP uncertainties could be reduced in future by increasing the counting times or increasing the primary beam size, both at the expense of increasing analytical volume.

However, even if the uncertainty cannot be reduced for SHRIMP II U-Th disequilibrium dating of zircon, the development of an exponential background correction on the SHRIMP II still has value as it opens up the possibility of further complex background corrections on the SHRIMP II for other applications. Additionally, given the apparent difference between the mathematical model for low counts developed here in the Crayfish program (Chapter 3) and those currently utilised in SQUID 3 (Bodorkos et al., 2020), the latter could be re-examined and potentially enhanced using the mathematical models developed in this work.

Moving away from the particulars of the instrumentation, one issue with the current U-Th disequilibrium dating methodologies is that the uncertainty is positively correlated with age, and therefore older crystallisation ages usually have larger uncertainties. This is due to the nature of the age calculation from isotope ratios. While the relative uncertainty on the isotope measurements is the same, the relative uncertainty on the ages increases. One possible method of decreasing the uncertainty on older crystallisation ages, would be to increase the precision of the isotope measurements. This could be attempted by increasing the counting times on isotopes of interest. However, this may not be possible without consuming a greater volume of sample (e.g., LA-ICPMS U-Pb).

6.2 ZDD work flow

The research in this thesis has resulted in a new ZDD protocol for zircon crystals in secular disequilibrium with protracted crystallisation histories (Figure 6.1; Marsden et al., 2021b). This protocol aims to reduce a (potential) systematic disequilibrium over-correction of individual (U-Th)/He dates (which leads to a systematic over-corrected sample eruption age) by ensuring that the core crystallisation ages of individual zircon crystals are determined. These interior crystallisation ages are then used alongside the rim crystallisation ages to disequilibrium correct the same (U-Th)/He date for the crystal to yield a range for sample eruption age for zircon grains with a protracted crystallisation history. This work has shown that, in some cases, the difference between a rim-corrected eruption age and a core-corrected eruption age can be up to 15% and that the simplifying assumption of a single crystallisation age could lead to an over-correction of the eruption age. This amendment to the ZDD analytical protocol may be applicable to other double-dating approaches as they are developed (e.g., (U-Th)/He dating of apatite, magnetite or monazite combined with crystallisation ages on the same grain for applications such as combined crystal system dating of volcanic deposits).

6.2.1 ZDD future work

While this research has analysed the effects of crystallisation age zonation on ZDD ages, it has focussed on calculating both a rim-corrected eruption age and a core-corrected eruption age and using the resulting range. The next step would be to create a 3D model of how crystallisation age varies throughout the crystal based on multiple crystallisation age measurements (Friedrichs et al., 2021). This model of crystallisation age could then be used to calculate a whole crystal disequilibrium corrected eruption age. Furthermore, these models could incorporate parent isotope concentrations to improve the accuracy of the Ft correction factor calculation (Hourigan et al., 2005; Bargnesi et al., 2016; Danišík et al., 2017).
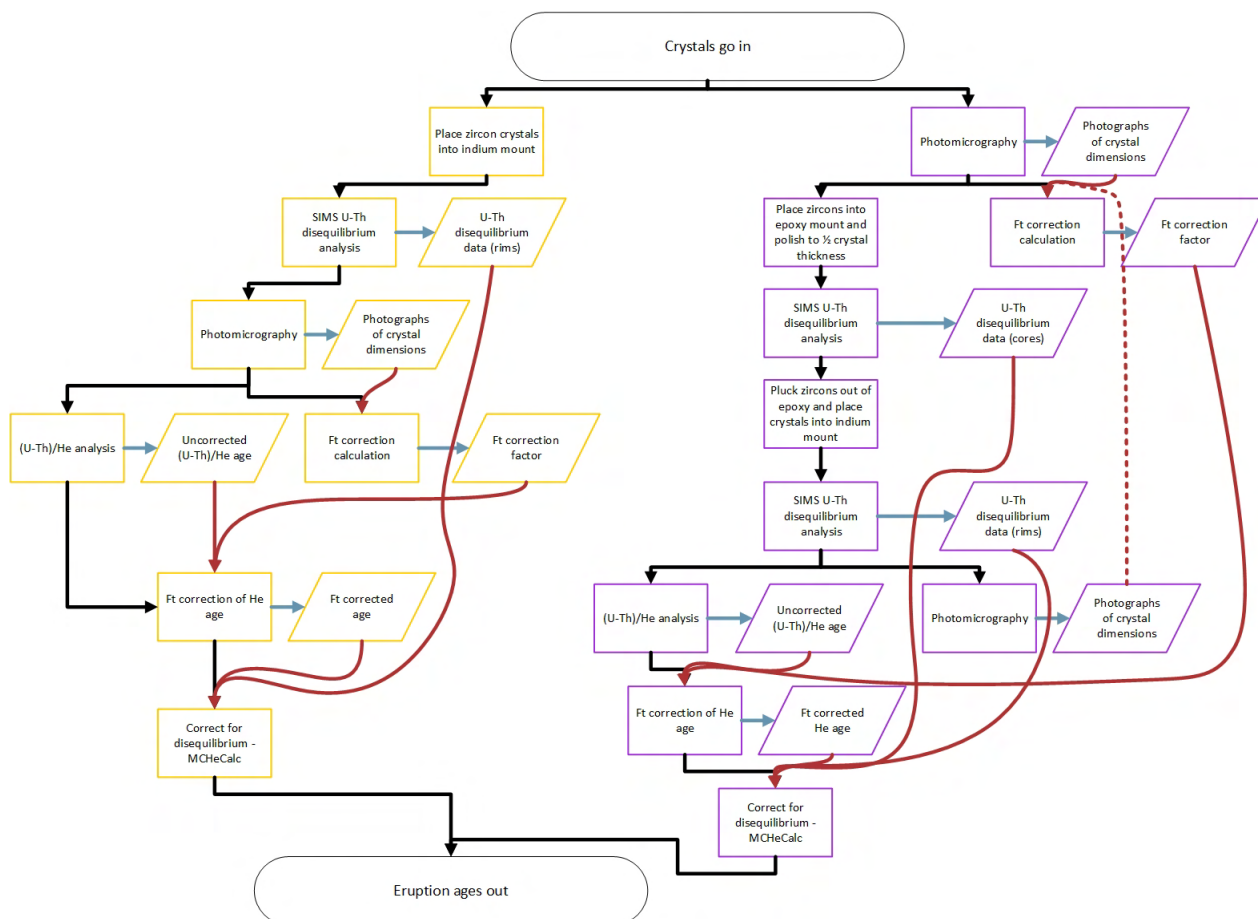
Figure 6.1: Flowchart comparing the protocol before this thesis (yellow boxes) and the proposed protocol in this thesis (purple boxes). Red arrows indicate data, blue arrows indicate a process. Black arrows show the order of the protocol (Marsden et al., 2021b).

Such a model could be used to test whether over-dispersion of individual crystal disequilibrium rim-corrected (U-Th)/He ages is due to the simplifying assumptions of both age and parent isotope concentration homogeneity.

6.3   Dating of volcanic deposits

This thesis has applied ZDD to two case studies: South West Hokkaido (Japan) and Jeju Island (South Korea). The eruption ages obtained for Jeju Island show that there were periods of increased trachyte eruption on the island, as well a recent volcanic eruption at 2 $\pm$ 1 ka ($\sim$0 Common Era). This is one of the youngest geochronological eruption ages ever measured using ZDD. Importantly, the results indicate that Jeju Island is an active volcano which has important implications both for the inhabitants of the island, and the many tourists who visit this UNESCO world heritage site. Additionally, the zircon crystallisation age spectra of trachytes on Jeju Island are simple with single population of maximum crystallisation, when compared to other alkaline systems globally. This suggests that the Jeju Island trachytes underwent a relatively simple magma petrogenesis, presumably in a simple plumbing system (Marsden et al., 2021a).

The case study from SW Hokkaido, Japan, led to the finding that the regionally important Toya tephra may be younger than previously reported at $< 96 \pm 5$ ka rather than 109 ± 3 ka, using ages from bracketing tephra (Marsden et al., 2021b).

Further ZDD analysis could be applied to both of these regions. For example, directly determining the eruption age using ZDD of the Toya tephra would give a further geochronological result for the tephra and test the ZDD methodology. This would help to improve the Quaternary tephrostratigraphic framework of Japan. ZDD could be carried out on many other volcanoes in the surrounding Pacific Ring of Fire to either validate the current age from another dating method or determine an age which has not been possible before. This largescale regional work could be done in locations such as New Zealand, Kamchatka and the Philippines, while keeping existing dating work carried out by methods such as chronostratigraphy in mind.

Additionally, further trachyte from cores on Jeju Island could be dated to ensure there was no sampling bias from trachyte selection. Alternatively, other types of analyses could also be carried out to complement the ZDD data, such as trace element analyses on zircon crystals and their fluid inclusions to further elucidate the genesis of trachyte within Jeju Island volcanic field.

6.4 Summary

Zircon double-dating is a critical tool for dating Quaternary volcanic eruptions. Increasing the accuracy and precision of this method while taking analytical scale into account, increases the resolution at which we can date volcanic eruptions and increases confidence in the resultant ages. Understanding the evolution and recharge of magma within a volcanic setting gives insight into the rate of change of volcanic systems and can inform on eruptive periodicity. This, in turn, can improve our preparedness for large explosive volcanic eruptions and our hazard prediction capabilities.

6.5 References

Bargnesi E. A., Stockli D. F., Hourigan J. K. and Hager C. (2016) Improved accuracy of zircon (U–Th)/He ages by rectifying parent nuclide zonation with practical methods. Chemical Geology 426, 158–169.

Blockley S. P. E., Blockley S. M., Donahue R. E., Lane C. S., Lowe J. J. and Pollard A. M. (2006) The chronology of abrupt climate change and Late Upper Palaeolithic human adaptation in Europe. Journal of Quaternary Science 21, 575–584.

Bodorkos S., Bowring J. F. and Rayner N. M. (2020) Squid3: next-generation data processing software for sensitive high-resolution ion microprobe (SHRIMP)., Geoscience Australia.

Danišík M., McInnes B. I. A., Kirkland C. L., McDonald B. J., Evans N. J. and Becker T. (2017) Seeing is believing: Visualization of He distribution in zircon and implications for thermal history reconstruction on single crystals. Science Advances 3, e1601121.

Friedrichs B., Schmitt A. K., Lovera O. M. and Atıcı G. (2021) Zircon as a recorder of contrasting magma recharge and eruptive recurrence patterns. Earth and Planetary Science Letters 571, 117104.

Hourigan J. K., Reiners P. W. and Brandon M. T. (2005) U-Th zonation-dependent alpha-ejection in (U-Th)/He chronometry. Geochimica et Cosmochimica Acta 69, 3349–3365.

Marsden R. C., Danišík M., Ahn U.-S., Friedrichs B., Schmitt A. K., Kirkland C. L., McDonald B. and Evans N. J. (2021a) Zircon double-dating of Quaternary eruptions on Jeju Island. Journal of Volcanology and Geothermal Research, 107171.

Marsden R. C., Danišík M., Ito H., Kirkland C. L., Evans N. J., Miura D., Friedrichs B., Schmitt A. K., Uesawa S. and Daggitt M. L. (2021b) Considerations for double dating zircon in secular disequilibrium with protracted crystallisation histories. Chemical Geology, 120408.

Reid M. R., Coath C. D., Mark Harrison T. and McKeegan K. D. (1997) Prolonged residence times for the youngest rhyolites associated with Long Valley Caldera: ^{230}Th—^{238}U ion microprobe dating of young zircons. Earth and Planetary Science Letters 150, 27–39.

Schmitt A. K. (2006) Laacher See revisited: High-spatial-resolution zircon dating indicates rapid formation of a zoned magma chamber. Geology 34, 597–600.

Stelten M. E., Cooper K. M., Vazquez J. A., Calvert A. T. and Glessner J. J. G. (2015) Mechanisms and Timescales of Generating Eruptible Rhyolitic Magmas at Yellowstone Caldera from Zircon and Sanidine Geochronology and Geochemistry. Journal of Petrology 56, 1607–1642.

Wotzlaw J.-F., Bindeman I. N., Stern R. A., D'Abzac F.-X. and Schaltegger U. (2015) Rapid heterogeneous assembly of multiple magma reservoirs prior to Yellowstone supereruptions. Sci Rep 5, 14026.

Appendix A - MCHeCalc

MCHeCalc - A Monte Carlo numerical solution for zircon double-dating (ZDD)

MCHeCalc is a piece of statistics software written in Fortran by O. Lovera (Lovera et al., 2009; Schmitt et al., 2010). MCHeCalc uses Monte Carlo simulation to calculate sample eruption age from multiple zircon crystals which are in disequilibrium. Monte Carlo simulation is a numerical method which uses repeated random sampling to determine probabilities of results. It runs tests in a repeated manner and counts the results to create a probability distribution. In this case the probability distribution for sample eruption age gives the 'likeliest' sample eruption age (with uncertainty) as a result.

Numerical methods for calculating sample eruption age are used to estimate the error propagation for the eruption age. The degree of disequilibrium in the ^{238}U series which affects the production of alpha particles (^{4}He) depends on the time between crystallisation and eruption of the zircon crystal. MCHeCalc calculates a disequilibrium corrected (U-Th)/He date for each crystal by taking a random value from the probability distribution of the uncorrected (for disequilibrium) (U-Th)/He date, and a random value from the probability distribution of the crystallisation age. These probability distributions are modelled as normal distributions using the value and uncertainty input by the user. These randomly selected 'age' values and the user input value for D_{230Th} and D_{231Pa} are used to calculate a disequilibrium corrected (U-Th)/He date. This is repeated either 10^5 or 10^6 times (each result from this repeated calculation is called a trial), depending on the choice of the user (for the results in this thesis 10^6 repetitions were used). If the single trial disequilibrium corrected (U-Th)/He date is greater than the crystallisation age the trial result is not used in the final disequilibrium corrected (U-Th)/He date result and is instead re-run. These results are given as a disequilibrium corrected (U-Th)/He date probability distribution for an individual crystal. The resulting individual disequilibrium corrected (U-Th)/He dates are then used to calculate a sample eruption age, with uncertainties and a goodness of fit parameter.

References

Lovera O., Schmitt A. K. and Stockli D. (2009) Improving combined U-Th and (U-Th)/He geochronology by Monte Carlo statistical corrections for uranium series disequilibrium. 2009 Portland GSA Annual Meeting

Schmitt A. K., Stockli D. F., Niedermann S., Lovera O. M. and Hausback B. P. (2010) Eruption ages of Las Tres Vírgenes volcano (Baja California): A tale of two helium isotopes. Quaternary Geochronology 5, 503-511.

Appendix B - GriFt calculated Ft correction factors

Crystal name	Full z-dimension (um)	Ft correction factor[a]	uncertainty[b]	Width after grinding (um)	Depth ground (um)[d]	Ft correction factor
Km-1 a	239	0.900	0.045	158	61	0.916
Km-1 b	137	0.832	0.042	60	74	0.817
Km-1 c	150	0.841	0.042	90	60[f]	0.854
Km-1 d	104[e]	0.801	0.040	44	60[f]	0.782
Km-1 e	131	0.828	0.041	64	67	0.825
Km-1 f	110	0.789	0.039	43	67	0.757
Km-1 g	165	0.868	0.043	95	70	0.879
Km-1 h	71	0.725	0.036	51	20	0.768
Km-1 i	186	0.870	0.044	101[c]	79	0.884
Km-1 j	123	0.819	0.041	82	41	0.842
Km-2 a	116	0.813	0.041	64	52	0.820
Km-2 b	104	0.786	0.039	53	51	0.787
Km-2 c	131	0.838	0.042	65	66	0.838
Km-2 d	118	0.807	0.040	67	51	0.820
Km-2 f	116	0.805	0.040	57	59	0.802
Km-2 g	163	0.843	0.042	92	71	0.852
Km-2 h	132	0.820	0.041	80	52	0.838
Km-2 i	140[e]	0.834	0.042	89	51	0.851
Km-2 j	132	0.813	0.041	68	64	0.818

a) This Ft correction factor is calculated using GriFt which is moderately different to Flojt due to measurements being taken for each crystal point rather than just length, width and height.

b) This uncertainty is 5% - however, it is represented as an absolute in this table in order to allow for comparison between the Ft correction factor calculated for a full crystal and the actual crystal width.

c) This crystal was ground at a clear angle and GriFt was used to model this and so 101 is a representation of this.

d) This depth is highly variable, however the Ft corrections are not affected outside of 5% uncertainty. This variability is partially due to the fact the measurements made in this study were opportunistic.

e) Unfortunately this is an estimate z-dimension due to an insufficient quality of microscope images taken for this grain.

f) This depth ground was estimated from the average of all other depths ground.

Appendix C - Copyright statements

The chapters in this thesis consist of journal papers that were either in-press or under review at time of submission. The following copyright statements are relevant for Chapters 2-5.

Chapter 2 - Considerations for double-dating zircon in secular disequilibrium with protracted crystallisation histories.

Published Elsevier articles are suitable for the public version of the thesis on Curtin University library e-space. The full citation and DOI is as follows:

Ruby C. Marsden, Martin Danišík, Hisatoshi Ito, Christopher L. Kirkland, Noreen J. Evans, Daisuke Miura, Bjarne Friedrichs, Axel K. Schmitt, Shimpei Uesawa, Matthew L. Daggitt, Considerations for double-dating zircon in secular disequilibrium with protracted crystallisation histories, Chemical Geology, Volume 581, 2021, 120408, ISSN 0009-2541, https://doi.org/10.1016/j.chemgeo.2021.120408.

Chapter 3 - A new approach to SHRIMP II zircon U-Th disequilibrium dating

Published Elsevier articles are suitable for the public version of the thesis on Curtin University library e-space. The full citation and DOI is as follows:

Ruby C. Marsden, Christopher L. Kirkland, Martin Danišík, Matthew L. Daggitt, Ung-San Ahn, Bjarne Friedrichs, Noreen J. Evans, A new approach to SHRIMP II zircon U-Th disequilibrium dating, Computers & Geosciences, Volume 158, 2022, 104947, ISSN 0098-3004, https://doi.org/10.1016/j.cageo.2021.104947.

Chapter 4 - SS14-28: an age reference material for zircon U-Th disequilibrium dating

Accepted Wiley manuscripts are suitable for the public version of the thesis on Curtin University library e-space with the following copyright statement:

Chapter 5 - Zircon double-dating of Quaternary eruptions on Jeju Island, South Korea

Published Elsevier articles are suitable for the public version of the thesis on Curtin University library e-space. The full citation and DOI is as follows: